



HAL
open science

Exploring the coordination properties of acridine-based tridentate ligands on ruthenium

Ali Awada

► **To cite this version:**

Ali Awada. Exploring the coordination properties of acridine-based tridentate ligands on ruthenium. Inorganic chemistry. Université Grenoble Alpes, 2019. English. NNT : 2019GREAV072 . tel-03132486v2

HAL Id: tel-03132486

<https://theses.hal.science/tel-03132486v2>

Submitted on 27 May 2021

HAL is a multi-disciplinary open access archive for the deposit and dissemination of scientific research documents, whether they are published or not. The documents may come from teaching and research institutions in France or abroad, or from public or private research centers.

L'archive ouverte pluridisciplinaire **HAL**, est destinée au dépôt et à la diffusion de documents scientifiques de niveau recherche, publiés ou non, émanant des établissements d'enseignement et de recherche français ou étrangers, des laboratoires publics ou privés.

THÈSE

Pour obtenir le grade de

DOCTEUR DE LA

COMMUNAUTE UNIVERSITE GRENOBLE ALPES

Spécialité : Chimie inorganique et Bio inorganique

Arrêté ministériel : 25 mai 2016

Présentée par

Ali AWADA

Thèse dirigée par **Frédérique LOISEAU**, UGA

et codirigée par **Damien JOUVENOT**, UGA

Préparée au sein du **Laboratoire Département de Chimie Moléculaire**

dans **l'Ecole Doctorale Chimie et Sciences du Vivant**

Etude des propriétés de coordination de ligands tridentés à base d'acridine sur le ruthénium

Exploring the coordination properties of acridine-based tridentate ligands on ruthenium

Thèse soutenue publiquement le **26 novembre 2019**,
devant le jury composé de :

Monsieur Benoit COLASSON

Maître de Conférences, Université Paris Descartes, Sorbonne Paris Cité,
Rapporteur

Monsieur Benjamin ELIAS

Professeur, Université catholique de Louvain, Belgique, Rapporteur

Madame Chantal ANDRAUD

Directeur de Recherche, ENS de Lyon, Examineur

Madame Martine DEMEUNYNCK

Directeur de Recherche, Université Grenoble Alpes, Président

Madame Frédérique LOISEAU

Professeur, Université Grenoble Alpes, Directeur de thèse

Monsieur Damien JOUVENOT

Maître de Conférences, Université Grenoble Alpes, Co-directeur de thèse



Dedicated to my father “Abo Ghofran” & my Love “Rola”

Acknowledgments

In this piece of text, I would like to express my sincerest thankfulness to:

Frédérique LOISEAU & Damien JOUVENOT – My great supervisors, I could not have wished for a better advisor than you. Not only that but also as great friends. I would like to thank you for your enormous support, advices, the knowledge you gave me, laughs and everything else. This work would not have been possible without you and your guidance, we have been a great team!

All of the collaborators – I would like to thank the technical supports and all DCM members, Selim Sirach (for the help at the lab), Florian Molton (the engineer of the lab), Christian Philouze (for crystallography), Yohann MOREAU (for TD-DFT calculations) and Guy ROYAL (the head of our small team and for his friendly relation).

My thesis committee – Benoit COLASSON, Benjamin ELIAS, Chantal ANDRAUD, and Martine DEMEUNYNCK for their time and their valuable comments on the manuscript, and for giving me the opportunity to present my Ph.D. research.

My friends and collaborators at the lab – Many thanks to them, whom I shared nice moments within our team: Suzanne ADAM (the engineer of my English), Catalina ASTUDILLO NEIRA, Emiliano MARTINEZ VOLLBERT, Lorna RAMIREZ MELLA, Romain SANAHUGES, Javier GUTIERREZ SALAFRANCA, Ibrahim SHALAYEL, Sparta YOUSSEF SALIBA, Wathiq Sattar ABDUL-HASSAN, Laura WILSON, Angélica MORENO-BETANCOURT, and Monika TRIPATHI.

My family – All of you, both my old (AWADA) one and my new one (ABOU HAMDAN). And mainly so to my father and mother, likely the reason I turned so curious.

My Love & wife, Rola ABOU HAMDAN – Thank you for all your love, care and encouragement, and for our future together. I love you, and would not have managed this without you being beside me.

Table of contents

Chapter 1: General Introduction	7
I. <i>Renewable energy</i>	9
I.1. Environmental and energetic crisis	9
I.2. Solar energy	10
I.3. Inspiration from nature	10
II. <i>Artificial photosynthesis – Mimicking natural photosynthesis</i>	14
II.1. Donor moiety	15
II.2. Acceptor moiety	17
II.3. Photosensitizer	18
II.4. Photosensitizer requirements	19
II.4.1. Stability	19
II.4.2. Absorption properties	19
II.4.3. Redox properties	20
II.4.4. Excited state properties	20
II.5. Solar Fuel Generation	20
III. <i>Ruthenium(II) polypyridyl complexes</i>	26
III.1. Tris-bidentate ligand ruthenium complex $[\text{Ru}(\text{bpy})_3]^{2+}$	27
III.2. $[\text{Ru}(\text{bpy})_3]^{2+}$ excited state reactivity	32
III.2.1. Energy transfer mechanisms	34
III.2.2. Electron transfer mechanism	38
III.3. Stability and induced isomerization of $[\text{Ru}(\text{bpy})_3]^{2+}$	44
III.4. Bis-terdentate ligand ruthenium complex $[\text{Ru}(\text{tpy})_2]^{2+}$	45
IV. <i>Strategies for enhancing the excited state lifetime of Ru(II) complexes with tridentate ligands</i>	47
IV.1. Electron withdrawing and electron donating groups	48
IV.2. Extending the π -conjugated system	51
IV.3. π -accepting ligands	54
IV.4. Optimizing the octahedral coordination geometry (chelate ring expansion)	55
V. <i>Scope of the thesis</i>	59
VI. <i>References</i>	61
Chapter 2: Di-pyridyl acridine-based ligand and its Ru(II) complexes emitting in the NIR region	73
I. <i>Introduction</i>	75
II. <i>Synthesis</i>	76

II.1.	Ligand synthesis	76
II.1.1.	Acyclic starting compound	77
II.1.2.	Cyclic starting compound	78
II.2.	Ru(II) complexes synthesis	82
II.2.1.	Homoleptic Ru(II) complex synthesis	82
II.2.2.	Heteroleptic Ru(II) complex synthesis	86
II.2.3.	X-ray diffraction of complex 13	88
III.	<i>Electrochemistry</i>	90
III.1.	Oxidation redox processes	92
III.2.	Reduction redox processes	94
III.3.	DFT-calculations	95
IV.	<i>Photophysics</i>	96
IV.1.	Ligand spectroscopic properties	97
IV.1.1.	Absorption spectroscopy	97
IV.1.2.	Fluorescence spectroscopy	98
IV.2.	Ru(II) complexes spectroscopic properties	98
IV.2.1.	Absorption spectroscopy	98
IV.2.2.	DFT-calculations	101
IV.2.3.	Phosphorescent spectroscopy	103
V.	<i>Conclusion</i>	105
VI.	<i>References</i>	106
Chapter 3: Going to a bigger NNN-coordination cavity: di-pyrazolyl acridine-based ligand		109
I.	<i>Introduction</i>	111
II.	<i>Synthesis</i>	112
II.1.	Ligand synthesis	112
II.2.	Ru(II) complexes synthesis	114
II.2.1.	Homoleptic Ru(II) complex	114
II.2.2.	Heteroleptic Ru(II) complex	117
III.	<i>Electrochemistry</i>	121
III.1.	Redox properties of dtdpza ligand	123
III.2.	Redox properties of the Ru(II) complexes	124
III.2.1.	Oxidation process	126
III.2.2.	Reduction redox process	126
IV.	<i>Photophysics</i>	127
IV.1.	Ligand spectroscopic properties	127

IV.2. Ru(II) complexes spectroscopic properties	128
V. Conclusion	131
VI. References	132
Chapter 4: SNS-thioether acridine-based ligand and its Ru(II) complexes	135
I. Introduction	137
II. Synthesis	138
II.1. Ligand synthesis	138
II.2. Ru(II) complexes synthesis	140
II.2.1. Homoleptic Ru(II) complex	140
II.2.2. Heteroleptic Ru(II) complex	141
II.2.3. X-ray diffraction of complex 19	143
III. Electrochemistry	145
III.1. Thioether ligand redox properties	146
III.2. Redox properties of the Ru(II) complexes	148
IV. Photophysics	150
IV.1. Ligand spectroscopic properties	151
IV.2. Ru(II) complexes spectroscopic properties	152
V. Photochemistry	156
VI. Conclusion	157
VII. References	158
Chapter 5: SNS-thioanisole ligand and its photochemically active Ru(II) complexes	161
I. Introduction	163
II. Synthesis	164
II.1. Ligand synthesis	164
II.2. Ru(II) complexes synthesis	165
II.2.1. Homoleptic Ru(II) complex	165
II.2.1. Heteroleptic Ru(II) complex	168
III. Electrochemistry	172
III.1. Thioanisole ligand redox properties	173
III.2. Redox properties of the Ru(II) complexes	175
IV. Photophysics	178
IV.1. Thioanisole ligand spectroscopic properties	178

Table of contents

IV.2. Ru(II) complexes spectroscopic properties	179
V. <i>Photochemistry</i>	182
V.1. Heteroleptic complex photoactivity	183
V.2. Homoleptic complex photoactivity.....	186
VI. <i>Conclusion</i>	192
VII. <i>References</i>	193
General Conclusion	197
Experimental Section	201
Appendix	221

List of abbreviations

aq:	Aqueous
A:	Acceptor
bpy:	2,2'-bipyridine
CSS:	Charge Separated State
CV:	Cyclic Voltammetry
D:	Donor
DCM:	Dichloromethane
DMF:	Dimethylformamide
DMSO:	Dimethyl Sulfoxide
ESI-MS:	Electrospray Mass Spectrometry
ET:	Electron Transfer
E _n T:	Energy Transfer
GS:	Ground State
HOMO:	Highest Occupied Molecular Orbital
ISC:	Intersystem Crossing
IC:	Internal Conversion
<i>J</i> :	Coupling constant in Hz
LC:	Ligand Centered
LUMO:	Lowest Unoccupied Molecular Orbital
MC:	Metal Centered
MLCT:	Metal to Ligand Charge Transfer
NIR:	Near Infrared
NMR:	Nuclear Magnetic Resonance
Ox:	Oxidation
P:	Photosensitizer
PET:	Photoinduced Electron Transfer

PSI:	Photosystem I
PSII:	Photosystem II
Py:	Pyridine
Q:	Quencher
Red:	Reduction
R _f :	Retention factor
r.t.:	Room temperature
TBAPF ₆ :	Tetrabutylammonium hexafluorophosphate
THF:	Tetrahydrofuran
TMS:	Trimethylsilyl
tpy:	2,2';2'',6'-terpyridine
ttpy:	4'-(<i>p</i> -tolyl)-2,2';2'',6'-terpyridine
Vis:	Visible
MV:	Methyl Viologen
τ:	Lifetime
Φ:	Quantum yield
ΔG:	Free Enthalpy difference

Chapter 1: General Introduction

I. Renewable energy

I.1. Environmental and energetic crisis

Humanity will face a combination of struggles in the coming decades. The most important problems can be described comprehensively as “climate change”. The study from the Intergovernmental Panel on Climate Change (IPCC) in 2013 reported that human activity is the main cause of the observed temperature increase during the last 50 years.¹ The main reason for increasing temperatures is the emission of greenhouse gases like methane, carbon monoxide, and nitrous oxide. However, the greenhouse gas that affects increasing world temperatures most significantly is carbon dioxide, which comes from industries, vehicles, etc. Therefore, due to human activities and the rise of energy consumption depending on fossil fuels, CO₂ concentration in the atmosphere increased from 278 parts per million (ppm) to 391 ppm between the beginning of the industrial era and 2011.² The massive emission of these gases disrupts the natural equilibrium and forms a layer in the atmosphere around the earth. This layer traps most of the thermal heat from the earth, preventing its reflection into outer space. That is why the global earth temperature rises, as a result from the emission of these greenhouse gases.

Fuel combustion leads to massive emissions of carbon dioxide. At the same time, humanity is facing a crucial issue that is illustrated by the depletion of fossil fuel resources in the near future, which impacts most of the energy sources in the world.³ Energy is necessary for human life; it is vital for food production, for transportation, and for other electrical or industrial purposes, etc. Moreover, it is trivial that the number of people in the world continues to rise. Thus, logically according to the UNDP report (World Energy Assessment), energy consumption will double by 2035 relative to 1998, and triple or even more by 2050. Therefore, the necessity for a new source of energy that is renewable and environmental friendly is clear.⁴

In order to provide sufficient energy for human needs, there are three main energy sources that can potentially satisfy our demands. Theoretically, the geothermal energy from the interior of the earth can provide humanity with the thermal and electrical energy we need. However, technologically it is difficult to utilize this energy source. Nuclear energy supply from fission reactions is another choice. However, the fear of spreading nuclear waste

generated from fission reactions of uranium is an issue that needs to be resolved before, and thus makes the nuclear power as a source of unclean energy. The third choice is solar energy, in which case, the sun is an unlimited source of clean energy powerful enough to meet our colossal necessities.⁵

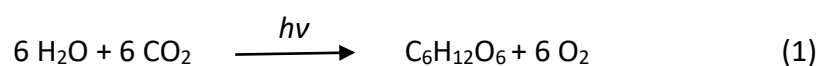
I.2. Solar energy

In general, the energy provided to the entire earth in the form of solar radiation each hour is more than the energy consumed by people on the earth during one year. For example, in 2001 the total human consumption of energy was 13.5 TW, and the sunlight provides 1.7×10^5 TW of power per day. During the daytime, this power is provided in the range of 0.3 to 1 KW per square meter depending on the latitudinal position.^{4,5} Furthermore, due to economic evolution and population rising 2.3 percent per year, the energy consumption rate is estimated to increase to approximately 40.8 TW in 2050.⁵ Therefore, even if we do not have enough advanced technology to get efficient conversion of solar energy to usable energy, theoretically, all our energy needs could be provided by the sun. Therefore, solar energy is the largest source of renewable and clean energy available and should be our target source.⁵

I.3. Inspiration from nature

Much effort in research is aimed toward more efficient solar energy conversion processes, where inspiration from nature itself is one approach. One of the most efficient examples for the photochemical conversion of solar energy is nature's photosynthetic mechanism carried out by green plants and bacteria.⁶ Even though all the detailed steps of the photosynthetic process are not known, the major features are objectively well understood.⁷ Thus, the question is how green plants fabricate their own fuel by photosynthesis?

Natural photosynthesis in green plants can be summarized by the following photochemical equation (1).



This chemical reaction process seems simple reaction done by green plants. In reality, this mechanism requires many different and complex reaction steps. This synthetic photochemical mechanism can be classified into two types of reactions, one depends on light and is called a “light-driven reaction”, and the second is independent of light and called a “dark reaction”. The light-driven reaction is our interest since it works using the solar energy of the sun to produce the plant’s fuel (Figure 1.1).

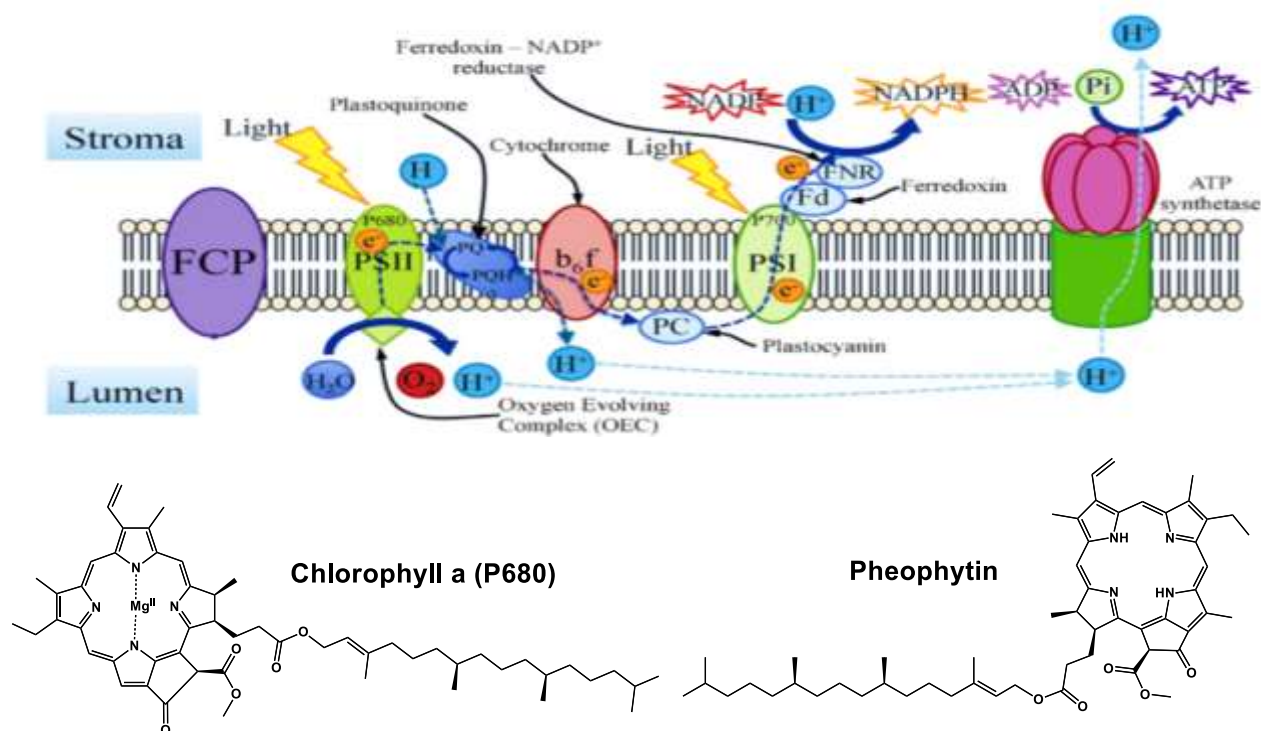


Figure 1.1. A representation of main steps in photosynthesis, showing the electron and proton flow through the thylakoids protein membrane of complexes PS II, Cyt bf, and PS I, and production of ATP fuel by an electron and proton gradient across the protein membrane.⁸

This process takes place in two membrane-bound protein complexes, specifically, at the multi-subunit complexes, photosystem I (PS I) and photosystem II (PS II), which are implanted in the thylakoid membrane of green plants.⁷ In PS II, there is a photoreceptor consisting of several chlorophylls and pigment molecules that can absorb the sunlight and channel the energy to the reaction center (RC) which is composed of two types of proteins (D1 and D2). These RC proteins bind all the redox active cofactors responsible for the energy conversion process. Then, an excitation trap chlorophyll called P680 absorbs the energy and is converted to a strong reducing agent (P680*⁷). It then triggers an electron transfer process to a

neighboring electron acceptor (pheophytin) within a few picoseconds. This is called the first charge separated state (CSS), from which a sequence of successive electron transfer reactions occur from PS II to PS I. Additionally, hydro-nicotinamide adenine dinucleotide (NADPH) is formed by reducing nicotinamide adenine dinucleotide (NADP⁺) *via* this gradient of electrons from PS II. In a parallel process, ATP synthase fuels the production of adenosine triphosphate (ATP), which is the major energy storage molecule used by living things, from adenosine diphosphate (ADP) and inorganic phosphate.⁹ These reactions in their most efficient form and all the related processes are illustrated in Figure 1.1.⁸

In each single electron transfer step, there is a slight decrease in energy. This delays the back-electron transfer reaction, which would result in a loss of absorbed energy. The photo-oxidized P680⁺ is a very strong biological oxidizing agent, which renders it able to oxidize water during oxygenic photosynthesis. Thereby, it is reduced by an electron originating from water via the oxygen evolving complex (OEC) of PS II. Oxidation of water is carried out at a metal ion cluster composed of one calcium ion and four manganese ions connected mainly by μ -oxo bridges and amino acids with carboxylic acid side chains. Electron transfer from the OEC to P680⁺ is favored *via* tyrosine residue (Figure 1.2).^{7,9,10}

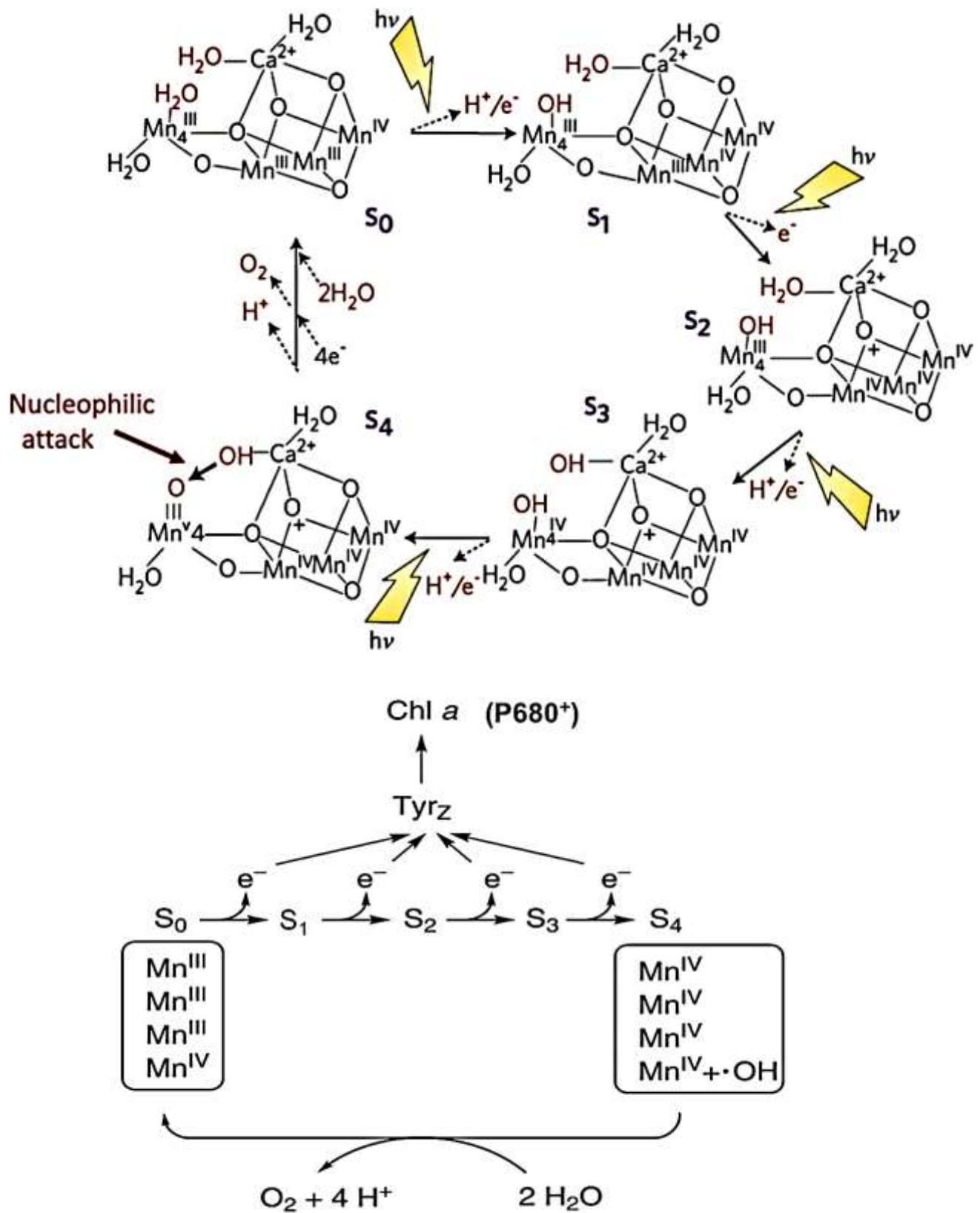
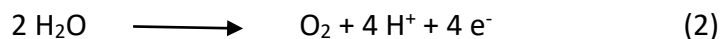


Figure 1.2. Proposed mechanism during water oxidation for oxygen generation at the OEC and regeneration of P680⁺ by reductive electron flow *via* a conserved tyrosine residue.⁷

At the manganese cluster, the oxidation of water takes place in four steps, where the oxidation potential is built up at increasingly higher oxidation states of Mn ions. Lastly, two molecules of water are oxidized as this process continues, according to equation (2).



If this photochemical process could be exploited to make a usable fuel such as hydrogen, instead of NADPH and ATP, it could be possible to produce fuel directly from solar energy and water to meet our energy needs.

In addition to photosynthesis and production of ATP fuel, some types of green plants, especially algae such as *Chlamydomonas reinhardtii*, can produce hydrogen fuel by light-induced proton reduction.¹¹ This process is initiated by a photosynthetic reaction where the liberated electrons are transported to enzymes called hydrogenases. The hydrogenase acts as a catalyst with two roles, where it can either oxidize dihydrogen (H_2) to protons (H^+), or the reverse reaction process of proton reduction to hydrogen. However, iron-containing hydrogenase shows a higher rate for hydrogen formation than for hydrogen consumption. Thus, synthetic iron complexes can be interesting models to study as they are inspired by how nature is able to fabricate its own fuel. If the mechanistic details of the photo-induced reduction process can be understood and controlled, these concepts can be used to convert the protons released by water oxidation into hydrogen fuel.¹²

II. Artificial photosynthesis – Mimicking natural photosynthesis

The goal of artificial photosynthesis is functional and not structural mimicking of PS II in green plants. Specifically, this requires elucidating the key reactions, mechanisms, and structures needed to be able to perform water splitting and hydrogen production induced by sunlight.^{6,13,14,15}

One strategy employed in order to convert solar energy into chemical energy at the molecular level uses three different molecular units that are required for building an artificial

photosynthetic system. This requires the preparation of molecular systems that are able to absorb light and transfer electron(s) from its excited state, thereby mimicking the function of P680 in nature, and this unit is known as a photosensitizer (**P**). In addition to that, we need an electron acceptor (**A**) that can take the transferred electron from (**P**). Then, the reduced species (**A⁻**) of the acceptor can be used as reducing agent for some substrates. Finally, we need an electron donor (**D**) which donates an electron to the vacancy on (**P**), and the oxidized species (**D⁺**) of the donor can be used in oxidation reactions for specific substrates. Thereby the whole system will return to its original ground state, and the catalytic cycle can start again, see Figure 1.3.¹⁴

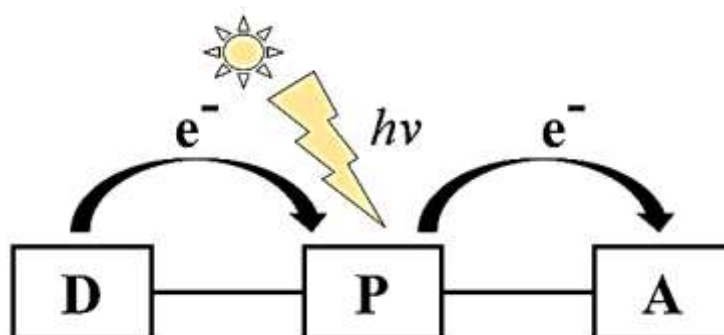


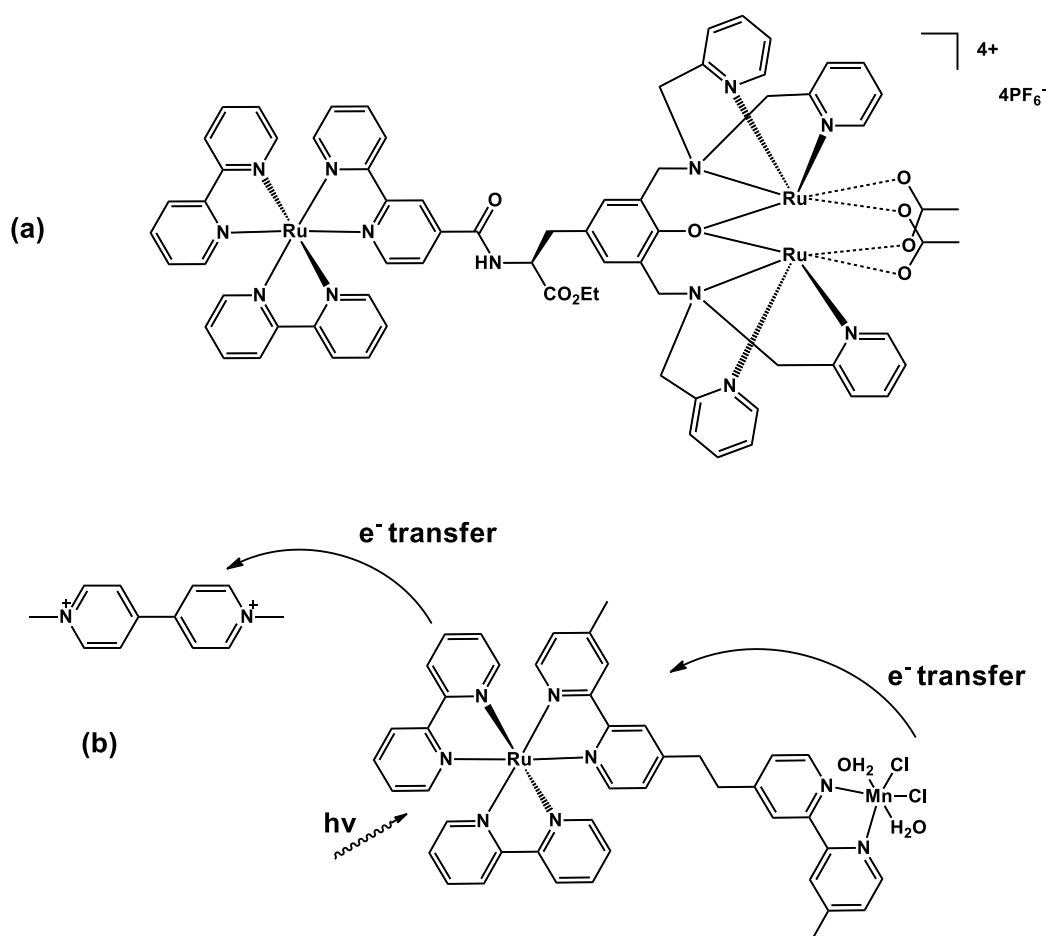
Figure 1.3. Schematic picture of the three building blocks of an artificial photosynthetic triad of electron transfer processes, where **D** is the electron donor, **P** is the photosensitizer, and **A** is the electron acceptor.¹⁴

In the chlorophyll thylakoid membrane, the three active sites are placed in close proximity without any strong coupling interaction, as they are directed by hydrogen bonding and protein interaction. With regard to molecular arrangement, it is important to connect these three parts strongly. Therefore, whenever this triad chain (D-P-A) is exposed to solar light, it will generate the charge separated state (CSS) of the formula, $D^+P^-A^-$.

II.1. Donor moiety

Many ruthenium complexes had been synthesized to mimic the donor side of PS II,^{15,16} and some attempts with limited success have also been carried out using ruthenium. For example, in 2005 the group of L. Hammarström and B. Akermark constructed the first binuclear

ruthenium complex that could be used as an electron donor for the covalently linked photo-oxidized $[\text{Ru}(\text{bpy})_3]^{3+}$ photosensitizer (Figure 1.4, a), exemplifying a new approach in mimicking the donor side of photosystem II. However, due to the very short excited state lifetime of the tri-nuclear ruthenium complex, in the range of picoseconds (100 ps) to a few nanoseconds, it was difficult to perform a photo-oxidation of the excited $[\text{Ru}(\text{bpy})_3]^{2+}$ photosensitizer by an external electron acceptor, and for that reason, no electron transfer from the binuclear complex to the $[\text{Ru}(\text{bpy})_3]^{2+}$ photosensitizer was detected.¹⁷ On the other hand, with manganese complexes, it has been proven that the photo-oxidized ruthenium(III) can oxidize manganese(II) *via* a covalent linkage (Figure 1.4, b).¹⁶ The linked photosensitizer tris-bipyridyl ruthenium(II) complex and manganese(II) complex shows reduction of the photo-oxidized Ru(III) by intramolecular electron transfer from this attached Mn(II) with a rate constant of $1.8 \times 10^5 \text{ s}^{-1}$, thereby mimicking the electron transfer step from the manganese cluster to P680⁺ in photosystem II. Moreover, some reports on binuclear manganese complexes with ruthenium photosensitizers exhibit catalytic oxidation of water with the aid of external oxidants.^{18,19}



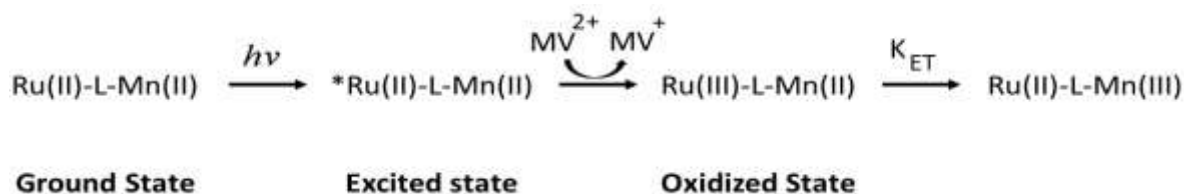


Figure 1.4. (a) Ruthenium tri-nuclear complex, (b) Ruthenium-manganese binuclear complex with its electron-transfer processes.

II.2. Acceptor moiety

Additional experiments were carried out using different electron acceptors to prove the possibility of an electron transfer reaction from the photosensitizer to an electron acceptor branch. For example, in 2003, L. Hammarström and coworkers validated the electron transfer from a $[\text{Ru}(\text{bpy})_3]^{2+}$ photosensitizer to a benzoquinone acceptor with a rate constant of $5 \times 10^9 \text{ s}^{-1}$.²⁰ In addition to this work, another example was since described by the same team, by connecting a naphthalenediimide acceptor to a polypyridyl Ru(II) photosensitizer complex, and detect an electron-transfer reaction from the photoexcited Ru(II) complex to the naphthalenediimide triplet state.²¹

In artificial photosynthesis, the hydrogen evolving side has been thoroughly explored. Again, the goal is a functional mimic of the catalytic site of iron hydrogenase, and much effort in this research area is invested towards model studies as well as functional and mechanistic studies of this iron enzyme.²² So far, electrochemical catalytic hydrogen evolution has been accomplished.²³ For example, in 2006 S. Ott's team prepared the first ruthenium-diiron complex in which the light harvesting photoactive ruthenium complex is used as a photosensitizer, and it was linked by a phosphorous ligand directly to one of the iron centers, which is used as a model of the iron hydrogenase active site for hydrogen production (Figure 1.5). However, no electron transfer from the ruthenium chromophore to the di-iron site was detected. Instead, and due to the mild redox potentials required for the reduction of the acetylenic bipyridine ligand as well as the easy oxidation of di-iron portion, the ruthenium excited state of this tri-nuclear system was reductively quenched by the di-iron site. Moreover, this transient oxidation of the di-iron portion explains why this system was highly air-sensitive and unstable upon irradiation with light.²⁴

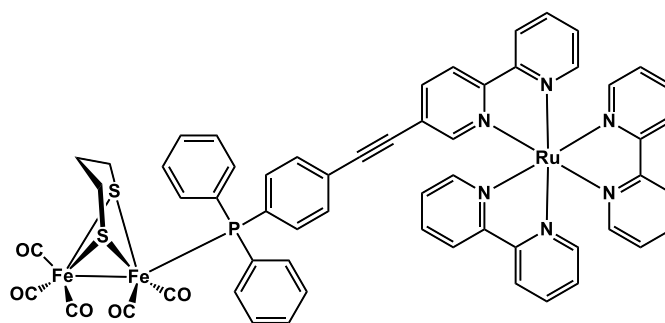


Figure 1.5. The ruthenium^{II}-diiron complex.

II.3. Photosensitizer

For a functional artificial photosynthetic system, light harvesting is very important and therefore the photosensitizer is considered to be of prime importance. Aromatic organic molecules can be used, but their short excited state lifetimes, and not easy to tune their redox properties make them less convenient. However, unlike other aromatic molecules, chlorophyll-like-porphyrin compounds are good enough to be used as photosensitizers in many artificial photosynthetic applications. As an applicable example of using porphyrin, in 2006 F. Odobel and L. Hammarström had studied the electronic interactions and energy transfer between two porphyrins linked by an oligothiophene bridge, in which this photosensitizer can be used successfully in the construction of electron and energy donor-acceptor systems.²⁵ The same authors also prepared a new photo-electrochemical device based on a phosphorus porphyrin, by which a nanocrystalline NiO electrode coated with a phosphorus porphyrin gives a cathodic photocurrent due to the flow of electrons from the NiO electrode into the solution. This work opened the door to new photovoltaic devices based on hole photoinjection.²⁶

The second common class of photosensitizers used were transition metal complexes based on Iridium(III), Rhodium(III), Osmium(II), or most commonly, Ruthenium(II).^{27,28,29}

Even though processes such as accumulative electron transfer are very important for artificial photosynthesis, the photosensitizer itself is of great importance. Ruthenium(II) complexes, which are the main theme of the thesis, are not only used as photosensitizers in solar energy conversion, but they are also useful for applications such as molecular electronics,³⁰ light

emitting devices (red light emitting device),³¹ molecular sensors, switches (depending on fluorescence emission property),³² molecular machines,³³ and finally, for therapeutic applications depending on the transition metal affinity for reversible binding to DNA.³⁴ Ruthenium(II) complexes additionally have the advantages of relatively good stability and absorption properties in the visible region, with a fairly long-lived excited state.³²

Nevertheless, appropriate steric, photophysical, and chemical properties that are rarely present in the same complex at the same time, are required to have a perfect photosensitizer candidate.

II.4. Photosensitizer requirements

Many general and important requirements must be fulfilled in order to have a good photosensitizer, regardless of the application for which it is designed. Therefore, a large extent of compromises between wanted and unwanted properties will be considered to apply desirable properties of the photosensitizers used for different applications. Hence, some requirements for the photosensitizer will be discussed for absorption of solar energy to drive further electron transfer reactions, as in artificial photosynthesis.

II.4.1. Stability

A good photosensitizer candidate must be stable at the excited, ground, and different redox states. In addition, in order to work properly, it should also be inert to any side reactions, thus, it can be used many times in a catalytic cycle to support the desired electron transfer reactions. Absolutely, it must be stable towards light-induced decomposition.

II.4.2. Absorption properties

For a good photosensitizer, it is essential to absorb strongly in a suitable spectral region (high molecular absorption coefficient), where it can capture photons effectively, especially in the

region where sun emits radiation. Most natural pigments absorb in the range of 300-600 nm, which is also the region where complexes based on ruthenium(II), osmium(II), and other transition metals absorb, and this range normally refers to metal-to-ligand-charge-transfer transition states (MLCT transition).²⁹

II.4.3. Redox properties

A fundamental requirement is that the oxidation and reduction reactions must be reversible, and at the same time, the oxidized and reduced photosensitizer should be stable in the ground and excited states.²⁹ Moreover, the oxidation and reduction potentials of the photosensitizer will determine the thermodynamic parameters for the electron transfer reactions.

II.4.4. Excited state properties

Since the redox reactions and charge transfer processes occur from the excited state, then the excited state properties are considered to be the main property when designing a functional photosensitizer. The excited state energy, and its lifetime and quantum yield are of the utmost importance. Thus, to allow for the desired electron transfer reactions to take place before relaxation of the excited photosensitizer to its ground state, the excited state lifetime should be long enough to facilitate this transfer. Moreover, having an energetic excited state is important since it is the driving force for further electron transfer reactions. The structure of the complex is essential, since it influences the photophysical and redox properties of the sensitive excited state, therefore, the choice of ligands and their substituents is of great importance in tuning the excited state.³⁵

II.5. Solar Fuel Generation

In artificial photosynthesis, the goal is to mimic a green plant's ability to make chemical energy in which chemical bonds are broken and formed to generate their photosynthetic fuel using

sunlight.⁵ Many different approaches have been tested to achieve conversion and storage of solar energy in recent years.¹³

The preparation of a solar fuel cell, which has activity complementary to a classic fuel cell based on oxygen and hydrogen gases, is shown in Figure 1.6.⁵

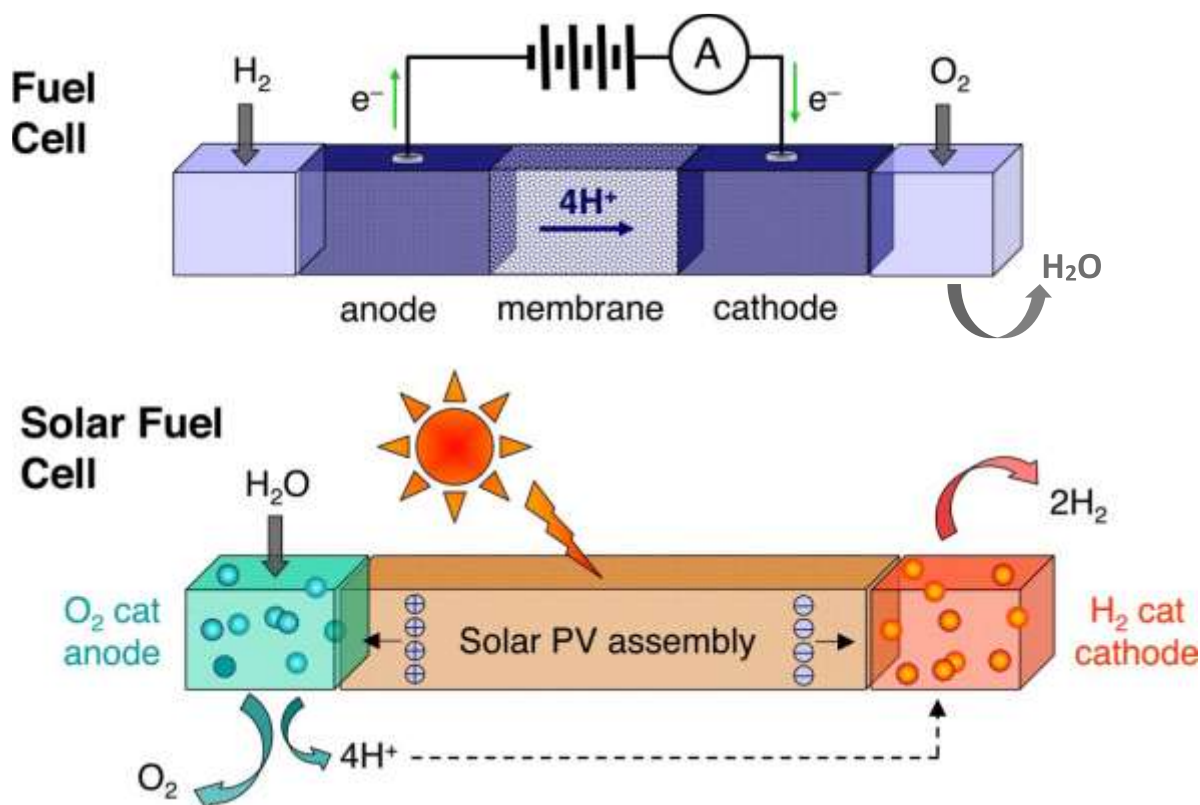


Figure 1.6. Water splitting process into hydrogen and oxygen in a solar fuel cell (bottom), to be used in a classic fuel cell (top) for generating a flow of electrons and protons across a membrane to produce electricity.⁵

Catalytic water splitting and hydrogen formation using electron donors and electron acceptors in order to mimic the photosynthetic machinery has been a great challenge. Some examples will be described here to outline various attempts to achieve water splitting which have been developed by scientists using ruthenium tris-bipyridine derivatives as photosensitizers adsorbed on a hybrid mesoporous nano metal oxide photoanode (TiO_2).

The first approach for using a photoanode (platinized semiconductors) to transfer electrons in a closed circuit was described by Bard in 1980. He worked on the wide-band-gap titanium oxide (TiO_2 , $SrTiO_3$) semiconductors doped with platinum on its surface. He showed its efficiency for electron transfer from the excited species to a suitable acceptor species using

UV band-gap excitation. Thus, the solar energy is stored as redox chemical energy, and if the electron is pumped through a wire, the liberated energy will be converted into an electric current.³⁶ This approach established the basic principles of photochemical processes occurring on semiconductor materials to be used and developed later in photosynthetic machinery applications, especially for photochemical water splitting.

Further efforts have been made to find devices with a greater operative antenna effect based on a donor-photosensitizer-acceptor approach and targeted for a photo-induced long-lived charge-separation state (CSS).

In 2009, Mallouk and coworkers prepared a new binuclear complex based on a ruthenium tris-bipyridine derivative photosensitizer, connected to an iridium oxide particle $\text{IrO}_2 \cdot n\text{H}_2\text{O}$ (stable catalyst with efficient activity for water oxidation) by means of a carboxylic acid group (bidentate malonate substitution) at the 4-position of one of the bipyridine ligands of ruthenium.³⁷ Another one of the bipyridine ligands of the ruthenium dye was di-substituted with two phosphonate groups, also at 4-4'-positions, allowing the binuclear system to be adsorbed onto the porous nanocrystalline titanium oxide (TiO_2) semiconductor. Then, this semiconductor was connected to a cathode platinum wire electrode, which can be used to reduce the protons produced from water splitting into hydrogen fuel (Figure 1.7).

The measurements for this system were performed in a photochemical cell, with the binuclear system ($\text{Ru}(\text{bpy})_3\text{-IrO}_2 \cdot n\text{H}_2\text{O}$) adsorbed on titanium oxide constituting the working electrode, a silver reference electrode, and a platinum counter electrode. The system was immersed and studied in an aqueous buffer solution of $\text{pH} = 5.75$.

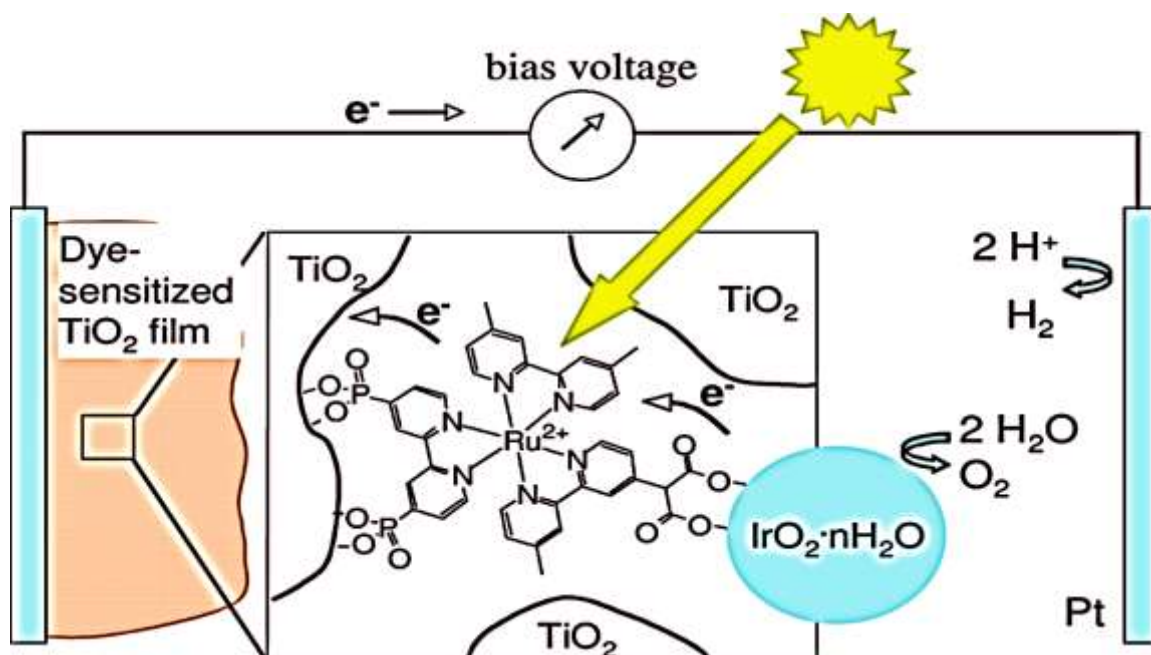


Figure 1.7. Water splitting and hydrogen production schematic representation.³⁷

First, upon irradiation at 450 nm, an electron transfer from the photo-excited ruthenium complex to the TiO_2 semiconductor occurs, then the photo-oxidized Ru(III) which is generated returns to its initial redox state, Ru(II) , via another electron donation from the iridium(III) particle, and finally the oxidized iridium(IV) completes the catalytic cycle by returning to its initial redox state after the water oxidation reaction is complete. The measurement of the produced photocurrent at $7.8 \text{ mW}\cdot\text{cm}^{-2}$ intensity was $12.7 \mu\text{A}\cdot\text{cm}^{-2}$, which corresponds to approximately 1% steady-state quantum efficiency of this cell. Gas chromatography allowed for the detection of the evolution of oxygen gas, and the current efficiency for the photo-anodic O_2 generation was calculated to be 20%. The low quantum yield efficiency originates from two sources. The first problem comes from the structural design, in which each iridium particle was capped with 10 to 20 ruthenium photosensitizers, thus relatively few were linked to the semiconductor surface (for greater efficiency, each sensitizer should bind one iridium catalyst and also adsorb to the semiconductor from the second side). The second problem was due to slow electron transfer from the iridium catalyst to the photooxidized ruthenium photosensitizer, which was considered to be 6 times slower than the back donation from titanium oxide semiconductor to the oxidized dye (a faster electron transfer from Ir(IV) to Ru(III) would result in a more efficient quantum yield). Therefore, the photo-induced water

splitting quantum yield in this dye-sensitized binuclear system is very low, due to the fact that the charge recombination process is faster than the catalytic four electron oxidation to accomplish water splitting.

In 2012, successive work from Mallouk and coworkers improved upon the quantum yield efficiency of their previous work, more than doubling it from 1% to 2.3%. This quantum yield enhancement is achieved by inserting benzimidazole-phenol (BIP) as an electron transfer mediator between the slow electron donating iridium catalyst and the fast photo-oxidizing ruthenium dye acceptor, mimicking the role of tyrosine found in photosystem II in nature (Figure 1.8).³⁸

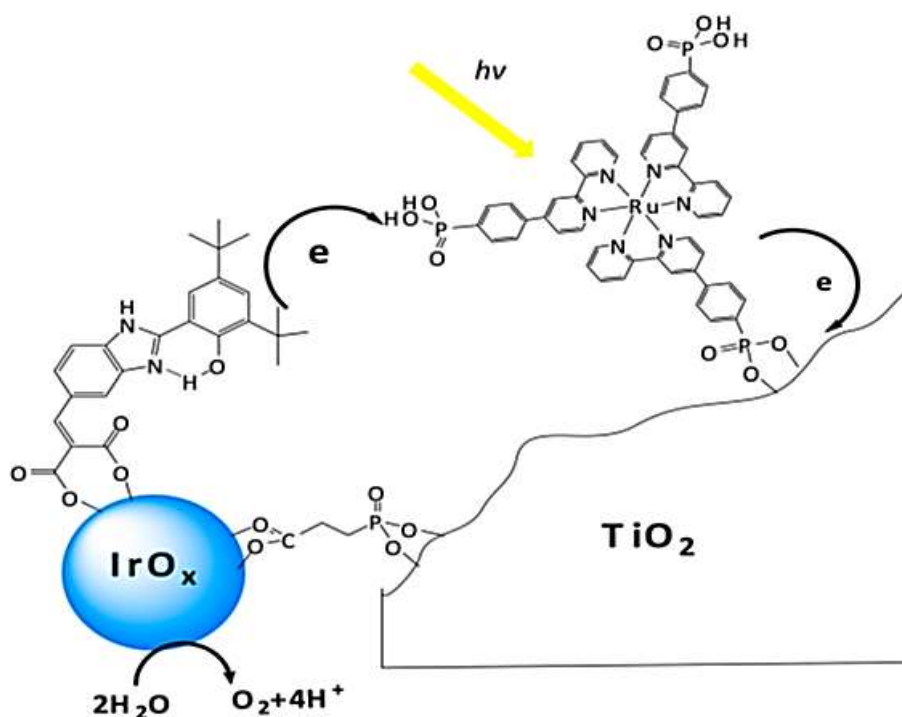


Figure 1.8. Mallouk et al.'s improved water oxidation system including the BIP mediator between Ir(cat.) and Ru-dye.³⁸

The system was built in a way to allow for co-adsorption of both the iridium oxide catalyst and the ruthenium photosensitizer onto the titanium oxide semiconductor (opposite to their previous work in 2009). To achieve the structure for this system, iridium particles were bound to the BIP electron transfer mediator from one side, and then it was linked to the TiO₂ semiconductor from the opposite side by means of the 2-carboxyethyl phosphonic acid

(CEPA). Upon irradiation, successive electron transfer reactions occurred between the binuclear complex and TiO₂ semiconductor, in which the intensity of photoelectric current density was recorded up to 80 $\mu\text{A}\cdot\text{cm}^{-2}$ (three times more than what was observed before without BIP mediator), with a stability over 100 s (also three times more stable than when there is no BIP). Therefore, this result demonstrates the faster electron transfer process between iridium nanoparticles and Ru(III) in the presence of BIP electron mediator. However, one disadvantage was clear in this system, which is illustrated by the limited control of electron transfer between iridium catalyst and ruthenium dye sensitizer, due to the separate adsorptions of each molecule on the TiO₂ semiconductor surface.

In contrast to these two attempts, Schanze and coworkers developed a recent binuclear system adsorbed on TiO₂ for solar fuel generation, composed of ruthenium tris-bipyridine complex used as the photosensitizer and another ruthenium(II) complex used for the water splitting reaction, in which both were assembled together by a polystyrene polymer (Figure 1.9).³⁹ This light-driven water splitting system was prepared by a special arrangement and relative stoichiometry of the first ruthenium dye and the second ruthenium catalyst responsible for the water oxidation reaction. Both complexes were assembled onto a polystyrene chain and adsorbed on a mesoporous titanium oxide semiconductor surface. After that, the whole system was supported on a planar fluorine-doped tin oxide (FTO) conductive surface. This new system depends on the polymer chain to hold both the dye sensitizer and the oxidation catalytic parts, therefore the chain length was of significant importance. In the case of long polymer chains, the tendency towards aggregation becomes higher, and that leads to a lower surface coverage of the polymer on the TiO₂ semiconductor surface. In that way, the authors used polystyrene polymers of a relatively low degree of polymerization, and both ruthenium complexes were attached to the polymer *via* an azide-alkyne Huisgen cycloaddition reaction in a ratio of 1 : 4 of Ru(catalyst) to Ru(dye sensitizer) respectively.

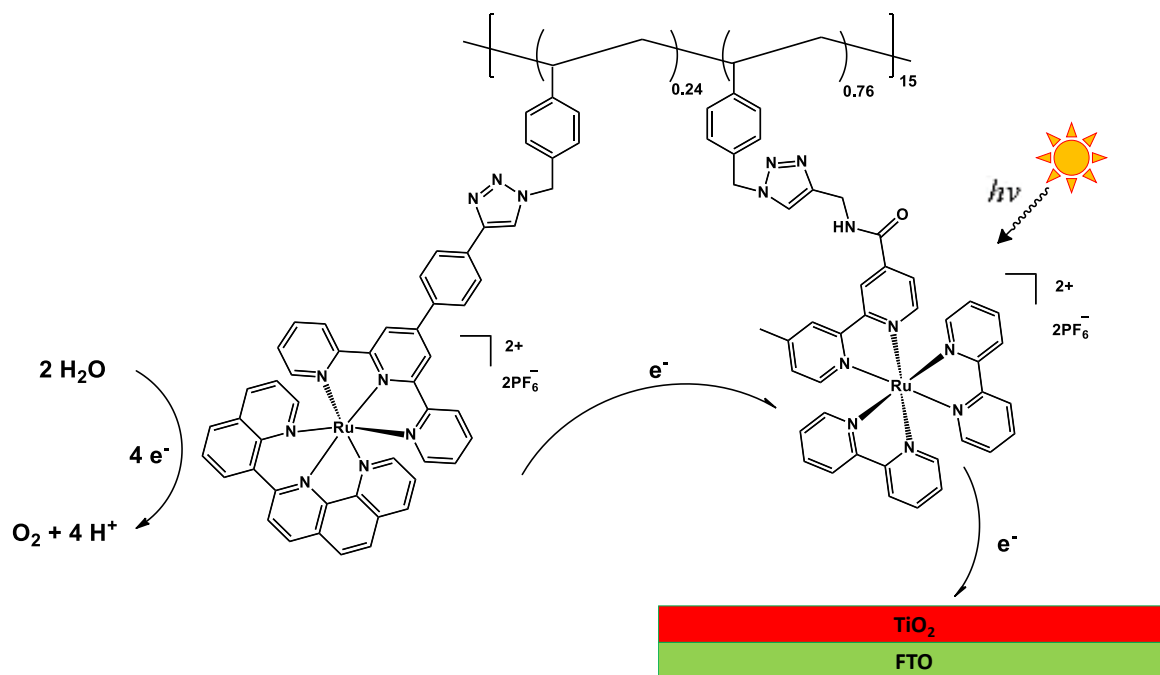


Figure 1.9. Schematic representation of a polystyrene chain possessing chromophore-catalyst complexes coated on a FTO//TiO₂ mesoporous substrate.³⁹

Upon irradiation of $[\text{Ru}(\text{bpy})_3]^{2+}$, the excited state was quenched by electron transfer to the photo-anode electron acceptor surface. This photo-oxidized complex returned to its initial redox state following another electron donation from the second tri-dentate ruthenium complex, giving rise to a photoelectric current of $18.5 \mu\text{A}\cdot\text{cm}^{-2}$, which is attributed to the catalytic light driven water oxidation reaction.

III. Ruthenium(II) polypyridyl complexes

Many transition metals like ruthenium(II), osmium(II), and iridium(III) have been used in many different applications like photocatalysis, and as a central metal of different triads to mimic photosynthetic reactions due to their beneficial photophysical and redox properties.^{28,40} In this thesis, I will focus on ruthenium(II) complexes, and how their properties can be tuned in order to achieve better function. The main issue to be discussed is the remarkable difference between tris-bidentate and bis-tridentate ruthenium complexes, for example, the two archetypical complexes $[\text{Ru}(\text{bpy})_3]^{2+}$ and $[\text{Ru}(\text{tpy})_2]^{2+}$ respectively.

III.1. Tris-bidentate ligand ruthenium complex $[\text{Ru}(\text{bpy})_3]^{2+}$

The prototype ruthenium complex $[\text{Ru}(\text{bpy})_3]^{2+}$ (bpy = 2,2'-bipyridine) shown in Figure 1.10, is one of the most studied ruthenium complexes and broadly used in research during the last forty years.⁴¹ It has attracted many researchers due to its appropriate photophysical and electrochemical properties:

- Strong absorption in the visible region
- Long excited state lifetime
- Relatively high luminescence quantum yield
- Appropriate redox potential
- Reversible electron transfer processes in both excited and ground states.⁴¹

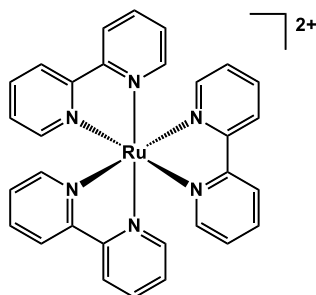


Figure 1.10. $[\text{Ru}(\text{bpy})_3]^{2+}$ complex.

To understand the origin of these properties, we need to understand closely the electronic structure of this complex. The ruthenium transition metal possesses five degenerate d-orbitals when it is uncoordinated to any ligand, but this degeneracy is split upon coordination with the polypyridine ligands, here the 2,2'-bipyridine ligand that is a strong σ donor through the nitrogen atoms with a π donor, and π^* acceptor character found on the two pyridine rings. The resulting energy levels of the created $[\text{Ru}(\text{bpy})_3]^{2+}$ octahedral geometry complex, as well as some electronic transitions are presented in Figure 1.11.

Metal-to-ligand charge transfer (MLCT) excited state which normally gives the emission properties of the photosensitizer and is important for its function, is produced by electron promotion from the metal centered t_{2g} orbital (HOMO) to the ligand centered π^* acceptor orbital (LUMO).⁴⁰ The symmetry forbidden metal-centered (MC) excited state (d-d transition)

is obtained by electron promotion from metal centered t_{2g} to e_g^* orbitals of ruthenium metal, lastly the promotion from ligand centered $\pi_{(L)}$ donor orbital to its $\pi^*_{(L)}$ acceptor orbital will give rise to ligand-centered (LC) transition.

The multiplicity of these excited states could be singlet or triplet. Moreover, an important singlet-triplet multiplicity mixing is obtained especially for MLCT and MC excited states due to spin orbit coupling (SOC).

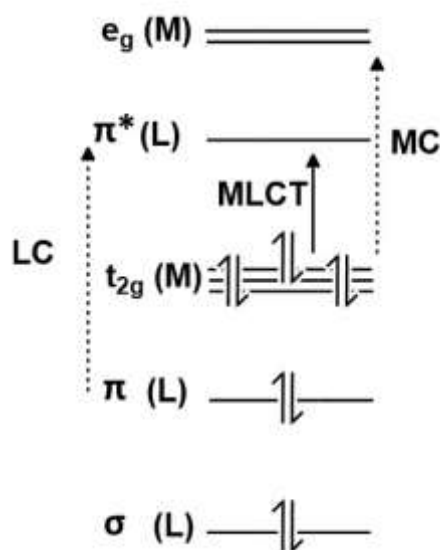


Figure 1.11. Schematic molecular orbital energy diagram for d^6 ruthenium(II) complex in an octahedral environment, showing by arrows the different types of transition.

Upon absorption a photon of energy ($h\nu$) matching the energy gap between the HOMO and LUMO, a singlet metal-to-ligand charge transfer ($^1\text{MLCT}$) excited state is formed first. Then due to spin orbit coupling and the effect of ruthenium heavy metal, the spin state changes by a fast intersystem crossing (ISC) in less than 50 fs.⁴² ISC is followed after that by a rapid relaxation to the lowest triplet excited state, to give the triplet metal-to-ligand charge transfer excited state ($^3\text{MLCT}$) in around 1 ps depending on the solvent.⁴³ This new excited state ($^3\text{MLCT}$), can thermally populate the low lying metal centered (^3MC) state by internal conversion (IC), or can deactivate to the ground state again by radiative process (phosphorescence), or *via* non-radiative decay (in the form of thermal energy), (Figure 1.12).⁴⁴

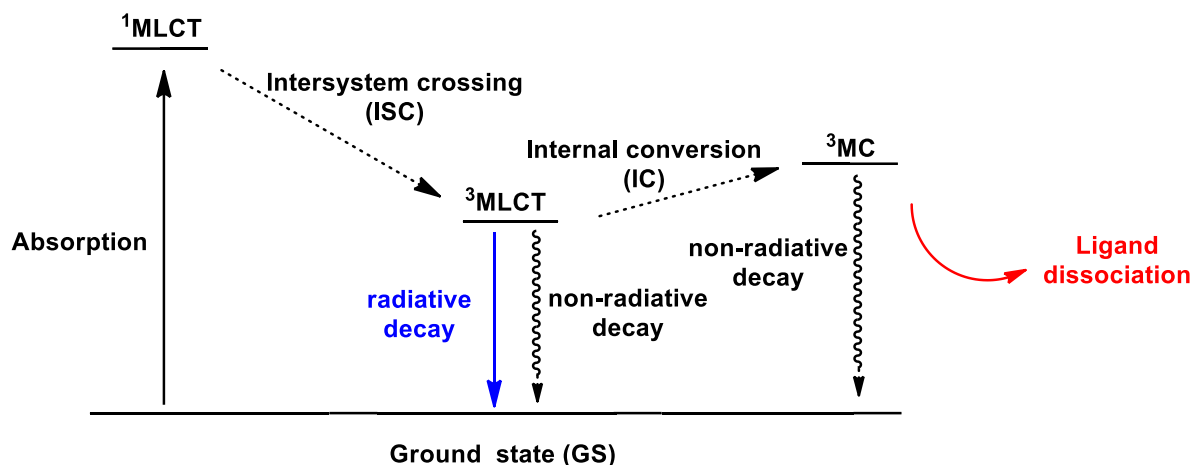


Figure 1.12. Perrin-Jablonski diagram for the different decay pathways of ruthenium(II) polypyridine complexes.

The non-emissive metal centered (^3MC) excited state can be involved in photochemical reactions, like the loss of ligand by the cleavage of the elongated coordination ruthenium-nitrogen bond, and form the square pyramidal complex. At that point, this five-coordinated species can reform the $[\text{Ru}(\text{bpy})_3]^{2+}$ again in the absence of coordinating ions (PF_6^- as counter ion), or undergo the loss of one bipyridine ligand (bpy) in the presence of coordinating anions like halogens (X^-) if present as counter ion, that leads to the formation of $[\text{Ru}(\text{bpy})_2\text{X}_2]$ (Figure 1.13).⁴¹

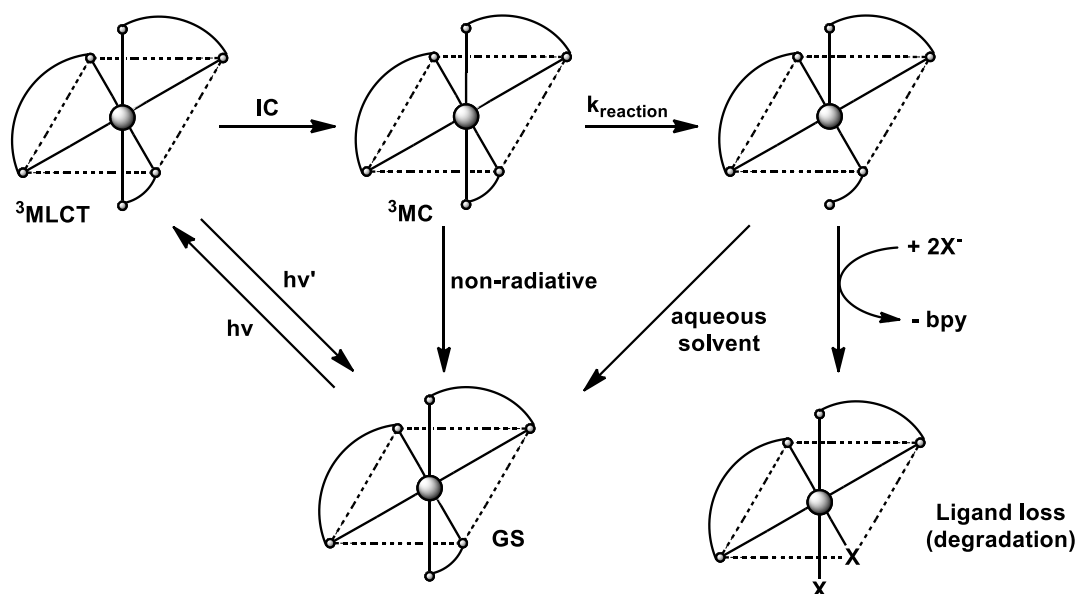


Figure 1.13. Proposed mechanism pathway for the photoactive $[\text{Ru}(\text{bpy})_3]^{2+}$ complex depending on the solvent environment.

Moreover, ligand loss can be controlled or reduced by “chelate ring closing process” that is known by self-annealing, to re-form $[\text{Ru}(\text{bpy})_3]^{2+}$ complex and avoid dissociation by stabilizing the cationic $[\text{Ru}(\text{bpy})_3]^{2+}$ species in aqueous solution. On the other hand, in low polarity solvents, it is more favored to lose one ligand and form the neutral $[\text{Ru}(\text{bpy})_2\text{X}_2]$ complex.

Triplet metal-to-ligand charge transfer state ($^3\text{MLCT}$) is the most important excited state that specifies the photoactivity of any ruthenium photosensitizer. The main two properties at this point that describe the excited state, are the excited state lifetime and emission quantum yield, that are directly dependent on the energy difference between $^3\text{MLCT}$ and ^3MC . These two properties can be expressed by equations 3 and 4 respectively.

- Lifetime: $\tau = \frac{1}{k_r + k_{nr}}$ (3)

- Quantum yield: $\Phi = \frac{k_r}{k_r + k_{nr}}$ (4)

The two rate constants k_r and k_{nr} represent the radiative and non-radiative relaxation rate constants respectively.

Short lifetime excited state of ruthenium(II) complexes is due to small $^3\text{MLCT}$ - ^3MC energy difference, that makes the excited state deactivate faster by thermally populating of triplet metal centered (^3MC) excited state (figure 1.14, a).⁴⁵ However, the activation barrier to populate this ^3MC excited state can be higher in case it is significantly destabilized.⁴⁶ Consequently, destabilizing ^3MC will raise the energy difference between this non-emitting excited state and the $^3\text{MLCT}$ emitting state of the complex. Therefore, the emission quantum yield of the complex becomes higher and its lifetime longer (Figure 1.14, b).

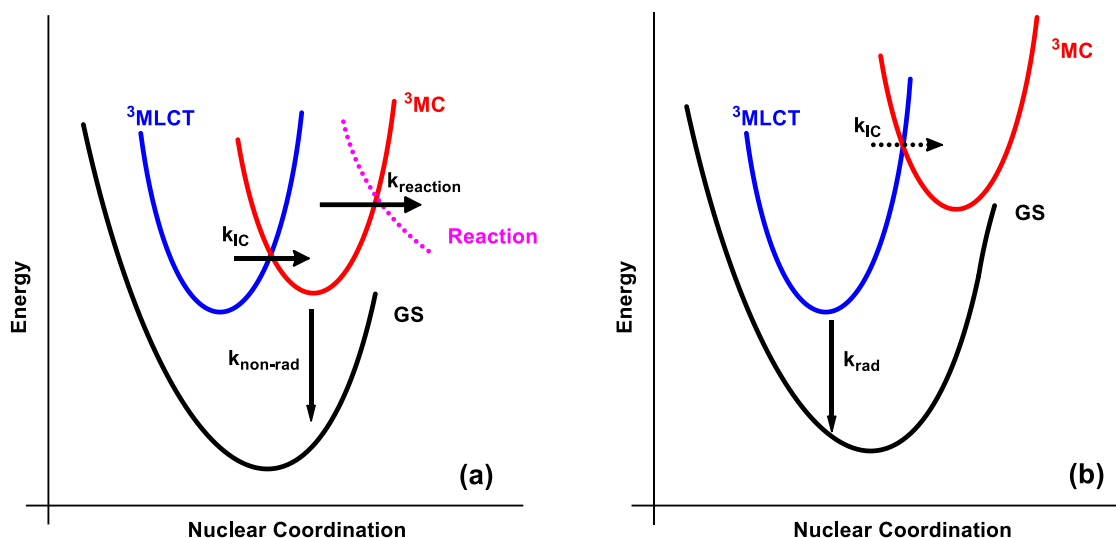


Figure 1.14. Small ^3MC - $^3\text{MLCT}$ energy splitting (a), resulting in fast $k_{(\text{IC})}$. A significant slower thermal populating of ^3MC with a bigger gap energy (b).

On the electronic absorption spectrum, the strong absorption in the blue region centered at 450 nm of $[\text{Ru}(\text{bpy})_3]^{2+}$ leads to the lowest singlet metal-to-ligand charge transfer ($^1\text{MLCT}$) excited state, that emits strongly after a spin change from the lowest triplet state at 610 nm as shown in Figure 1.15, with a Stoke's shift of 0.72 eV.

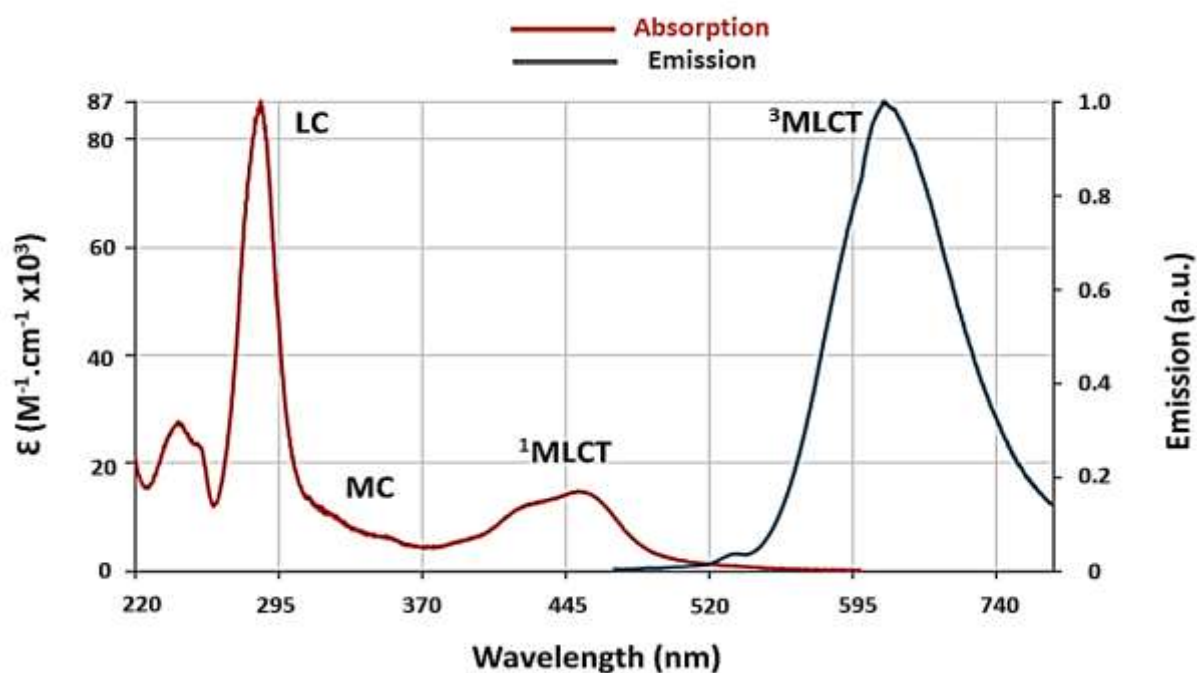


Figure 1.15. Absorption and emission spectra of $[\text{Ru}(\text{bpy})_3]^{2+}$ in acetonitrile at room temperature.

The three transition types that were seen in Figure 1.11, are present on this absorption spectrum. The absorption band at 285 nm is assigned to the spin allowed ligand centered transition (LC) from $\pi_{(L)}$ to $\pi^*_{(L)}$. The two small absorption bands at 322 nm and 344 nm might be assigned to the metal centered (MC) d-d transition, while the moderately intense absorption band at 450 nm refers to the spin and symmetry allowed singlet metal-to-ligand charge transfer ($^1\text{MLCT}$) transition from $d_{(M)}$ to $\pi^*_{(L)}$. The $[\text{Ru}(\text{bpy})_3]^{2+}$ complex at the MLCT excited state has a formally reduced bpy ligand with oxidized ruthenium metal from Ru(II) to Ru(III), to give this formula $[\text{Ru}^{\text{III}}(\text{bpy})_2(\text{bpy})]^{-*}$.^{40,41} Thus, $^1\text{MLCT}$ is sensitive to solvent polarity due to the formation of this dipolar excited state $[\text{Ru}^{\text{III}}(\text{bpy})_2(\text{bpy})]^{-*}$.

According to Kasha's rule, excitation of $[\text{Ru}(\text{bpy})_3]^{2+}$ at any of these absorption bands will lead to the emission from the lowest $^3\text{MLCT}$, and its energy is of 2.1 eV. In addition to that, $^3\text{MLCT}$ excited state lifetime (solvent and temperature dependent) is around 1 μs in deaerated acetonitrile at room temperature (of around 6% emission quantum yield), and is around 5 μs in rigid matrix glass at 77 K.⁴¹

III.2. $[\text{Ru}(\text{bpy})_3]^{2+}$ excited state reactivity

$[\text{Ru}(\text{bpy})_3]^{2+}$ is considered to be a weak electron donor or acceptor at the ground state. On the other hand, this ruthenium complex at the excited state is a strong oxidizing and reducing agent. As it is seen in Figure 1.16, after excitation of ruthenium tris-bipyridine complex, the promoted electron on the π^* orbital can be donated easily, when the photoexcited complex works as reducing agent. Moreover, putting an electron in the vacant t_{2g} orbital at excited state is easier and needs less energy than putting it at the LUMO of the complex when it is at the ground state. As a consequence, photoexcited ruthenium complex is a stronger oxidizing and reducing agent than when it is at the ground state.

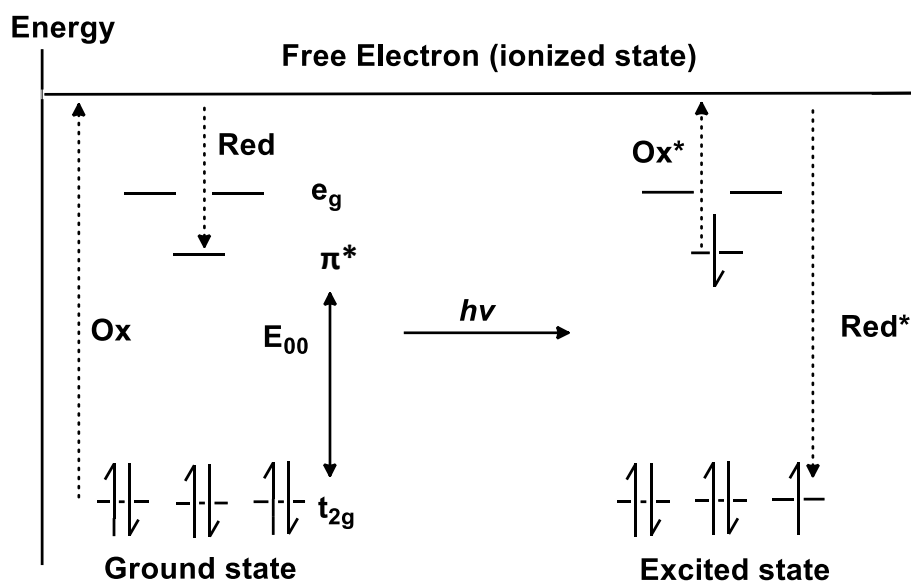


Figure 1.16. The redox properties of [Ru(bpy)₃]²⁺ at excited state and ground state.

The photoexcited species is more oxidant and reductant than the ground species, with a reduction potential for the photooxidized complex of +0.77 V versus saturated calomel electrode (SCE) in acetonitrile at room temperature, while it is -1.33 V vs SCE at ground state under the same condition in acetonitrile. Moreover, the oxidation potential at excited state in acetonitrile is of -0.81 V vs SCE at room temperature, while it is +1.29 V vs SCE at ground state under the same conditions in acetonitrile.⁴⁷ These potentials at excited state can be calculated following the Rehm-Weller equation (5).⁴⁸

$$E_{1/2}^{* \text{ red}} = E_{1/2}^{\text{ red}} + E_{00} \quad \text{and} \quad E_{1/2}^{* \text{ ox}} = E_{1/2}^{\text{ ox}} - E_{00} \quad (5)$$

E* represents the oxidation and reduction potentials at photoexcited states, (E) is for potentials at ground state that can be determined experimentally by cyclic voltammetry, and (E₀₀) corresponds to the energy of the excited state and can be approximated to the emission energy of the complex at 77 K.

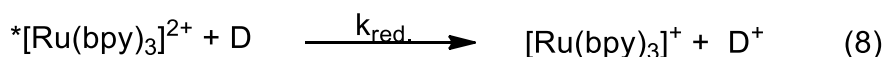
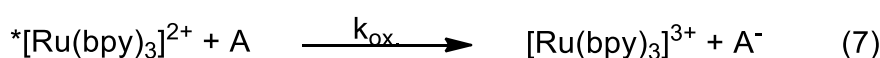
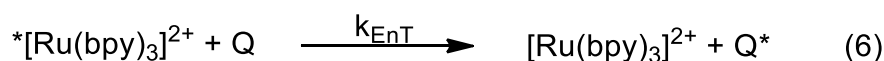
As a consequence, such redox potential properties make the photoexcited [Ru(bpy)₃]²⁺ complex a good candidate in many bimolecular light-induced single-electron-transfer or energy transfer applications.⁴⁰ For instance, this complex and its analogs were applied in photoredox catalysis in the reduction of carbon dioxide,⁴⁹ and the splitting of water into hydrogen and oxygen⁵⁰ as artificial photosynthetic device mimicking the role of photosystem

II (PS II) in green plants. In addition, other broad applications using $[\text{Ru}(\text{bpy})_3]^{2+}$ complex were in molecular photosynthesis,⁶ in some medical therapies,⁵¹ in sensor devices,⁵² and it has been used broadly in the area of organic synthesis.⁵³

The quenching reaction pathway of the ruthenium(II) complexes $^3\text{MLCT}$ excited state is directly depending on:

- Redox potentials of both donor complex and acceptor quencher.
- Quencher absorption spectrum.
- Emission spectrum and emission energy of ruthenium donor complex.

The photoexcited complex can undergo energy transfer process (equation 6), or an electron transfer process to be used as reducing or oxidizing agent for specific substrates (equation 7 and 8 respectively).⁵⁴ (A) is an electron acceptor, (D) an electron donor, and (Q) is any quencher that undergoes excitation by energy transfer from the excited ruthenium complex.



III.2.1. Energy transfer mechanisms

Equation (6) illustrates the energy transfer reaction pathway, by which the energy of the excited ruthenium complex center is transferred to energy acceptor (Q). Energy transfer reaction could be radiative if the emitted photon from the excited complex is re-absorbed by the energy acceptor quencher (Q). However, energy transfer can also be achieved through a non-radiative process. There are two different mechanisms to describe non-radiative energy transfer known by Förster mechanism (energy transfer by resonance) and Dexter mechanism (energy transfer by exchange) as it is shown in Figure 1.17 below.⁵⁴ Moreover, the condition for these processes to occur, the orbital energy of the energy donor (ruthenium) should be higher than the orbital energy of the acceptor (Q).

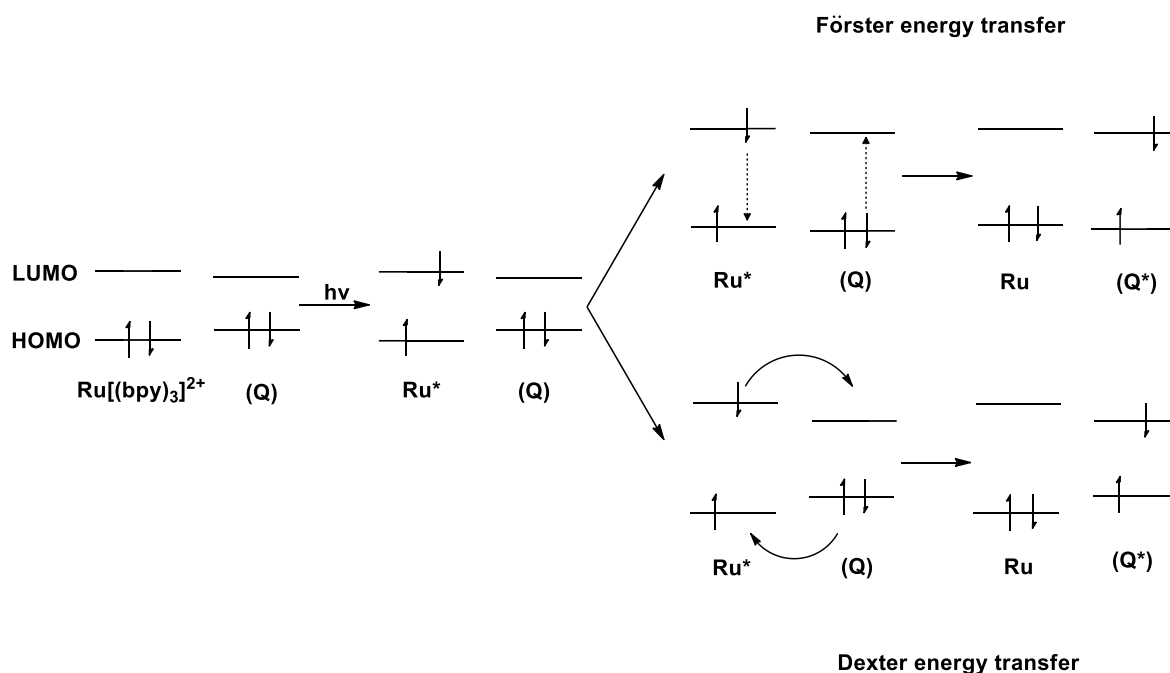


Figure 1.17. Förster & Dexter energy transfer quenching mechanisms.

Förster mechanism, also called coulombic mechanism or long-range mechanism, is a dipolar interaction mechanism that can take place through space. Thus, there is no need for a physical contact between the ruthenium donor center and the energy acceptor (Q), there is no orbital overlapping or electron mixing between them. This remote energy transfer operates experimentally over a distance ranging from 10 to 100 Å.⁵⁴ In this energy transfer mechanism, the two excited states of the energy acceptor and donor should hold the same spin multiplicity for the allowed transition. The rate constant for Förster energy transfer can be expressed theoretically in equation (9).

$$k_{EnT} = \frac{1.25 \times 10^{17} \Phi_D I}{(\eta^4)(\tau_D)(R^6)} \quad (9)$$

Φ_D and τ_D are the emission quantum yield and luminescence lifetime of the excited ruthenium donor complex respectively, and R is the distance between the energy donor and the energy acceptor (Q), I is the normalized overlap integral between the emission spectrum of ruthenium energy donor center and the absorbance spectrum of energy acceptor (Q), lastly η is the refractive index of the solvent.

Dexter mechanism on the other side, known as the exchange mechanism, requires the formation of a collision intermediate complex between Ru* excited complex and the acceptor quencher to make energy transfer reaction. Thus, in this mechanism, both excited complex and quencher should require physical contact and orbital overlapping to occur, in a distance that is less than 10 Å. It is called double exchange mechanism, since when an electron goes from the LUMO of the ruthenium donor to the LUMO of the energy acceptor, another exchange directly occurs by giving an electron from the HOMO of the acceptor to the HOMO of ruthenium complex center. Dexter's mechanism is limited by diffusion and directly dependent on the nature of the bridge between both acceptor and donor. In the mechanism of Dexter, the reactions are done with spin conservation (from triplet Ru complex excited state to triplet quencher excited state, the same if it was at singlet state). The rate constant that is distance dependent had been developed theoretically by Dexter in equation (10).

$$k_{EnT} = J \cdot e^{-2R/L} \quad (10)$$

Where J is the normalized spectral overlap integral, R is the distance between both acceptor and donor, and L is the sum of Van der Waals radii of both acceptor and donor.

The three mechanisms can coexist, but the Dexter one dominates at very short distances, whereas the Förster mechanism can function over longer distances.

Many systems based on the metal complex $[\text{Ru}(\text{bpy})_3]^{2+}$ were explored and showed evidence of energy transfer, in which the ruthenium complex can have a double role acting either as a donor or as an acceptor depending on the surrounding system.

A recent example was described by T. Yui in 2017 showing that $[\text{Ru}(\text{bpy})_3]^{2+}$ complex can work as an energy acceptor, and the light energy accumulator pyrene derivative acts as energy donor (Figure 1.18).⁵⁵ A stoichiometric amount of the cationic pyrene derivative (five molecules) absorbs strongly photons, followed by energy transfer to one molecule of ruthenium(II) complex on a clay surface. Energy transfer efficiency was 85% with a rate constant (k_q) of $10^{17} \text{ L}\cdot\text{mol}^{-1}\cdot\text{s}^{-1}$ approximately. This rate constant is of 10^7 - 10^8 times higher than the diffusion rate constant in a homogeneous solution. Such efficient photoreaction behavior (highly efficient in energy transfer pathway) on a clay surface may open a new strategical way to be employed in efficient photocatalytic reactions.

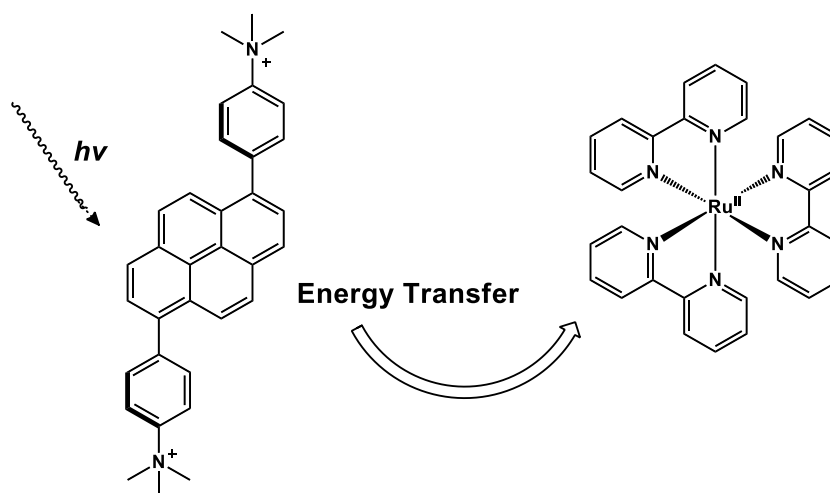


Figure 1.18. Schematic picture for light energy transfer from pyrene derivative to $[\text{Ru}(\text{bpy})_3]^{2+}$ complex on a clay surface.

A second example of energy transfer decay will be illustrated. In this case $[\text{Ru}(\text{bpy})_3]^{2+}$ complex participates as energy donor center, and a specific substrate acts as the acceptor of energy and can be used in organometallic synthesis. A few organic transformations were done by triplet-triplet energy transfer (TTET) with the photoexcited $[\text{Ru}(\text{bpy})_3]^{2+}$ catalyst. Relaxation of excited ruthenium complex from its lowest excited state through Förster mechanism pathway leads to an excitation of another organic molecule to go from its ground state to its lowest triplet excited state. As example of this TTET process, the photoexcited $[\text{Ru}(\text{bpy})_3]^{2+}$ complex promotes norbornadiene from its ground state to its triplet excited state, and results in the bond rearrangement to give quadricyclane cyclic product (Figure 1.19).⁵⁶ Reductive and oxidative quenching of the photoexcited ruthenium complex (electron transfer process) are disfavored here, taking in consideration that the oxidation and reduction potentials of norbornadiene are higher than the redox potentials of ruthenium complex at both ground and excited states. Similar bond rearrangement reactions like dimerization of anthracene can occur by triplet-triplet energy transfer process from photoexcited $[\text{Ru}(\text{bpy})_3]^{2+}$ complex.⁵⁷

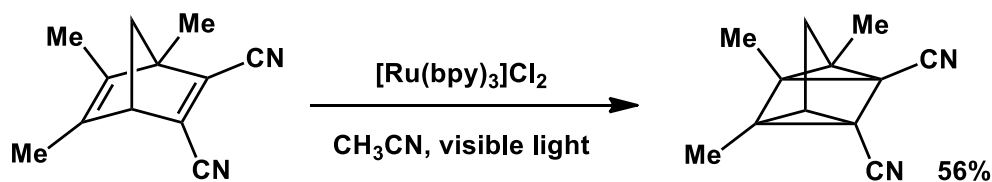


Figure 1.19. Quadricyclane rearrangement from norbornadiene *via* energy transfer process.

This direct energy transfer from the photoexcited $[\text{Ru}(\text{bpy})_3]^{2+}$ complex to the organic molecules for bond rearrangement (cyclization) is limited (energy transfer vs electron transfer) as discussed by Yoon and his co-workers in 2012.⁵⁸ In [2+2] styrene cycloaddition, the reaction pathway was disabled by energy transfer process using $[\text{Ru}(\text{bpy})_3]^{2+}$, since the triplet state energy of photoexcited ruthenium complex is $46.8 \text{ kcal}\cdot\text{mol}^{-1}$ which is lower than the triplet state energy of styrene that is $60 \text{ kcal}\cdot\text{mol}^{-1}$. Therefore, this let the reaction decay to go through electron transfer pathway (oxidative pathway) by radical cation to give [4+2] adduct, instead of energy transfer decay that is responsible to give [2+2] cyclized product. The energy transfer reaction is favorable when the HOMO energy of the donor is higher than the LUMO energy of the acceptor. This was clearly seen by using iridium(III) complex as a photocatalyst for this cyclization reaction, taking into consideration that its triplet excited state is $61 \text{ kcal}\cdot\text{mol}^{-1}$, which is a little bit higher than the energy state of styrene. As a result, the reaction pathway goes through the triplet-triplet energy transfer pathway and not in the electron transfer process, and gives the desired product going through [2+2] cyclization reaction (Figure 1.20).⁵⁸

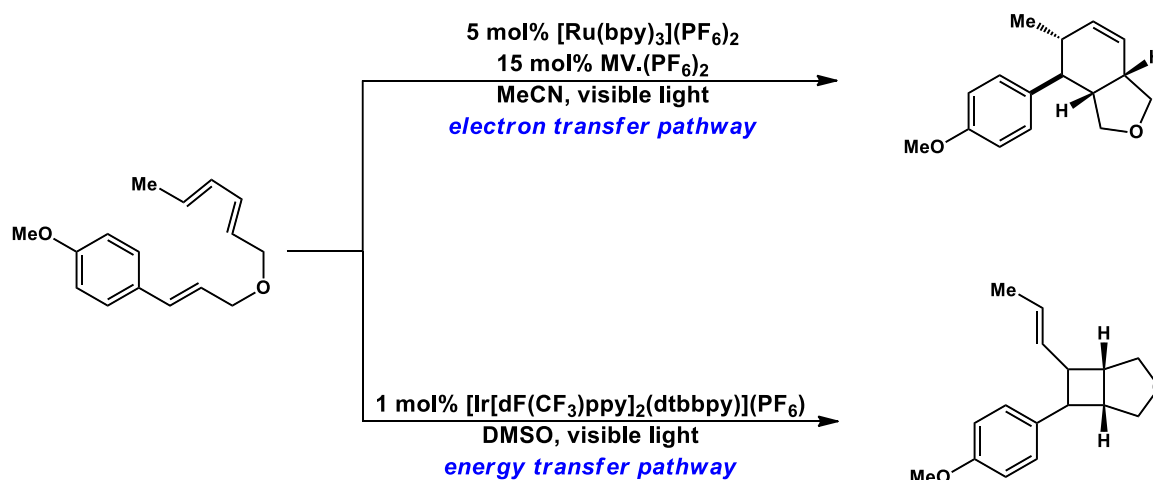


Figure 1.20. Styrene cycloaddition depending on the decay pathway of the photoexcited catalyst.

III.2.2. Electron transfer mechanism

Equations (7 & 8) illustrate the electron transfer reactions pathway. The excited ruthenium(II) complex center can either go through oxidative quenching pathway by donating a single

electron to a specific electron acceptor (A), or through reductive quenching pathway by taking a single electron from an electron donor (D).

In order to have such an electron transfer between the donor and the acceptor, the electron transfer quenching pathway should be thermodynamically allowed. The reactivity of the excited state is usually improved with a higher energy difference between the relaxed excited state and the ground state (E_{00}), as it is seen in the equation of Gibbs free energy of photo-induced electron transfer (equation 11).⁵⁹

$$\Delta G^0 = e[E_{ox.}(D) - E_{red.}(A)] - E_{00} - \frac{e^2}{\epsilon_s R_c} - \frac{e^2}{r} \left(\frac{1}{37} - \frac{1}{\epsilon_s} \right) \quad (11)$$

In this equation ΔG^0 represents the free energy of the reaction. $E_{ox.}(D)$ and $E_{red.}(A)$ corresponds to the oxidation and reduction potentials of the electron donor and electron acceptor half-reactions respectively, the correction value of the ion-pair solvation difference in which these redox potentials were measured is illustrated by the last term. The third term represents the Coulombic interaction between both positively and negatively charged donor and acceptor moieties respectively. ϵ_s is the dielectric constant of the solvent, R_c is the distance of separation between the centers of both electron acceptor and donor, and finally r is the average ionic radius.

In photoredox catalysis it is important to have reversible redox reactions for both electron donor and electron acceptor.⁵⁴ In 1956 Marcus gave the first proposition of electron transfer theory.⁶⁰ This theory described the kinetics of electron transfer process between the weakly coupled electron acceptor and donor, where the outer sphere electron transfer rate constant (k_{ET}) could be illustrated in the following equation (12).^{54,61} Generally, the photo-induced electron transfer reaction liberates energy (exothermic), and according to Marcus theory in the inverted region, if the transfer reaction becomes more thermodynamically favored (the driving force becomes increasingly negative) then the rate of electron transfer will slow down (depending on the nature of each system).

$$k_{ET} = \frac{2\pi}{h} |H_{AD}|^2 \frac{1}{\sqrt{4\pi\lambda K_B T}} \exp \left[\frac{(-\Delta G^0 + \lambda)^2}{4\lambda K_B T} \right] \quad (12)$$

In this expression, ΔG^0 is dependent on the redox potentials of both electron donor and acceptor, this free enthalpy energy is considered to be the driving force of electron transfer decay. $|H_{AD}|$ is the electronic coupling between the electron donor and acceptor states, and the magnitude of this electronic coupling is dependent on the distance and orientation of both donor and acceptor states, and that makes it difficult to be specified in solution for bimolecular reactions. λ represents the reorganization energy, upon the electron transfer reaction in progress the charge distribution changes in the molecule, as well as the solvent molecules reorganization due to charge redistribution that goes along with electron transfer step.⁵⁴

In the literature, many bimetallic systems were reported that are composed of ruthenium(II) tris-bipyridine complex and other transition metals (used to quench the photoexcited ruthenium complex by electron transfer).^{62,63,64} However, if we are planning to mimic natural photosynthesis, it is important to have the ruthenium complex center connected with an electron donor and/or electron acceptor moieties (forming the favorable triads or dyads), and by that it is possible to reach the charge separated state (CSS) as found in nature, as well as it can be used in photocatalytic applications (splitting water into oxygen and hydrogen molecules) by the aid of electron transfer between the three components of the triad or dyad systems.

At the beginning, the first prepared triads based on ruthenium tris-bipyridine complex were lacking symmetry and linearity, by having two electron acceptor or two donor units on the ruthenium center that gives the two different isomers (*fac* and *mer*). Thus, it leads to a short lifetime and inefficient charge separated state (CSS). As it is seen in the following example (Figure 1.21), the triad which was built around ruthenium tris-bipyridine complex was formed by connecting to this center two phenothiazine (PTZ) which act as electron donor moieties, and one N,N'-di-quaternary-2,2'-bipyridinium (diquat, DQ^{2+}) which acts as an electron acceptor. This unsymmetrical triad with a flexible connecting neighbor acceptor-donor moiety, leads to a fast recombination of the created ions of the triad. As a result, the lifetime of CSS in such triad becomes shorter (150 ns).^{65,66}

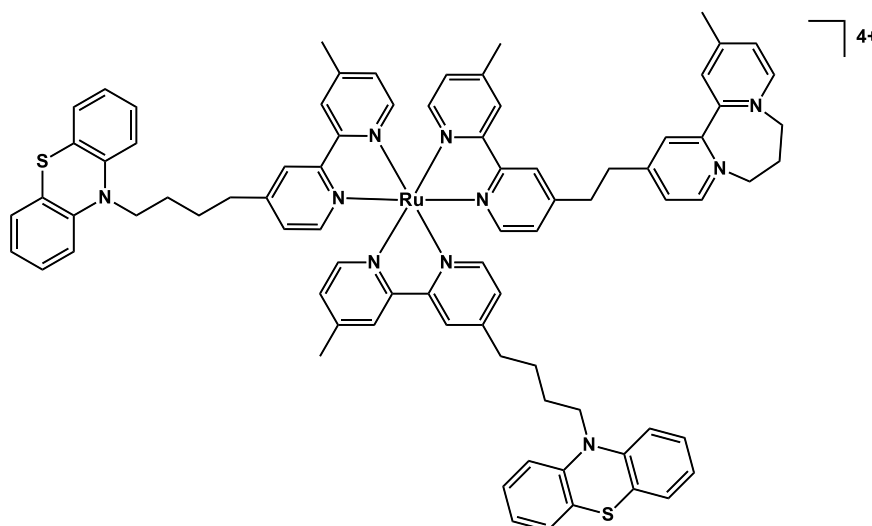


Figure 1.21. Ruthenium tris-bipyridyl complex with diquat and phenothiazine moieties.

As a consequence, different approaches come to minimize the charge recombination between the oxidized electron donor and reduced acceptor to have efficient CSS (longer lifetime), by making the distance between the electron donor and electron acceptor as long as possible. An elegant example was done by Wenger, by attaching both electron donor (triarylamine, TAA) and the electron acceptor (9,10-anthraquinone, AQ) on the same bipyridine ligand at positions 5 and 5' to avoid isomerization first, and by using *p*-xylene linker in order to have a non-conjugated and much rigid triad system (Figure 1.22).^{67,68} Therefore, upon this good separation between the electron donor and acceptor moieties and breaking the electron conjugation in the triad (22 Å distance of electron separation), the formed CSS (TAA⁺-Ru^{II}-AQ⁻) after successive electron transfer process was of quantum yield greater than 64% with a long lifetime (1.3 μs in acetonitrile).

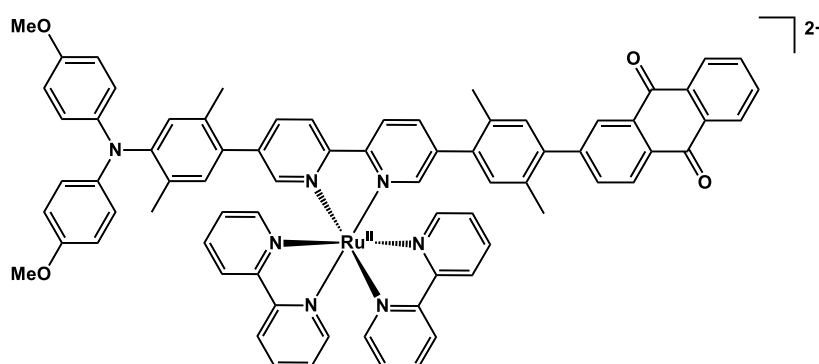


Figure 1.22. TAA(donor)-Ru(II)(photosensitizer)-AQ(acceptor) triad.

$\text{Ru(II)-Py}^*-\text{MV}^{2+}$. Electron transfer decay occurs from the excited pyrene to the viologen electron acceptor, to generate $\text{Ru(II)-Py}^+-\text{MV}^+$ intermediate.

Then another electron transfer process occurs from ruthenium(II) to the oxidized pyrene, to have at the end this charge separated state $\text{Ru(III)-Py}-\text{MV}^+$, which lasts for $100 \mu\text{s}$ before the system goes back to its ground state by back electron transfer process (BET) (Figure 1.24).

This long-lived CSS is due to the large separation distance between Ru(III) and MV^+ moieties in the supramolecular assembly.

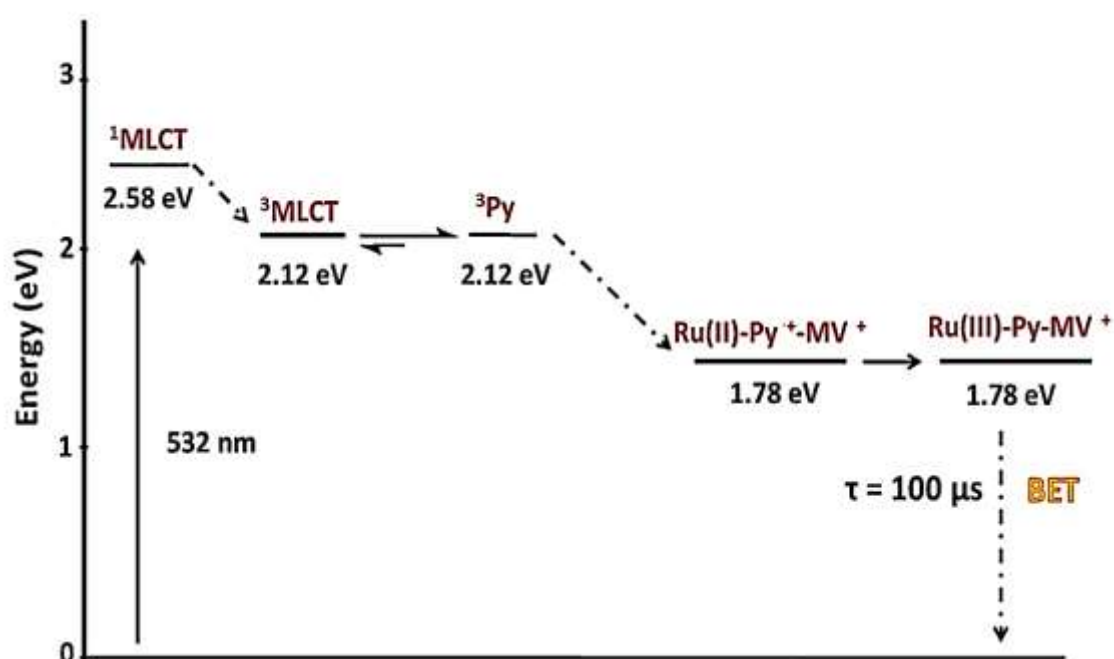


Figure 1.24. Energy and electron transfer decay to create the long-lived CSS $\text{Ru(III)-Py}-\text{MV}^{*+}$.

This $\text{Ru(II)-Py-Ad@CD-MV}^{2+}$ supramolecular assembly is suggested to be a good candidate for photocatalytic applications and for solar water splitting reactions at its charge separated state, due to the strong oxidation potential of the photo-oxidized $[\text{Ru}(\text{bpy})_3]^{3+}$ complex, that is capable to oxidize water.

Moreover, the redox potential of $\text{MV}^{2+}/\text{MV}^+$ couple is -0.45 V vs standard hydrogen electrode (SHE), that is considered enough for platinum catalyzed hydrogen production.

III.3. Stability and induced isomerization of $[\text{Ru}(\text{bpy})_3]^{2+}$

It has been discussed before that the advantages of $[\text{Ru}(\text{bpy})_3]^{2+}$ complex makes it a widely used photosensitizer in many different applications (due to its appropriate photophysical and redox potential properties). However, some limitations can arise in using this complex. Its stability upon irradiation is considered to be one of the main problems, and the formation of (stereo) isomers upon substitution of the bpy ligand with functional groups is the second problem that will be discussed.

One of the important properties of a photosensitizer is stability in the ground and excited states. Even though $[\text{Ru}(\text{bpy})_3]^{2+}$ complex is photo-stable in general, nevertheless, this bidentate ruthenium(II) complex faces a ligand dissociation over a long period of light exposure in catalysis conditions.^{70,71,72} As it was explained in details before, once ^3MC state is formed, the ruthenium-nitrogen bond can undergo cleavage leading to the degradation of this tris-bidentate complex. Thus, to overcome this stability problem, shifting from bidentate to tridentate ligands would be a suitable solution. In general, bis-terdentate ruthenium(II) complexes are more resistant to photo-dissociation reactions (having three coordinating bonds instead of two).

On the other hand, tris-bidentate metal complexes can lead to Λ and Δ enantiomers. Furthermore, the substitution of this bpy ligand with functional groups in $[\text{Ru}(\text{bpy})_3]^{2+}$ complex or by using unsymmetrical bidentate ligands like 8-(pyrid-2'-yl) quinoline (8-Qpy) leads to the formation of *meridional* (*mer*) and *facial* (*fac*) isomers.^{73,74,75} This isomer formation of ruthenium(II) complex based on bidentate ligands will give rise to a clear problem in vectorial charge separation devices.

Therefore, the appropriate solution for all of that is to use bis-terdentate equivalent of $[\text{Ru}(\text{bpy})_3]^{2+}$ namely $[\text{Ru}(\text{tpy})_2]^{2+}$ (tpy = 2,2':6',2''-terpyridine) in order to avoid isomerism, to gain stability and to have linearity with maximal separation between electron donor and electron acceptor moieties in donor-photosensitizer-acceptor triads at their CSS.

III.4. Bis-terdentate ligand ruthenium complex $[\text{Ru}(\text{tpy})_2]^{2+}$

The tridentate 2,2':6',2''-terpyridine ligand that is consisting of three imine atoms (Figure 1.25, a), is considered to be an interesting *N*-heterocyclic ligand. This ligand possesses a remarkable high binding affinity toward transition metal ions (our interest toward ruthenium ion), that comes from its chelation property, in addition to $d_{(\text{metal})}-\pi^*_{(\text{ligand})}$ back donation of the metal ion to the pyridine rings. Consequently, tpy ligand can coordinate in a ratio of 2 to 1 with ruthenium metal ion respectively, to form a stable octahedral metal complex, with a linear assembly when it is functionalized at 4'-position (Figure 1.25, b).⁷⁶

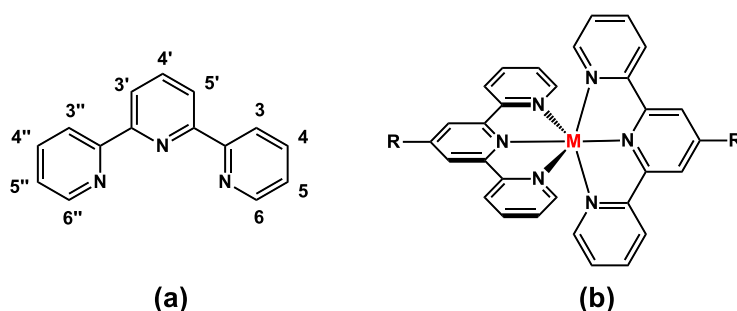


Figure 1.25. “a” is the non-functionalized 2,2':6',2''-terpyridine with its assignment. “b” is the 4'-functionalized octahedral metal complex.

Many new organic-inorganic hybrid materials were developed and synthesized based on $[\text{Ru}(\text{tpy})_2]^{2+}$ complex over the last few decades due to the symmetrical geometry it affords, in addition to the easy functionalization at its 4'-position. $[\text{Ru}(\text{tpy})_2]^{2+}$ complex has been used in many fields. For example, recently different kinds of polymers like poly-ethylene glycol, polystyrene, bio-macromolecules, micelles were synthesized and doped with $[\text{Ru}(\text{tpy})_2]^{2+}$ complex into their polymeric structure. As well as this ruthenium(II) complex was incorporated in the manufacturing of electro-catalytic surfaces⁷⁷, also it has been used in biological applications as it can have a good antibacterial and antifungal activity.⁷⁸

However, unlike $[\text{Ru}(\text{bpy})_3]^{2+}$ complex, there is a big obstacle using $[\text{Ru}(\text{tpy})_2]^{2+}$ complex in the photophysical processes like the conversion of solar light into usable energy, due to its weak photophysical properties. $[\text{Ru}(\text{tpy})_2]^{2+}$ is a quasi-non-emitting complex with a $^3\text{MLCT}$ excited state lifetime of 250 ps in degassed acetonitrile at room temperature, compared to the long excited state lifetime about 1 μs of $[\text{Ru}(\text{bpy})_3]^{2+}$.^{29,35,41} The reason for such mediocre

photophysical properties at room temperature comes from the distorted octahedral geometry of this ruthenium(II) complex that was built with rigid tridentate polypyridine ligands. Thus, such distorted geometry gives rise to a weaker ligand field strength (Δ_o), that results in reducing the energy gap between 3MC state and 3MLCT state, by reducing the energy of 3MC . Therefore, 3MC state (d-d) can be easily thermally populated from 3MLCT state by fast internal conversion process for $[Ru(tpy)_2]^{2+}$ complex, and this leads to a fast deactivation of excited state back to the ground state by non-radiative decay, opposite to the luminescent $[Ru(bpy)_3]^{2+}$ complex (Figure 1.26). However, at 77 K in a rigid matrix, $[Ru(tpy)_2]^{2+}$ complex exhibits a long luminescence excited state lifetime by suppressing the thermal internal conversion process.

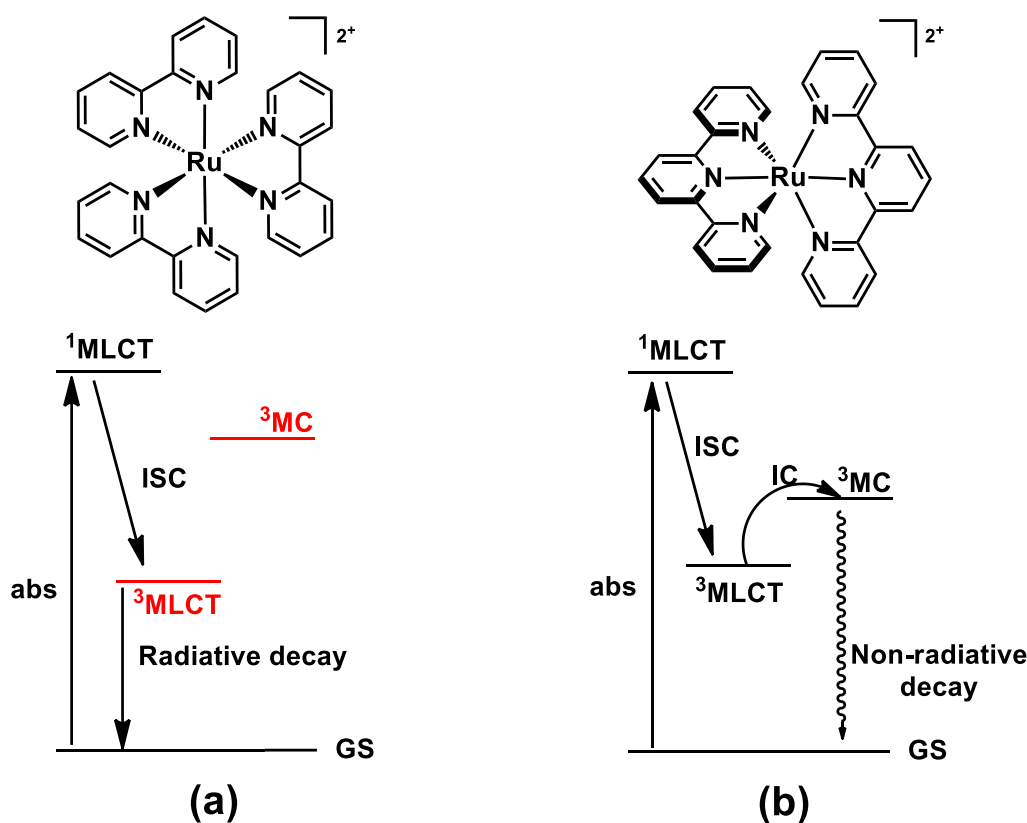


Figure 1.26. Perrin-Jablonski diagram for $[Ru(bpy)_3]^{2+}$ (a) vs $[Ru(tpy)_2]^{2+}$ (b).

The direct contribution from the 3MLCT state to ground state (GS) through thermal population of 3MC state is one of the pathways for non-radiative deactivation.

IV. Strategies for enhancing the excited state lifetime of Ru(II) complexes with tridentate ligands

Much effort has been dedicated to designing bis-tridentate polypyridine ruthenium(II) complexes with improved photophysical properties, mainly extending the excited state lifetime to have better photosensitization functionality in electron and energy transfer processes. Different strategies have been developed to minimize the thermal population of the ^3MC excited state from the emissive $^3\text{MLCT}$ excited state, either by destabilizing ^3MC and/or stabilizing $^3\text{MLCT}$ thereby increasing the energy gap separation between them. Extending excited state lifetime at room temperature can be realized using any of the following techniques:

- Incorporation of electron withdrawing and electron donating functional groups at the 4'-position of tpy ligand in a $[\text{Ru}(\text{tpy})_2]^{2+}$ complex.
- Extending the π -conjugation of the system.
- Using π -accepting ligands.
- Enhancing the ligand field (Δ_o), as a result of optimizing the octahedral coordination geometry.

In addition to these, there are other strategies that were done like (we will not develop):

- Using bichromophoric systems.
- Using strong σ -donor ligands (cyclometallation)

In my thesis, the target is to prepare new ruthenium(II) complexes based on tridentate ligands possessing an extended π -conjugated system, and coordinating with a 6-member metallacycle fashion to enhance the complex geometry.

IV.1. Electron withdrawing and electron donating groups

The substitution of polypyridine ruthenium(II) complexes with electron withdrawing groups (EWGs) and/or electron donating groups (EDGs) leads to a change in the energy of molecular orbitals.⁷⁹ In this context, direct attachment of these EDGs and EWGs on the central pyridine ring of the tpy ligand on $[\text{Ru}(\text{tpy})_2]^{2+}$ complexes is one method employed to tune its photophysical properties. In general, EWGs withdrawing electron density from the ruthenium center *via* the π^* -system of the ligand leads to a stabilization of the LUMO, and thus gives rise to a stabilized $^3\text{MLCT}$ excited state. This stabilization increases the $^3\text{MLCT}$ - ^3MC energy gap and therefore lowers the thermal population of the non-emissive ^3MC excited state. As a result, an increase in the luminescence lifetime of these complexes can be observed. On the contrary, EDGs destabilize the HOMO without significantly affecting the LUMO.

$[\text{Ru}(\text{tpy-x})(\text{tpy-y})]^{2+}$ type complexes (where x and y are wide ranges of EWGs and EDGs), with all possibilities of x and y, absorb with a red-shift of both $^1\text{MLCT}$ and the emissive $^3\text{MLCT}$ transitions as compared to the parent $[\text{Ru}(\text{tpy})_2]^{2+}$ complex which has a maximum at 475 nm for $^1\text{MLCT}$ and emission from its $^3\text{MLCT}$ at 629 nm.⁸⁰

In addition to the observed spectroscopic effect, we can see the effect of these groups electrochemically as a change in the oxidation potential of Ru(II) in the presence of EWGs (difficult to oxidize), or EDGs (easier to oxidize). Moreover, the reduction potential of the tpy ligand can also be affected in the presence of these functional groups. Therefore, the $\text{Ru}^{3+}/\text{Ru}^{2+}$ and ligand/ligand $^-$ potentials are directly affected by the withdrawal or addition of electron density from or to the metal center.

Some examples of strong EWGs, such as CN and MeSO_2 will be illustrated and discussed in terms of how efficiently they improve the luminescence excited state lifetime of $[\text{Ru}(\text{tpy})_2]^{2+}$ complexes when they are connected at the 4'-position of the tpy ligand. $[\text{Ru}(\text{tpy})_2]^{2+}$ complexes can be either functionalized at one or both tpy ligands, to give the heteroleptic or homoleptic complexes, respectively. In heteroleptic complexes, i.e., with one CN group, the LUMO is stabilized to give a low lying $^3\text{MLCT}$ with absorption maximum at 701 nm, and therefore a longer excited state lifetime of 75 ns is obtained with 2% quantum yield at room temperature in deaerated solvent. In contrast, in the homoleptic complex with two strong

electron withdrawing CN groups, the ruthenium(II) center is relatively electron poor and difficult to oxidize, thus the $^3\text{MLCT}$ energy increases to emit with a blue shift at 680 nm as compared to that of the heteroleptic complex. By slightly decreasing the energy gap between both excited states, this homoleptic complex has a lower excited state lifetime of 50 ns under the same conditions as the heteroleptic one.⁸¹ All of these data with the enhanced excited state lifetimes of the homoleptic and heteroleptic complexes using MeSO_2 another strong EWGs,⁸² are summarized in Table 1.1 below. Furthermore, an improvement was observed for the complex with both a strong MeSO_2 EWG and a hydroxyl EDG at the same time, resulting in a 50 ns excited state lifetime with a red shifted emission maximum at 706 nm and 0.5% quantum yield. This result was explained by the effect of the OH group which destabilized the HOMO in addition to the effect of the MeSO_2 group, which stabilized the LUMO at the same time, resulting in a very low energy $^3\text{MLCT}$, and thus having a longer excited state lifetime as compared to both homoleptic and heteroleptic complexes with MeSO_2 EWGs at the same conditions.

Triarylpyridinium (TP^+) shown in Figure 1.27, is another EWG substituent that can be functionalized at its phenyl ring and connected to an electron acceptor moiety forming the triad molecule with the ruthenium(II) chromophore. A simple incorporation of one TP^+ into the non-luminescent $[\text{Ru}(\text{tpy})_2]^{2+}$ complex extends the excited state lifetime from 0.25 ns to 55 ns at room temperature. However, as explained above, in the case of di-substitution in a homoleptic complex, the excited state lifetime was decreased to 27 ns compared to the heteroleptic complex under the same conditions.⁸³

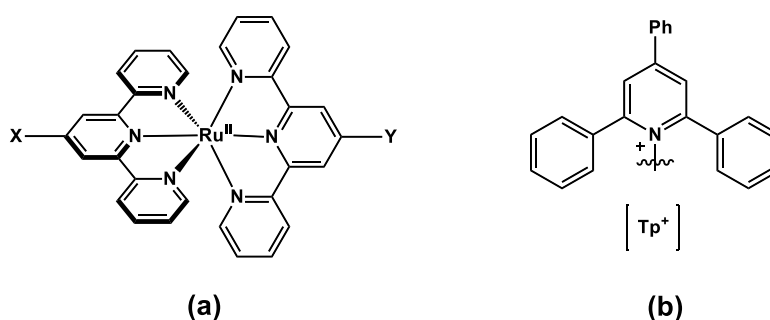
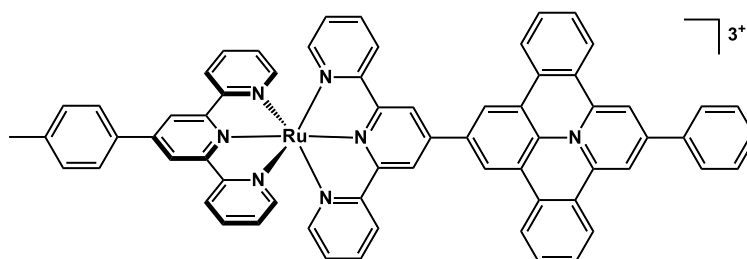


Figure 1.27. Substituted $[\text{Ru}(\text{tpy})_2]^{2+}$ (a), and the triarylpyridinium (Tp^+) EWG (b).

Table 1.1. Photophysical properties of substituted $[\text{Ru}(\text{tpy})_2]^{2+}$ complexes with different EWGs., recorded in deaerated acetonitrile solution at room temperature.

X	Y	Emission ($\lambda_{\text{max.}}$, nm)	Excited state lifetime (τ, ns)	Quantum yield (Φ)
H	H	629	0.25	$0.5 \times 10^{-3}\%$
CN	H	701	75	2%
CN	CN	680	50	2%
MeSO ₂	H	679	36	0.4%
MeSO ₂	MeSO ₂	666	25	0.5%
MeSO ₂	OH	706	50	0.5%
Tp ⁺	H	670	55	0.73%
Tp ⁺	Tp ⁺	644	27	0.39%

However, an 8 ns decrease of the excited state lifetime at room temperature was observed when a phenyl spacer was introduced between the tpy ligand and the TP⁺ moiety (Figure 1.28). This photophysical property is attributed to the diminishing electron withdrawing effect of pyridinium on ruthenium center caused by the phenyl spacer.⁸⁴

**Figure 1.28.** Ruthenium(II) complex substituted with the phenyl-spaced-pyridinium acceptor.

IV.2. Extending the π -conjugated system

Increasing the extent of π -conjugation in the system, by aromatic substituents introduced on the backbone of the tpy ligand, is the second way to tune the photophysical properties of bis-tridentate ruthenium complexes. A charge delocalization over a larger surface area can occur with an extended π -system that leads to a stabilized emitting $^3\text{MLCT}$ excited state relative to the non-emissive ^3MC state.⁸⁵ Aromatic ring substituted at the 4'-position of the tpy ligand can lead to a prolongation of the excited state lifetime, as in $[\text{Ru}(\text{ttpy})_2]^{2+}$ (ttpy = 4'-toluyl-2,2':6':2''-terpyridine) where the lifetime reaches 0.95 ns in deaerated acetonitrile at room temperature. However, this excited state lifetime does not vary that much from the $[\text{Ru}(\text{tpy})_2]^{2+}$ complex. This result was explained by the phenyl ring twisting from the central pyridine ring on the tpy ligand that was induced by the steric interaction between the *ortho* hydrogens at the inter-annular bond between the two rings. Thus, it leads to a break in the planarity of the π -conjugated system and no significant enhancement of the lifetime was observed.

An approach for extending the π -system of $[\text{Ru}(\text{ttpy})_2]^{2+}$ complexes with a lifetime enhancement (more than 0.95 ns), is to introduce imidazole substituents connected to the phenyl rings at the *para* positions. A blue shifted excited state at 660 nm maximum with an extended lifetime of 8.5 ns was detected, by increasing the $^3\text{MLCT}$ - ^3MC energy gap after stabilizing $^3\text{MLCT}$ state by extensive delocalization over the imidazole group. Moreover, the excited state lifetime can be extended, up to 15.8 ns, by stabilizing the $^3\text{MLCT}$ excited state even more when the imidazole ring is more conjugated (Figure 1.29).⁸⁶

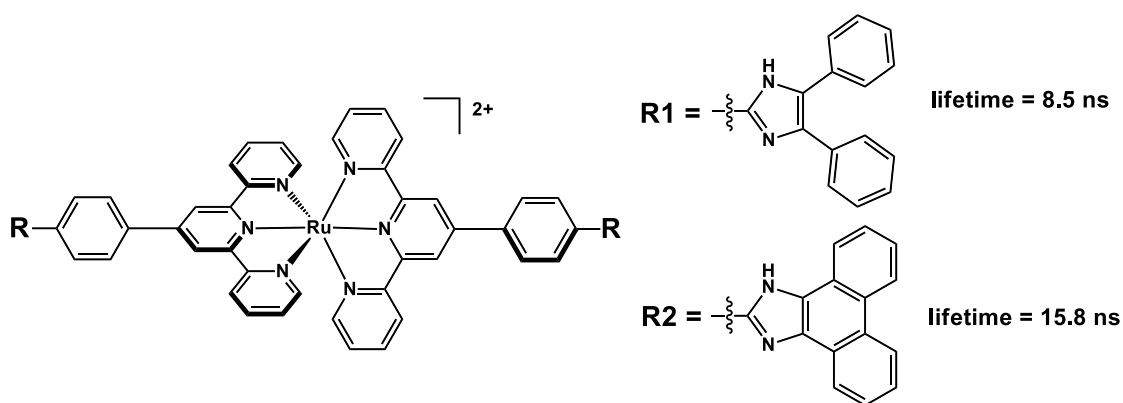


Figure 1.29. Imidazole substitution at the 4'-position of $[\text{Ru}(\text{tpy})_2]^{2+}$ complex.

More elegant work extending the π -conjugated system is accomplished by incorporating an acetylene electron-withdrawing group on a tpy ligand which was introduced first by Zissel and coworkers.^{87,88} The direct substitution of such sp -hybridized acetylene groups at the 4'-positions of tpy ligands, aligns the π -orbitals to form a coplanar system, which can lead to enhanced electronic delocalization between the tpy ligand unit and an aryl group connected on the second side of the alkynyl spacer. Therefore, an extra stabilization of the LUMO of the polypyridine ruthenium(II) complex occurs. Consequently, this LUMO stabilization leads to a decrease in the energy of the 3MLCT excited state, thus increasing the energy gap between 3MLCT and 3MC states. The resulting effect increases the excited state lifetime with a red shift of the absorption and emission maxima. Moreover, the excited state lifetime increases and the emission energy drops when there are two acetylene molecules as compared to only one acetylene spacer.⁸⁰ The longest excited state lifetime at room temperature for a $[Ru(tpy)_2]^{2+}$ complex attached to an acetylene unit corresponds to the acetylene-pyrene unit (Figure 1.30).⁸⁹ This complex has an excited state lifetime of 580 ns at room temperature in deaerated solvent. This long-lived excited state is attributed to the π - π^* orbital mixing between the higher triplet state of ethynyl-pyrene (3Py) moiety and the 3MLCT of the ruthenium complex. Thus, due to the thermal population of 3Py from 3MLCT , the lifetime is longer as a result of delaying the emission by a "reservoir effect".⁸⁹ A terthiophene based acetylene complex attached to $[Ru(tpy)_2]^{2+}$ was also synthesized and gave a similar effect of extending the excited state lifetime at room temperature (435 ns).⁹⁰

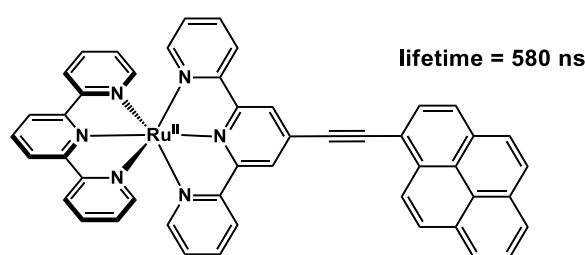


Figure 1.30. Pyrene-acetylene substituted on a $[Ru(tpy)_2]^{2+}$ complex.

A fruitful approach for extending the π -system of $[Ru(Ph-tpy)_2]^{2+}$ complex with a longer excited state lifetime (more than 0.95 ns) was applied by introducing a pyrimidinyl spacer instead of the phenyl unit (Figure 1.31).^{74,91,92} The intermolecular interaction between the nitrogen atoms of the 2-pyrimidinyl and the hydrogen atoms of the central pyridine ring of the

tpy ligand, allowed both the pyrimidyl ring and the tpy ligand to lie in a co-planar fashion. Therefore, the system has better π -conjugation, which gives rise to a stabilized LUMO, and a larger ${}^3\text{MLCT}$ - ${}^3\text{MC}$ energy gap, resulting in a much improved excited state lifetime at room temperature. Moreover, a combination of both electron withdrawing effects (using strong EWGs such as a cyano group at the 5-pyrimidyl position) and efficient electron delocalization over a co-planar system, contribute to further stabilization of the LUMO. These attributes enhance the excited state lifetime more and more.

Examples of homoleptic and heteroleptic complexes using pyrimidyl spacers are summarized in Table 1.2 below.

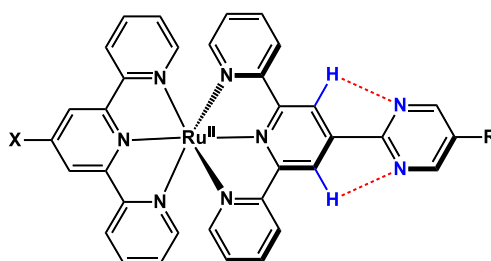


Figure 1.31. Substituted $[\text{Ru}(\text{tpy})_2]^{2+}$ with a pyrimidyl spacer.

Table 1.2. Photophysical properties of substituted $[\text{Ru}(\text{tpy})_2]^{2+}$ complex with different pyrimidyl unit.

X	R	Emission (λ_{max} , nm)	Excited state lifetime (τ , ns)	Quantum yield (Φ)
H	H	675	8	0.2 %
2-pyrimidyl	H	673	11	0.25 %
H	2-pyrimidyl	690	43	0.38 %
H	CN	713	200	0.89 %
5-cyano-2-pyrimidyl	CN	705	231	1.2 %

IV.3. π -accepting ligands

Decreasing the energy level of the $^1\text{MLCT}$ state and consequently the energy of the emitting $^3\text{MLCT}$ excited state can be achieved by using strong π electron accepting ligands, thereby increasing the luminescent excited state lifetime of the non-emitting $[\text{Ru}(\text{tpy})_2]^{2+}$ complex. Tridentate triazine based ligands (trz) are well-known π electron accepting ligands. These types of ligands can be synthesized by replacing the central pyridine ring of a tpy ligand by a triazine hetero-aromatic ring, maintaining the (NNN) chelation mode.⁹³ The heteroleptic ruthenium(II) complex, $[\text{Ru}(\text{trz})(\text{tpy})]^{2+}$, with an aromatic phenyl ring at the pendant position (Figure 1.32) emits with a red shift at 740 nm, and a longer excited state lifetime of 9 ns at room temperature as compared to the $[\text{Ru}(\text{tpy})_2]^{2+}$ complex.⁹⁴ This enhanced excited state lifetime attributed to a stabilized $^3\text{MLCT}$ state, comes from the π electron accepting nature of the trz ligand. Furthermore, the $^3\text{MLCT}$ stabilization was achieved by the enhanced coplanarity arising from the intermolecular hydrogen bonding between the nitrogen atoms of the trz ring and the hydrogen atoms of the pendant phenyl ring.

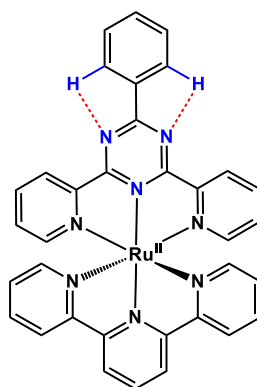


Figure 1.32. Ruthenium(II) complex with a tridentate triazine-tpy-based ligand.

IV.4. Optimizing the octahedral coordination geometry (chelate ring expansion)

As it has been discussed above with all the strategies, increasing the excited state lifetime of polypyridine ruthenium(II) complexes based on tridentate ligands is not an impossible task to achieve. A different approach has been developed by the team of Hammarström that does not stabilize $^3\text{MLCT}$ excited state like the previous work, but rather, it destabilizes the non-emissive ^3MC state. This new approach was established based on ligand field theory, in which a greater splitting between the t_{2g} and e_g metal orbitals can be reached by optimizing the octahedral coordination geometry. Consequently, the $^3\text{MLCT}$ - ^3MC energy gap would increase by destabilization of the ^3MC state, which leads to less interaction between the arising electronic states ($^3\text{MLCT}$ and ^3MC) and thus decreases the thermal population of ^3MC from the emissive $^3\text{MLCT}$ excited state. Therefore, the excited state lifetime becomes longer at room temperature. In contrast, in this new strategy it is not necessary to stabilize the excited state energy as in the previously described strategies, and it is better to keep the $^3\text{MLCT}$ excited state high, to maintain a high driving force for eventual successive electron transfer processes. Designing tridentate ligands with larger trans-bite-angles than those obtained for the $[\text{Ru}(\text{tpy})_2]^{2+}$ complex by extending the chelation angle when going from five to six-membered chelate rings is one way to achieve this goal.

This approach of Hammarström and his team was developed through three steps, or rather, through three examples starting in 2004. The first example was generated by opening the chelate angle of the tpy ligand through addition of one methylene linker between the two pyridine rings in a normal tpy ligand (Figure 1.33).^{95,96,46}

In this example, the excited state energy is not significantly lowered (emits at 655 nm), and at the same time, the luminescent excited state lifetime is increased by 50-fold (to 15 ns) with a remarkable enhancement in emission quantum yield (2%) with respect to the parent $[\text{Ru}(\text{tpy})_2]^{2+}$ complex. Moreover, in the X-ray crystallography of the complex illustrated in Figure 1.33, shows a bite angle (170°) closer to a perfect octahedral coordination than that of the $[\text{Ru}(\text{tpy})_2]^{2+}$ complex. However, the crystal structure also shows a twisting between the pyridine ring and the bipyridine of the ligand due to the presence of the additional carbon between them. Thus, the bite angle was reduced.

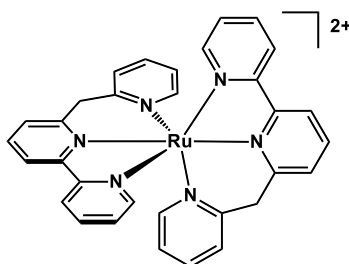


Figure 1.33. First example for optimizing the octahedral geometry of bis-tridentate Ru(II) complexes.

In the second example, the chelate angle was increased to a greater extent compared to the first one. However this time, by using more rigid ligands such as phenanthroline and quinoline motifs, greater planarity of the ligands was maintained, thus increasing the bite angle even more.⁷⁵ In this second example, the ligand was built with the same design as the first example by mixing five and six membered chelate rings. The extended π -conjugated system in this generation, achieved by having such rigid and planar ligands, leads to a stabilized LUMO, and thus the emission spectrum is more red shifted compared to the first example, with an emission at 712 nm for the complex shown in Figure 1.34. Moreover, the excited state lifetime of this complex increased dramatically to be similar to that of $[\text{Ru}(\text{bpy})_3]^{2+}$, with 810 ns and 5% emission quantum yield. Such enhanced lifetime is due to the extended π -conjugated system effect, which decreases the $^3\text{MLCT}$ state, as well as having a more octahedral geometry that gives a destabilized ^3MC state. These effects together result in an even bigger energy gap and a decrease in the thermal population of the ^3MC state.

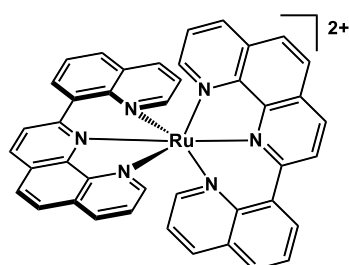


Figure 1.34. Second example for optimizing the octahedral geometry of bis-tridentate Ru(II) complexes.

Lastly the third example that was achieved by this team, maintained the rigid structure like the second example by using two quinoline units linked to a central pyridine ring (2,6-bis(8'-quinolinyl)pyridine ligand) as seen in Figure 1.35.⁹⁷

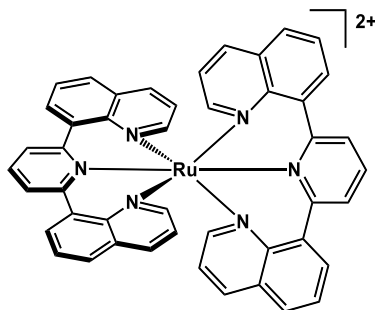


Figure 1.35. Third example for optimizing the octahedral geometry of bis-tridentate Ru(II) complexes.

This ligand gives a perfect octahedral bis-tridentate ruthenium(II) complex with a trans quinoline angles of 179.6° as confirmed by X-ray crystallography, and it is based only on six membered chelate rings. Moreover, this symmetrical complex structure can be functionalized at the 4-positions of the central pyridine rings, to incorporate electron donor and acceptor moieties. Therefore, it can be a building block for further construction of linear donor-photosensitizer-acceptor triad assemblies for vectorial electron transfer process.^{98,99}

A lower $^3\text{MLCT}$ excited state energy is detected for such complex with an emission at 700 nm, due to a large π -conjugated system that stabilizes the LUMO. On the other hand, due to the strong ligand field originating from the optimized octahedral geometry, the ^3MC is destabilized and has a high energy. Therefore, the energy gap between the two excited states becomes big enough to decrease the thermal population of ^3MC , and consequently, a microsecond excited state lifetime ($3 \mu\text{s}$) is obtained with a dramatic improvement of emission quantum yield to 20% at room temperature.

Furthermore, due to this pioneering work, other groups have begun to use this strategy to enhance the photophysical properties of ruthenium(II) complexes based on tridentate ligands.^{100,101,102}

Indeed, increasing the energy level of the non-emissive ^3MC excited state by optimizing the coordination octahedral geometry is not enough to have a long luminescent excited state lifetime with high emission quantum yield. Actually, we need less interaction between the arising electronic states, by having a greater $^3\text{MLCT}$ - ^3MC energy gap, i.e., there will be no enhancement by raising both excited state at the same time. Clear work demonstrating this point has been described in 2011, by preparing a new bis-tridentate ruthenium(II) complex based on *N*-Heterocyclic Carbene ligand (NHC ligand).⁷³ In the complex shown in Figure 1.36, the presence of a methylene linker between the pyridine and the imidazole rings interrupts the π -conjugated system for the whole ligand. Therefore, the LUMO energy level increases, and consequently, the energy level of the emissive $^3\text{MLCT}$ excited state increases. As a result, the $^3\text{MLCT}$ - ^3MC energy gap is reduced, even in the presence of a high ^3MC state due to the perfect octahedral geometry, and therefore the complex is not emitting at room temperature by thermal deactivation of the $^3\text{MLCT}$ to ^3MC excited state.

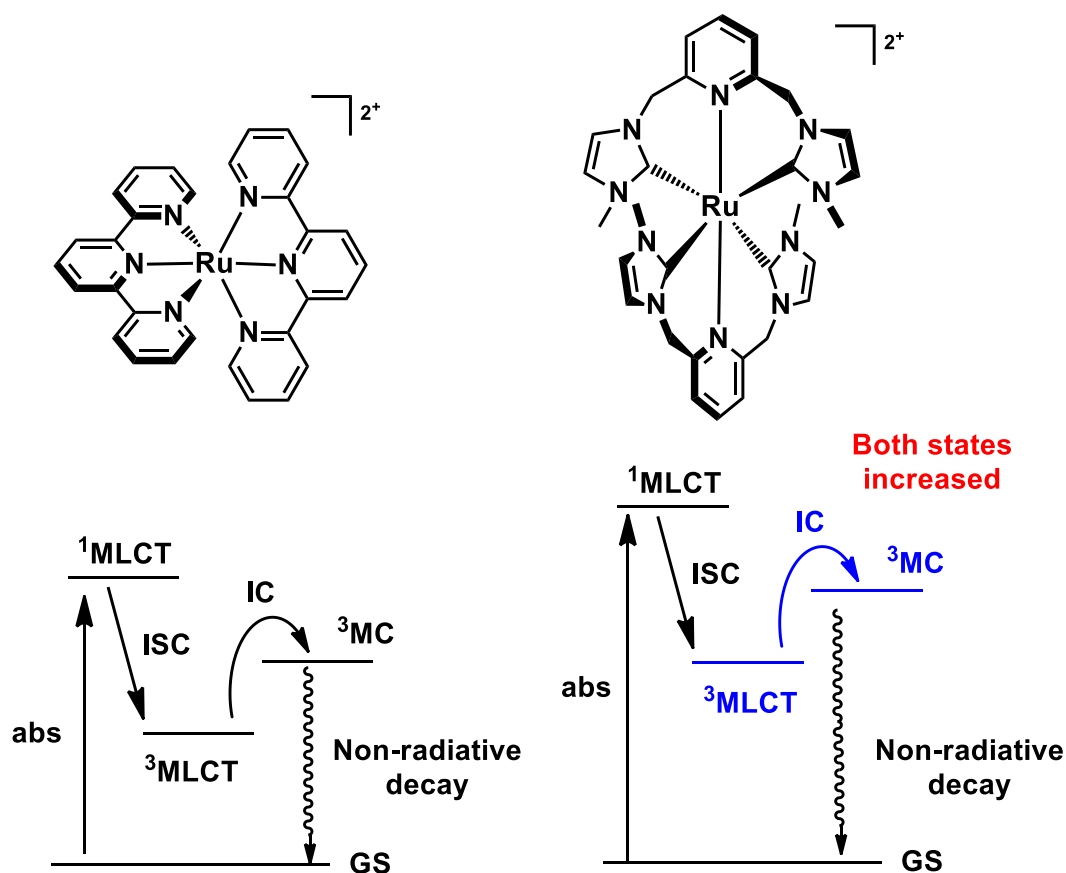


Figure 1.36. Perrier-Jablonski diagram comparing between $[\text{Ru}(\text{tpy})_2]^{2+}$ complex and Ru(II) complex based on *N*-Heterocyclic Carbene (NHC) ligands.

V. Scope of the thesis

Mimicking the natural photosynthesis process, by converting the absorbed solar energy into chemical energy, aiming to produce clean and renewable fuel from the sun is targeted strongly by scientists nowadays. In this general field, the thesis is focused more specifically on designing and characterizing new photosensitizers ruthenium(II) complexes. The geometry of the ruthenium(II) complexes is of pronounced importance especially in specifying their photophysical, photochemical, and electrochemical properties. We aim of preparing new stable bis-tridentate ruthenium(II) complexes that could be used in many different applications such as: catalysis, biological applications or treatment.

The main theme of the thesis is studying and exploring the coordination properties of new acridine-based tridentate ligands on ruthenium transition metal, mainly by changing the energy of the functionally active excited states (^3MC and $^3\text{MLCT}$) and tuning their energy levels by playing on the complex ligand field and ligand π -system.

In particular, enhancing the ligand field of such complexes can be reached by having a perfect octahedral geometry, which consequently increases the energy of the ^3MC excited state. Decreasing the energy level of the $^3\text{MLCT}$ state is directly affected by the degree of electron conjugation on the coordinated ligands. Moreover, separating as much as possible these two states helps to avoid the thermal contribution from ^3MC to $^3\text{MLCT}$ by internal conversion.

In this context, we prepared and explored new ligands based on acridine *N*-heterocycle platform, that can fit with our demands, by having low lying π^* energy orbital and thus could stabilize $^3\text{MLCT}$. Moreover, coordinating *via* six-membered metallacycles with Ru(II) metal by a tridentate fashion leads to destabilize ^3MC and gain stability respectively. The structure-function relationships between electrochemical, photophysical and photochemical behaviors of the newly obtained Ru(II) complexes have been studied.

The second chapter illustrates in details the synthetic ways that were followed and optimized to prepare a functionalized acridine backbone, and the explorations of the coordination properties of our first new (NNN) triimine ligand, named **dtdpa**, on ruthenium(II) metal.

The third chapter illustrates the preparation of the second (NNN) triimine acridine-based ligand, named **dt dpza**, of bigger coordination cavity by functionalization of the acridine platform with smaller pyrazole rings and see its coordination properties on the ruthenium(II) metal.

The fourth chapter will discuss in details the preparation of new Ru(II) complexes based on (SNS) tridentate acridine-based thioether ligand, named **dt dsa**, and explore the effect of sulfur coordinating atoms on complexes structure and photophysical properties.

The fifth chapter will discuss the preparation of flexible (SNS) thioanisole tridentate ligand, and explore its ruthenium(II) complexes properties, mainly their photoactivity and photosensitivity upon light irradiation, especially by featuring long Ru-S bonds.

VI. References

- (1) Stocker, T. F.; Qin, D.; Plattner, G.-K.; Tignor, M.; Allen, S. K.; Boschung, J.; Nauels, A.; Xia, Y.; Bex, V.; Midgley, P. M. IPCC, 2013: Summary for Policymakers. In: *Climate Change 2013: The Physical Science Basis. In Contribution of Working Group I to the Fifth Assessment Report of the Intergovernmental Panel on Climate Change*; Cambridge University Press, Cambridge, United Kingdom and New York, NY, USA Press.
- (2) Le Quéré, C.; Andres, R. J.; Boden, T.; Conway, T.; Houghton, R. A.; House, J. I.; Marland, G.; Peters, G. P.; van der Werf, G.; Ahlström, A.; Andrew, R. M.; Bopp, L.; Canadell, J. G.; Ciais, P.; Doney, S. C.; Enright, C.; Friedlingstein, P.; Huntingford, C.; Jain, A. K.; et al. The Global Carbon Budget 1959–2011. *Earth Syst. Sci. Data Discuss.* **2012**, 5 (2), 1107–1157.
- (3) Balzani, V.; Credi, A.; Venturi, M. Photochemical Conversion of Solar Energy. *ChemSusChem* **2008**, 1, 26–58.
- (4) Goldemberg, J. United Nations Development Programme/ United Nations Department of Economic and Social Affairs, World Energy Council: New York. In *World energy assessment: Energy and the Challenge of Sustainability*; 2000.
- (5) Lewis, N. S.; Nocera, D. G. Powering the Planet: Chemical Challenges in Solar Energy Utilization. *Proc. Natl. Acad. Sci.* **2006**, 103 (43), 15729–15735.
- (6) Alstrum-Acevedo, J. H.; Brennaman, M. K.; Meyer, T. J. Chemical Approaches to Artificial Photosynthesis. 2. *Inorg. Chem.* **2005**, 44 (20), 6802–6827.
- (7) Barber, J. Photosystem II: The Engine of Life. *Q. Rev. Biophys.* **2003**, 36 (1), 71–89.
- (8) Hashimoto, H.; Sugai, Y.; Uragami, C.; Gardiner, A. T.; Cogdell, R. J. Natural and Artificial Light-Harvesting Systems Utilizing the Functions of Carotenoids. *J. Photochem. Photobiol. C Photochem. Rev.* **2015**, 25, 46–70.
- (9) Andreiadis, E. S.; Chavarot-Kerlidou, M.; Fontecave, M.; Artero, V. Artificial Photosynthesis: From Molecular Catalysts for Light-Driven Water Splitting to Photoelectrochemical Cells. *Photochem. Photobiol.* **2011**, 87 (5), 946–964.

- (10) Debus, R. J.; Barry, B. A.; Sithole, I.; Babcock, G. T.; McIntosh, L. Directed Mutagenesis Indicates That the Donor to Photo-Oxidized P680 in Photosystem II Is Tyrosine-161 of the D1 Polypeptide. *Biochemistry* **1988**, *27* (26), 9071–9074.
- (11) Rupprecht, J.; Hankamer, B.; Mussnug, J. H.; Ananyev, G.; Dismukes, C.; Kruse, O. Perspectives and Advances of Biological Hydrogen Production in Microorganisms. *Appl. Microbiol. Biotechnol.* **2006**, *72* (3), 442–449.
- (12) Tamagnini, P.; Axelsson, R.; Lindberg, P.; Oxelfelt, F.; Wunschiers, R.; Lindblad, P. Hydrogenases and Hydrogen Metabolism of Cyanobacteria. *Microbiol. Mol. Biol. Rev.* **2002**, *66* (1), 1–20.
- (13) Meyer, T. J. Chemical Approaches to Artificial Photosynthesis. *Acc. Chem. Res.* **1989**, *22* (5), 163–170.
- (14) Sun, L.; Hammarström, L.; Åkermark, B.; Styring, S. Towards Artificial Photosynthesis: Ruthenium–manganese Chemistry for Energy Production. *Chem. Soc. Rev.* **2001**, *30* (1), 36–49.
- (15) Hammarstrom, L. Towards Artificial Photosynthesis: Ruthenium-Manganese Chemistry Mimicking Photosystem II Reactions. *Curr. Opin. Chem. Biol.* **2003**, *7* (6), 666–673.
- (16) Berglund-Baudin, H.; Sun, L.; Davidov, R.; Sundahl, M.; Styring, S.; Åkermark, B.; Almgren, M.; Hammarström, L. Intramolecular Electron Transfer from Manganese(II) Coordinatively Linked to a Photogenerated Ru(III)–Polypyridine Complex: A Kinetic Analysis. *J. Phys. Chem. A* **1998**, *102* (15), 2512–2518.
- (17) Xu, Y.; Eilers, G.; Borgström, M.; Pan, J.; Abrahamsson, M.; Magnuson, A.; Lomoth, R.; Bergquist, J.; Polívka, T.; Sun, L.; Sundström, V.; Styring, S.; Hammarström, L.; Åkermark, B. Synthesis and Characterization of Dinuclear Ruthenium Complexes Covalently Linked to Ru(II) Tris-Bipyridine: An Approach to Mimics of the Donor Side of Photosystem II. *Chem. Eur. J.* **2005**, *11* (24), 7305–7314.
- (18) Ruttinger, W.; Dismukes, G. C. Synthetic Water-Oxidation Catalysts for Artificial Photosynthetic Water Oxidation. *Chem. Rev.* **1997**, *97* (1), 1–24.

- (19) Yagi, M.; Kaneko, M. Molecular Catalysts for Water Oxidation. *Chem. Rev.* **2001**, *101* (1), 21–35.
- (20) Borgström, M.; Johansson, O.; Lomoth, R.; Baudin, H. B.; Wallin, S.; Sun, L.; Åkermark, B.; Hammarström, L. Electron Donor-Acceptor Dyads and Triads Based on Tris(Bipyridine)Ruthenium(II) and Benzoquinone: Synthesis, Characterization, and Photoinduced Electron Transfer Reactions. *Inorg. Chem.* **2003**, *42* (17), 5173–5184.
- (21) Johansson, O.; Borgström, M.; Lomoth, R.; Palmblad, M.; Bergquist, J.; Hammarström, L.; Sun, L.; Åkermark, B. Electron Donor-Acceptor Dyads Based on Ruthenium(II) Bipyridine and Terpyridine Complexes Bound to Naphthalenediimide. *Inorg. Chem.* **2003**, *42* (9), 2908–2918.
- (22) Rauchfuss, T. B. Research on Soluble Metal Sulfides: From Polysulfido Complexes to Functional Models for the Hydrogenases. *Inorg. Chem.* **2004**, *43* (1), 14–26.
- (23) Ott, S.; Kritikos, M.; Åkermark, B.; Sun, L.; Lomoth, R. A Biomimetic Pathway for Hydrogen Evolution from a Model of the Iron Hydrogenase Active Site. *Angew. Chem. Int. Ed.* **2004**, *43* (8), 1006–1009.
- (24) Ekström, J.; Abrahamsson, M.; Olson, C.; Bergquist, J.; Kaynak, F. B.; Eriksson, L.; Sun, L.; Becker, H.-C.; Åkermark, B.; Hammarström, L.; Ott, S. Bio-Inspired, Side-on Attachment of a Ruthenium Photosensitizer to an Iron Hydrogenase Active Site Model. *Dalton. Trans.* **2006**, No. 38, 4599–4606.
- (25) Wallin, S.; Hammarström, L.; Blart, E.; Odobel, F. Electronic Interactions and Energy Transfer in Oligothiophene-Linked Bis-Porphyrins. *Photochem. Photobiol. Sci.* **2006**, *5* (9), 828–834.
- (26) Borgström, M.; Blart, E.; Boschloo, G.; Mukhtar, E.; Hagfeldt, A.; Hammarström, L.; Odobel, F. Sensitized Hole Injection of Phosphorus Porphyrin into NiO: Toward New Photovoltaic Devices. *J. Phys. Chem. B* **2005**, *109* (48), 22928–22934.
- (27) Sauvage, J.-P.; Collin, J.-P.; Chambron, J.-C.; Guillerez, S.; Coudret, C.; Balzani, V.; Barigelletti, F.; De Cola, L.; Flamigni, L. Ruthenium(II) and Osmium(II) Bis(Terpyridine) Complexes in Covalently-Linked Multicomponent Systems: Synthesis, Electrochemical

- Behavior, Absorption Spectra, and Photochemical and Photophysical Properties. *Chem. Rev.* **1994**, *94* (4), 993–1019.
- (28) Baranoff, E.; Collin, J.-P.; Flamigni, L.; Sauvage, J.-P. From Ruthenium(II) to Iridium(III): 15 Years of Triads Based on Bis-Terpyridine Complexes. *Chem. Soc. Rev.* **2004**, *33* (3), 147–155.
- (29) Juris, A.; Balzani, V.; Barigelletti, F.; Campagna, S.; Belser, P.; Von Zelewsky, A. Ru(II) Polypyridine Complexes: Photophysics, Photochemistry, Electrochemistry, and Chemiluminescence. *Coord. Chem. Rev.* **1988**, *84*, 85–277.
- (30) Barigelletti, F.; Flamigni, L. Photoactive Molecular Wires Based on Metal Complexes. *Chem. Soc. Rev.* **2000**, *29*, 1–12.
- (31) Jia, W.; Hu, Y.-F.; Gao, J.; Wang, S. Linear and Star-Shaped Polynuclear Ru(II) Complexes of 2-(2'-Pyridyl)Benzimidazolyl Derivatives: Syntheses, Photophysical Properties and Red Light-Emitting Devices. *Dalton. Trans.* **2006**, 1721–1728.
- (32) de Silva, A. P.; Gunaratne, H. Q. N.; Gunnlaugsson, T.; Huxley, A. J. M.; McCoy, C. P.; Rademacher, J. T.; Rice, T. E. Signaling Recognition Events with Fluorescent Sensors and Switches. *Chem. Rev.* **1997**, *97* (5), 1515–1566.
- (33) Ashton, P. R.; Ballardini, R.; Balzani, V.; Boyd, S. E.; Credi, A.; Gandolfi, M. T.; Gomez-Lopez, M.; Iqbal, S.; Philp, D.; Preece, J. A.; Prodi, L.; Ricketts, H. G.; Stoddart, J. F.; Tolley, M. S.; Venturi, M.; White, A. J. P.; Williams, D. J. Simple Mechanical Molecular and Supramolecular Machines: Photochemical and Electrochemical Control of Switching Processes. *Chem. Eur. J.* **1997**, *3* (1), 152–170.
- (34) Metcalfea, C.; Thomas, J. A. Kinetically Inert Transition Metal Complexes That Reversibly Bind to DNA. *Chem. Soc. Rev.* **2003**, *32*, 215–224.
- (35) Medlycott, E. A.; Hanan, G. S. Designing Tridentate Ligands for Ruthenium(II) Complexes with Prolonged Room Temperature Luminescence Lifetimes. *Chem. Soc. Rev.* **2005**, *34* (2), 133–142.
- (36) Bard, A. J. Photoelectrochemistry. *Science*. **1980**, *207* (4427), 139–144.

- (37) Youngblood, W. J.; Lee, S. A.; Maeda, K.; Mallouk, T. E. Visible Light Water Splitting Using Dye-Sensitized Oxide Semiconductors. *Acc. Chem. Res.* **2009**, *42* (12), 1966–1973.
- (38) Zhao, Y.; Swierk, J. R.; Megiatto, J. D.; Sherman, B.; Youngblood, W. J.; Qin, D.; Lentz, D. M.; Moore, A. L.; Moore, T. A.; Gust, D.; Mallouk, T. E. Improving the Efficiency of Water Splitting in Dye-Sensitized Solar Cells by Using a Biomimetic Electron Transfer Mediator. *PNAS* **2012**, *109* (39), 15612–15616.
- (39) Jiang, J.; Sherman, B. D.; Zhao, Y.; He, R.; Ghiviriga, I.; Alibabaei, L.; Meyer, T. J.; Leem, G.; Schanze, K. S. Polymer Chromophore-Catalyst Assembly for Solar Fuel Generation. *ACS Appl. Mater. and Interfaces* **2017**, *9* (23), 19529–19534.
- (40) Thompson, D. W.; Ito, A.; Meyer, T. J. Ruthenium Tris-Bipyridine Complex and Other Remarkable Metal-to-Ligand Charge Transfer (MLCT) Excited States. *Pure Appl. Chem.* **2013**, *85* (7), 1257–1305.
- (41) Campagna, S.; Puntoriero, F.; Nastasi, F.; Bergamini, G.; Balzani, V. Photochemistry and Photophysics of Coordination Compounds: Ruthenium. *Springer berlin Heidel-b. New York* **2007**, *280*, 117–214.
- (42) McCusker, J. K. Femtosecond Absorption Spectroscopy of Transition Metal Charge-Transfer Complexes. *Acc. Chem. Res.* **2003**, *36* (12), 876–887.
- (43) Bhasikuttan, A. C.; Suzuki, M.; Nakashima, S.; Okada, T. Ultrafast Fluorescence Detection in Tris(2,2'-Bipyridine)Ruthenium(II) Complex in Solution: Relaxation Dynamics Involving Higher Excited States. *J. Am. Chem. Soc.* **2002**, *124* (28), 8398–8405.
- (44) Dixon, I. M.; Lebon, E.; Sutra, P.; Igau, A. Luminescent Ruthenium-Polypyridine Complexes & Phosphorus Ligands: Anything but a Simple Story. *Chem. Soc. Rev.* **2009**, *38* (6), 1621–1634.
- (45) Österman, T.; Abrahamsson, M.; Becker, H.-C.; Hammarström, L.; Persson, P. Influence of Triplet State Multidimensionality on Excited State Lifetimes of Bis-Tridentate Ru(II) Complexes: A Computational Study. *J. Phys. Chem. A* **2012**, *116* (3), 1041–1050.
- (46) Abrahamsson, M.; Lundqvist, M. J.; Wolpher, H.; Johansson, O.; Eriksson, L.; Bergquist,

- J.; Rasmussen, T.; Becker, H.-C.; Hammarström, L.; Norrby, P.-O.; Åkermark, B.; Persson, P. Steric Influence on the Excited-State Lifetimes of Ruthenium Complexes with Bipyridyl-Alkanylene-Pyridyl Ligands. *Inorg. Chem.* **2008**, *47* (9), 3540–3548.
- (47) Takasu, N. Toward Green and Efficient Reaction. *Photoredox Catal. Org. Chem.* **2010**, 2–3.
- (48) Rehm, D.; Weller, A. Kinetics of Fluorescence Quenching By Electron and H-Atom Transfer. *Isr. J. Chem.* **1970**, *8*, 259–271.
- (49) Takeda, H.; Ishitani, O. Development of Efficient Photocatalytic Systems for Carbondioxide Reduction Using Mononuclear and Multinuclear Metal Complexes Based on Mechanistic Studies. *Coord. Chem. Rev.* **2010**, *254*, 346–354.
- (50) Li, L.; Duan, L.; Xu, Y.; Gorlov, M.; Hagfeldt, A.; Sun, L. A Photoelectrochemical Device for Visible Light Driven Water Splitting by a Molecular Ruthenium Catalyst Assembled on Dye-Sensitized Nanostructured TiO₂. *Chem. Commun.* **2010**, *46* (39), 7307–7309.
- (51) Gill, M. R.; Thomas, J. A. Ruthenium(II) Polypyridyl Complexes and DNA - From Structural Probes to Cellular Imaging and Therapeutics. *Chem. Soc. Rev.* **2012**, *41* (8), 3179–3192.
- (52) Ma, D.-L.; Ma, V. P.-Y.; Chan, D. S.-H.; Leung, K.-H.; He, H.-Z.; Leung, C.-H. Recent Advances in Luminescent Heavy Metal Complexes for Sensing. *Coord. Chem. Rev.* **2012**, *256* (23–24), 3087–3113.
- (53) Prier, C. K.; Rankic, D. A.; MacMillan, D. W. C. Visible Light Photoredox Catalysis with Transition Metal Complexes: Applications in Organic Synthesis. *Chem. Rev.* **2013**, *113* (7), 5322–5363.
- (54) Arias-Rotondo, D. M.; McCusker, J. K. The Photophysics of Photoredox Catalysis: A Roadmap for Catalyst Design. *Chem. Soc. Rev.* **2016**, *45* (21), 5803–5820.
- (55) Morimoto, D.; Yoshida, H.; Sato, K.; Saito, K.; Yagi, M.; Takagi, S.; Yui, T. Light Energy Accumulation from Pyrene Derivative to Tris(Bipyridine)Ruthenium on Clay Surface. *Langmuir* **2017**, *33* (15), 3680–3684.

- (56) Ikezawa, H.; Kotal, C.; Yasufuku, K.; Yamazaki, H. Direct and Sensitized Valence Photoisomerization of a Substituted Norbornadiene. Examination of the Disparity between Singlet and Triplet State Reactivities. *J. Am. Chem. Soc.* **1986**, *108* (7), 1589–1594.
- (57) Islangulov, R. R.; Castellano, F. N. Photochemical Upconversion: Anthracene Dimerization Sensitized to Visible Light by a Ru(II) Chromophore. *Angew. Chem. Int. Ed.* **2006**, *45* (36), 5957–5959.
- (58) Lu, Z.; Yoon, T. P. Visible Light Photocatalysis of [2+2] Styrene Cycloadditions by Energy Transfer. *Angew. Chem. Int. Ed.* **2012**, *51* (41), 10329–10332.
- (59) Kroon, J.; Verhoeven, J. W.; Paddon-Row, M. N.; Oliver, A. M. Solvent Dependence of Photoinduced Intramolecular Electron Transfer: Criteria for the Design of Systems with Rapid, Solvent-Independent Charge Separation. *Angew. Chem. Int. Ed.* **1991**, *30* (10), 1358–1361.
- (60) Marcus, R. A. On the Theory of Oxidation-Reduction Reactions Involving Electron Transfer. *J. Chem. Phys.* **1956**, *24* (5), 966–978.
- (61) Marcus, R. A. Electron Transfer Reactions in Chemistry: Theory and Experiment. *Angew. Chem. Int. Ed. Engl.* **1993**, *32* (8), 1111–1121.
- (62) Hankache, J.; Wenger, O. S. Photoinduced Electron Transfer in Covalent Ruthenium-Anthraquinone Dyads: Relative Importance of Driving-Force, Solvent Polarity, and Donor-Bridge Energy Gap. *Phys. Chem. Chem. Phys.* **2012**, *14* (8), 2685–2692.
- (63) Nitadori, H.; Takahashi, T.; Inagaki, A.; Akita, M. Enhanced Photocatalytic Activity of α -Methylstyrene Oligomerization through Effective Metal-to-Ligand Charge-Transfer Localization on the Bridging Ligand. *Inorg. Chem.* **2012**, *51* (1), 51–62.
- (64) Murata, K.; Araki, M.; Inagaki, A.; Akita, M. Syntheses, Photophysical Properties, and Reactivities of Novel Bichromophoric Pd Complexes Composed of Ru(II)-Polypyridyl and Naphthyl Moieties. *Dalton. Trans.* **2013**, *42* (19), 6989–7001.
- (65) Danielson, E.; Elliott, C. M.; Merkert, J. W.; Meyer, T. J. Photochemically Induced Charge

- Separation at the Molecular Level. A Chromophore Quencher Complex Containing Both an Electron Donor and an Acceptor. *J. Am. Chem. Soc.* **1987**, *109* (8), 2519–2520.
- (66) Klumpp, T.; Linsenmann, M.; Larson, S. L.; Limoges, B. R.; Bürssner, D.; Krissinel, E. B.; Elliott, C. M.; Steiner, U. E. Spin Chemical Control of Photoinduced Electron-Transfer Processes in Ruthenium(II)-Trisbipyridine-Based Supramolecular Triads. *J. Am. Chem. Soc.* **1999**, *121* (5), 1076–1087.
- (67) Hankache, J.; Niemi, M.; Lemmetyinen, H.; Wenger, O. S. Hydrogen-Bonding Effects on the Formation and Lifetimes of Charge-Separated States in Molecular Triads. *J. Phys. Chem. A* **2012**, *116* (31), 8159–8168.
- (68) Hankache, J.; Wenger, O. S. Microsecond Charge Recombination in a Linear Triarylamine–Ruthenium Tris-Bipyridine–anthraquinone Triad. *Chem. Commun.* **2011**, *47* (36), 10145.
- (69) Rakhi, A. M.; Gopidas, K. R. Generation of Long-Lived Methyl Viologen Radical Cation in the Triplet-State Mediated Electron Transfer in a β -Cyclodextrin Based Supramolecular Triad. *Chem. Phys. Lett.* **2015**, *618* (2), 192–197.
- (70) Nippe, M.; Khnayzer, R. S.; Panetier, J. A.; Zee, D. Z.; Olaiya, B. S.; Head-Gordon, M.; Chang, C. J.; Castellano, F. N.; Long, J. R. Catalytic Proton Reduction with Transition Metal Complexes of the Redox-Active Ligand Bpy2PYMe. *Chem. Sci.* **2013**, *4* (10), 3934.
- (71) Laemmel, A.-C.; Collin, J.-P.; Sauvage, J.-P. Efficient and Selective Photochemical Labilization of a Given Bidentate Ligand in Mixed Ruthenium(II) Complexes of the Ru(Phen)₂(L)₂⁺ and Ru(Bipy)₂(L)₂⁺ Family (L = Sterically Hinderig Chelate). *Eur. J. Inorg. Chem.* **1999**, *2* (3), 383–386.
- (72) Collin, J.-P.; Jouvenot, D.; Koizumi, M.; Sauvage, J.-P. Light-Driven Expulsion of the Sterically Hinderig Ligand L in Tris-Diimine Ruthenium(II) Complexes of the Ru(Phen)₂(L)₂⁺ Family: A Pronounced Ring Effect. *Inorg. Chem.* **2005**, *44* (13), 4693–4698.
- (73) Dinda, J.; Liatard, S.; Chauvin, J.; Jouvenot, D.; Loiseau, F. Electronic and Geometrical Manipulation of the Excited State of Bis-Terdentate Homo- and Heteroleptic

- Ruthenium Complexes. *Dalton. Trans.* **2011**, *40* (14), 3683–3688.
- (74) Fang, Y. Q.; Taylor, N. J.; Hanan, G. S.; Loiseau, F.; Passalacqua, R.; Campagna, S.; Nierengarten, H.; Van Dorsselaer, A. A Strategy for Improving the Room-Temperature Luminescence Properties of Ru(II) Complexes with Tridentate Ligands. *J. Am. Chem. Soc.* **2002**, *124* (27), 7912–7913.
- (75) Abrahamsson, M.; Becker, H.-C.; Hammarström, L.; Bonnefous, C.; Chamchoumis, C.; Thummel, R. P. Six-Membered Ring Chelate Complexes of Ru(II): Structural and Photophysical Effects. *Inorg. Chem.* **2007**, *46* (24), 10354–10364.
- (76) Schulze, B.; Friebe, C.; Hager, M. D.; Winter, A.; Hoogenboom, R.; Görls, H.; Schubert, U. S. 2,2':6',2''-Terpyridine Meets 2,6-Bis(1H-1,2,3-Triazol-4-yl)pyridine: Tuning the Electro-Optical Properties of Ruthenium(II) Complexes. *Dalton. Trans.* **2009**, No. 5, 787–794.
- (77) Andres, P. R. Supramolecular Assemblies and Materials Based on 2,2':6',2''-Terpyridine Metal Complexes. *Tech. Univ. Eindhoven* **2004**.
- (78) Ezhilarasu, T.; Balasubramanian, S. Synthesis, Characterization, Photophysical and Electrochemical Studies of Ruthenium(II) Complexes with 4'-Substituted Terpyridine Ligands and Their Biological Applications. *ChemistrySelect* **2018**, *3* (43), 12039–12049.
- (79) Ashford, D. L.; Glasson, C. R. K.; Norris, M. R.; Concepcion, J. J.; Keinan, S.; Brennaman, M. K.; Templeton, J. L.; Meyer, T. J. Controlling Ground and Excited State Properties through Ligand Changes in Ruthenium Polypyridyl Complexes. *Inorg. Chem.* **2014**, *53* (11), 5637–5646.
- (80) Pal, A. K.; Hanan, G. S. Design, Synthesis and Excited-State Properties of Mononuclear Ru(II) Complexes of Tridentate Heterocyclic Ligands. *Chem. Soc. Rev.* **2014**, *43* (17), 6184–6197.
- (81) Wang, J.; Fang, Y.-Q.; Hanan, G. S.; Loiseau, F.; Campagna, S. Synthesis and Properties of the Elusive Ruthenium(II) Complexes of 4'-Cyano-2,2':6',2''-Terpyridine. *Inorg. Chem.* **2005**, *44* (1), 5–7.

- (82) Maestri, M.; Armaroli, N.; Balzani, V.; Constable, E. C.; Cargill Thompson, A. M. W. Complexes of the Ruthenium(II)-2,2':6',2''-Terpyridine Family. Effect of Electron-Accepting and -Donating Substituents on the Photophysical and Electrochemical Properties. *Inorg. Chem.* **1995**, *34* (10), 2759–2767.
- (83) Laine, P.; Bedioui, F.; Amouyal, E.; Albin, V.; Berruyer-Penaud, F. Triarylpyridinium-Functionalized Terpyridyl Ligand for Photosensitized Supramolecular Architectures: Intercomponent Coupling and Photoinduced Processes. *Chem. Eur. J.* **2002**, *8* (14), 3162–3176.
- (84) Fortage, J.; Dupeyre, G.; Tuyères, F.; Marvaud, V.; Ochsenbein, P.; Ciofini, I.; Hromadová, M.; Pospíšil, L.; Arrigo, A.; Trovato, E.; Puntoriero, F.; Lainé, P. P.; Campagna, S. Molecular Dyads of Ruthenium(II)– or Osmium(II)–Bis(Terpyridine) Chromophores and Expanded Pyridinium Acceptors: Equilibration between MLCT and Charge-Separated Excited States. *Inorg. Chem.* **2013**, *52* (20), 11944–11955.
- (85) Medlycott, E. A.; Hanan, G. S. Synthesis and Properties of Mono- and Oligo-Nuclear Ru(II) Complexes of Tridentate Ligands: The Quest for Long-Lived Excited States at Room Temperature. *Coord. Chem. Rev.* **2006**, *250*, 1763–1782.
- (86) Bhaumik, C.; Das, S.; Maity, D.; Baitalik, S. Luminescent Bis-Tridentate Ruthenium(II) and Osmium(II) Complexes Based on Terpyridyl-Imidazole Ligand: Synthesis, Structural Characterization, Photophysical, Electrochemical, and Solvent Dependence Studies. *Dalton. Trans.* **2012**, *41* (8), 2427–2438.
- (87) Harriman, A.; Mayeux, A.; De Nicola, A.; Ziessel, R. Synthesis and Photophysical Properties of Ruthenium(II) Bis(2,2':6',2''-Terpyridine) Complexes Constructed from a Diethynylated-Thiophene Residue. *Phys. Chem. Chem. Phys.* **2002**, *4* (11), 2229–2235.
- (88) Benniston, A. C.; Chapman, G.; Harriman, A.; Mehrabi, M.; Sams, C. A. Electron Delocalization in a Ruthenium(II) Bis(2,2':6',2''-Terpyridyl) Complex. *Inorg. Chem.* **2004**, *43* (14), 4227–4233.
- (89) Hissler, M.; Harriman, A.; Khatyr, A.; Ziessel, R. Intramolecular Triplet Energy Transfer in Pyrene-Metal Polypyridine Dyads : A Strategy for Extending the Triplet Lifetime of

- the Metal Complex. *Chem. Eur. J.* **1999**, *5* (11), 3366–3381.
- (90) Manca, P.; Pilo, M. I.; Sanna, G.; Zucca, A.; Bergamini, G.; Ceroni, P. Ru(II) Complexes Comprising Terpyridine Ligands Appended with Terthiophene Chromophores: Energy Transfer and Energy Reservoir Effect. *Chem. Commun.* **2011**, *47* (12), 3413–3415.
- (91) Polson, M. I. J.; Loiseau, F.; Campagna, S.; Hanan, G. S. Bridging Ligand Planarity as a Route to Long-Lived, near Infrared Emitting Dinuclear Ruthenium(II) Complexes. *Chem. Commun.* **2006**, 1301–1303.
- (92) Fang, Y.-Q.; Taylor, N. J.; Laverdiere, F.; Hanan, G. S.; Loiseau, F.; Nastasi, F.; Campagna, S.; Nierengarten, H.; Leize-Wagner, E.; Van Dorsselaer, A. Ruthenium(II) Complexes with Improved Photophysical Properties Based on Planar 4'-(2-Pyrimidinyl)-2,2':6',2''-Terpyridine Ligands. *Inorg. Chem.* **2007**, *46* (7), 2854–2863.
- (93) Polson, M. I. J.; Taylor, N. J.; Hanan, G. S. Facile Syntheses of Tridentate Ligands for Room-Temperature Luminescence in Ruthenium Complexes. *Chem. Commun.* **2002**, 1356–1357.
- (94) Polson, M. I. J.; Medlycott, E. A.; Hanan, G. S.; Mikelsons, L.; Taylor, N. J.; Watanabe, M.; Tanaka, Y.; Loiseau, F.; Passalacqua, R.; Campagna, S. Ruthenium Complexes of Easily Accessible Tridentate Ligands Based on the 2-Aryl-4,6-Bis(2-Pyridyl)-s-Triazine Motif: Absorption Spectra, Luminescence Properties, and Redox Behavior. *Chem. Eur. J.* **2004**, *10*, 3640–3648.
- (95) Wolpher, H.; Johansson, O.; Abrahamsson, M.; Kritikos, M.; Sun, L.; Åkermark, B. A Tridentate Ligand for Preparation of Bisterpyridine-like Ruthenium(II) Complexes with an Increased Excited State Lifetime. *Inorg. Chem. Commun.* **2004**, *7* (3), 337–340.
- (96) Abrahamsson, M.; Wolpher, H.; Johansson, O.; Larsson, J.; Kritikos, M.; Eriksson, L.; Norrby, P. O.; Bergquist, J.; Sun, L.; Åkermark, B.; Hammarström, L. A New Strategy for the Improvement of Photophysical Properties in Ruthenium(II) Polypyridyl Complexes. Synthesis and Photophysical and Electrochemical Characterization of Six Mononuclear Ruthenium(II) Bisterpyridine-Type Complexes. *Inorg. Chem.* **2005**, *44* (9), 3215–3225.
- (97) Abrahamsson, M.; Jäger, M.; Österman, T.; Eriksson, L.; Persson, P.; Becker, H. -

- christian.; Johansson, O.; Hammarström, L. A 3.0 Micro-Second Room Temperature Excited State Lifetime of a Bistridentate Ru(II)-Polypyridine Complex for Rod-like Molecular Arrays. *J. Am. Chem. Soc.* **2006**, *128*, 12616–12617.
- (98) Abrahamsson, M.; Jäger, M.; Kumar, R. J.; Österman, T.; Persson, P.; Becker, H. -christian.; Johansson, O.; Hammarström, L. Bistridentate Ruthenium(II) Polypyridyl-Type Complexes with Microsecond 3 MLCT State Lifetimes: Sensitizers for Rod-Like Molecular Arrays. *J. Am. Chem. Soc.* **2008**, *130*, 15533–15542.
- (99) Abrahamsson, M.; Becker, H.-C.; Hammarström, L. Microsecond Triplet-MLCT Excited State Lifetimes in Bis-Tridentate Ru(II)-Complexes: Significant Reductions of Non-Radiative Rate Constants. *Dalton. Trans.* **2017**, *46* (39), 13314–13321.
- (100) Ragazzon, G.; Verwilt, P.; Denisov, S. A.; Credi, A.; Jonusauskas, G.; McClenaghan, N. D. Ruthenium(II) Complexes Based on Tridentate Polypyridine Ligands That Feature Long-Lived Room-Temperature Luminescence. *Chem. Commun.* **2013**, *49* (80), 9110–9112.
- (101) Laramée-Milette, B.; Hanan, G. S. Ruthenium Bistridentate Complexes with Non-Symmetrical Hexahydro-Pyrimidopyrimidine Ligands: A Structural and Theoretical Investigation of Their Optical and Electrochemical Properties. *Dalton. Trans.* **2016**, *45* (31), 12507–12517.
- (102) Schramm, F.; Meded, V.; Fliegl, H.; Fink, K.; Fuhr, O.; Qu, Z.; Klopper, W.; Finn, S.; Keyes, T. E.; Ruben, M. Expanding the Coordination Cage: A Ruthenium(II)-Polypyridine Complex Exhibiting High Quantum Yields under Ambient Conditions. *Inorg. Chem.* **2009**, *48* (13), 5677–5684.

Chapter 2: Di-pyridyl acridine-based ligand and its Ru(II) complexes emitting in the NIR region

I. Introduction

The acridine platform participates in a wide range of biological activities. It is used in anti-tumor chemotherapies¹, serves as an anti-viral agent², and its high binding affinity for DNA and RNA makes it a key component in chemical biology.^{3,4} As a consequence, this acridine scaffold is included in many biological therapeutic agents,⁵ for example, just in 2018, more than 200 articles were published in this field using acridine.

Despite this wide utility of such a motif in biological applications, the acridine platform was not broadly used as a coordinating ligand (other than as a monodentate ligand)^{6,7} in the field of transition metal complexes and coordination photochemistry. However, due to the extended π -conjugated system of the compound, this nitrogenated anthracene analogue could be an interesting building block precursor to prepare many ligands used efficiently, for energy storage, in coordination chemistry, and that was the first proposition of our work to start exploring the acridine platform.

Simply, when the acridine backbone is functionalized with other chelating moieties at its 4 and 5 positions (Figure 2.1, a), a new tridentate ligand can be prepared. Our goal can be achieved by going forward to prepare a (NNN) tridentate chelating ligand, when connecting two pyridine *N*-heterocycles from their ortho position at the 4 and 5 positions of the acridine backbone (Figure 2.1, b). Thus, with such design, we can get a ligand with a low lying π^* orbital, which can form 6-membered chelating cycles with the desired cationic transition metal. These properties together should stabilize the ³MLCT excited state with regular octahedral geometry to have a high energetic ³MC state.

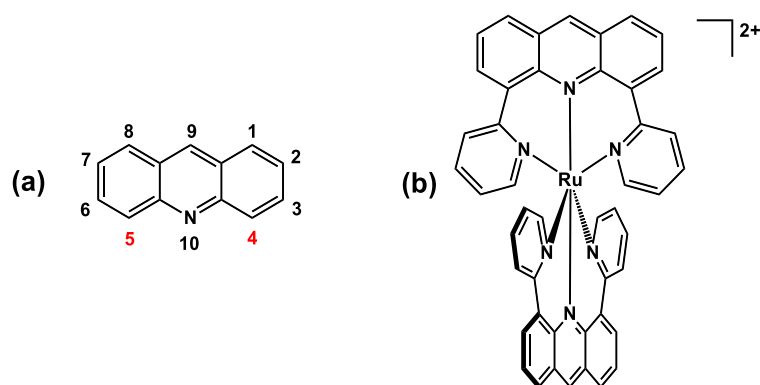


Figure 2.3. Structural formula of the proposed Ru(II)-complex.

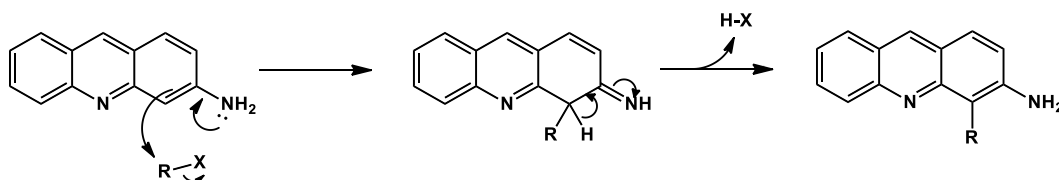
Great progress has been made in the catalytic C-H bond functionalization of hetero-aromatic rings that has allowed many applications of the traditionally used pyridine rings.⁸ However, such methods cannot be used with the acridine heterocycle, due to the deficiency of activated C-H bonds adjacent to the nitrogen atom. Indeed, acridine substitutions have been described.⁵ However, despite some recent C-H bond functionalization chemistry of the fused phenylenes, specifically at positions 4 and 5,⁹ the C-H functionalization of these sites on acridine are not widely studied and have been met with limited examples.

Taking everything into account, our work was first directed toward optimizing and exploring different synthetic strategies in order to get this simple tri-imine ligand built around the acridine backbone. After that, it is important to find the optimal conditions to coordinate such a rigid structural compound to ruthenium(II). After preparation, the electrochemical and photophysical properties of the new compounds will be studied and compared to the results obtained by TD-DFT calculations.

II. Synthesis

II.1. Ligand synthesis

Most of the widely studied commercially available acridine derivative compounds are non-functionalized at their 4 and 5 positions. Moreover, despite the electrophilic regioselective substitution of proflavin at the 4 and 5 positions by Martin in 1979¹⁰ to obtain the desired 3,6-diamino-4,5-diiodoacridine compound, 4,5-dihalogenated acridine precursors are still rare in the literature. Even more, direct electrophilic regioselective substitution of 4 and 5 position on acridine using the same protocol as Martin gives no reaction, due to the fact that their success was forced by the presence of the amino groups at the 3 and 6 positions of the acridine backbone, as illustrated in the suggested general mechanism in Scheme 2.1. It is difficult to use proflavin as starting compound to prepare our target ligand due to the presence of the coordinating amine group which could change the chelation properties of the proposed target ligand.



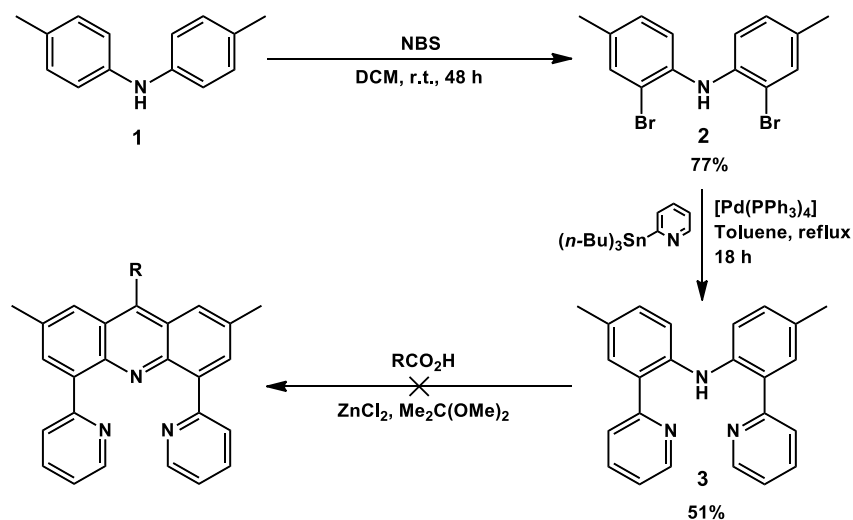
Scheme 2.1. Proposed mechanism for amino-acridine electrophilic substitution reaction.

Thus, there could be two ways of preparation which we can follow to reach the target compound. The first way could be through synthesizing a functionalized acridine which is greatly dependent from the beginning upon ring construction from functionalized acyclic substrates such as diphenylamine or condensation from functionalized anilines to give the desired scaffold. The second way is through trying to start from cyclic compounds like acridone and then get a functionalized acridine at 4 and 5 positions.

II.1.1. Acyclic starting compound

Toward this goal, we tried first to start from acyclic compounds followed by some synthetic steps to construct the estimated ligand. An idea came for such preparation of the acridine target ligand by starting from di-*para*-tolylamine (**1**), which is commercially available, instead of using the acridine heterocycle directly. Recent fruitful work described an easy bromination at the *ortho*-positions of this compound **1**.¹¹ Indeed, to avoid the *ortho*-*para* competition in the electrophilic substitution reaction, this commercially compound was already blocked by two methyl groups at the *para*-positions. A bromination step at the *ortho* positions with 77% yield was completed by mixing NBS (*N*-bromosuccinimide) reagent with the compound **1** in DCM (dichloromethane) solvent at room temperature. The obtained bis(2-bromo-4-methylphenyl)amine compound (**2**) could be then used as a key intermediate which could be substituted with many different groups to give a wide range of ligands. In the present work, our goal was targeted toward NNN chelating ligands specially with pyridine moieties. Then, the dipyridyl substituted compound, bis(4-methyl-2-(pyridin-2-yl)phenyl)amine (**3**), was successfully obtained by Stille coupling with 2-(tributylstannyl)pyridine in the presence of palladium(0) under inert conditions.¹² After this success, the last synthetic step to obtain the dipyridylacridine target ligand is to close the center ring with a methine group between the

two phenyl rings (Scheme 2.2). We tried to follow the protocol used by Bratulescu, who succeeded in synthesizing 9-alkylacridine compounds from dimethoxypropane and diphenylamine using microwaves.¹³ However, for reactivity reasons, possibly due to the presence of the two electron withdrawing pyridyl rings that make the system weaker in nucleophilic reaction, we failed in this last step to close between the two tolylamine rings and obtain the acridine platform.

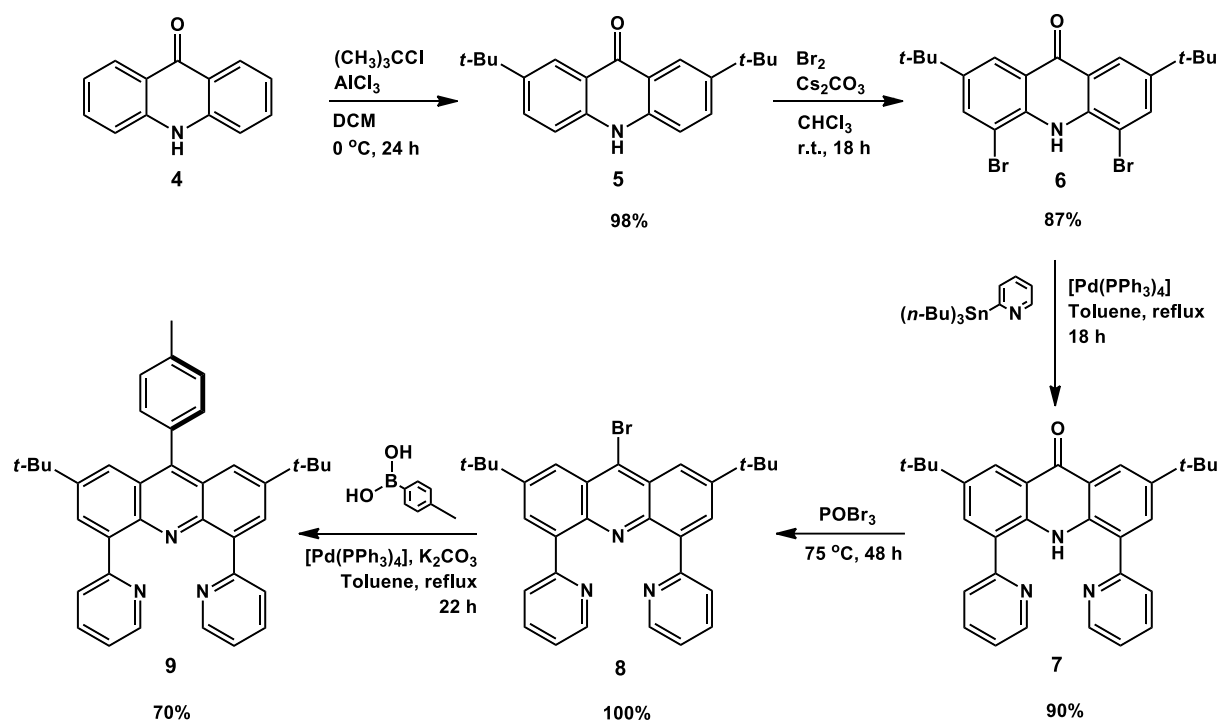


Scheme 2.2. Synthesis starting from acyclic di-tolylamine compound.

II.1.2. Cyclic starting compound

After the failure in adding a single carbon (C-9) and affording the acridine backbone, the next step was to find another commercially available compound, but cyclic one, that could undergo a similar synthetic pathway to end with an acridine substituted with two pyridines at 4 and 5 positions. A new idea was inspired from a recent article, with some adaptations in order to improve the reaction yield, describing a direct bromination of positions 4 and 5 on an acridone precursor (**4**).¹⁴ The synthetic pathway started by blocking the highly reactive *para* (2 and 7) positions of the electron donating amine group with a Friedel-Crafts alkylation. This alkylation process was done using 2-chloro-2-methylpropane in the presence of aluminium chloride which serves as a Lewis acid, to graft a *tertio*-butyl group at these two positions to give compound (**5**). A bromination reaction by regioselective electrophilic substitution at the *ortho* (4 and 5) positions of the directing amine group took place as a second step in the presence

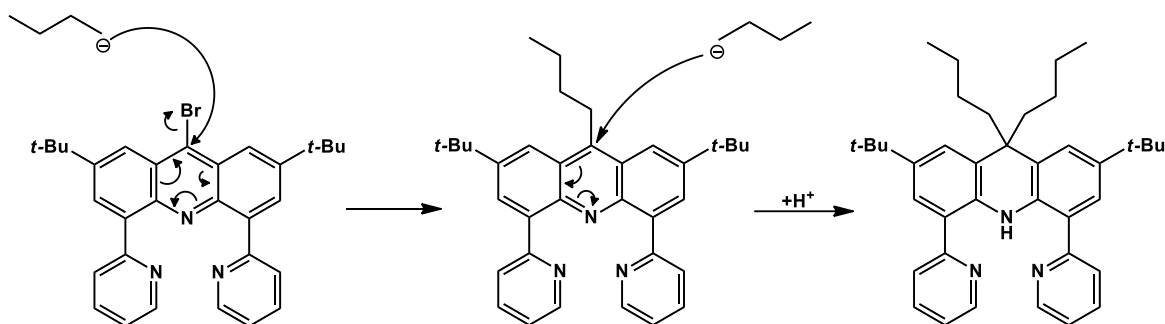
of cesium carbonate in chloroform at room temperature. As a result, the 2,7-di-*tert*-butyl-4,5-dibromo-9(10H)-acridone compound (**6**) was obtained with 85% yield over two steps. This dihalogenated acridone **6** undergoes Stille coupling with the same protocols as what did with compound **2**. Finally, 2,7-di-*tert*-butyl-4,5-di(pyridin-2-yl)-acridone (**7**) was obtained with 90% yield after purification on silica gel column chromatography (Scheme 2.3), and this new compound was fully characterized by ^1H and ^{13}C NMR spectra, in addition to ESI mass spectrometry.



Scheme 2.3. Target ligand synthesis with tolyl substituent at C-9.

At this point, we were one step away from reaching the target ligand. Simply, a functionalized acridine platform with a bromine at the C-9 position was obtained with a quantitative yield, after treating compound **7** with phosphoryl bromide (POBr_3) reagent and sealed in a pressure tube at $80\text{ }^\circ\text{C}$ overnight.¹⁵ This new compound 9-bromo-2,7-di-*tert*-butyl-4,5-di(pyridin-2-yl)-acridone (**8**) was also fully characterized by ^1H , ^{13}C , and 2D NMR, and ESI-MS.

The next idea was to carry out the lithium halogen exchange reaction with the bromine atom at position C-9. Therefore, compound **8** found in dry THF solution was treated with *n*-butyllithium (*n*-BuLi), which was then quenched with dry methanol. In this reaction, a hydrogen atom replaces the bromine, affording the acridine backbone of our target ligand. However, the highly electrophilic site (position 9) undergoes an S_N2 substitution by the butyl anion faster than and instead of a Li-Br exchange reaction, to have a di-substituted acridane compound rather than the conjugated acridine scaffold (Scheme 2.4).



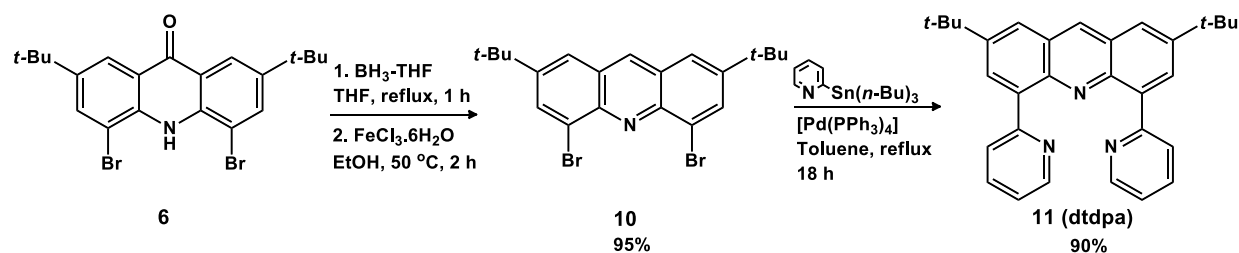
Scheme 2.4. Proposed mechanism for acridine substitution by nucleophilic anion.

Following this result, another idea was raised to rather benefit from this bromine group at position 9 of acridine, the center of symmetry, and use this reactive site for further functionalization in higher order molecular structures. Thus, the target ligand with a tolyl linker at C-9 was obtained (**9**) by Suzuki coupling between compound **8** and *p*-tolylboronic acid in the presence of palladium(0). Therefore, the final ligand was efficiently obtained in a 54% overall yield over five steps (Scheme 2.3).

On the other hand, a second, faster and cheaper synthetic pathway was optimized (4 steps) for synthesizing the target ligand, deriving from the prepared intermediate **6** precursor and follows with some modifications the same protocols found in the literature.¹⁶ Refluxing compound **6** with one molar solution of borane tetrahydrofuran complex (BH₃-THF) in dry tetrahydrofuran (THF) was enough to reduce in one hour the ketone group and gives the acridane derivative. Afterwards, an oxidation reaction of acridane into acridine was successfully done using iron(III) chloride hexahydrate (FeCl₃·6H₂O) in a mixture of ethanol and water for an hour. At this point, a second key intermediate compound (**10**) is obtained, which

can react with many different substrates and incorporate the second two coordinating moieties at position 4 and 5 of the acridine base.

The dipyridylacridine compound (**11**; **dtdpa** = 2,7-di-tert-butyl-4,5-di(pyridin-2-yl)acridine) was lastly obtained by Stille coupling. As a result, the target ligand was efficiently obtained with a 73% overall yield (Scheme 2.5), which is higher than the yield obtained in the case of the pathway described in Scheme 2.3.



Scheme 2.5. **dtdpa** target ligand synthetic pathway.

The prepared **dtdpa** *N*-heterocycle ligand which suits all the desired characteristics was fully characterized by 500 MHz NMR spectrometer, in a deuterated acetone. All the protons on this ligand could be assigned on its ¹H-NMR spectrum as seen in Figure 2.2.

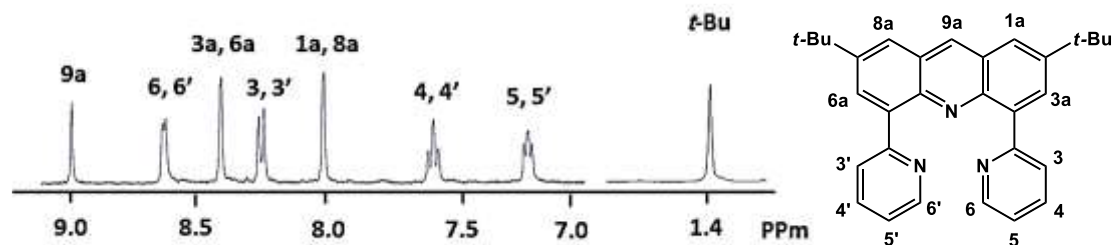


Figure 2.2. The **dtdpa** ligand proton assignment on its ¹H-NMR spectrum, recorded in D₂O at 500 MHz NMR spectrometer.

The obtained target ligand **11** was confirmed by ESI-mass spectrometry. In the spectrum, a mass peak at 446.2 with 1+ charge was detected, which matches with [M+H]⁺ (m/z calculated to be 446.3).

II.2. Ru(II) complexes synthesis

The **dtdpa** ligand follows the clear geometrical and electronic specifications. This fully conjugated architecture of high rigidity, due to the presence of acridine backbone, was then coordinated to a ruthenium(II) center to form the desired Ru(II) complexes. A homoleptic Ru(II) complex (**12**) consisting of two **dtdpa** ligands and a heteroleptic complex (**13**) composed of one terpyridine ligand and one **dtdpa** ligand could be prepared (Figure 2.3).

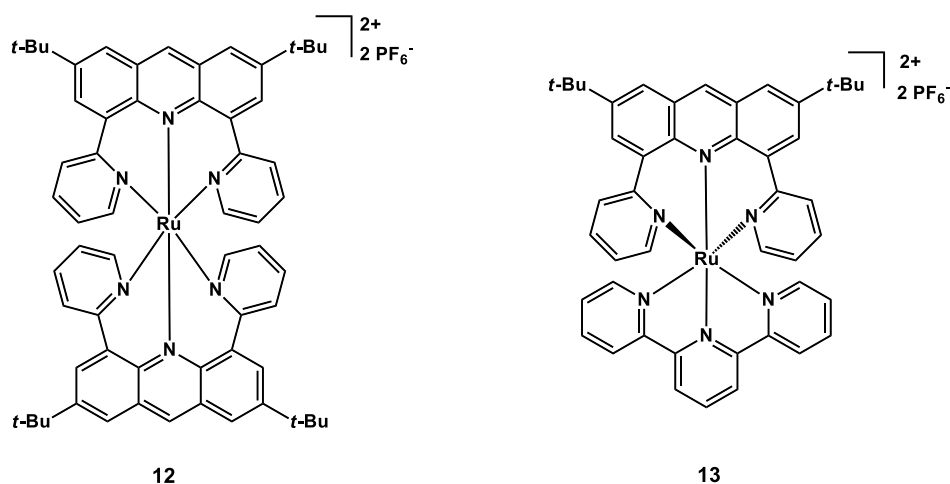
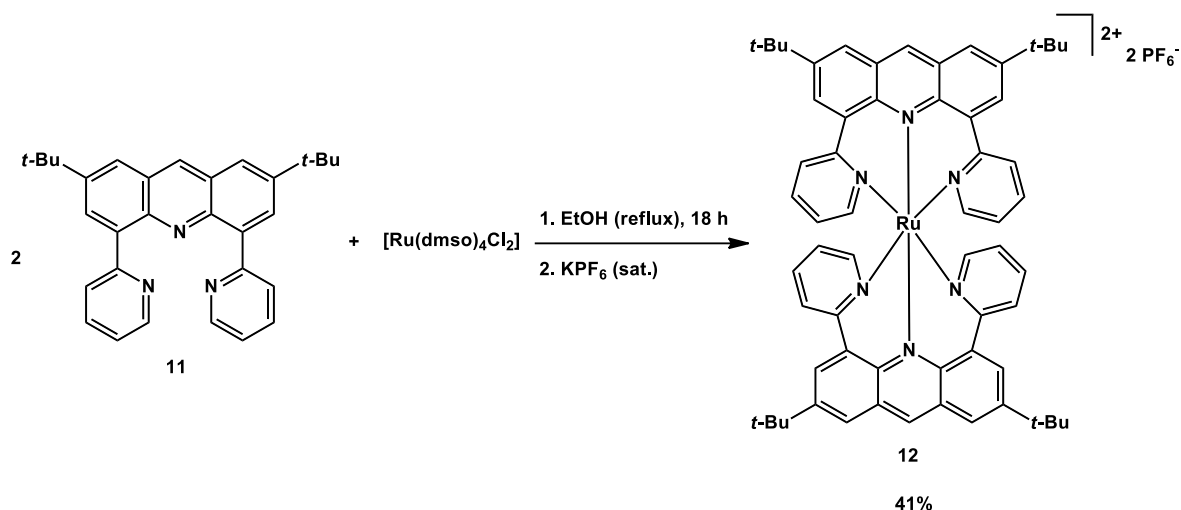


Figure 2.3. Homoleptic (**12**) and heteroleptic (**13**) complexes structure.

II.2.1. Homoleptic Ru(II) complex synthesis

Different attempts performed, under hard conditions, failed to give the desired complex. A softer condition in ethanol solution was enough to proceed with the complexation reaction. The desired homoleptic complex **12** was synthesized by refluxing two equivalents of **dtdpa** with $[\text{Ru}(\text{dmsO})_4\text{Cl}_2]$ precursor in ethanol overnight. As a result, a green colored compound was obtained. This complex was isolated in 41% yield with a molecular formula $[\text{Ru}(\text{dtdpa})_2](\text{PF}_6)_2$ after a chromatographic purification on a silica gel column followed by anion exchange with a saturated aqueous solution of potassium hexafluorophosphate (KPF_6), as shown in Scheme 2.6.



Scheme 2.6. Homoleptic complex **12** synthesis.

The molecular formula $[\text{Ru}(\text{dtdpa})_2]^{2+}$ of complex **12** was verified by ESI-mass spectrometry. In the spectrum, a mass peak at 496.2 with 2+ charge was detected, which matches with $[\text{Ru}(\text{dtdpa})_2]^{2+}$ (m/z calculated to be 496.2), in addition to the observation of a peak at $m/z = 1137.3$ with 1+ charge, which matches with $[\text{Ru}(\text{dtdpa})_2](\text{PF}_6)^+$ (m/z calculated to be 1137.4).

However, the $^1\text{H-NMR}$ spectrum of this complex shows a signal splitting of each proton peak on the **dtdpa** ligand into two sets of peaks, as seen in Figure 2.5. This means that the two ligands are positioned in an unsymmetrical fashion.

Indeed, the expected *meridional* configuration should have symmetrical ligands (Figure 2.4), and accordingly this suggests that the complex is obtained with a distorted *facial-gauche* geometry ($\text{C}_2\text{-fac}$).

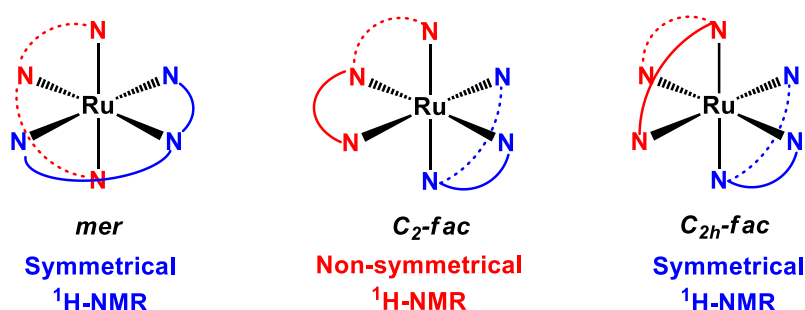


Figure 4.4. The three different octahedral geometries of bis-tridentate Ru(II) complexes.

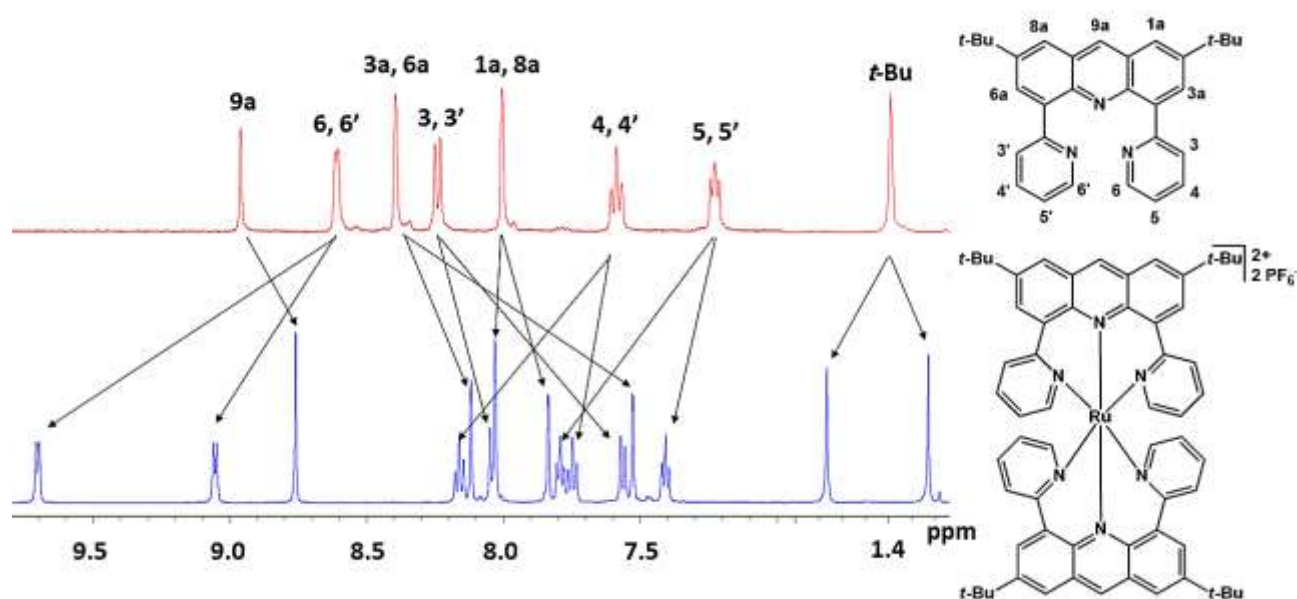


Figure 2.5. ^1H -NMR spectra of **dtdpa** (top) and the homoleptic complex **12** (bottom), recorded in D-acetone at 500 MHz spectrometer.

Following deeper analysis of such results, we can see clearly by 2D NOESY NMR (Figure 2.6) a strong nuclear overhauser effect (NOE) correlation between the two protons (6 and 6') of both pyridine rings of the ligand. In *meridional* coordination there is no interaction between the two *trans* pyridine rings, and that is why such detected correlation is only possible if both pyridine rings are in a *cis* position relative to each other. To this point, having the pyridine rings in *cis* position certifies the *facial* coordination geometry of the ligands. However, this alone is not enough to validate the unsymmetrical *fac* coordination. Indeed, *fac* geometry could be symmetrical with a dihedral plane of symmetry (C_{2h} -*fac*) or non-symmetrical and therefore have a *facial-gauche* geometry (C_2 -*fac*). For that, careful analysis of the same 2D NMR also shows another NOE correlation between one of the *tertio*-butyl groups and the hydrogen atom at C-9 of the acridine scaffold, which also indicates that the two acridine rings are in *cis* position. This kind of interaction confirms the *facial-gauche* geometry of the homoleptic complex **12**.

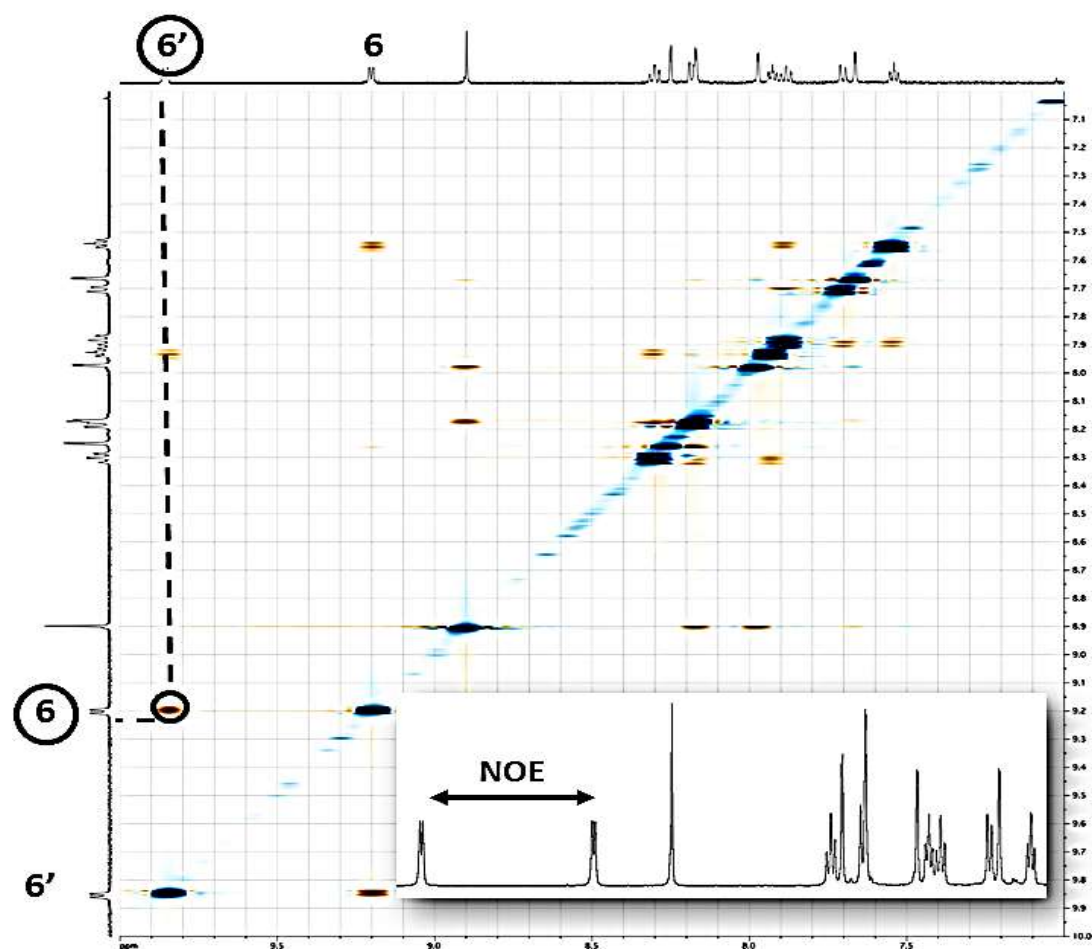


Figure 2.6. Aromatic region of complex **12**, showing the NOE correlation detected in 2D NOESY NMR, recorded in D-acetone at 500 MHz NMR spectrometer.

Some attempts were made to coordinate the two **dtdpa** ligands in a symmetric *meridional* fashion by increasing the reaction temperature (to get the thermodynamic product), working in ethylene glycol solvent, or even work with microwaves. However, none of these harsher conditions were sufficient to optimize the Ru(II) complex geometry. Thus, a theoretical study was performed by density functional theory (DFT) calculations to compare the energy between the three proposed configurations (C_{2h} -*fac*, C_2 -*fac* and *mer* geometries) for complex **12**. The result was as we proposed, in which the ligands coordinate more easily with Ru(II) in a non-symmetrical C_2 -*fac* geometry (most stable configuration), while the symmetrical C_{2h} -*fac* was more energetic by $1.3 \text{ kcal.mol}^{-1}$ and the desired *mer* was $8.2 \text{ kcal.mol}^{-1}$ greater in energy (Figure 2.7). Therefore, the coordination pathway tends towards giving the C_2 -*fac* geometry instead of the *mer* one.

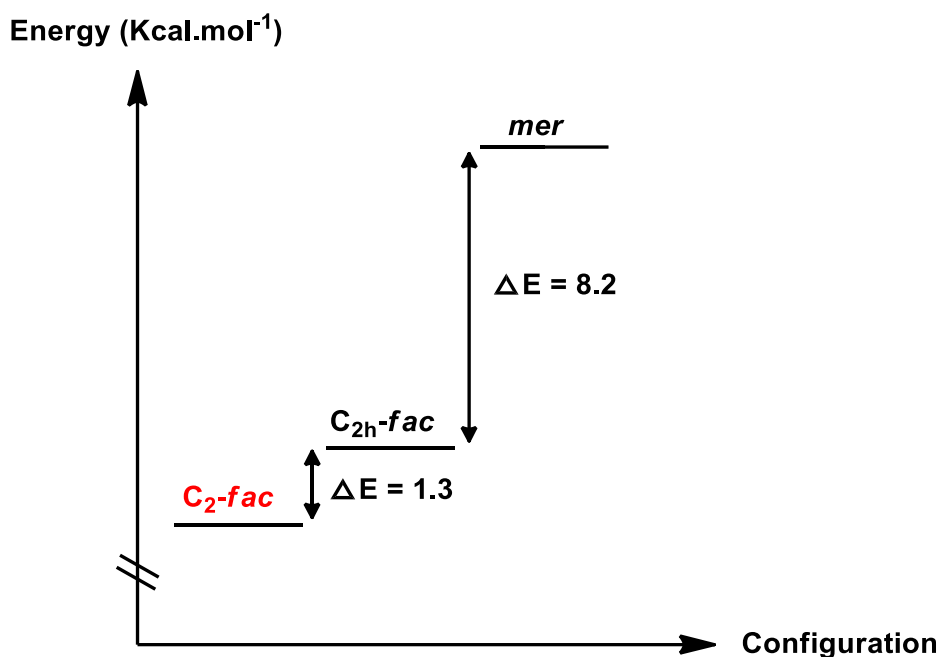


Figure 2.7. Complex **12** configurations estimated by TD-DFT calculations.

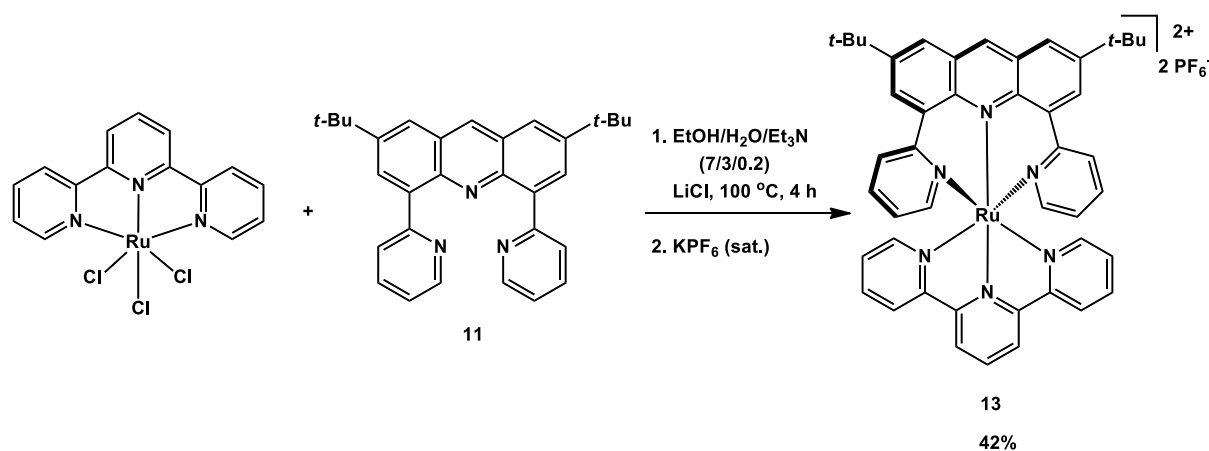
II.2.2. Heteroleptic Ru(II) complex synthesis

The geometric design, as explained in the introduction of this manuscript, is of a great importance to give a functional photosensitizer. Therefore, a second complex was synthesized using a ruthenium(III) chloride precursor coordinated already with one terpyridine ligand. The presence of this terpyridine ligand forces the second tridentate **dtdpa** ligand to coordinate exclusively in a *meridional* fashion.

A deep blue heteroleptic complex (**13**) was obtained after refluxing the **dtdpa** ligand in one-to-one molar equivalent ratio with a [Ru(tpy)Cl₃] precursor in ethanol/water (70%/30%) for 4 hours in the presence of lithium chloride. The pure compound was isolated in 42% yield as a hexafluorophosphate salt after silica gel chromatography followed by anion exchange using a saturated aqueous solution of KPF₆, as shown in Scheme 2.7 below.

The molecular formula [Ru(**dtdpa**)(tpy)](PF₆)₂ of the heteroleptic complex **13** was verified and characterized by ESI-mass spectrometry. In the spectrum, a mass peak at $m/z = 390.10$ with 2+ charge was detected, which matches with [Ru(**dtdpa**)(tpy)]²⁺ (m/z calculated to be 390.15),

in addition to the observation of a peak at $m/z = 925.20$ with 1+ charge, which matches with $[\text{Ru}(\text{dtdpa})(\text{tpy})](\text{PF}_6)^+$ (m/z calculated to be 925.20).



Scheme 2.7. Heteroleptic complex **13** synthesis.

The symmetric coordination of complex **13** was confirmed by $^1\text{H-NMR}$ spectrum, in which both the terpyridine and the **dtdpa** ligands display signals corresponding to half of the molecule. As shown in Figure 2.8, each proton of the ligand (bottom) is seen distinctly without any peak splitting in the heteroleptic complex spectrum (top), whereas, all the peaks denoted by stars are assigned to the terpyridine ligand.

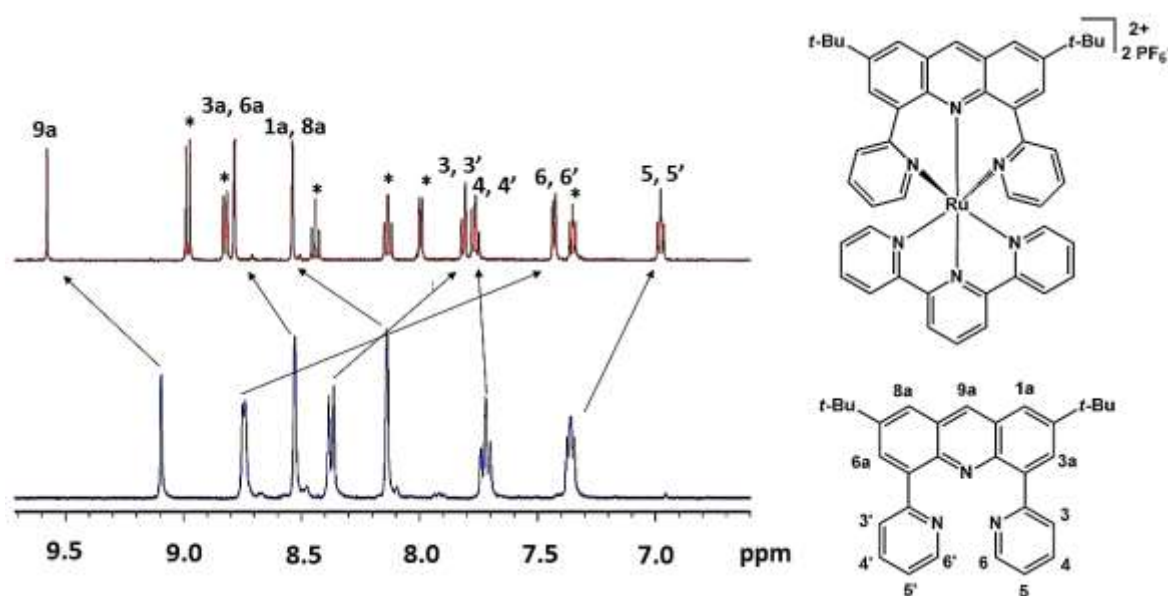


Figure 2.8. $^1\text{H-NMR}$ spectra of **dtdpa** ligand (bottom) and the heteroleptic complex **13** (top), recorded in D-acetone at 500 MHz spectrometer.

A careful analytical comparison between the $^1\text{H-NMR}$ spectra for both complexes **12** and **13**, shows a dramatic upfield shifting of the isochronous protons 6 and 6' of the pyridine rings by more than 2 ppm, from 9.2 and 9.85 ppm, respectively, for complex **12**, to 7.43 ppm for complex **13**. This shielding effect on these two protons is explained by the effect of the shielding cone created by the adjacent terpyridine ligand.

II.2.3. X-ray diffraction of complex **13**

A slow diffusion of diethylether into an acetone solution of the heteroleptic complex **13** was suitable to grow single crystals. As a result, the symmetrical *mer* geometry of complex **13** was also validated by X-ray diffraction crystallography. The complex structure is shown from different perspectives in Figure 2.9.

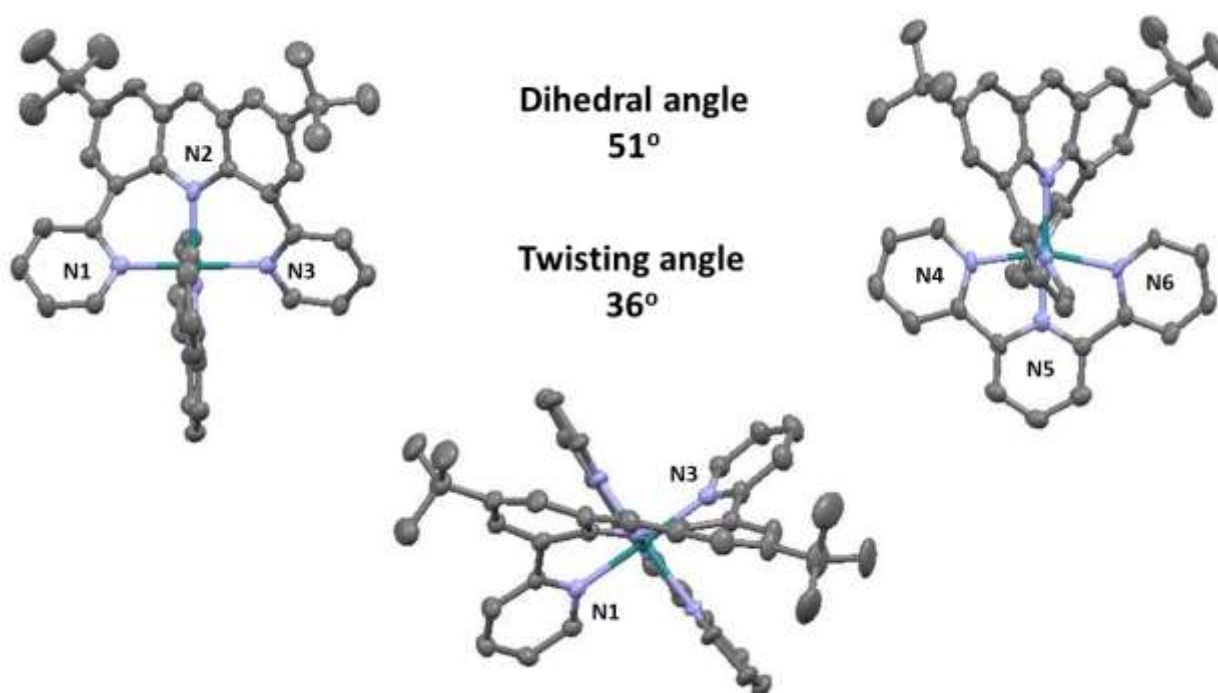


Figure 2.9. Different views of the crystal structure of the heteroleptic complex **13** (40% ellipsoids). Solvent molecules, H atoms, and the PF_6^- counter anions are removed for clarity.

All selected bond angles and bond lengths for complex **13** as well as for $[\text{Ru}(\text{tpy})_2](\text{PF}_6)_2^{17}$ (for comparison) are listed in Table 2.1. Optimized bond lengths and bond angles as computed by DFT calculations are presented in gray. It is clear that there is a great agreement between the

X-ray experimental data and the theoretical calculations, with an accuracy of calculated angles and bond lengths of less than 1° and 0.1 Å of difference respectively.

Table 2.1. Selected bond angles and bond lengths for the corresponding heteroleptic complex (**13**) [Ru(**dtdpa**)(tpy)](PF₆)₂ and the archetype [Ru(tpy)₂](PF₆)₂ complexes.

Complex	[Ru(dtdpa)(tpy)](PF ₆) ₂	[Ru(tpy) ₂](PF ₆) ₂
Angle (°)		
N1 Ru1 N2	89.3(2) 89.06	
N2 Ru1 N3	90.0(2) 89.06	
N1 Ru1 N3	178.8(2) 180.00	
N5 Ru1 N4	79.8(2) 79.02	79.5(3)
N5 Ru1 N6	79.7(3) 79.02	79.0(3)
N4 Ru1 N6	159.4(3) 158.04	158.4(3)
N2 Ru1 N5	179.1(2) 180.00	
Bond length (Å)		
Ru1 N1	2.068(6) 2.116	
Ru1 N2	2.076(7) 2.149	
Ru1 N3	2.058(6) 2.116	
Ru1 N5	1.946(6) 1.989	1.981(7)
Ru1 N4	2.107(5) 2.125	2.079(6)
Ru1 N6	2.078(5) 2.125	2.067(7)

The first goal of preparing this new ligand (**dtdpa**), for optimizing the octahedral coordination geometry, is achieved. It is clear from the X-ray diffraction results that complex **13** is decorated in a geometry close to a regular octahedron, with a 178.8° N1-Ru-N3 trans chelation angle, in addition to the formation of 89.3° and 90.0° angles between the acridine platform and the pyridine rings respectively with the ruthenium center.

Moreover, in this complex it seems that the terpyridine ligand is coordinated closer to the central metal, by having a shorter bond length between the central pyridine ring of tpy ligand and Ru(II) metal (Ru-N5 was reduced by 0.035 Å). Thus, the N4-Ru-N6 tpy trans angle was enhanced slightly and opened by 1.0° with respect to its parent complex. However, this was not enough and the tpy ligand is still coordinating to the Ru(II) central metal with the usual distortion, like what used to be observed with the parent [Ru(tpy)₂]²⁺ complex.

Moreover, based on the analysis of the X-ray crystal shown in Figure 2.9, we can see clearly an important twisting on the usually planar acridine platform. In fact, due to the high rigidity of this ligand, it was obligatory for the planar acridine heterocycle to twist with a dihedral angle of 36° in order to chelate the ruthenium metal cation, in which this twisting also was established in good agreement with DFT calculations (i.e. having less than 2° difference (37.96°) as compared to the experimental data).

Lastly, from DFT calculations we can understand the high rigidity of such ligand. By calculating the energy needed for the twisting step, we see that it accounts for double that of the energy needed for the whole complexation reaction. Computational optimization revealed a 23.3 kcal.mol⁻¹ energy needed for acridine twisting, while only a 13 kcal.mol⁻¹ energy are needed for the complexation reaction to proceed.

III. Electrochemistry

The redox potentials of **dtdpa** ligand as well as its corresponding homoleptic and heteroleptic Ru(II) complexes **12** and **13** were recorded using cyclic voltammetry (Figure 2.10).

All reversible monoelectronic potentials that were recorded in the positive region are attributed to the anodic oxidation from the HOMO which is mainly centered on the metal center (Ru³⁺/Ru²⁺) in the localized orbitals approximation.¹⁸ In contrast, all potentials that were recorded in the negative region correspond to the cathodic reduction on the orbitals which are localized on the different ligands (tpy or **dtdpa**).

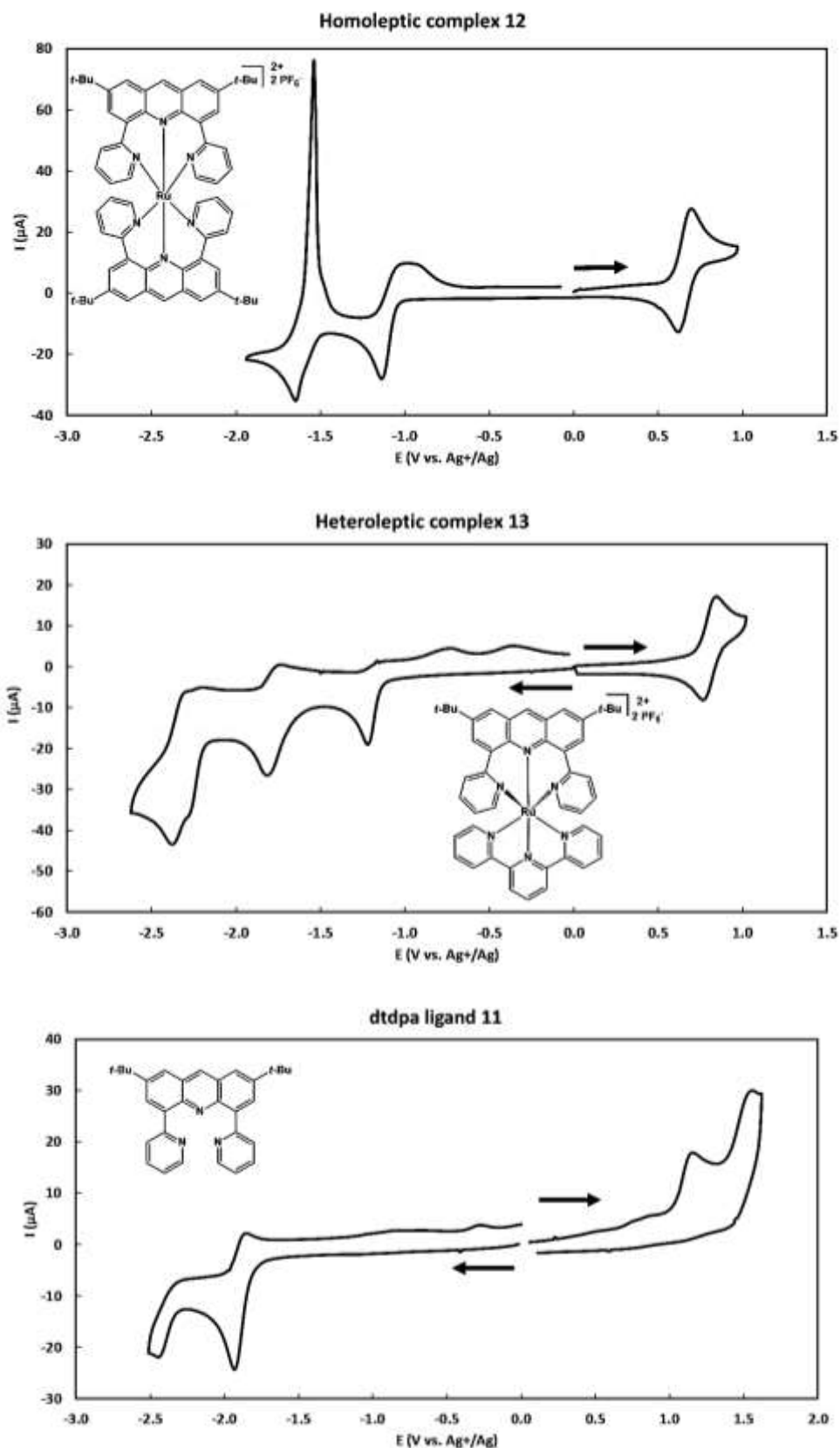


Figure 2.10. Cyclic voltammograms of complexes **12** (top), **13** (middle), and **dtdpa** ligand (bottom) in a 10^{-3} M deaerated acetonitrile solution + 0.1 M $[\text{BuN}]_4\text{PF}_6$ (TBAPF₆), at a scan rate of $100 \text{ mV}\cdot\text{s}^{-1}$ using vitreous carbon electrode (5 mm diameter), $E_p(\text{V})$ vs AgNO_3 (0.01 M)/Ag.

All the obtained redox potentials from the cyclic voltammograms are gathered in Table 2.2, in which the results of the homoleptic (**12**) and heteroleptic (**13**) Ru(II) complexes were analyzed in comparison to those of the parent $[\text{Ru}(\text{tpy})_2]^{2+}$ complex as a reference. The redox potentials of $[\text{Ru}(\text{tpy})_2]^{2+}$ complex have already been reported in the literature,¹⁹ where it was shown to exhibit a reversible monoelectronic oxidation wave at $E_{1/2} = 0.97$ V ($\Delta E_p = 80$ mV) vs. AgNO_3 (0.01 M)/Ag reference electrode, and two successive reversible reductions at -1.57 V ($\Delta E_p = 60$ mV), and -1.83 V ($\Delta E_p = 70$ mV) centered on both ligands respectively.

Table 2.2. Redox potentials of complexes $[\text{Ru}(\text{tpy})_2]^{2+}$, $[\text{Ru}(\text{tpy})(\text{dtdpa})]^{2+}$, $[\text{Ru}(\text{dtdpa})_2]^{2+}$, and **dtdpa** ligand. $E_{1/2}$ (V) = $(E_{pa} + E_{pc})/2$, (ΔE_p (mV) = $E_{pc} - E_{pa}$) vs Ag^+ (0.01 M)/Ag. *Irreversible process.

Compounds	$E_{1/2}$ reduction (ΔE_p , mV)		$E_{1/2}$ oxidation (ΔE_p , mV)		
$[\text{Ru}(\text{tpy})_2]^{2+}$	-1.83 (70)	-1.57 (60)	0.97 (80)		
$[\text{Ru}(\text{tpy})(\text{dtdpa})]^{2+}$ (13)	-2.38*	-2.28*	-1.78 (70)	-1.22*	0.81 (69)
$[\text{Ru}(\text{dtdpa})_2]^{2+}$ (12)	-1.63*		-1.11*	0.65 (65)	
dtdpa (11)	-2.43*		-1.90 (60)	1.14*	1.52*
tpy ²⁰	-2.95		-2.36		

III.1. Oxidation redox processes

To see the influence of the newly prepared **dtdpa** ligand on the oxidation potential of the ruthenium(II) metal, a comparison was made with respect to $[\text{Ru}(\text{tpy})_2]^{2+}$ complex. This comparison starts by replacing tpy ligands one by one with a **dtdpa** ligand **11** to go from the parent complex, to the heteroleptic complex **13**, and finally to the homoleptic one **12**. The

oxidation potential of the central metal on the heteroleptic complex which is at $E_{1/2} = 0.81$ V ($\Delta E_p = 69$ mV), was lowered by 160 mV as one tpy ligand was replaced by one **dtdpa** ligand. A further 160 mV potential drop was also observed for the oxidation on the homoleptic complex, of $E_{1/2} = 0.65$ V ($\Delta E_p = 65$ mV), when two **dtdpa** ligands are coordinated to the metal. Therefore, we can clearly see the effect of **dtdpa** ligands on decreasing the potential needed to oxidize the central Ru(II) metal.

This unusual oxidation potential drop for Ru(II) complexes based on trimine ligands can be explained by the different geometrical distortion of both complexes upon complexation. Indeed, as it was expected for the homoleptic complex, due to its *facial-gauche* geometry, the acridine backbone was coordinated in a distorted way. Thereby, such a coordination mode prevents appropriate π back-bonding from the d_{xz} orbital of the metal to the π -system on the ligand. Furthermore, despite the *meridional* symmetrical geometry of the heteroleptic complex, the same retrodonation hindrance was also observed. A careful analysis of the X-ray diffraction structure of complex **13** shows a torsion angle around 50° between the acridine scaffold and the central pyridine ring of tpy ligand, which is lower than the 90° value obtained in the reference complex $[\text{Ru}(\text{tpy})_2]^{2+}$. Indeed, these two heterocycles were expected to be perpendicular to each other in order to have an appropriate overlapping between the acridine and pyridine π -systems from one side and the d_{xz} and d_{yz} hybrid orbitals of Ru(II) metal from the second side. Thus, this results in an efficient π back-bonding. Therefore, complexes **12** and **13**, even with their different geometries, both acquired a lower oxidation potential due to the same retrodonation hindrance effect, which leads to more electron density on the metal center and thereby leads to an easy oxidation.

Not-surprisingly, two irreversible oxidation potentials at 1.14 V and 1.52 V were observed for the highly conjugated **dtdpa** ligand.²¹ Globally these two oxidations occurred at the most conjugated part of the ligand which is the acridine scaffold. Moreover, this proposition is validated by DFT calculations which predict the localization of the HOMO on the acridine part in the **dtdpa** ligand (Figure 2.11). Oxidation process occurs from the nitrogen electrons lone pair of the acridine to give acridinium, in which these processes are irreversible due to the high reactivity of the formed acridinium with another acridine to form the dimer.²²

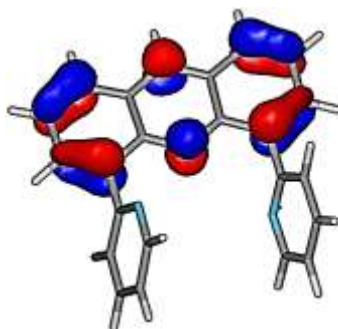


Figure 2.11. HOMO localization on **dtdpa** ligand, optimized by DFT calculations.

III.2. Reduction redox processes

The **dtdpa** ligand undergoes a monoelectronic reversible reduction at $E_{1/2} = -1.90$ V in addition to an irreversible one at -2.34 V. The second irreversible reduction process may be due to the formation of the acridane derivative after two successive electron reductions. In a comparison of the **dtdpa** ligand reduction potentials to that of a tpy ligand (reduces at -2.36 V and -2.95 V), we can clearly see an easier reduction of the **dtdpa** ligand relative to tpy. Thus, that indicates the more π -conjugated character of **dtdpa** ligand as compared to the reference one. This proves that **dtdpa** ligand should possess a lower lying π^* orbital compared to that of the tpy ligand.

Similarly, several reduction potentials that are localized on the ligands were observed in the cathodic region for both Ru(II) complexes. The homoleptic complex **12** exhibits two irreversible reduction peaks at -1.11 V and -1.63 V attributed to each **dtdpa** ligand respectively. Thus, this shows the electronic communication between both ligands through the central Ru(II) metal.

However, in the back wave two oxidation peaks were appeared at -1.02 V and -1.54 V for each reduction peak respectively, with a complex deposition on the working electrode after the second reduction process.

In the same pattern, the heteroleptic complex **13** exhibits an irreversible reduction potential at -1.22 V that took place on the lower π^* -orbital of the **dtdpa** ligand, whereas the second reversible reduction potential at $E_{1/2} = -1.78$ V was assigned to be on the facing tpy ligand.

Moreover, two partially overlapped irreversible reduction peaks at -2.28 V and -2.38 V were observed, which are globally attributed to a reduction process on both ligands.

Furthermore, the shifting in reduction of the **dtdpa** ligand and even for the tpy ligand to less negative potentials, is simply due to the electron lone pair donation from the imine to the Ru(II) metal center after the coordination reaction. Thus, the electron density at the ligands decrease, leading consequently to their easier reduction on their complexes.

III.3. DFT-calculations

The theoretical calculations were in great agreement with the results obtained from the electrochemical studies. The electrochemical analysis for the heteroleptic complex **13**, indicates that the LUMO is mainly localized on the **dtdpa** ligand, and the HOMO is globally localized on the ruthenium metal ($\text{Ru}^{3+}/\text{Ru}^{2+}$).

DFT calculations optimized the frontier orbitals of complex **13**, indicating that the HOMO is localized at the d-orbitals of the ruthenium center and the LUMO is localized mainly on the **dtdpa** ligand (Figure 2.12).

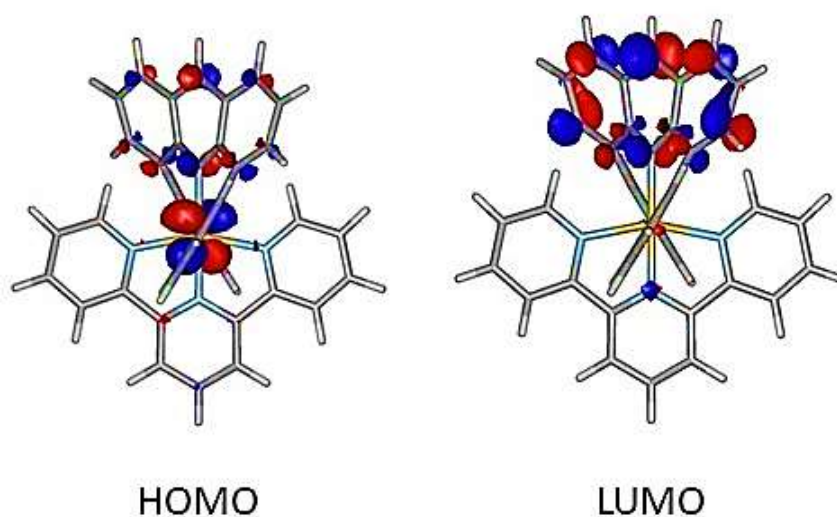


Figure 2.12. HOMO and LUMO localization on complex **13**, optimized by DFT calculations.

Moreover, we can see theoretically from the molecular orbital diagram presented in Figure 2.13, that the energy transition from the Ru(II) central metal to the **dtdpa** ligand is less energy costing than to tpy ligand.

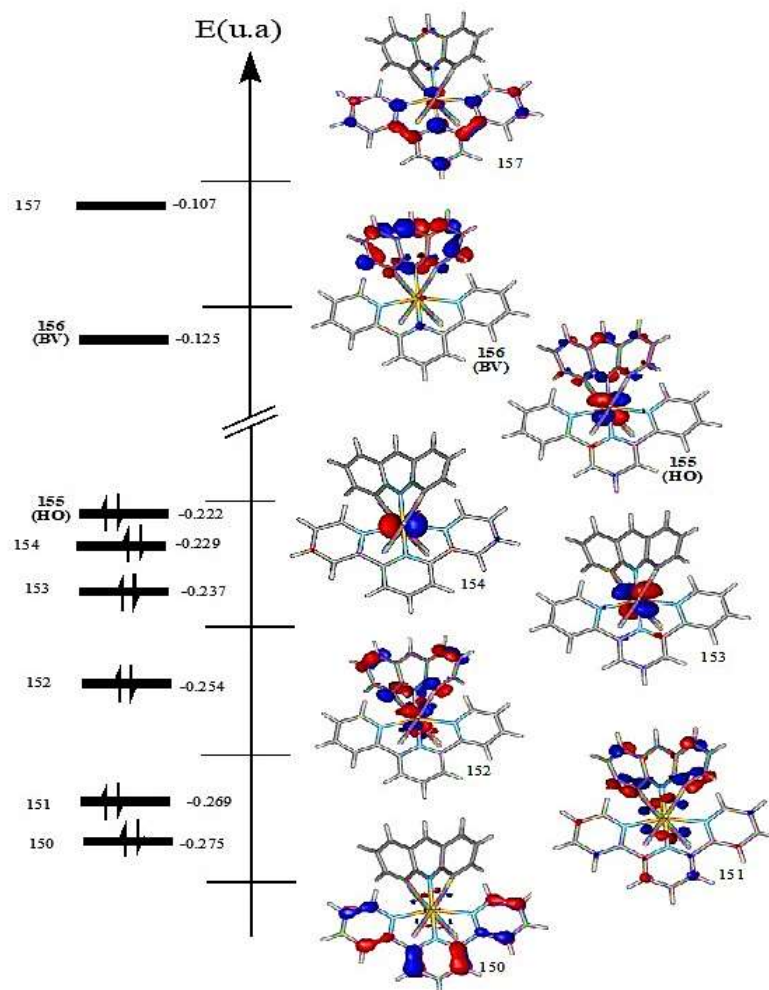


Figure 2.13. Molecular orbital diagram of complex **13**, optimized by DFT calculations.

IV. Photophysics

The absorption and emission properties of the **dtdpa** ligand (**11**) as well as its corresponding homoleptic and heteroleptic Ru(II) complexes (**12** and **13**) were studied in deaerated acetonitrile solution at room temperature and in a butyronitrile rigid matrix at 77 K. The photophysical behavior of both ruthenium complexes were analyzed in comparison to the reference $[\text{Ru}(\text{tpy})_2]^{2+}$ complex.

IV.1. Ligand spectroscopic properties

IV.1.1. Absorption spectroscopy

The typical absorption and emission spectra of **dtdpa** ligand are shown in Figure 2.14. This **dtdpa** ligand displays the expected typical absorbance of the aromatic organic molecules in the UV region which expands from 240 to 300 nm with a maximum centered at 262 nm, and a molar absorption coefficient $9.67 \times 10^4 \text{ M}^{-1} \text{ cm}^{-1}$. This band is attributed to the $\pi\text{-}\pi^*$ ligand centered (LC) transition (Figure 14, a).

Moreover, a broad structured absorption near the visible region which expands from 320 to 470 nm was also observed, with a maximum centered at 365 nm of a molar absorption coefficient $7.50 \times 10^3 \text{ M}^{-1} \text{ cm}^{-1}$ (Figure 14, a). This moderately intense absorption, could be attributed to the $n\text{-}\pi^*$ transition on the acridine platform.²³ Furthermore, the proposition of having a localized transition and not charge transfer process between the different rings, is verified by the absorption spectrum of compound **10** which exhibits both intense absorption peak at 261 nm and the broad-moderate intensity peak at 362 nm.

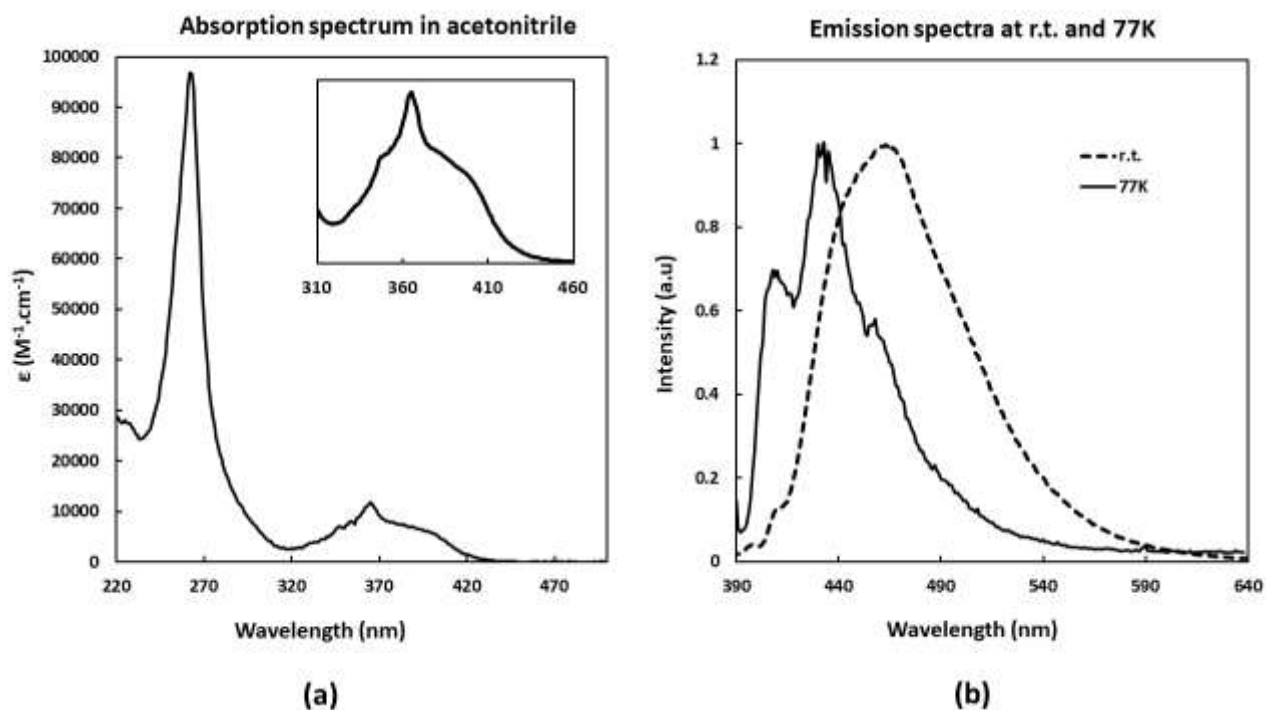


Figure 2.14. Absorption and emission spectra of **dtdpa** ligand.

IV.1.2. Fluorescence spectroscopy

The **dtdpa** ligand emits at low temperature (77 K) and room temperature, after excitation at 365 nm. The maximum wavelength of the fluorescence emission of the ligand at room temperature in acetonitrile is 463 nm (Figure 14, b), with a short detected excited state lifetime of 0.2 ns and with a 2.2% emission quantum yield. Moreover, in a frozen rigid matrix using butyronitrile solvent, the emission excited state wavelength was blue shifted to be centered at 442 nm, with an excited state lifetime of 1.4 ns (Figure 14, b). The blue shifting of the emission wavelength at 77 K is justified due to removing the solvent re-organization, which is usually stabilizes the excited state and lowers its energy. The maximum emission wavelength in a frozen solvent is considered as a measurement of the excited state energy.

IV.2. Ru(II) complexes spectroscopic properties

IV.2.1. Absorption spectroscopy

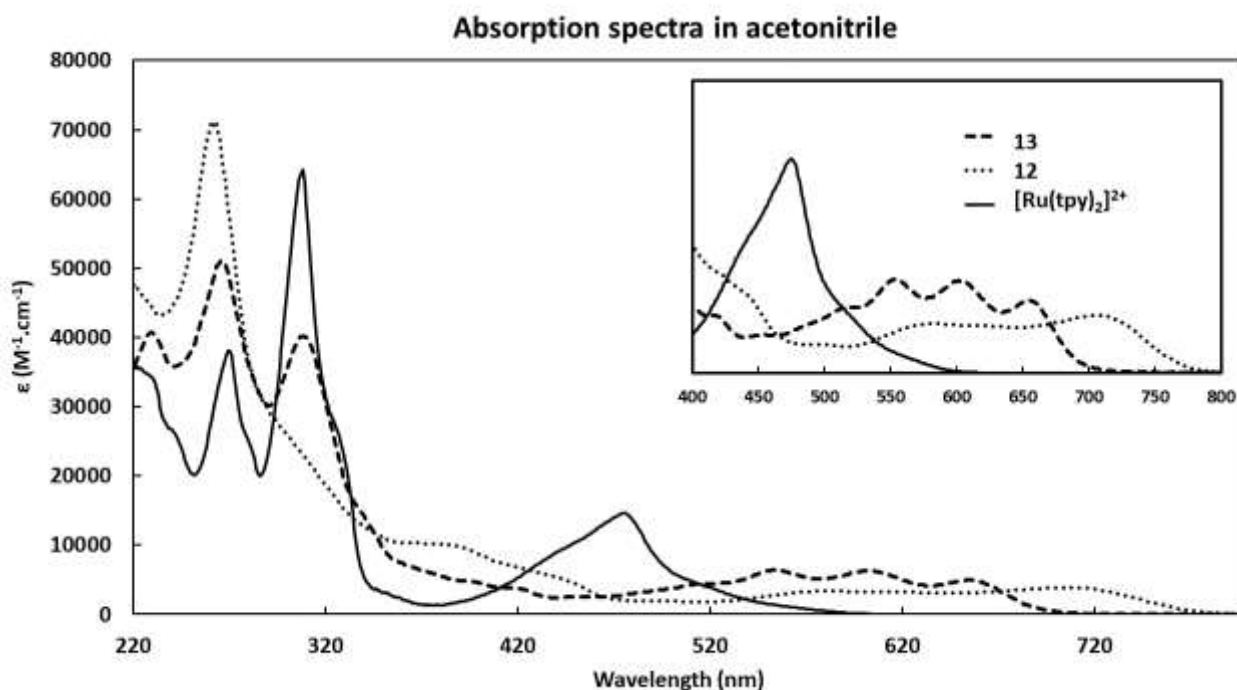


Figure 2.15. UV-vis absorption spectra in deaerated acetonitrile of complexes **12** (dotted), **13** (dashed), and $[\text{Ru}(\text{tpy})_2]^{2+}$ (full line).

In this section, I will present the photophysical properties of the homoleptic and heteroleptic Ru(II) complexes (**12** and **13**) and their structure-function relationship. The absorption spectra of these two complexes, in addition to that of the parent complex $[\text{Ru}(\text{tpy})_2]^{2+}$ for comparison, were recorded in deaerated acetonitrile ($C = 10^{-5} \text{ M}$) as shown in Figure 2.15.

Both ruthenium complexes display a strong spin allowed, π - π^* ligand centered transition (LC) in the UV region. However, relative to each other, the homoleptic complex **12** shows a stronger absorption (higher ϵ) in this region. Complex **12** (dotted line) exhibits a single intense band, which is attributed to the π - π^* transition on the coordinated **dtdpa** ligand, with a maximum wavelength centered at 261 nm. The molar absorption coefficient of this band at the maximum wavelength reaches $7.12 \times 10^4 \text{ M}^{-1} \text{ cm}^{-1}$. On the second hand, complex **13** (dashed line) displays three absorption bands with maximum wavelengths centered at 231 nm, 266 nm, and 309 nm. The molar absorption coefficient at the maximum wavelengths were $\epsilon = 4.05 \times 10^4 \text{ M}^{-1} \text{ cm}^{-1}$, $5.12 \times 10^4 \text{ M}^{-1} \text{ cm}^{-1}$, and $4.02 \times 10^4 \text{ M}^{-1} \text{ cm}^{-1}$ respectively. The energetic bands at 231 nm and 266 nm could be attributed to the transitions on the **dtdpa** ligand, whereas the band at 309 nm which is in the same range of ϵ as the $[\text{Ru}(\text{tpy})_2]^{2+}$ complex, is attributed to the transition on the coordinated terpyridine ligand.

More importantly, the bands which are observed in the visible region for both complex **12** and **13**, are attributed to the $d_{(M)}-\pi^*$ transitions (MLCT). Both MLCT bands are significantly red shifted with respect to the reference $[\text{Ru}(\text{tpy})_2]^{2+}$ complex, as we see in Figure 2.14. The moderately intense MLCT transition in complex **12** expands from 520 nm up to the end of the visible region at 800 nm, with a maximum wavelength centered at 706 nm and a molar absorption coefficient of $3.90 \times 10^3 \text{ M}^{-1} \text{ cm}^{-1}$. On the other hand, the structured MLCT transition in complex **13** which was more energetic than in complex **12**, is expanding from 450 nm to 700 nm, with maximum wavelengths centered at 553 nm ($\epsilon = 6.40 \times 10^3 \text{ M}^{-1} \text{ cm}^{-1}$), 602 nm ($\epsilon = 6.30 \times 10^3 \text{ M}^{-1} \text{ cm}^{-1}$), and 655 nm ($\epsilon = 5.00 \times 10^3 \text{ M}^{-1} \text{ cm}^{-1}$).

All the spectroscopic properties of all the prepared chromophoric **dtdpa** ligand and complexes **12** and **13** are summarized in Table 2.3.

Table 2.3. Spectroscopic data for complexes **12** and **13** in addition to the **dtdpa** (**11**) ligand in deaerated acetonitrile solution.

Compounds	λ_{abs} , nm (ϵ , $\text{M}^{-1} \text{cm}^{-1}$)	Room temperature			77 K	
		λ_{em} , nm	ϕ	τ , ns	λ_{em} , nm	τ , ns
[Ru(dtdpa) ₂] ²⁺ (12)	261 (71,200), 386 (10,000), 443 (5,200), 583 (3,400), 706 (3,900)					
[Ru(tpy)(dtdpa)] ²⁺ (13)	231 (40,500), 266 (51,200), 309 (40,200), 521 (4,500), 553 (6,400), 602 (6,300), 655 (5,000)	1030				
dtdpa (11)	262 (96,700), 365 (7,500)	463	0.022	0.2	442	1.4

The unpredicted red shifting of the ¹MLCT bands can be justified, as shown in Figure 2.16, based on the electrochemical analysis which was illustrated before. This movement towards lower energies is in assessable agreement with the electrochemical data which displayed lower oxidation potentials of both ruthenium(II) complexes, due to the high electron density on the metal as explained earlier as a result of the weak π -retrodonation to the ligands in the geometrically distorted complexes. As a result, the HOMO (t_{2g}) rises in energy as we go from twisted *mer* complex **13** (less distortion) to the remarkable *fac* distorted complex **12**, as seen in Figure 2.16. Moreover, due to the same weak π -retrodonation, the LUMO which is centered on the ligand π^* orbitals is stabilized by the electron poor **dtdpa** ligand, which has a lower reduction potential. Consequently, the HOMO-LUMO energy gap decreases, resulting in a low lying MLCT excited state.

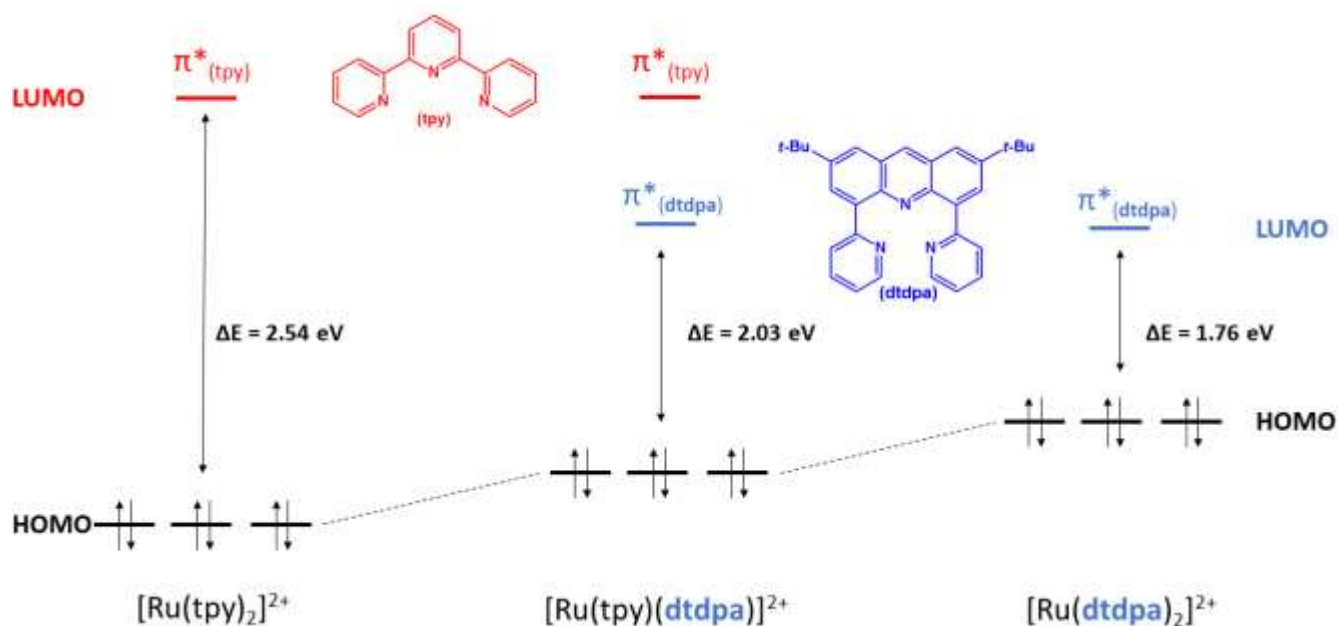


Figure 2.16. Relative molecular orbitals energy level for complexes **12**, **13**, and $[\text{Ru}(\text{tpy})_2]^{2+}$.

The second remarkable observation from this spectroscopic data is related to the structured MLCT band transition observed in the visible region of the heteroleptic complex **13**. This observed band can be rationalized by the octahedral coordination geometry upon complexation of the **dtdpa** ligand with the Ru(II) central metal. The highly rigid **dtdpa** ligand, as explained before, should undergo an important twisting to coordinate with the metal and adopt the constrained *mer* geometry. Thus, such locked chelation will allow the vibronic progression of the transition to be apparent.

IV.2.2. DFT-calculations

TD-DFT calculations were performed and were in agreement with the spectroscopic behavior for both the homoleptic and heteroleptic complexes. Figure 2.17 shows the absorption spectra for both complexes after attempts of deconvolution of the experimental spectra into Lorentzian functions, in which the oscillator strength was normalized to largest transition (LC).

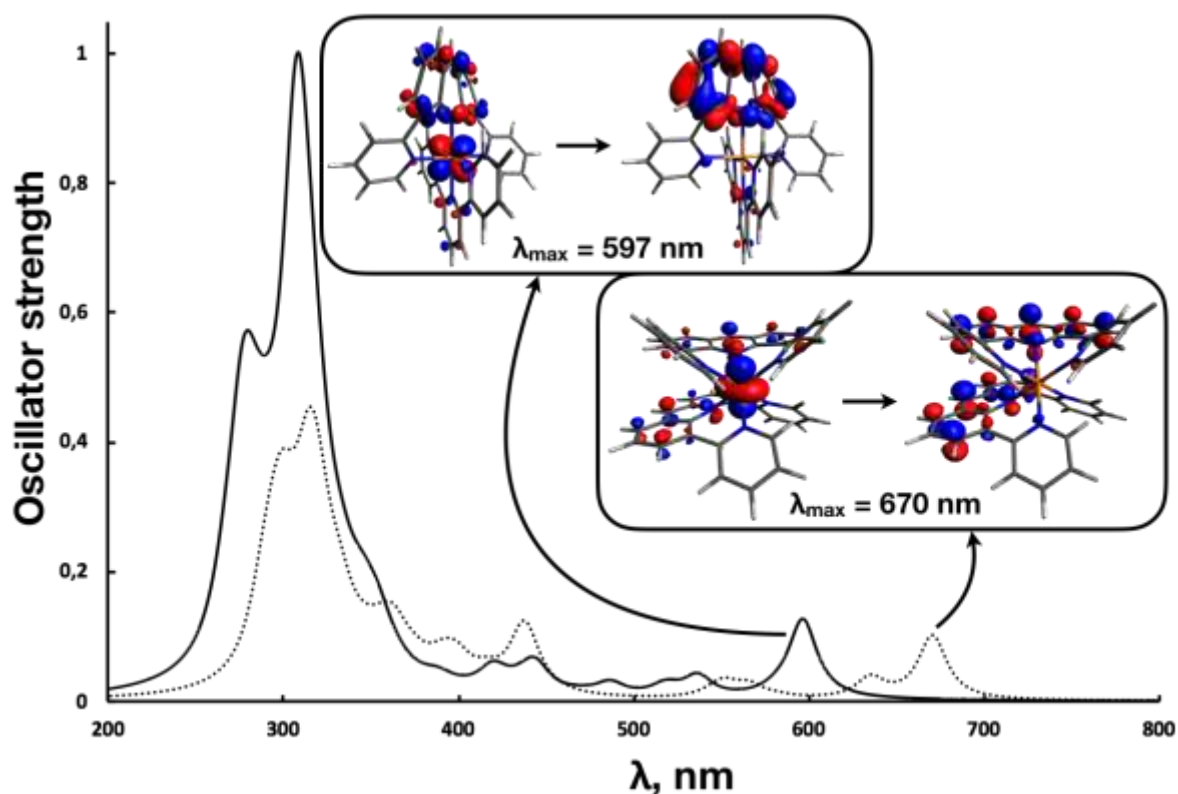


Figure 2.17. UV-vis absorption spectra of complexes **12** (dotted line), and **13** (solid line) optimized by TD-DFT calculations.

All the MLCT ($d_M-\pi^*$) transitions in the visible region for complexes **12** and **13** are well presented with their wavelengths and energy difference in addition to a schematic presentation for each kind of transition in Table App.1 and Table App.2, respectively, in the appendix part.

In general, there was good agreement between the experimental data and that obtained by TD-DFT calculations. However, all the transitions seem to be more energetic than those obtained by experiment (on average, more energetic by 0.23 eV). The least energetic MLCT transition (HOMO-LUMO transition) was expanded in the visible region with maximum wavelengths at 583 nm, and 706 nm experimentally for complex **12** and at 553 nm, 602 nm, and 655 nm for complex **13**, respectively (Figure 2.15), whereas it was calculated to be at 566 nm, and 670 nm for complex **12** and at 536 nm, 581 nm, and 597 nm for complex **13** respectively, by DFT (Figure 2.17).

The important separation between the π^* -orbitals of tpy and **dtdpa** ligands in the heteroleptic complex is observed clearly from DFT calculations. As we see in Table App.2 (appendix part), the lowest three MLCT transitions are observed from the HOMO, HOMO-1 and HOMO-2 located on the ruthenium metal to the LUMO localized on the **dtdpa** ligand of lower π^* -orbital. Moreover, the transition at 518 nm seems to be a junction between the two ligands, in which the MLCT occurs from the HOMO on the metal to the LUMO+1 that is localized on both ligands. Furthermore, all the more energetic transitions after 518 nm, towards the UV region, are considered to be generated from the HOMO to the orbitals localized on the tpy ligand which possesses the higher π^* -orbital.

IV.2.3. Phosphorescent spectroscopy

The phosphorescent properties of complexes **12** and **13** were studied experimentally at room temperature in acetonitrile solution and also in a butyronitrile rigid matrix at 77 K, following excitation in the least energetic $^1\text{MLCT}$, in the visible region, relative to the absorbance for each complex. The results were compared to those obtained by TD-DFT calculations.

The homoleptic complex **12** did not show any emission under either set of conditions. This result can be rationalized by this highly geometrically distorted complex which possesses the *facial* octahedral geometry. It seems from DFT calculations that this complex with a very low $^1\text{MLCT}$ state, which absorbs in the red region of the visible light extending to the near-infrared region, could theoretically emit at 1431 nm, however this could not be detected.

The heteroleptic complex **13** shows a weak emission experimentally from its $^3\text{MLCT}$ excited state in the near-infrared region of wavelength around 1030 nm in acetonitrile at room temperature. This result is in good agreement with DFT calculations, which computed a phosphorescence of this complex at 1130 nm, with a 0.1 eV difference from the experimental data. Indeed, such red shifting of the $^3\text{MLCT}$ energy is not a surprising result by taking into consideration the Stoke's shift between the lowest $^1\text{MLCT}$ and $^3\text{MLCT}$ excited states. The Stoke's shift in our system is in the same range as what had been obtained in the bis-tridentate polypyridyl ruthenium(II) complexes. For example, the reference $[\text{Ru}(\text{tpy})_2]^{2+}$ complex, with $^1\text{MLCT}$ and $^3\text{MLCT}$ maxima at 475 nm and 629 nm, respectively,²⁴ has a Stoke's

shift of about 0.64 eV, which is comparable to the result we obtained for complex **13**, which possesses a Stoke's shift of about 0.69 eV.

Furthermore, one of the propositions for having a weak emission from the heteroleptic complex and lack of luminescence from the homoleptic complex, could be due to some further non-radiative decay pathways of the excited state. It can be hypothesized that a direct intersystem crossing from the ¹MLCT excited state to the low lying organic triplet of **dtbpa** ligand could be one of these non-radiative pathways.

V. Conclusion

The first goal of preparing this new **dtdpa** ligand, which is separating as much as possible the emitting and non-emitting excited states, was generally achieved. By imparting a low lying π^* energy orbital to stabilize $^3\text{MLCT}$. In addition, through chelating Ru(II) in a six-membered metallacycles to destabilize ^3MC , thereby avoiding the thermal population of ^3MC from $^3\text{MLCT}$ by IC. However, the main goal of having new Ru(II) complexes with improved excited state properties, mainly having a long lived excited state lifetime with a good quantum yield, was not accomplished. This un-optimized photophysical property results mainly from the rigid structure of the **dtdpa** ligand, which requires a very tight coordination cavity. This rigidity was the direct cause of obtaining the thermodynamic *facial* geometry of the homoleptic complex. Starting with ruthenium precursor having one tpy ligand was of great importance to drive the chelation of the **dtdpa** ligand in the *meridional* geometry. However, forcing the **dtdpa** ligand to adopt such a constrained coordination leads to a significant twisting of the acridine scaffold. Consequently, this suppresses the π -back donation from Ru metal to the ligand. Thus, the t_{2g} metal orbital was destabilized, resulting in a small HOMO-LUMO energy gap. Therefore, a much stabilized, low lying $^3\text{MLCT}$ excited state was created, to produce unexpected spectroscopic properties for the heteroleptic complex **13**, by emitting in the NIR region. This compound could be interesting, it may be useful in biological applications as luminescent sensors in cell-imaging systems.²⁵

Therefore, enlarging the coordinating cavity and have a less strained coordination geometry could be a suitable solution, by coupling a smaller heterocycle rings at positions 4 and 5 of the acridine scaffold, like pyrazole rings, starting from the key intermediate compound **10**.

VI. References

- (1) Denny W. A. Acridine Derivatives as Chemotherapeutic Agents. *Curr. Med. Chem.* **2002**, *9* (18), 1655–1665.
- (2) Tonelli, M.; Vettoretti, G.; Tasso, B.; Novelli, F.; Boido, V.; Sparatore, F.; Busonera, B.; Ouhtit, A.; Giliberti, G.; La Colla, P. Acridine Derivatives as Anti-BVDV Agents. *Antiviral Res.* **2011**, *91* (2), 133–141.
- (3) Zelenka, K.; Borsig, L.; Alberto, R. Metal Complex Mediated Conjugation of Peptides to Nucleus Targeting Acridine Orange: A Modular Concept for Dual-Modality Imaging Agents. *Bioconjugate. Chem.* **2011**, *22* (5), 958–967.
- (4) Collie, G. W.; Sparapani, S.; Parkinson, G. N.; Neidle, S. Structural Basis of Telomeric RNA Quadruplex-Acridine Ligand Recognition. *J. Am. Chem. Soc.* **2011**, *133* (8), 2721–2728.
- (5) Chiron, J.; Galy, J.-P. Reactivity of the Acridine Ring: A Review. *Synthesis.* **2004**, No. 3, 313–325.
- (6) Daw, P.; Ben-david, Y.; Milstein, D. Acceptorless Dehydrogenative Coupling Using Ammonia: Direct Synthesis of N-Heteroaromatics from Diols Catalyzed by Ruthenium. *J. Am. Chem. Soc.* **2018**, *140*, 11931–11934.
- (7) Xie, Y.; Ben-david, Y.; Shimon, L. J. W.; Milstein, D. Highly Efficient Process for Production of Biofuel from Ethanol Catalyzed by Ruthenium Pincer Complexes. *J. Am. Chem. Soc.* **2016**, *138*, 9077–9080.
- (8) Nakao, Y. Transition-Metal-Catalyzed C – H Functionalization for the Synthesis of Substituted Pyridines. *Synthesis.* **2011**, No. 20, 3209–3219.
- (9) Hyodo, I.; Tobisu, M.; Chatani, N. Regioselective C-H Bond Functionalizations of Acridines Using Organozinc Reagents. *Chem. Commun.* **2012**, *48* (2), 308–310.
- (10) Martin, R. F.; Kelly, D. P. Synthesis and N.M.R. Spectra of Substituted Aminoiodoacridines. *Aust. J. Chem.* **1979**, *32*, 2637–2646.

- (11) Davidson, J. J.; Demott, J. C.; Douvris, C.; Fafard, C. M.; Bhuvanesh, N.; Chen, C. H.; Herbert, D. E.; Lee, C. I.; McCulloch, B. J.; Foxman, B. M.; Ozerov, O. V. Comparison of the Electronic Properties of Diarylamido-Based PNZ Pincer Ligands: Redox Activity at the Ligand and Donor Ability toward the Metal. *Inorg. Chem.* **2015**, *54*, 2916–2935.
- (12) Mudadu, M. S.; Singh, A. N.; Thummel, R. P. Preparation and Study of 1,8-Di (Pyrid-2'-Yl)Carbazoles. *J. Org. Chem.* **2008**, *73* (4), 6513–6520.
- (13) Bratulescu, G. 9-Alkylacridine Synthesis Using 2,2-Dimethoxypropane As Water Scavenger. *Heterocycles* **2014**, *89* (8), 1877–1884.
- (14) Yamamoto, K.; Higashibayashi, S. Synthesis of Three-Dimensional Butterfly Slit-Cyclobisazaanthracenes and Hydrazinobisanthenes through One- Step Cyclodimerization and Their Properties. *Chem. Eur. J.* **2016**, *22*, 663–671.
- (15) Constable, E. C.; Housecroft, C. E.; Neuburger, M.; Schmitt, C. X. Platinamacrocycles Containing 2,5-Thiophenediyl and Poly(2,5-Thiophenediyl)-Linked Azaaromatic Ligands: New Structural Paradigms for Metallosupramolecular Chemistry. *Polyhedron* **2006**, *25* (8), 1844–1863.
- (16) Desbois, N.; Szollosi, A.; Maisonia, A.; Weber, V.; Moreau, E.; Teulade, J.-C.; Chavignon, O.; Blache, Y.; Chezal, J. M. Simple and Convenient Conversion of Acridones into 9-Unsubstituted Acridines via Acridanes Using Borane Tetrahydrofuran Complex. *Tetrahedron Lett.* **2009**, *50* (49), 6894–6896.
- (17) Lashgari, K.; Kritikos, M.; Norrestam, R.; Norrby, T. Bis(Terpyridine) Ruthenium(II) Bis(Hexafluorophosphate) Diacetonitrile Solvate. *Acta Crystallogr. Sect. C* **1999**, *55*, 64–67.
- (18) Juris, A.; Balzani, V.; Barigelletti, F.; Campagna, S.; Belser, P.; Von Zelewsky, A. Ru(II) Polypyridine Complexes: Photophysics, Photochemistry, Electrochemistry, and Chemiluminescence. *Coord. Chem. Rev.* **1988**, *84*, 85–277.
- (19) Jacquet, M.; Lavolet, F.; Cobo, S.; Loiseau, F.; Bakkar, A.; Boggio-Pasqua, M.; Saint-Aman, E.; Royal, G. Efficient Photoswitch System Combining a Dimethyldihydropyrene Pyridinium Core and Ruthenium(II) Bis-Terpyridine Entities. *Inorg. Chem.* **2017**, *56* (8),

- 4357–4368.
- (20) Persaud, L.; Barbiero, G. Synthesis, Electrochemical and Spectroscopic Investigations of 2,2':4,4''-Terpyridine and 2,2':4,4'':6,2''-Quaterpyridine Ligands for Metal Complex Photoelectrochemistry. *Can. J. Chem.* **1991**, *69*, 315–321.
- (21) Pontinha, A. D. R.; Sparapani, S.; Neidle, S.; Oliveira-Brett, A. M. Triazole-Acridine Conjugates: Redox Mechanisms and in Situ Electrochemical Evaluation of Interaction with Double-Stranded DNA. *Bioelectrochemistry* **2013**, *89*, 50–56.
- (22) Marcoux, L.; Adams, R. N. ANODIC OXIDATION OF AROMATIC AZA HYDROCARBONS. *Electroanal. Chem. and Interfacial. Electrochem.* **1974**, *49*, 111–122.
- (23) Rak, J.; Blazejowski, J. Experimental and INDO CI Calculations of the Electronic Absorption Spectra of Acridine and 9-Acridinamine Free Bases and Their Protonated Forms with Regard to Tautomeric Phenomena. *J. Photochem. Photobiol. A Chem.* **1992**, *67*, 287–299.
- (24) Pal, A. K.; Hanan, G. S. Design, Synthesis and Excited-State Properties of Mononuclear Ru(II) Complexes of Tridentate Heterocyclic Ligands. *Chem. Soc. Rev.* **2014**, *43* (17), 6184–6197.
- (25) Pal, A. K.; Serroni, S.; Zaccheroni, N.; Campagna, S.; Hanan, G. S. Near Infra-Red Emitting Ru(II) Complexes of Tridentate Ligands: Electrochemical and Photophysical Consequences of a Strong Donor Ligand with Large Bite Angles. *Chem. Sci.* **2014**, *5*, 4800–4811.

Chapter 3: Going to a bigger NNN- coordination cavity: di-pyrazolyl acridine-based ligand

I. Introduction

As mentioned in the previous chapter, the very tight coordination pocket of the structurally rigid **dtdpa** (**11**) ligand was the main reason for obtaining the kinetic and thermodynamic *facial* homoleptic and twisted *meridional* heteroleptic ruthenium(II) complexes. Thus, one of the solutions was to enlarge the coordinating cavity and have a less strained coordination geometry. A straightforward approach to achieve that, was to replace the two pyridine rings (6-membered rings) at positions 4 and 5 of the acridine backbone by smaller *N*-heterocycle rings, such as pyrazole (5-membered rings) rings. Following this idea, the **dtdpza** (**14**) (2,7-ditertbutyl-4,5-di(pyrazol-1-yl)acridine) ligand was obtained, as shown in Figure 3.1. This new (NNN) tridentate ligand with a larger coordinating cavity can still form the favorable 6-membered metallacycles with the cationic ruthenium metal.

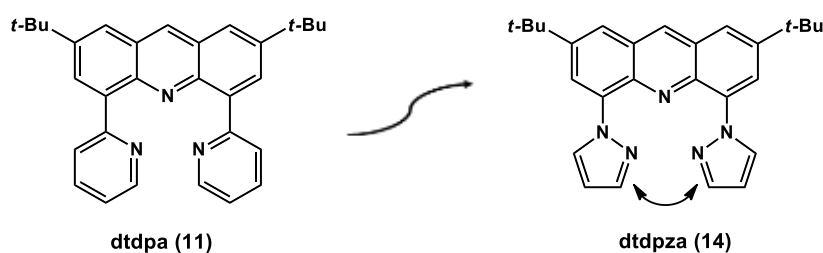


Figure 3.5. Opening the coordination cavity, by changing from **dtdpa** (**11**) ligand to **dtdpza** (**14**) ligand.

Moreover, replacing pyridine rings with pyrazole ones, to enhance the coordinating ability of some bidentate or tridentate ligands, was described recently.^{1,2,3} For example, the bulky **8-QPy** (8-(pyridin-2-yl)quinoline) ligand that precludes the formation of its tris-homoleptic complex was modified into **8-Q3PzH** (8-(pyrazol-3-yl)quinoline) and **8-Q1Pz** (8-(pyrazol-1-yl)quinoline) ligands by replacing the pyridine rings with pyrazole ones, to have a less inter-ligand steric interaction and open the coordination cavity (Figure 3.2). Thus, their corresponding homoleptic Ru(II) complexes could be synthesized, whereas it was difficult to prepare such complexes with the bulk **8-QPy** ligand.

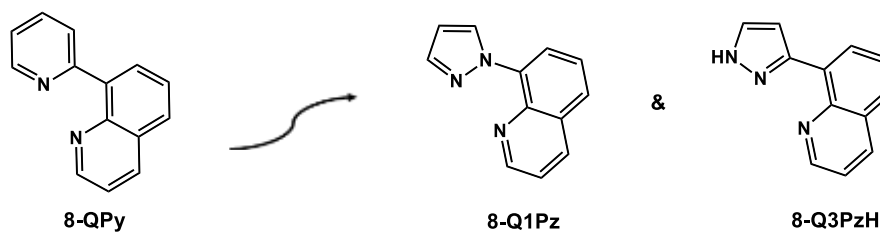


Figure 3.6. Chemical structures of quinoline ligand derivatives.

II. Synthesis

The new proposed **dtdpza (14)** ligand and its corresponding homoleptic ruthenium(II) complex (**15**), as well as the heteroleptic complex (**16**) which has one **dtdpza** ligand and one tpy ligand were prepared (Figure 3.3). Both of these complexes were fully characterized by $^1\text{H-NMR}$, $^{13}\text{C-NMR}$, 2D-NMR, mass spectrometry, and X-ray crystallography.

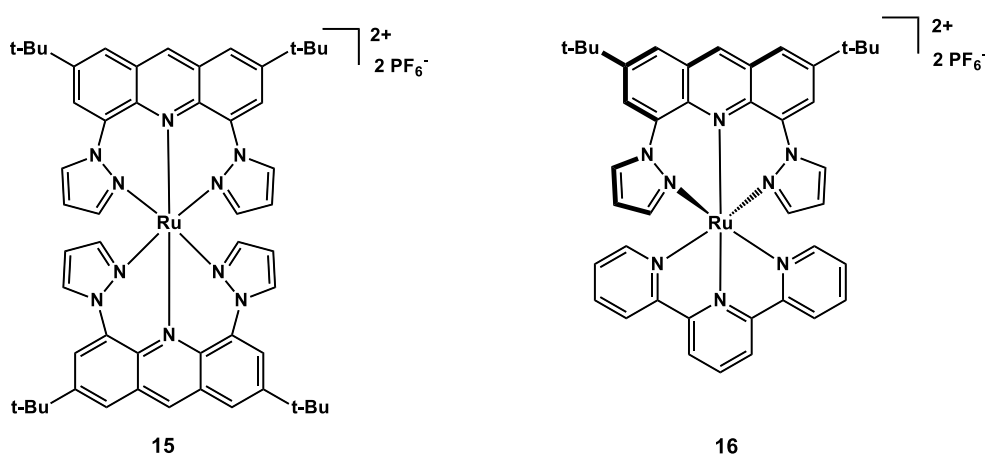
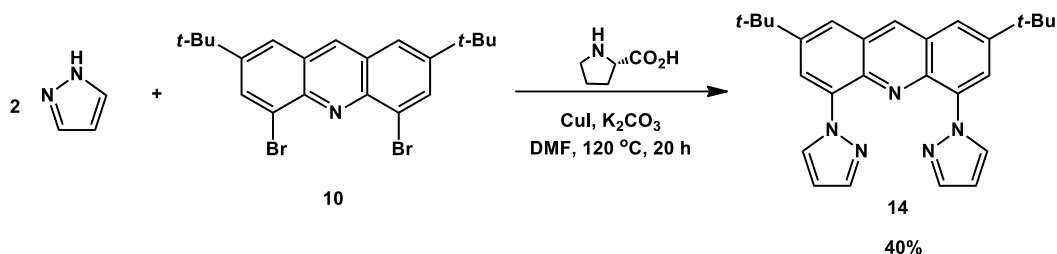


Figure 3.3. The corresponding Ru(II)-complexes of **dtdpza** ligand (**14**).

II.1. Ligand synthesis

The preparation of the new target ligand presented in Scheme 3.1 was fast and simple, in which one synthetic step was enough to have the new ligand starting from the previously prepared key intermediate **10**.^{4,5} The di-brominated compound undergoes Ullman-type amination with 1H-pyrazole heterocycle in the presence of copper(I) iodide and anhydrous potassium carbonate in dry dimethylformamide at 120 °C under argon atmosphere during an

overnight reaction. Following some modifications, the same protocols found in the literature dealing with 1H-pyrazole and different aromatic compounds coupling reactions were employed.^{3,6} As a result, the bright yellowish **dt dpza** (**14**) ligand was obtained with a 40% yield after purification *via* silica gel column chromatography (Scheme 3.1).



Scheme 3.1. dt dpza target ligand synthesis.

All the protons of **dt dpza** ligand **14** were assigned on the ¹H-NMR spectrum registered in deuterated acetone at 500 MHz NMR spectrometer, as shown in Figure 3.4 below.

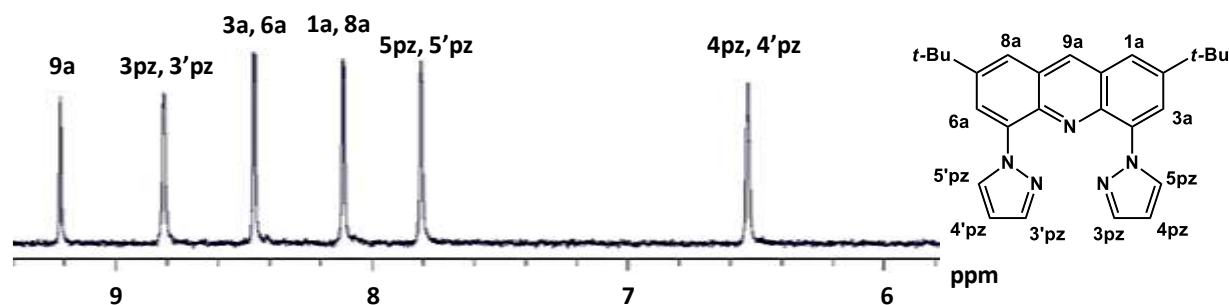


Figure 7.4. dt dpza ligand proton assignment on its ¹H-NMR spectrum, recorded in D-acetone at 500 MHz NMR spectrometer.

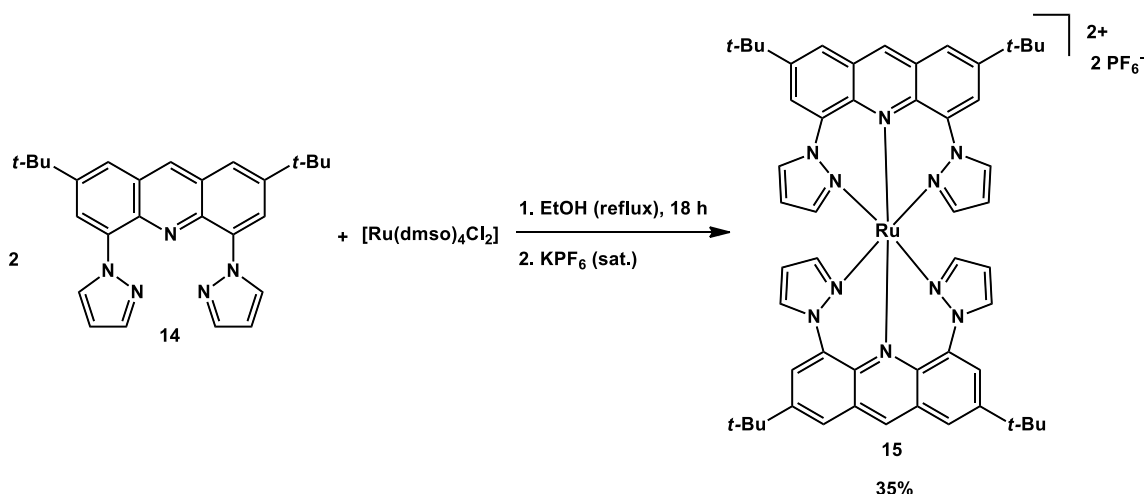
Lastly, after ¹H-NMR spectrum characterization, the obtained triimine ligand **14** was verified by ESI-mass spectrometry. In the spectrum, a mass peak at 424.2 with 1+ charge was detected, which matches with [M+H]⁺ (m/z calculated to be 424.3), in addition to the observation of a peak at m/z = 446.2 with 1+ charge, which matches with [M+Na]⁺ (m/z calculated to be 446.2).

II.2. Ru(II) complexes synthesis

II.2.1 Homoleptic Ru(II) complex

The Ru(II) homoleptic complex (**15**) composed of two **dtdpza** ligands was prepared. Refluxing a ratio of two to one of the di-pyrazole ligand to Ru(II) cation metal precursor in ethanol overnight lead to complexation (Scheme 3.2).

A light blue colored homoleptic complex was isolated in 35% yield after silica gel chromatography, followed by anion exchange using a saturated aqueous solution of KPF_6 , as shown in Scheme 3.2.



Scheme 3.2. Homoleptic complex **15** synthesis.

The molecular formula $[\text{Ru}(\text{dtdpza})_2](\text{PF}_6)_2$ of the obtained complex **15** was verified by ESI-mass spectrometry. In the spectrum, a mass peak at 474.2 with 2+ charge was detected, which matches with $[\text{Ru}(\text{dtdpza})_2]^{2+}$ (m/z calculated to be 474.2), in addition to the observation of a peak at $m/z = 1093.3$ with 1+ charge, which matches with $[\text{Ru}(\text{dtdpza})_2](\text{PF}_6)^+$ (m/z calculated to be 1093.4).

Complex **15** is the kinetic isomer, which still adopts the non-symmetrical *fac* geometry. The C_2 -*fac* geometry could be evidenced directly from the $^1\text{H-NMR}$ spectrum, as we see clearly in Figure 3.5, in which all of the proton signals in the spectrum of the symmetrical ligand **14** (bottom) were split into two sets of peaks in the homoleptic complex **15** spectrum (top).

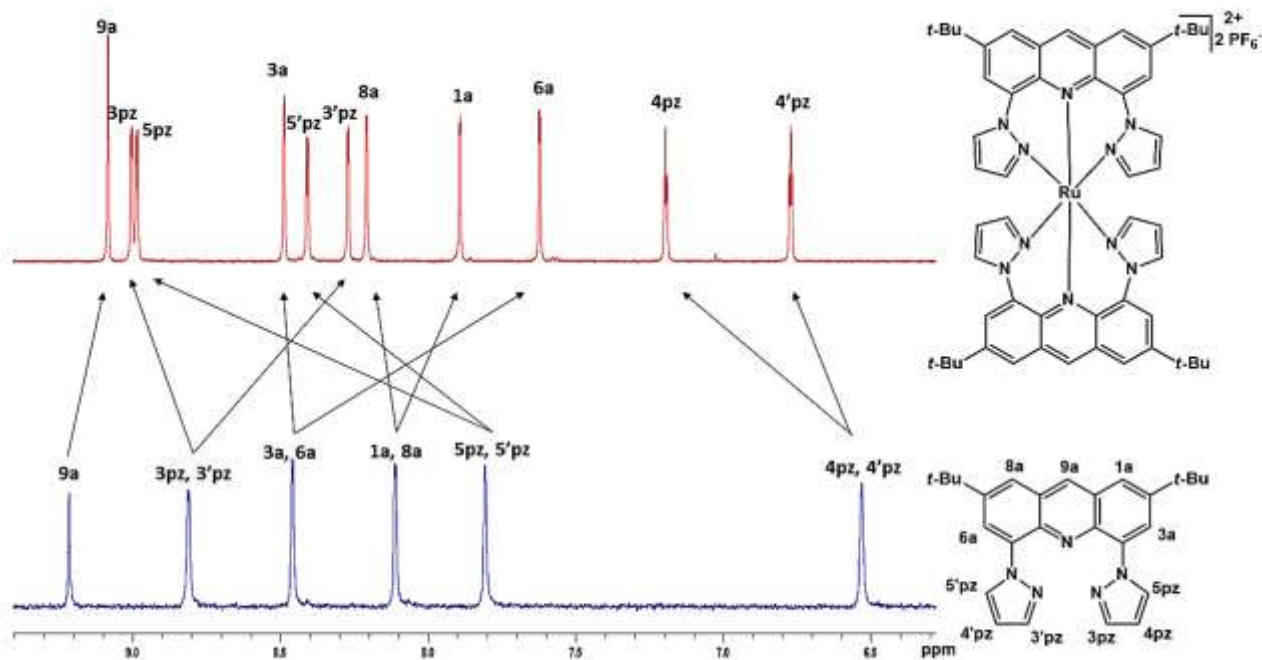


Figure 3.5. $^1\text{H-NMR}$ spectra of **dtdpza** ligand (bottom) and its homoleptic Ru(II) complex **15** (top), recorded in D-acetone at 500 MHz NMR spectrometer.

A strong nuclear overhauser effect (NOE) correlation between the 3pz and 3'pz protons for both pyrazole rings on the same **dtdpza** ligand can be observed clearly in the 2D-NOESY NMR (Figure 3.6).

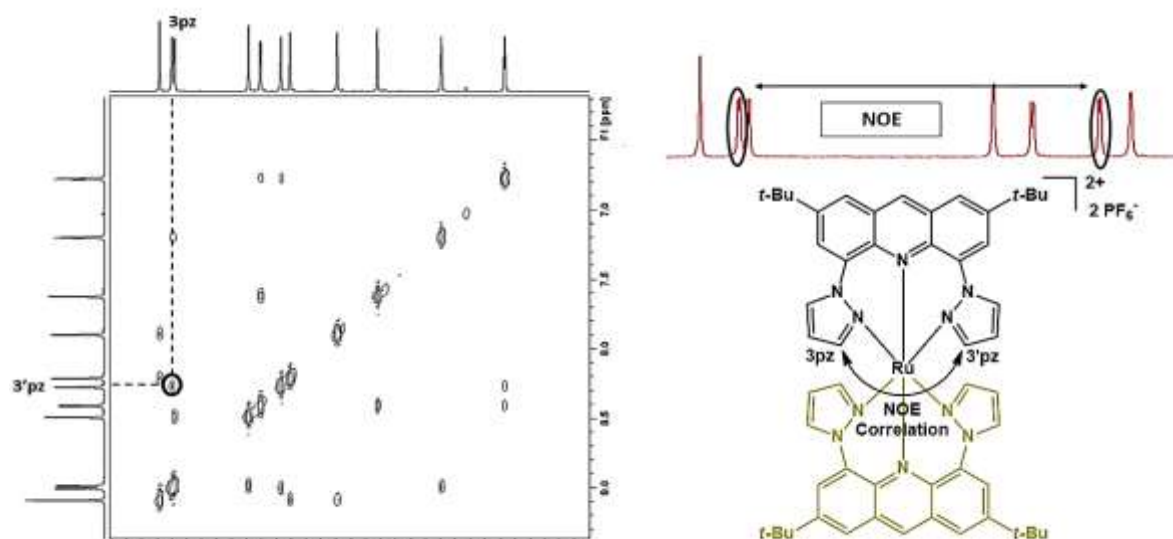


Figure 3.6. 2D-NOESY NMR spectrum (left) recorded in D-acetone at 500 MHz NMR spectrometer, in addition to a view of the crystal structure (right) of the homoleptic complex **15** (40% ellipsoids).

The result obtained from 2D-NOESY NMR, indicates the presence of both rings in a *cis* position relative to each other and confirms the *facial-gauche* (C_2 -*fac*) geometry of complex **15**.

In addition to the conclusions obtained from $^1\text{H-NMR}$ and 2D-NOESY NMR spectra analysis, some single crystals of this complex were obtained by slow solvent evaporation of an acetone solution of complex **15**, and the proposed geometry was verified by X-ray diffraction crystallography (Figure 3.7).

Different perspectives where the coordinating atoms of the homoleptic complex **15** are labeled, are presented in Figure 3.7.

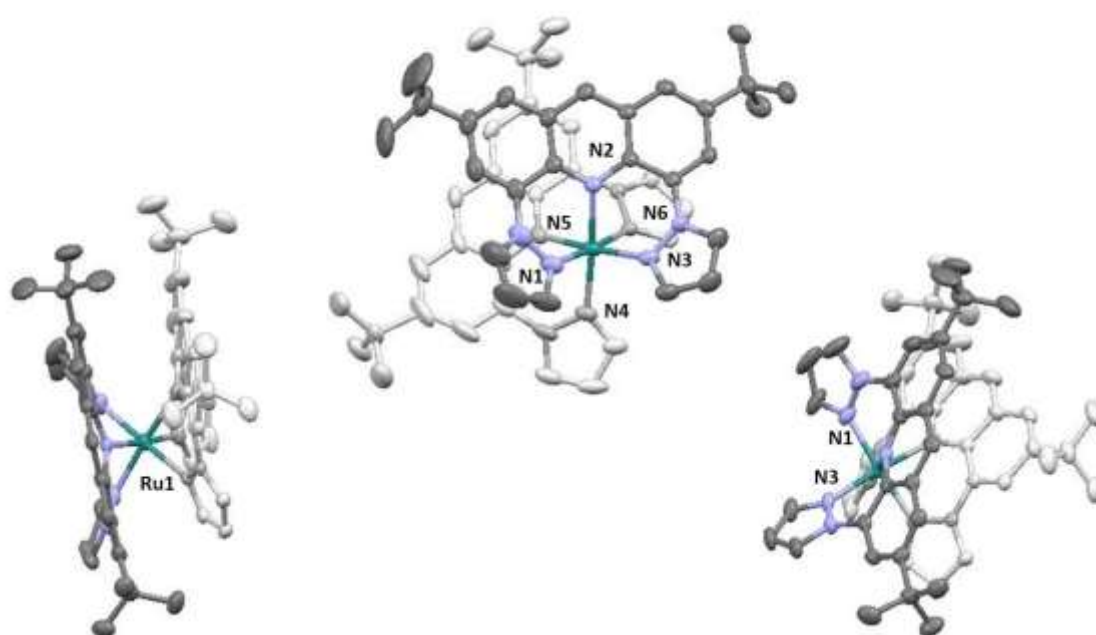


Figure 3.7. Different views of the crystal structure of complex **15** (40% ellipsoids). Solvent molecules, hydrogen atoms, and PF_6^- counter anion are omitted for clarity.

As shown clearly from the different views of the crystal structure of complex **15** in Figure 3.7, the two pyrazole rings of the same ligand are present in a *cis* position with respect to the Ru(II) metal center with an approximate angle of 93° (justifying the NOE correlation between 3pz and 3'pz protons). In addition, both acridine scaffolds are present in a *cis* position relative to each other with an approximate $\text{N}_{\text{acridine}}\text{-Ru}^{\text{II}}\text{-N}_{\text{acridine}}$ angle of 92.9° . As a result, this shows clearly the non-symmetrical *fac* geometry of complex **15**.

All of the selected angles and bond lengths of the complex are collected in Table 3.1.

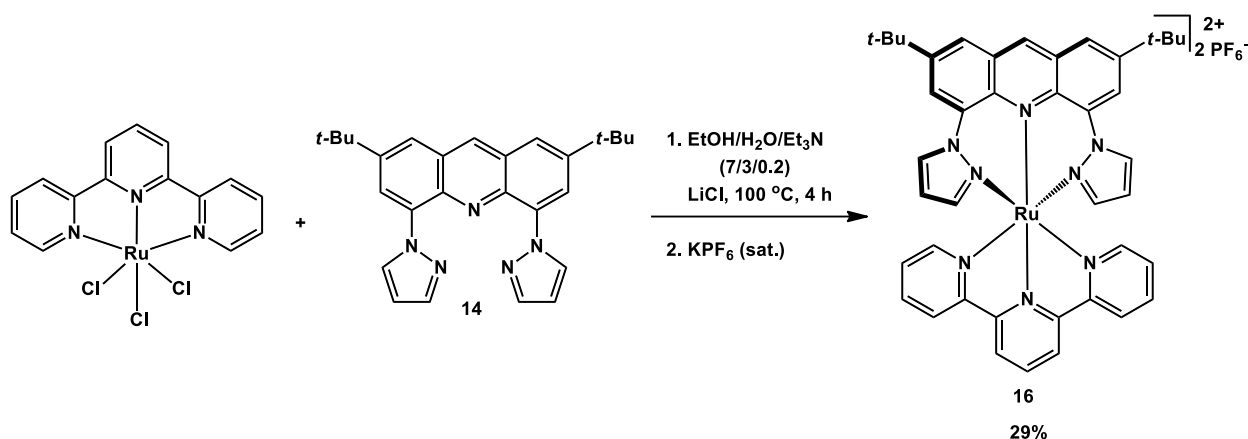
Table 3.3. The homoleptic complex (**15**) [Ru(**dtdpza**)₂](PF₆)₂ selected bond angles and lengths.

Bond angle (°)		Bond length (Å)	
N1 Ru1 N2	85.2(17)	Ru1 N1	2.044(4)
N2 Ru1 N3	85.9(2)	Ru1 N2	2.047(5)
N1 Ru1 N3	93.9(19)	Ru1 N3	2.047(5)
N5 Ru1 N4	85.9(19)	Ru1 N4	2.036(5)
N5 Ru1 N6	85.0(18)	Ru1 N5	2.054(4)
N4 Ru1 N6	93.5(2)	Ru1 N6	2.047(5)
N2 Ru1 N5	92.9(18)		

II.2.2. Heteroleptic Ru(II) complex

As indicated by the characterization of the homoleptic Ru(II) complex **15** based on **dtdpza** ligand in the *fac* geometry (analogous to our findings with the homoleptic [Ru(**dtdpa**)₂]²⁺ complex **12** described in the previous chapter), the preparation of the heteroleptic complex **16** is mandatory to force **dtdpza** to coordinate in a *meridional* octahedral geometry.

The heteroleptic complex **16** which is composed of one **dtdpza** (**14**) ligand and one tpy ligand was prepared. A mixture of one to one molar equivalent ratio of **dtdpza** ligand and [Ru(tpy)(Cl)₃] precursor was refluxed at 100 °C in the presence of lithium chloride salt in ethanol/water (70%/30%) solution for four hours. A pure blue colored heteroleptic complex **16** was isolated in 29% yield as a hexafluorophosphate salt after silica gel chromatography purification followed by anion exchange using a saturated aqueous solution of KPF₆ (Scheme 3.3).



Scheme 3.3. Heteroleptic complex **16** synthesis.

The heteroleptic Ru(II) complex **16** with the following molecular formula [Ru(**dtdpza**)(tpy)](PF₆)₂ was characterized by ESI-mass spectrometry. In the spectrum, a mass peak at $m/z = 379.07$ with 2+ charge was detected, which matches with [Ru(**dtdpza**)(tpy)]²⁺ (m/z calculated to be 379.12).

The symmetrical nature of the heteroleptic complex (*mer* octahedral geometry) was clearly deduced from its ¹H-NMR spectrum, as shown in Figure 3.8, and then was verified by X-ray diffraction crystallography.

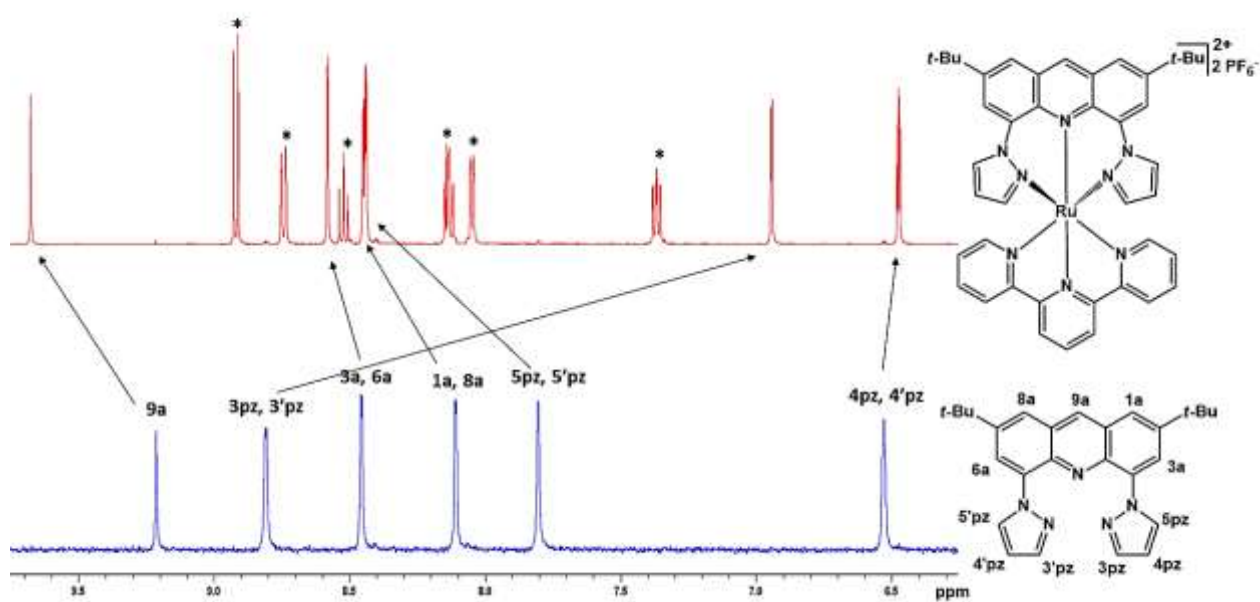


Figure 3.8. ¹H-NMR spectrum of both **dtdpza** (**14**) ligand (bottom) and its corresponding heteroleptic Ru(II) complex (**16**) (top), recorded in D-acetone at 500 MHz NMR spectrometer.

As shown in Figure 3.8, all the protons of **dtdpza** ligand (bottom), which correspond to half of the molecule, only undergo a change of their chemical shifts following the heteroleptic complexation reaction (top). This is in contrast to what was observed before with the *fac* homoleptic complexation reaction where the peaks were split for complex **15**. All peaks which are denoted with a star correspond to the facing tpy ligand.

Moreover, the NOE correlated 3pz and 3'pz protons with 9.0 and 8.27 ppm chemical shifts, respectively in the homoleptic complex **15**, were isochronous with a clear upfield shift in the NMR spectrum of the heteroleptic complex **16** at 6.94 ppm. This upfield shift is due to the shielding effect of the tpy ligand which is facing the corresponding **dtdpza** ligand.

Slow diethylether vapor diffusion into an acetonitrile solution of the heteroleptic complex **16** allowed to grow suitable single crystals of crystallographic quality. Afterwards, an X-ray diffraction was carried out and verified the *mer* octahedral geometry of this complex.

Different complex structure orientations in space with coordinating atoms labeled are illustrated in Figure 3.9. The selected bond angles and bond lengths (as well as for $[\text{Ru}(\text{tpy})_2](\text{PF}_6)_2$ for comparison as a reference complex) are noted in Table 3.2.

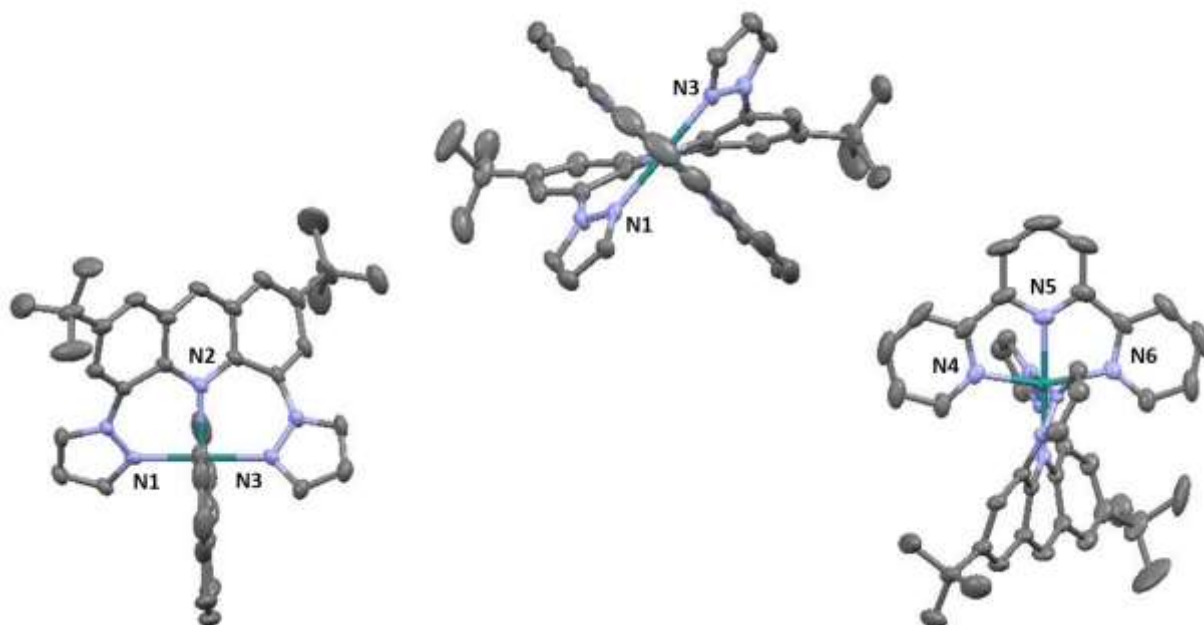


Figure 3.9. Different views of the crystal structure of complex (**16**) $[\text{Ru}(\text{dtdpza})(\text{tpy})](\text{PF}_6)_2$ (40% ellipsoids). Solvent molecules, hydrogen atoms, and the PF_6^- counter anions are omitted for clarity.

In addition to verifying the *mer* geometry by X-ray diffraction, it is also clear from Figure 3.9 and Table 3.2 that the **dtdpza** ligand was coordinated in a nearly perfect octahedral geometry with the central Ru(II) metal. A 178.9° $N_{\text{pyrazole}}\text{-Ru-}N_{\text{pyrazole}}$ trans angle was formed between the two pyrazole rings, in addition to 88.9° and 90.5° $N_{\text{acridine}}\text{-Ru-}N_{\text{pyrazole}}$ angles forming the 6-membered metallacycles. Moreover, the nitrogen atom of the acridine platform and the nitrogen atom of the central pyridine ring of tpy ligand were linearly coordinated to Ru(II) metal, with a 179.8° $N_2\text{-Ru-}N_5$ trans angle.

It seems from the crystal structure, that tpy ligand coordinates closer to the Ru(II) metal in complex **16** with respect to its parent complex $[\text{Ru}(\text{tpy})_2]^{2+}$. The bond length between Ru(II) metal and the central pyridine ring of the tpy ligand (Ru-N5) was reduced by 0.028 \AA . Thus, that explains the opening of the $N_4\text{-Ru-}N_6$ trans angle of tpy ligand by around 1.4° with respect to its parent complex.

Table 3.2. Illustration of the main bond angles and bond lengths of the heteroleptic complex (**16**) $[\text{Ru}(\text{dtdpza})(\text{tpy})](\text{PF}_6)_2$, as well as for the reference $[\text{Ru}(\text{tpy})_2](\text{PF}_6)_2$ complex.

Complex	$[\text{Ru}(\text{dtdpza})(\text{tpy})](\text{PF}_6)_2$	$[\text{Ru}(\text{tpy})_2](\text{PF}_6)_2$
Angle ($^\circ$)		
N1 Ru1 N2	88.9(18)	
N2 Ru1 N3	90.5(18)	
N1 Ru1 N3	178.9(19)	
N5 Ru1 N4	79.9(2)	79.5(3)
N5 Ru1 N6	79.9(2)	79.0(3)
N4 Ru1 N6	159.8(2)	158.4(3)
N2 Ru1 N5	179.8(2)	
Bond length (\AA)		
Ru1 N1	2.034(5)	
Ru1 N2	2.101(5)	
Ru1 N3	2.041(5)	
Ru1 N5	1.953(5)	1.981(7)
Ru1 N4	2.074(5)	2.079(6)
Ru1 N6	2.076(5)	2.067(7)

Lastly, as an unexpected result, even with a bigger coordinating cavity using smaller pyrazole rings, an important twisting of the planar acridine backbone was also observed in the crystal structure of complex **16**. The rigid **dt dpza** ligand, was forced to twist with an angle around 35° in order to coordinate with the Ru(II) cation (which is similar to that observed previously at the level of **dt dpa** ligand in complex **13**).

III. Electrochemistry

The electrochemical redox properties of the **dt dpza** ligand and its corresponding Ru(II) complexes, **15** and **16** respectively, were investigated by cyclic voltammetry in a deaerated acetonitrile solution in the presence of 0.1 M tetrabutylammonium hexafluorophosphate as a supporting electrolyte (Figure 3.10 and 3.11).

All the obtained redox peak potentials of these different compounds (in addition to the redox potentials of the previously reported **dt dpa** ligand with its complexes (**12** and **13**), in gray) are collected in Table 3.3 below, and were analyzed based on comparison to the reported parent [Ru(tpy)₂]²⁺ complex as a reference.⁸

Table 3.3. Redox potentials of **dtdpza** ligand (in black) and **dtdpa** ligand (in gray), in addition to their corresponding homoleptic (**12**, **15**) and heteroleptic (**13**, **16**) complexes with the parent $[\text{Ru}(\text{tpy})_2]^{2+}$ complex. $E_{1/2}$ (V) = $(E_{\text{pa}} + E_{\text{pc}})/2$, (ΔE_p) (mV) = $E_{\text{pc}} - E_{\text{pa}}$ vs $\text{Ag}^+(0.01 \text{ M})/\text{Ag}$. *Irreversible process.

Compounds	$E_{1/2}$ Reduction (ΔE_p , mV)		$E_{1/2}$ Oxidation (ΔE_p , mV)	
$[\text{Ru}(\text{tpy})_2]^{2+}$	-1.83 (70)	-1.57 (60)	0.97 (80)	
$[\text{Ru}(\text{tpy})(\text{dtdpa})]^{2+}$ (13)	-2.38*	-2.28*	-1.78 (70)	-1.22*
$[\text{Ru}(\text{tpy})(\text{dtdpza})]^{2+}$ (16)	-2.40*	-2.30*	-1.74 (80)	-1.22*
$[\text{Ru}(\text{dtdpa})_2]^{2+}$ (12)		-1.63*		-1.11*
$[\text{Ru}(\text{dtdpza})_2]^{2+}$ (15)		-1.51*		-1.06*
dtdpa (11)		-2.43*	-1.90 (60)	1.14*
dtdpza (14)		-2.47*	-1.80 (70)	1.12*
tpy ⁹	-2.95	-2.36		

All the anodic potentials are assigned to the oxidation processes from the HOMO which is mainly localized on the central ruthenium metal ($\text{Ru}^{3+}/\text{Ru}^{2+}$) for both complexes at the localized orbitals approximation.¹⁰ Whereas, for the ligand it may refer to the oxidation process on the highly π -conjugated acridine scaffold.¹¹ The peak potentials in the negative region correspond to the reduction processes on the orbitals which are localized on the different ligands (**dtdpza** and **tpy** ligands).

Consequently, the energy gap between the HOMO (t_{2g}) and LUMO (π^* -orbital) corresponds to the measured energy difference between the first oxidation and first reduction potentials respectively, and therefore, this measured energy difference would be linearly correlated to the expected energy needed for the $^1\text{MLCT}$ transition.

III.1. Redox properties of dtdpza ligand

The cyclic voltammogram of **dtdpza** ligand (**14**) is presented in Figure 3.10 below.

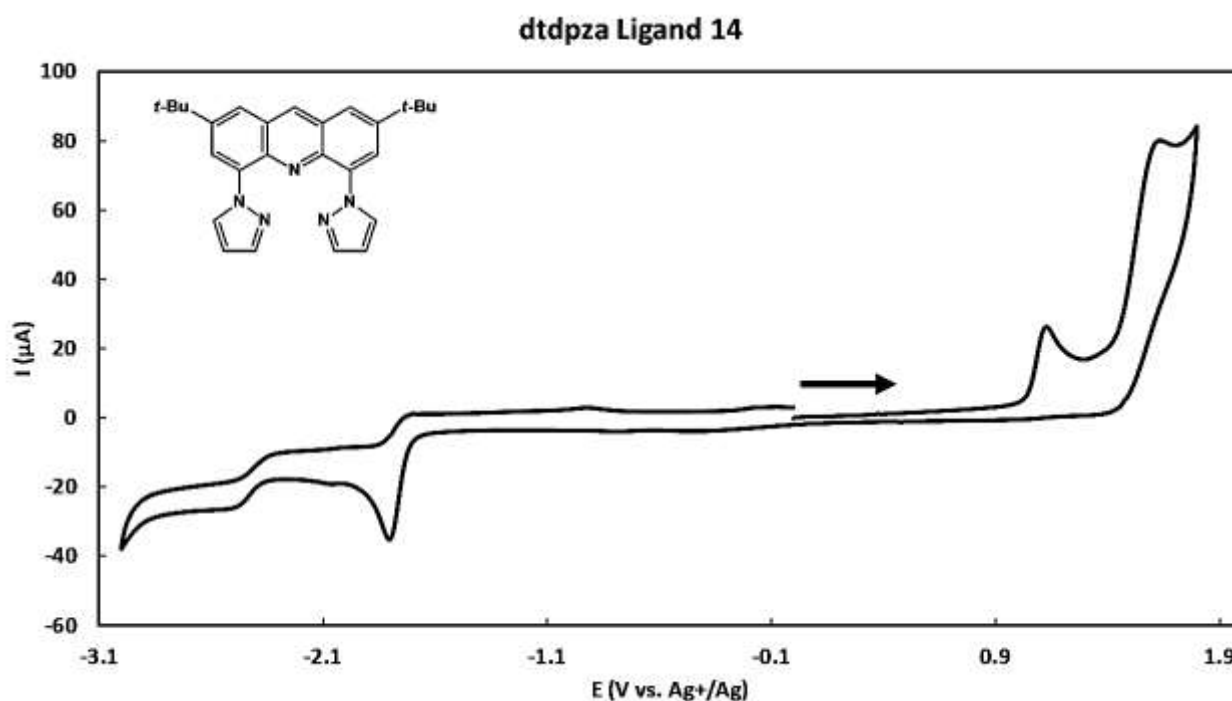


Figure 3.10. Cyclic voltammogram of **dtdpza** ligand in a 10^{-3} M deaerated acetonitrile solution + 0.1 M $[\text{BuN}]_4\text{PF}_6$ (TBAPF₆), at a scan rate of 100 mV s^{-1} using vitreous carbon electrode (5 mm diameter), $E_p(\text{V})$ vs AgNO_3 (0.01 M)/Ag.

From Figure 3.10, we can see that the **dtdpza** free ligand **14** has two successive irreversible oxidation peaks in the same range as the **dtdpa** free ligand **11**, at 1.12 V and 1.62 V. These could occur at the most conjugated acridine part, as has been discussed in the previous chapter.¹¹ Oxidation process occurs from the nitrogen electrons lone pair of the acridine to

give acridinium, in which these processes are irreversible due to the high reactivity of the formed acridinium with another acridine and form the dimer.¹²

Moreover, successive reversible and irreversible reduction peaks were observed in the cathodic part of **dtdpza** ligand cyclic voltammogram, at -1.8 V and -2.47 V respectively, to likely give the acridane compound (similar to what was proposed with **dtdpa** ligand **11**). The first reduction process of the ligand **14** relative to ligand **11** indicates the greater degree of electron withdrawing effect of pyrazole rings in such **dtdpza** ligand (**14**). Therefore, ligand **14** is reduced at higher potential and consequently, it has a lowest π^* -orbital. Moreover, these reduction potentials are less negative than those obtained for tpy ligand and therefore, ligand **14** has a more stabilized LUMO with respect to that of tpy ligand.

III.2. Redox properties of the Ru(II) complexes

The cyclic voltammograms of **dtdpza** Ru(II) complexes (**15** and **16**) are presented in Figure 3.11 below.

As expected, we can see from Figure 3.11, the Ru(II) complexes (**15**, **16**) show the same behavior in cyclic voltammetry as what was observed before with the Ru(II) complexes (**12**, **13**) with **dtdpa** (due to these complexes having the same geometrical coordination environment and especially the same acridine backbone twisting angle for their heteroleptic complexes). Thus, the distorted *facial-gauche* geometry of the homoleptic complex (**15**) $[\text{Ru}(\text{dtdpza})_2]^{2+}$, as well as the acridine twisted *meridional* geometry of the heteroleptic complex (**16**) $[\text{Ru}(\text{dtdpza})(\text{tpy})]^{2+}$ (with a 60° torsion angle between acridine backbone and the central pyridine ring of tpy ligand) may result in non-efficient π -back bonding between the hybrid orbitals of the central ruthenium metal (d_{xz} and d_{yz}) and their corresponding π -system. As a result, an important hindrance of the retrodonation from the metal center to the ligands is present, and consequently, an easy oxidation from the electron rich central metal and easy reduction on the electron poor ligands are obtained.

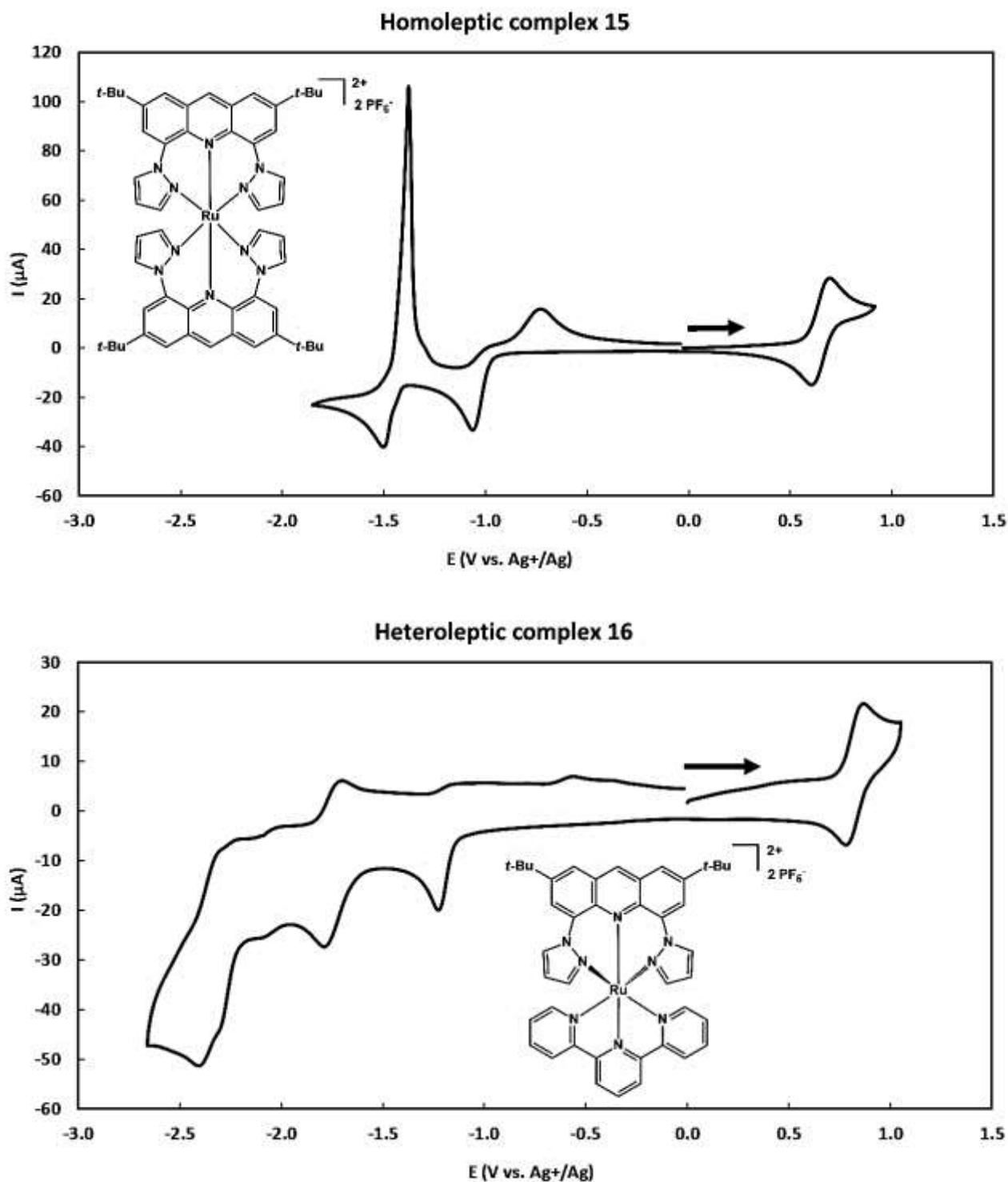


Figure 3.11. Cyclic voltammograms of the homoleptic complex **15** (top), and the heteroleptic complex **16** (bottom) in a 10^{-3} M deaerated acetonitrile solution + 0.1 M $[\text{BuN}]_4\text{PF}_6$ (TBAPF₆), at a scan rate of 100 mV s^{-1} using vitreous carbon electrode (5 mm diameter), $E_p(\text{V})$ vs AgNO_3 (0.01 M)/Ag.

III.2.1. Oxidation process

The influence of **dt dpza** ligand **14** on the oxidation potential of Ru(II) metal was analyzed, based on comparison to the $[\text{Ru}(\text{tpy})_2]^{2+}$ reference complex and the Ru(II) complexes (**12**, **13**) with the **dt dpza** ligand. The heteroleptic Ru(II) complex $[\text{Ru}(\text{dt dpza})(\text{tpy})]^{2+}$ **16** shows a monoelectronic reversible oxidation potential at $E_{1/2} = 0.82$ V with a 60 mV ΔE_p (same as complex **13**), thus **dt dpza** ligand lowers the oxidation potential of the central metal on complex **16** by 150 mV when one tpy ligand was replaced by one **dt dpza** ligand. Furthermore, when the second tpy was also substituted by another **dt dpza** to create the homoleptic complex (**15**) $[\text{Ru}(\text{dt dpza})_2]^{2+}$ the oxidation potential dropped furthermore by 180 mV, to have a monoelectronic reversible process at $E_{1/2} = 0.64$ V (same as complex **12**), with a $\Delta E_p = 60$ mV. Therefore, the **dt dpza** ligand has the same redox effect as **dt dpza** ligand by increasing the electron density on the Ru(II) central metal to have lower oxidation potentials.

III.2.2. Reduction redox process

In the cathodic region of both complexes' cyclic voltammograms, several reduction peaks were obtained which are mainly localized on the π^* -orbital of the different ligands. The homoleptic complex $[\text{Ru}(\text{dt dpza})_2]^{2+}$ shows two irreversible peaks at -1.06 V and -1.51 V that are attributed to the successive monoelectronic reduction of each ligand. Thus, this shows the electronic communication between the ligands *via* the Ru(II) central metal. However, in the back wave, complex deposition on the working electrode was observed.

In an analogous way, the heteroleptic complex $[\text{Ru}(\text{dt dpza})(\text{tpy})]^{2+}$ shows an irreversible reduction peaks at -1.22 V which took place on the low lying π^* -orbital of **dt dpza** ligand, and a second monoelectronic reversible reduction peak potential was obtained at $E_{1/2} = -1.74$ V with a $\Delta E_p = 80$ mV, which is attributed to the reduction process occurring on the tpy ligand. Lastly, two partially overlapped reduction peaks at -2.30 V and -2.40 V were observed and attributed to the reduction process that occurs on both ligands.

IV. Photophysics

The photophysical properties of the **dtdpza** ligand as well as the corresponding heteroleptic and homoleptic Ru(II) complexes (**15** and **16**) were measured, and all the values are collected in Table 3.4.

The absorption and emission spectra of the free **dtdpza** ligand were recorded in acetonitrile ($C = 10^{-5}$ M) at room temperature and in a butyronitrile rigid matrix at 77 K, as shown in Figure 3.12, whereas Figure 3.13 displays the UV-visible absorption spectra of both homoleptic and heteroleptic complexes ($C = 10^{-5}$ M) in comparison to the reference $[\text{Ru}(\text{tpy})_2]^{2+}$ complex.

IV.1. Ligand spectroscopic properties

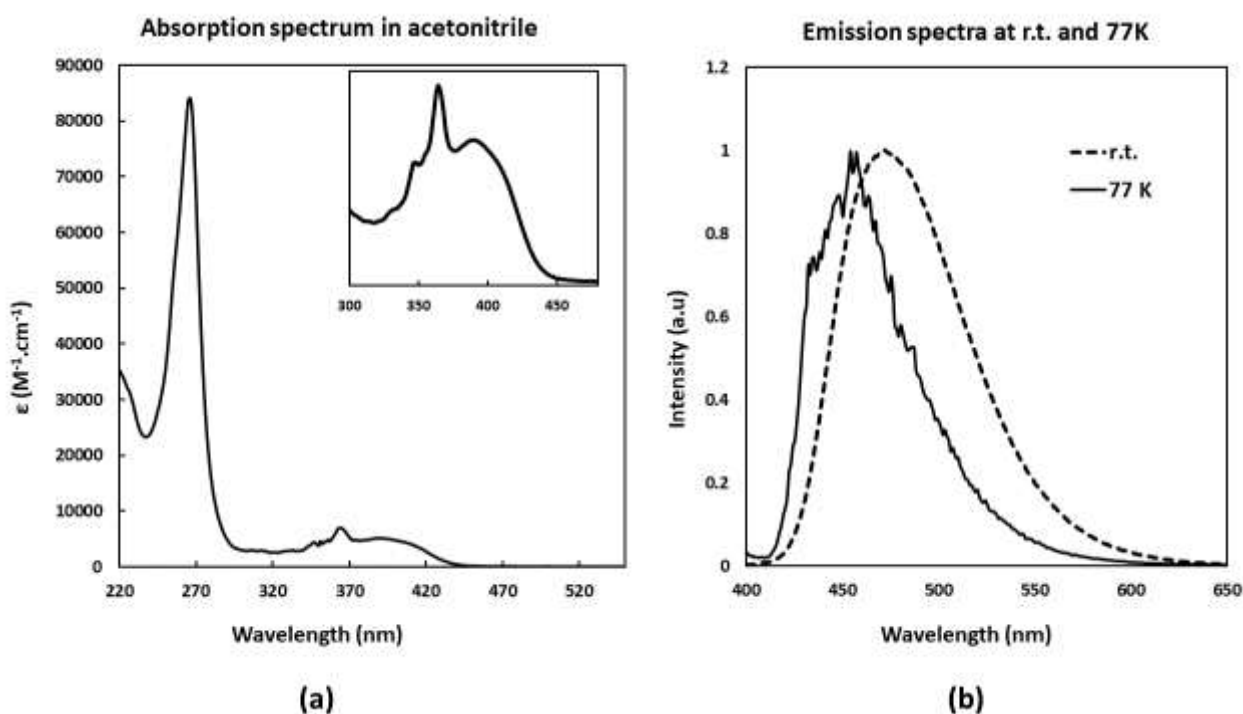


Figure 3.12. Absorption (a) and emission (b) spectra of the **dtdpza** ligand (**14**).

The **dtdpza** ligand displays a strong absorption in the UV region with a maximum centered at 266 nm, corresponding to a π - π^* transition, with a molar absorption coefficient of 8.4×10^4 $\text{M}^{-1}\text{cm}^{-1}$. Moreover, another broad absorption feature ranging from 328 nm to 450 nm was

observed, with a maximum centered at 364 nm of a molar absorption coefficient $9.3 \times 10^3 \text{ M}^{-1} \text{ cm}^{-1}$ (Figure 3.12, a). As explained in the previous chapter with ligand **11**, this moderately intense absorption could be attributed to the $n\text{-}\pi^*$ transition localized on the acridine platform,¹³ and not a charge transfer process between the acridine and pyrazole rings of the ligand.

A strong fluorescence emission with a maximum centered at 472 nm was detected for **dtdpza** ligand in deaerated acetonitrile solution at room temperature (after excitation at 364 nm), with a 5.1 ns excited state lifetime and 49% emission quantum yield. Furthermore, in a frozen rigid matrix of butyronitrile at 77 K with no solvent re-organization, the fluorescence emission (excited state energy) was blue shifted to 454 nm, with a longer excited state lifetime of 12.8 ns in comparison to the result obtained at room temperature (Figure 3.12, b).

IV.2. Ru(II) complexes spectroscopic properties

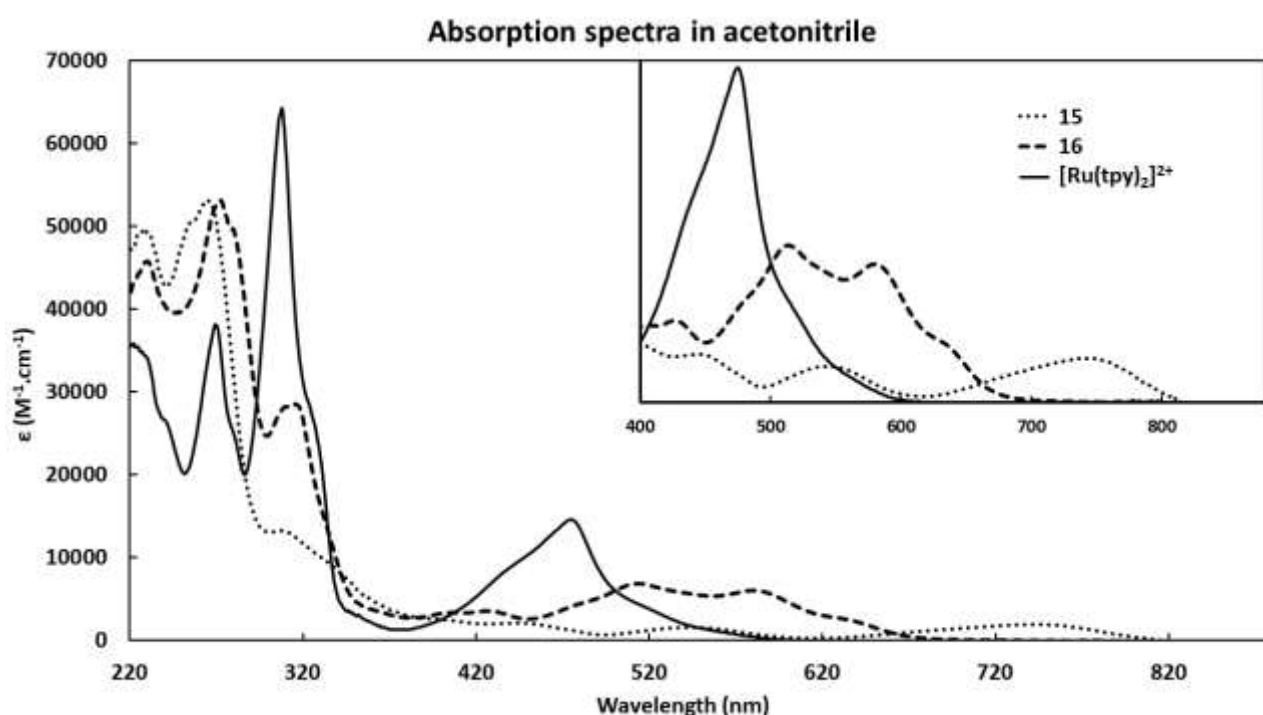


Figure 3.13. Absorption spectra of $[\text{Ru}(\text{dtdpza})_2]^{2+}$ **15** (dotted), $[\text{Ru}(\text{dtdpza})(\text{tpy})]^{2+}$ **16** (dashed), and $[\text{Ru}(\text{tpy})_2]^{2+}$ (full line) complexes in deaerated acetonitrile solution.

The spin-allowed ligand centered transition (LC) for both homoleptic and heteroleptic complexes (**15**, **16**), in addition to the parent $[\text{Ru}(\text{tpy})_2]^{2+}$ complex, were displayed in the UV region. The homoleptic $[\text{Ru}(\text{dtdpza})_2]^{2+}$ complex (dotted line) displays two intense $\pi\text{-}\pi^*$ transition bands in this range with maximum wavelengths centered at 228 nm and 265 nm, of a molar absorption coefficient $5.0 \times 10^4 \text{ M}^{-1} \text{ cm}^{-1}$ and $5.3 \times 10^4 \text{ M}^{-1} \text{ cm}^{-1}$ respectively, in addition to a moderately intense band at 307 nm of $1.3 \times 10^4 \text{ M}^{-1} \text{ cm}^{-1}$. These $\pi\text{-}\pi^*$ transitions are localized on the coordinated **dtdpza** ligand. The heteroleptic $[\text{Ru}(\text{tpy})(\text{dtdpza})]^{2+}$ complex (dashed line) displays three intense $\pi\text{-}\pi^*$ transition bands in the same region, centered at 229 nm, 272 nm, and 316 nm, with $\epsilon = 4.5 \times 10^4 \text{ M}^{-1} \text{ cm}^{-1}$, $5.3 \times 10^4 \text{ M}^{-1} \text{ cm}^{-1}$, and $2.8 \times 10^4 \text{ M}^{-1} \text{ cm}^{-1}$ respectively. The first two energetic bands could be attributed to the $\pi\text{-}\pi^*$ transition on the **dtdpza** ligand, whereas the third band at 315 nm is globally attributed to the transition on the terpyridine ligand (in the same range of ϵ as $[\text{Ru}(\text{tpy})_2]^{2+}$).

The metal to ligand charge transfer (MLCT) transition which is observed in the visible region is usually the transition responsible for ruthenium complexes emission, therefore it is of great importance. This $d_{(\text{M})}\text{-}\pi^*_{(\text{L})}$ transition is clearly red shifted in both complexes as compared to the reference $[\text{Ru}(\text{tpy})_2]^{2+}$ complex. This red shifting is rationalized by the small HOMO-LUMO energy gap in both complexes relative to the reference complex, in agreement with the obtained electrochemical data (lower metal oxidation potentials and higher ligand reduction potentials). The moderately intense MLCT absorption of the homoleptic complex **15** ranges from 500 nm till 820 nm, with two peak maxima at 540 nm (may refer to transition from Ru to pyrazole ring on the ligand) and 747 nm (may refer to transition from Ru to the lowest acridine π^* -orbital on the ligand). The molar absorption coefficient of these two maxima at MLCT band are $1.6 \times 10^3 \text{ M}^{-1} \text{ cm}^{-1}$ and $2.0 \times 10^3 \text{ M}^{-1} \text{ cm}^{-1}$ respectively. On the other hand, the heteroleptic complex **16** displays a blue shifted MLCT band in comparison to complex **15** and it is expanded from 450 nm to 750 nm, with two peak maxima at 514 nm and 580 nm and a molar absorption coefficient of $6.9 \times 10^3 \text{ M}^{-1} \text{ cm}^{-1}$ and $6.0 \times 10^3 \text{ M}^{-1} \text{ cm}^{-1}$ respectively. The higher energetic transition (514 nm) refers to the transition from the metal to the terpyridine ligand, and the second one (580 nm) refers to the transition from the metal to the lower π^* orbital energy localized on the **dtdpza** ligand.

Excitation of both $[\text{Ru}(\text{dtdpza})_2](\text{PF}_6)_2$ and $[\text{Ru}(\text{tpy})(\text{dtdpza})](\text{PF}_6)_2$ complexes at their $^1\text{MLCT}$ wavelengths, in the visible region, did not show any emission neither at room temperature in

acetonitrile nor at 77 K in a butyronitrile rigid matrix. This result can be rationalized for both geometrically distorted complexes with a very small HOMO-LUMO energy gap (as observed in the previous chapter). Thus, the $^1\text{MLCT}$ absorption bands is very low in energy. Consequently, the excited state is deactivated in non-radiative pathways according to energy gap law.

All the measured and collected spectroscopic data are illustrated in Table 3.4.

Table 3.4. Photophysical data of the **dtdpza** ligand in addition to the corresponding homoleptic and heteroleptic Ru(II) complexes (**15** and **16**) in acetonitrile solution.

Compounds	λ_{abs} , nm (ϵ , $\text{M}^{-1} \text{cm}^{-1}$)	Room temperature			77 K	
		λ_{em} , nm	ϕ	τ , ns	λ_{em} , nm	τ , ns
[Ru(dtdpza) ₂] ²⁺ (15)	228 (50,000), 265 (53,100), 307 (13,300), 404 (2,500), 448 (2,100), 540 (1,600), 747 (2,000)					
[Ru(tpy)(dtdpza)] ²⁺ (16)	229 (45,000), 272 (53,000), 316 (28,500), 405 (3,300), 427 (3,500), 514 (6,900), 580 (6,000)					
dtdpza (14)	266 (84,000), 347 (5,700), 364 (9,300), 389 (6,800)	472	0.49	5.1	454	12.8

V. Conclusion

Even with a larger coordination cavity due to the use of smaller pyrazole heterocycles, the pocket in the homoleptic and heteroleptic complexes **15** and **16** is still constrained, and not big enough to avoid ligand twisting of the acridine backbone in the heteroleptic complex. Also, the homoleptic complex with the **dt dpza** ligand still prefers the *fac* geometry. With such persistence of distorted octahedral geometries, the HOMO-LUMO gap energy is still small, resulting in a low lying $^1\text{MLCT}$ excited state, which consequently leads to non-emissive Ru(II) complexes according to energy gap law.

Therefore, maybe forming a 6-membered metallacycles with Ru(II) metal is closing the coordination cavity. Thus, another acridine-based ligand forming 5-membered metallacycles with a bigger coordination cavity (not like the *tpy* ones) could be a solution, by grafting simpler and smaller coordinating moieties on compound **10**.

VI. References

- (1) Jarenmark, M.; Fredin, L. A.; Hedberg, J. H. J.; Doverbratt, I.; Persson, P.; Abrahamsson, M. A Homoleptic Trisbidentate Ru(II) Complex of a Novel Bidentate Biheteroaromatic Ligand Based on Quinoline and Pyrazole Groups: Structural, Electrochemical, Photophysical, and Computational Characterization. *Inorg. Chem.* **2014**, *53*, 12778–12790.
- (2) Jarenmark, M.; Fredin, L. A.; Wallenstein, J. H.; Doverbratt, I.; Abrahamsson, M.; Persson, P. Diastereomerization Dynamics of a Bistridentate Ru(II) Complex. *Inorg. Chem.* **2016**, *55*, 3015–3022.
- (3) Wallenstein, J. H.; Fredin, L. A.; Jarenmark, M.; Abrahamsson, M.; Persson, P. Chemical Consequences of Pyrazole Orientation in Ru(II) Complexes of Unsymmetric Quinoline–pyrazole Ligands. *Dalton. Trans.* **2016**, *45*, 11723–11732.
- (4) Yamamoto, K.; Higashibayashi, S. Synthesis of Three-Dimensional Butterfly Slit-Cyclobisazaanthracenes and Hydrazinobisanthrenes through One-Step Cyclodimerization and Their Properties. *Chem. Eur. J.* **2016**, *22*, 663–671.
- (5) Desbois, N.; Szollosi, A.; Maisonia, A.; Weber, V.; Moreau, E.; Teulade, J.-C.; Chavignon, O.; Blache, Y.; Chezal, J. M. Simple and Convenient Conversion of Acridones into 9-Unsubstituted Acridines via Acridanes Using Borane Tetrahydrofuran Complex. *Tetrahedron Lett.* **2009**, *50* (49), 6894–6896.
- (6) Qichao, Y.; Yufang, W.; Baoji, Z.; Mingjie, Z. Direct N-Arylation of Azaheterocycles with Aryl Halides under Ligand-Free Condition. *Chin. J. Chem.* **2012**, *30*, 2389–2393.
- (7) Lashgari, K.; Kritikos, M.; Norrestam, R.; Norrby, T. Bis(Terpyridine) Ruthenium(II) Bis(Hexafluorophosphate) Diacetonitrile Solvate. *Acta Crystallogr. Sect. C* **1999**, *55*, 64–67.
- (8) Jacquet, M.; Lafolet, F.; Cobo, S.; Loiseau, F.; Bakkar, A.; Boggio-Pasqua, M.; Saint-Aman, E.; Royal, G. Efficient Photoswitch System Combining a Dimethyldihydropyrene Pyridinium Core and Ruthenium(II) Bis-Terpyridine Entities. *Inorg. Chem.* **2017**, *56* (8),

- 4357–4368.
- (9) Persaud, L.; Barbiero, G. Synthesis, Electrochemical and Spectroscopic Investigations of 2,2':4,4''-Terpyridine and 2,2':4,4'':6,2''-Quaterpyridine Ligands for Metal Complex Photoelectrochemistry. *Can. J. Chem.* **1991**, *69*, 315–321.
- (10) Juris, A.; Balzani, V.; Barigelletti, F.; Campagna, S.; Belser, P.; Von Zelewsky, A. Ru(II) Polypyridine Complexes: Photophysics, Photochemistry, Electrochemistry, and Chemiluminescence. *Coord. Chem. Rev.* **1988**, *84*, 85–277.
- (11) Pontinha, A. D. R.; Sparapani, S.; Neidle, S.; Oliveira-Brett, A. M. Triazole-Acridine Conjugates: Redox Mechanisms and in Situ Electrochemical Evaluation of Interaction with Double-Stranded DNA. *Bioelectrochemistry* **2013**, *89*, 50–56.
- (12) Marcoux, L.; Adams, R. N. ANODIC OXIDATION OF AROMATIC AZA HYDROCARBONS. *Electroanal. Chem. and Interfacial. Electrochem.* **1974**, *49*, 111–122.
- (13) Rak, J.; Blazejowski, J. Experimental and INDO CI Calculations of the Electronic Absorption Spectra of Acridine and 9-Acridinamine Free Bases and Their Protonated Forms with Regard to Tautomeric Phenomena. *J. Photochem. Photobiol. A Chem.* **1992**, *67*, 287–299.

Chapter 4: SNS-thioether acridine-based ligand and its Ru(II) complexes

I. Introduction

Following the results from the first two chapters, replacing the 6-membered pyridine rings by 5-membered pyrazole rings, at the 4 and 5 positions on the acridine platform, was not enough to enlarge the very tight metal coordination pocket. Thus, the *facial* octahedral geometry for the homoleptic Ru(II) complexes, in addition to the acridine backbone twisting for the heteroleptic Ru(II) complexes, with the 6-membered metallacycles, using the structurally rigid **dtdpa (11)** and **dtdpza (14)** ligands still required geometrical optimizations.

Therefore, the goal was to find other simpler and smaller coordinating moieties to be attached at the 4 and 5 positions of acridine in order to have a real flexible and large coordination cavity to avoid obtaining such geometrically distorted Ru(II) complexes. With this in mind, using the 5-membered metallacycles with Ru(II) metal to reduce the constraints on the coordination cavity, could be a suitable solution.

Among the polydentate ligands which coordinate to ruthenium metal, the most studied and known ligands do so through their nitrogen atoms¹, however, other ligands such as thioether coordinating moieties have been less studied, especially in photophysics.

Therefore, in this chapter, I have prepared and studied a set of complexes based on a new (SNS) tridentate thioether ligand with a larger coordination cavity, named **dtdsa (17)** (2,7-ditertbutyl-4,5-di(propylthio)acridine), as shown in Figure 4.1.

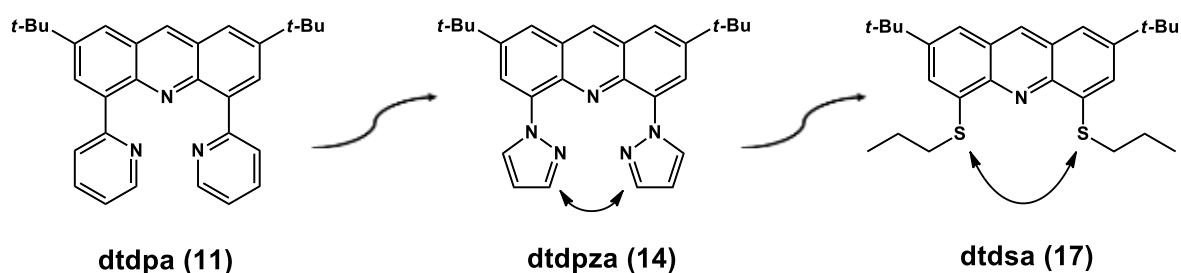


Figure 4.8. Opening the coordination pocket by using (SNS) thioether ligand **17** instead of (NNN) structurally rigid ligands, **11** and **14**.

This new thioether ligand will form 5-membered metallacycles with Ru(II) instead of the favorable 6-membered metallacycles. However, the presence of longer C-S bonds, which are

attached to the planar acridine heterocycle, provide a larger coordination cavity in comparison to that obtained for Ru(II)-bis-terpyridine complex.

II. Synthesis

The new proposed (SNS) thioether ligand **dtdsa** (**17**) was prepared successfully. Consequently, the corresponding homoleptic Ru(II) complex (**18**) which is composed of two **dtdsa** ligands, as well as the heteroleptic Ru(II) complex (**19**) which is built from one **dtdsa** ligand and one terpyridine ligand were also prepared, as shown in Figure 4.2.

Both complexes, in addition to the isolated **dtdsa** ligand were fully characterized by $^1\text{H-NMR}$ and $^{13}\text{C-NMR}$, as well as by mass spectrometry.

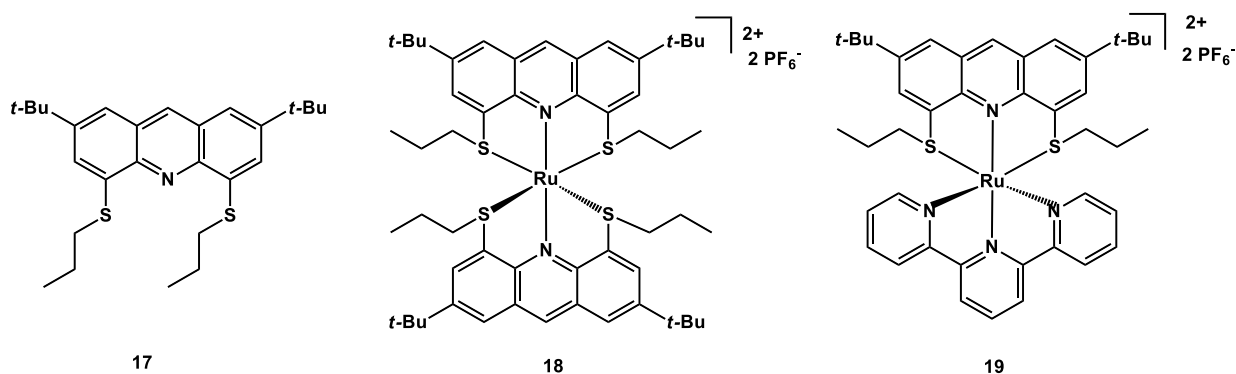
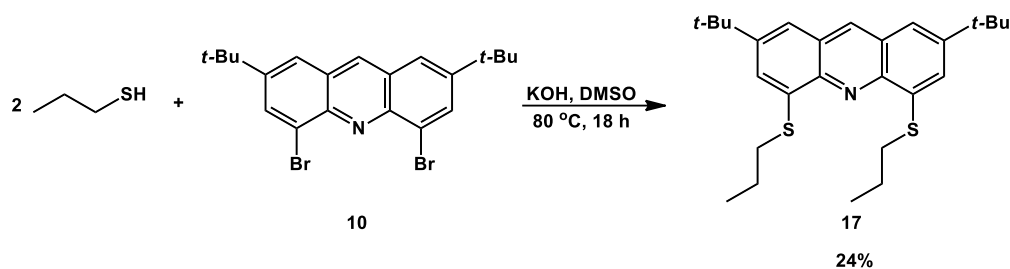


Figure 4.2. The **dtdsa** ligand (**17**) with its homoleptic (**18**) and heteroleptic (**19**) Ru(II)-complexes.

II.1. Ligand synthesis

Following the same protocols found in the literature, describing the preparation of different polydentate thioether ligands through a substitution reaction of different thiol reagents on different aromatic compounds,^{2,3} with some synthetic modifications, our new tridentate (SNS) thioether ligand **dtdsa** (**17**) was obtained directly through one synthetic step starting from the previously prepared key intermediate **10**,^{4,5} as it is shown in Scheme 4.1.



Scheme 4.1. The **dtdsa** target ligand (**17**) synthesis.

A strong nucleophilic 1-propanethiolate reagent was generated after heating a mixture of potassium hydroxide as a dry fine powder and 1-propanethiol in dry DMSO at 80 °C, under inert atmosphere. Then the di-brominated compound **10** undergoes a nucleophilic substitution at the bromine atoms by two molar equivalents of the obtained thiolate reagent. The final red-yellowish thioether ligand **17** was obtained with a 24% yield after silica gel column chromatography purification (a large fraction, 68%, of mono-substituted acridine side-product was obtained, even with excess use of thiol reagent, which explains the low reaction yield of ligand **17**). All the protons of the thioether ligand **17** were assigned on its ¹H-NMR spectrum in deuterated chloroform solution at 500 MHz NMR spectrometer, as shown in Figure 4.3 below.

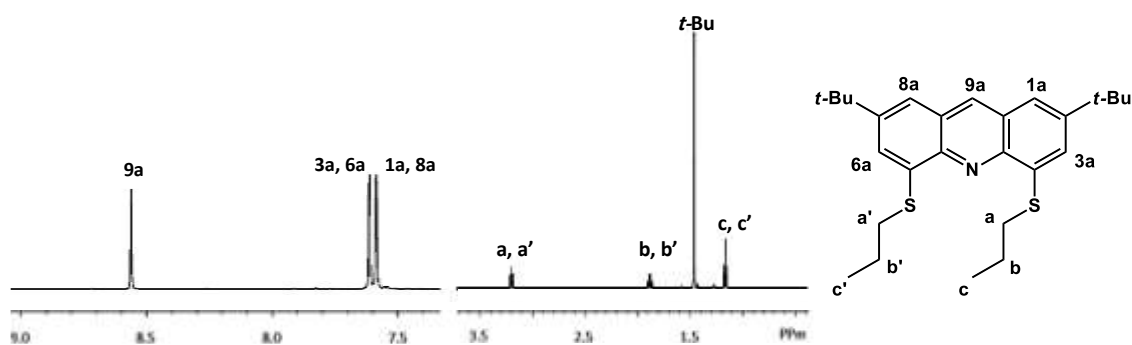


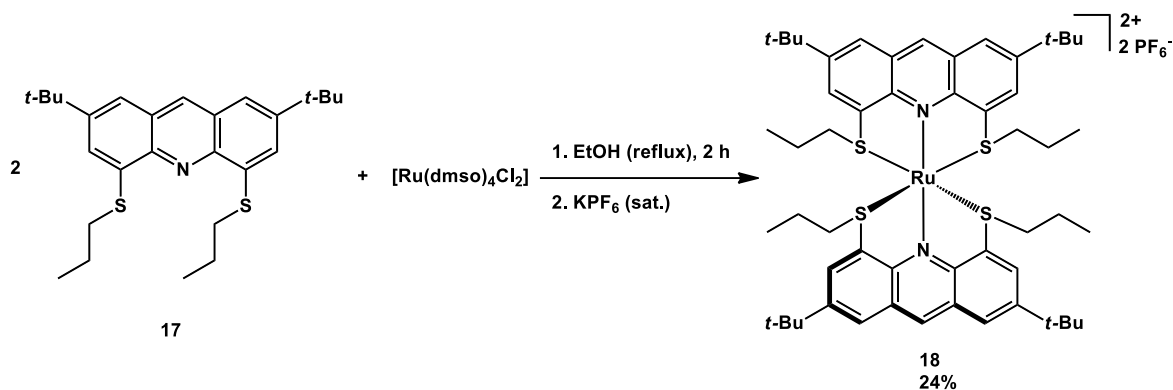
Figure 4.3. ¹H-NMR spectrum assignment of **dtdsa** (**17**) ligand, recorded in CDCl₃ solution at 500 MHz NMR spectrometer.

The obtained (SNS) thioether ligand **17** was verified by ESI-mass spectrometry. In the ESI mass spectrum, a mass peak at $m/z = 440.2$ with 1+ charge was detected, which matches exactly with $[\text{M}+\text{H}]^+$ (m/z calculated to be 440.2).

II.2. Ru(II) complexes synthesis

II.2.1. Homoleptic Ru(II) complex

The homoleptic Ru(II) complex **18**, which is composed of two **dtdsa** (**17**) ligands was prepared by refluxing a ratio of two to one of the thioether ligand **17** to $[\text{Ru}(\text{dms})_4\text{Cl}_2]$ precursor in dry ethanol, for 2 hours (Scheme 4.2).



Scheme 4.2. The homoleptic Ru(II) complex **18** synthesis.

A bright orange powder corresponding to complex **18** with a molecular formula $[\text{Ru}(\text{dtdsa})_2](\text{PF}_6)_2$ was obtained in 24% yield after a silica gel chromatography purification followed by anion exchange with a saturated aqueous solution of potassium hexafluorophosphate (KPF_6).

ESI mass spectrometry confirmed the molecular formula of the homoleptic complex **18**. In the spectrum, a mass peak at $m/z = 490.20$ with 2+ charge was detected, which matches with $[\text{Ru}(\text{dtdsa})_2]^{2+}$ (m/z calculated to be 490.19), in addition a peak of $m/z = 1125.30$ with 1+ charge was detected, which matches with $[\text{Ru}(\text{dtdsa})_2](\text{PF}_6)^+$ (m/z calculated to be 1125.34).

Unlike the distorted octahedral geometry of the previously prepared homoleptic complexes **12** and **15**, the newly prepared homoleptic complex **18** adopts a *meridional* octahedral geometry. In this complex, the rigid thioether ligand **17**, with long C-S bonds and a large coordination cavity, coordinates the Ru(II) cation in a symmetrical fashion. This symmetrical coordination was confirmed by $^1\text{H-NMR}$ spectrum, as shown in Figure 4.4, in which the

thioether ligand displays signals corresponding to half of the molecule (no signal splitting appeared, as had been shown in the previous two chapters).

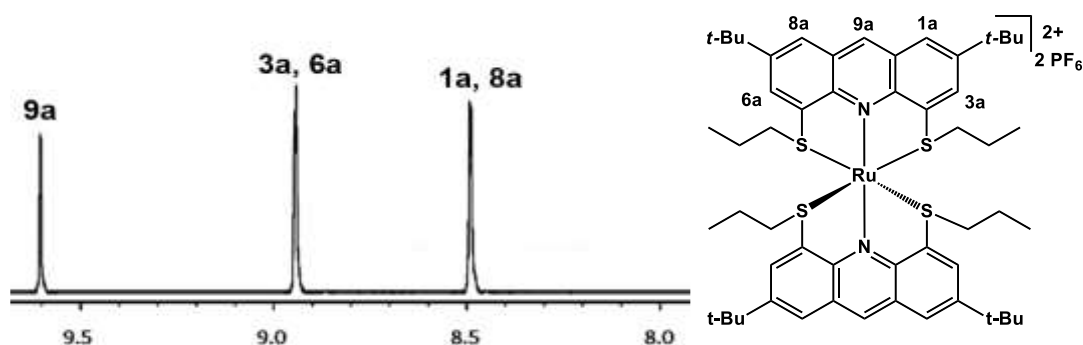


Figure 4.4. Aromatic region in ^1H -NMR spectrum of the homoleptic Ru(II) complex **18**, recorded in D-acetone solution at 500 MHz NMR spectrometer.

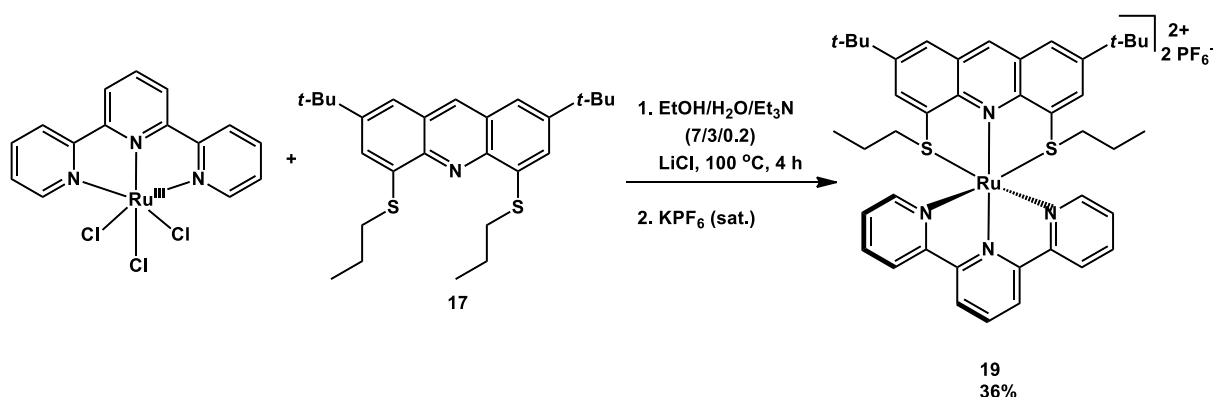
Moreover, no nuclear overhauser effect (NOE) correlation was observed between the propyl groups in the aliphatic region of the complex **18** (unlike the correlation observed before between the *cis*-positioned pyridine rings and pyrazole rings, shown in the previous two chapters respectively). Therefore, from the NMR analysis, it is clear that the complex does not adopt a *fac* geometry, so all of these analyses indicate the *meridional* octahedral geometry of the homoleptic complex **18**.

II.2.2. Heteroleptic Ru(II) complex

In addition to the fact that this new (SNS) thioether ligand coordinates to give the *mer* homoleptic complex **18** (unlike the first two (NNN) triimine ligands **11** and **14**, which formed *fac* homoleptic isomers), the heteroleptic complex **19**, which is composed of one **dtDSA** ligand and one terpyridine ligand, was prepared as a matter of comparison and not to force the *mer* coordination as for the previously prepared ligands.

Refluxing a one-to-one molar equivalent ratio of the thioether ligand **17** and the ruthenium precursor $[\text{Ru}(\text{tpy})\text{Cl}_3]$ for 4 hours in the presence of excess lithium chloride salt in an ethanol/water (70%/30%) solution lead to the desired heteroleptic complex. The obtained dark blue colored heteroleptic complex **19** was isolated in 36% yield as a pure

hexafluorophosphate salt after silica gel column chromatography followed by anion exchange using a saturated aqueous solution of KPF_6 , as shown in Scheme 4.3.



Scheme 4.3. The heteroleptic Ru(II) complex **19** synthesis.

The heteroleptic Ru(II) complex **19** with the following molecular formula, $[\text{Ru}(\text{dtDSA})(\text{tpy})](\text{PF}_6)_2$, was characterized by ESI-mass spectrometry. In the spectrum, a mass peak at $m/z = 387.14$ with 2+ charge was detected, which matches with $[\text{Ru}(\text{dtDSA})(\text{tpy})]^{2+}$ (m/z calculated to be 387.12).

The symmetric coordination of this heteroleptic complex **19** was clearly deduced from its ^1H -NMR spectrum, as shown in Figure 4.5, in which both the thioether ligand **dtDSA** and tpy ligand display signals corresponding to half of the molecule without any peak splitting or doubling. All the protons of the heteroleptic complex **19** were assigned as shown in Figure 4.5, below.

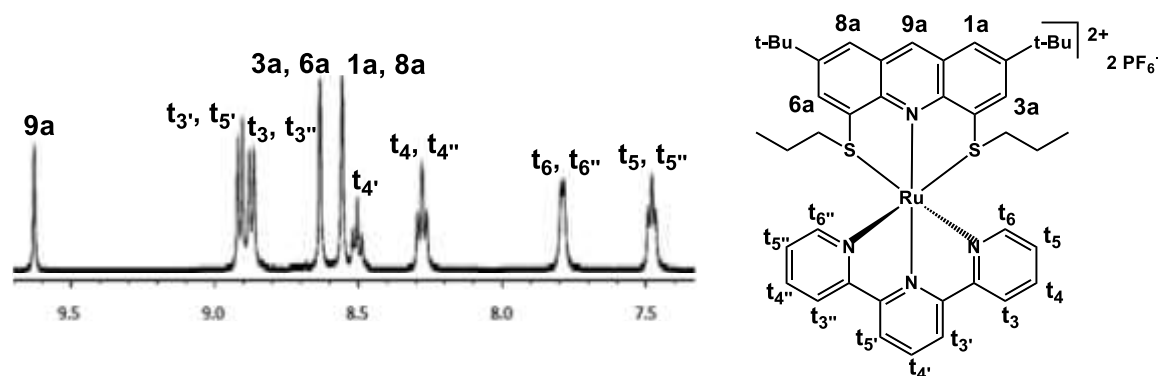


Figure 4.5. Aromatic region in ^1H -NMR spectrum of the heteroleptic Ru(II) complex **19** recorded in D-acetone solution at 500 MHz NMR spectrometer.

II.2.3. X-ray diffraction of complex **19**

In addition to the $^1\text{H-NMR}$ spectrum analysis, the symmetrical nature of the heteroleptic complex **19** was also verified by X-ray diffraction crystallography. Single crystals used in the X-ray diffraction crystallographic experiment were grown following slow diethylether vapor diffusion into an acetone solution of complex **19**. The structure is shown with its atom labeling from two different perspectives in Figure 4.6, below.

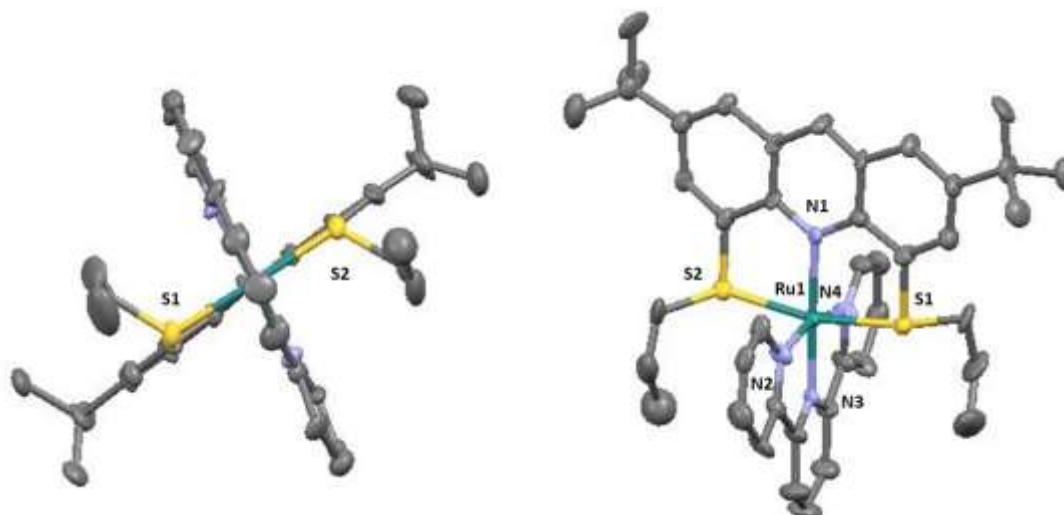


Figure 4.6. Different views of the crystal structure of the heteroleptic complex **19** (40% ellipsoids). Solvent molecules, H-atoms, and PF_6^- counter anions are omitted for clarity.

Despite the fact that the heteroleptic complex **19** is not bound in a geometry close to a perfect octahedron, like the previously prepared heteroleptic complexes **13** and **16**, the S-Ru-S trans chelation angle of the thioether ligand **17** was enhanced in comparison to the trans angle formed by tpy ligand in that, this S-Ru-S trans angle (166.9°) was expanded by around 9° . In addition, the 82.1° and 84.8° $\text{N}_{(\text{acridine})}\text{-Ru-S}$ angles, are enlarged in comparison to the 5-membered metallacycle angles formed by the tpy ligands and Ru(II) metal (79.5° and 79.0°). Moreover, the nitrogen atom of the acridine platform and the nitrogen atom of the central pyridine ring of the terpyridine ligand were linearly coordinated to Ru(II) metal with a 178.8° trans angle.

As explained previously, even with the 5-member metallacycles formation between the thioether ligand **17** and the Ru(II) central metal, but unlike the tpy ligand, the Ru-S bonds are

approximately 0.25-0.30 Å longer than Ru-N bonds (around 2.33 Å, in agreement with the bond lengths reported in the literature for similar chelates)⁶, which consequently lead to a larger coordination cavity. This indicates the great improvement of the coordination cavity by replacing the bulky heterocycles (pyridine and pyrazole rings) with single sulfur atoms on the acridine backbone. As a result, unlike the previously synthesized heteroleptic complexes (**13** and **16**), the acridine in this complex **19** remained planar and no twisting angle was observed (Figure 4.6).

The selected bond angles and bond lengths for the heteroleptic complex **19**, as well as for the reference complex [Ru(tpy)₂](PF₆)₂⁷ are listed in Table 4.1.

Table 4.4. Selected bond angles and bond lengths for the corresponding heteroleptic complex (**19**) with molecular formula, [Ru(**dtdsa**)(tpy)](PF₆)₂, as well as for the reference complex, [Ru(tpy)₂](PF₆)₂.

Complex	[Ru(dtdsa)(tpy)](PF ₆) ₂	[Ru(tpy) ₂](PF ₆) ₂
Angle (°)		
N1 Ru1 S1	82.1(7)	
N1 Ru1 S2	84.8(7)	
S1 Ru1 S2	166.9(3)	
N3 Ru1 N2	78.8(7)	79.5(3)
N3 Ru1 N4	79.8(10)	79.0(3)
N2 Ru1 N4	158.5(10)	158.4(3)
N1 Ru1 N3	178.8(10)	
Bond length (Å)		
Ru1 N1	2.06(2)	
Ru1 S1	2.351 (8)	
Ru1 S2	2.332(8)	
Ru1 N3	1.97(2)	1.981(7)
Ru1 N2	2.07(2)	2.079(6)
Ru1 N4	2.01(2)	2.067(7)

Moreover, from the X-ray crystal structure data, the tpy ligand in complex **19** coordinates closer to the central Ru(II) metal in comparison to its parent complex $[\text{Ru}(\text{tpy})_2]^{2+}$. In this case, the bond length between the Ru(II) metal and the central pyridine ring of tpy ligand (Ru-N3) was reduced by 0.011 Å (1.970 Å for complex **19** vs 1.981 Å for complex $[\text{Ru}(\text{tpy})_2]^{2+}$). However, the N2-Ru-N4 tpy ligand trans angle did not change significantly and remained around 158°, and displayed the usual distortion at the level of tpy ligand.

III. Electrochemistry

The electrochemical potentials of the thioether ligand **17**, as well as its corresponding Ru(II) complexes, **18** and **19** respectively, were recorded using cyclic voltammetry in a deaerated electrolyte solution of 0.1 M tetrabutylammonium hexafluorophosphate in acetonitrile (Figure 4.7 and Figure 4.8), and all obtained potentials were collected and listed in Table 4.2 and analyzed in comparison with the reference complex $[\text{Ru}(\text{tpy})_2]^{2+}$ found in the literature.⁸

Table 4.5. Redox potentials of **dtdsa** thioether ligand, in addition to its corresponding complexes $[\text{Ru}(\text{dtdsa})_2]^{2+}$ and $[\text{Ru}(\text{dtdsa})(\text{tpy})]^{2+}$, in comparison to the redox properties of the reference tpy ligand and its complex $[\text{Ru}(\text{tpy})_2]^{2+}$. $E_{1/2}$ (V) = $(E_{\text{pa}} + E_{\text{pc}})/2$, $(\Delta E_p \text{ (mV)}) = E_{\text{pc}} - E_{\text{pa}}$ vs Ag^+ (0.01 M)/Ag. *Irreversible redox process.

Compounds	$E_{1/2}$ reduction (ΔE_p , mV)		$E_{1/2}$ oxidation (ΔE_p , mV)	
$[\text{Ru}(\text{tpy})_2]^{2+}$	-1.83 (70)	-1.57 (60)	0.97 (80)	
$[\text{Ru}(\text{tpy})(\text{dtdsa})]^{2+}$ (19)	-2.39*	-1.74 (64)	-1.19*	1.01 (61)
$[\text{Ru}(\text{dtdsa})_2]^{2+}$ (18)	-1.35*		-1.16*	1.22 (170)
dtdsa (17)	-2.67*		-1.99 (90)	0.86* 1.18*
tpy ⁹	-2.95	-2.36		

III.1. Thioether ligand redox properties

The cyclic voltammogram of the (SNS) acridine-based thioether ligand **17** was recorded in deaerated electrolyte solution of 0.1 M TBAPF₆ in acetonitrile, as shown in Figure 4.7.

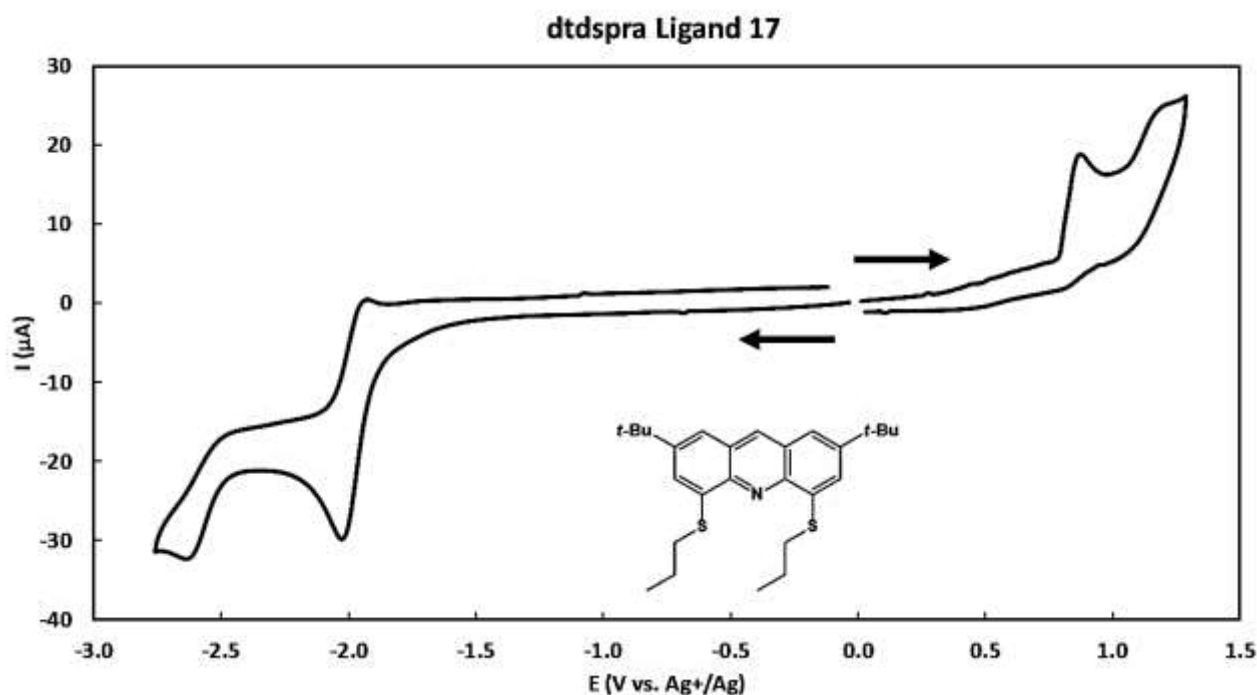


Figure 4.7. Cyclic voltammogram of the **dtdsa** ligand **17** (10^{-3} M) in deaerated acetonitrile containing 0.1 M [BuN]₄PF₆ (TBAPF₆), at a scan rate of $100 \text{ mV}\cdot\text{s}^{-1}$ using vitreous carbon working electrode (5 mm diameter), $E_p(\text{V})$ vs AgNO₃ (0.01 M)/Ag.

From the cyclic voltammogram shown in Figure 4.7 and collected data in Table 4.2, the free thioether ligand **17** has two successive irreversible oxidation peaks at $E_{pa} = 0.86 \text{ V}$ and $E_{pa} = 1.18 \text{ V}$. These two oxidation processes are believed to occur at the acridine platform,¹⁰ in which both are irreversible processes due to the formation of acridinium-acridine dimer,¹¹ as it has been analyzed in the previous chapters with ligands **11** and **14**.

Interestingly, these two oxidation potentials were clearly negatively shifted in comparison to what was obtained with ligands **11** (1.14 V and 1.52 V) and **14** (1.12 V and 1.62 V). This result can be rationalized by the σ -donor character of the two sulfur atoms at the 4 and 5 positions of the acridine, by that they increase the electron density at the acridine platform, and as a result, more accessible oxidation potentials are observed.

Furthermore, to avoid the doubt about the localization of both oxidations on the free thioether ligand, either on acridine or on the sulfur atoms, cyclic voltammograms were recorded after addition of water, going from 0.1 till 20 molar equivalents. All the obtained cyclic voltammograms were overlapped and no change neither in the intensity nor in the potential values was observed. This results, indicates that no sulfoxide or sulfone was formed by sulfur atom oxidation in the presence of water and both oxidation processes have exclusively occurred on the acridine platform.

A monoelectronic reversible reduction peak at $E_{1/2} = -1.99$ V and another irreversible reduction peak at $E_{pc} = -2.67$ V were observed in the cathodic region of the voltammogram. From these reduction potentials, it is clear that the electron rich thioether ligand **17** is difficult to reduce in comparison to the previously described triimine ligands, **11** (-1.90 V and -2.43 V) and **14** (-1.80 V and -2.47 V), in which both have less negative reduction potentials. Thus, the thioether ligand **17** would have a higher π^* -orbital energy in comparison to that of ligands **11** and **14**.

Indeed, these reduction potentials are still less negative than those obtained for the tpy ligand, and therefore, the thioether ligand **17** still has a stabilized LUMO with respect to that of tpy ligand.

III.2. Redox properties of the Ru(II) complexes

The cyclic voltammograms of the Ru(II) complexes **18** and **19** are presented in Figure 4.8.

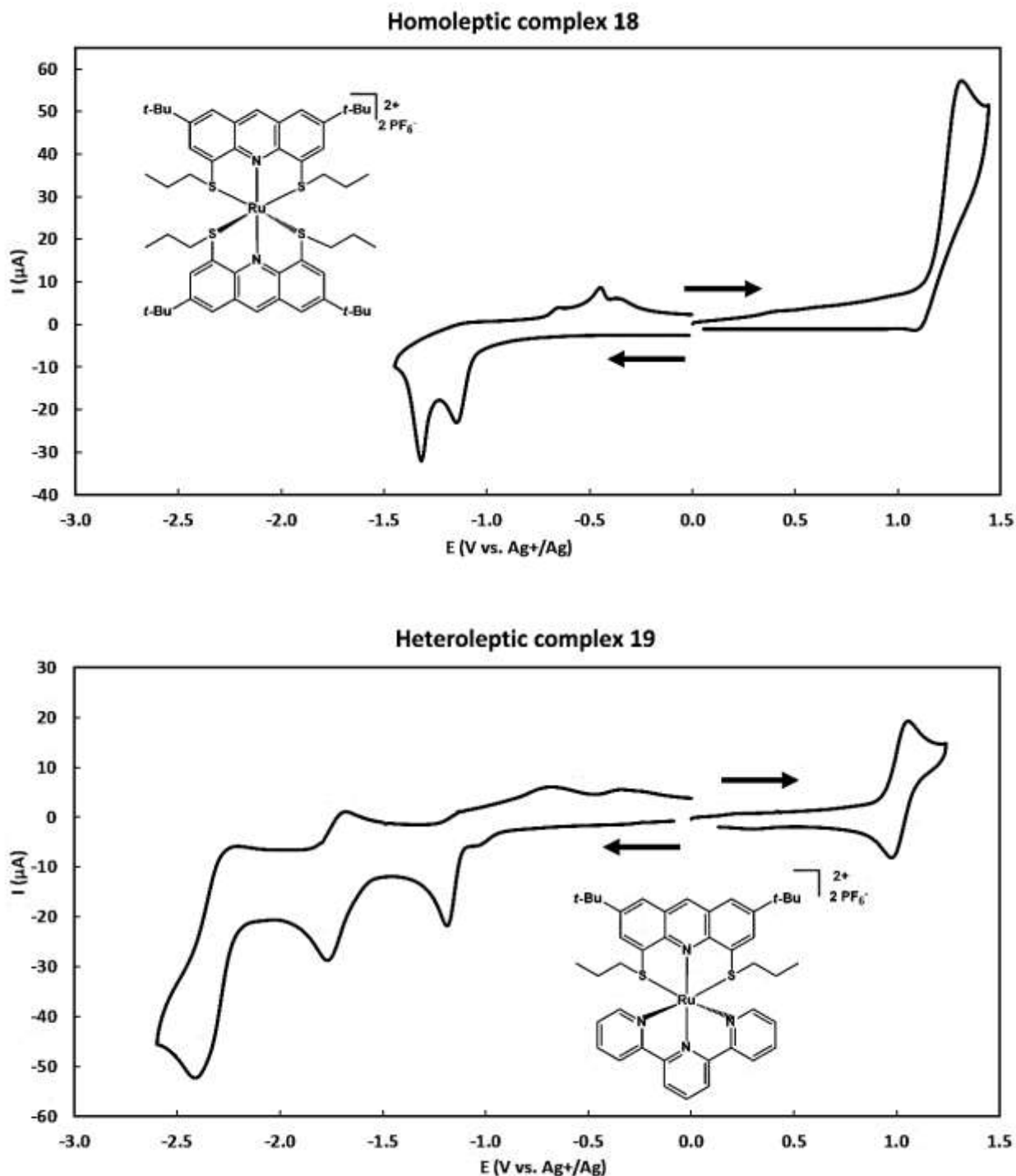


Figure 4.8. Cyclic voltammograms of the homoleptic complex **18** (top), and the heteroleptic complex **19** (bottom) at 10^{-3} M concentrations in deaerated acetonitrile solution with 0.1 M $[\text{BuN}]_4\text{PF}_6$ (TBAPF₆), at a scan rate of $100 \text{ mV}\cdot\text{s}^{-1}$ using vitreous carbon working electrode (5 mm diameter), $E_p(\text{V})$ vs AgNO_3 (0.01 M)/Ag.

In this chapter, we will describe the opposite redox behavior of the $\text{Ru}^{3+}/\text{Ru}^{2+}$ couple for both homoleptic and heteroleptic Ru(II) complexes with the thioether ligand (**18** and **19**), with respect to the previously discussed complexes (**12**, **13**, **15** and **16**).

The presence of a constrained coordination cavity for both ligands **11** and **14**, resulted in twisted acridine-based heteroleptic complexes and *facial* homoleptic ones. This results in non-efficient π -back bonding and thus leads to the presence of high electron density at the Ru(II) metal, which therefore renders it easier to oxidize. However, since ligand **17** has a larger coordination cavity, thus, no twisting of the acridine was observed for the heteroleptic Ru(II) complex, as shown in the crystallographic structure (Figure 4.6). Therefore, an efficient electron retrodonation would occur and thus, leads to a lower electron density on Ru(II).

Furthermore, in addition to this efficient electron retrodonation from the ruthenium central metal to the ligand, the electron density on the metal is further decreased by the π -accepting property of the sulfur coordinating atoms.

As we interpreted the influence of both triimine ligands **11** and **14** on the oxidation potential of Ru(II) metal by analyzing their redox properties in comparison to the $[\text{Ru}(\text{tpy})_2]^{2+}$ reference complex, the effect of the planar acridine-based thioether ligand **17** on the $\text{Ru}^{3+}/\text{Ru}^{2+}$ couple oxidation potential is investigated with the same interpretation.

The heteroleptic complex **19** exhibits a reversible monoelectronic oxidation potential at $E_{1/2} = 1.01$ V of $\Delta E_p = 61$ mV. This $\text{Ru}^{3+}/\text{Ru}^{2+}$ couple oxidation potential of complex **19** of molecular formula $[\text{Ru}(\text{dtdsa})(\text{tpy})]^{2+}$ was increased by 40 mV as one tpy ligand was replaced by one **dtdsa** ligand. However, as a second **dtdsa** ligand took the place of the other tpy ligand, to form the homoleptic complex **18**, the $\text{Ru}^{3+}/\text{Ru}^{2+}$ oxidation potential was dramatically shifted to more positive potential by furthermore 210 mV to have a quasi-reversible potential at $E_{1/2} = 1.22$ V with a $\Delta E_p = 170$ mV. Indeed, the quasi-reversible oxidation potential for Ru(II) metal complexes, as it is obtained with the homoleptic complex **18**, is rare in the literature, however, such quasi-reversible oxidation has been observed in some thioether Ru(II) complexes.¹² In the present case it could be due to adsorption phenomena on the electrode.

Therefore, we can clearly see the effect of the thioether ligand on increasing the $\text{Ru}^{3+}/\text{Ru}^{2+}$ oxidation potential. Such ligand influence on Ru(II) metal is attributed to its π -accepting

property, as we described above. Moreover, the Ru(II) metal becomes more electron deficient as the number of sulfur atoms increases, resulting in greater energy needed to initiate an oxidation process compared to bis-triimine complexes (**12**, **13**, **15** and **16**).

Several reduction peaks were observed in the cathodic region of the cyclic voltammograms of both complexes **18** and **19**, which are mainly localized on the different ligands. The homoleptic complex shows two successive irreversible reduction peaks at -1.16 V and -1.35 V, which are attributed to the reduction processes of each **dtdsa** thioether ligand, thus, showing the electronic communication between both ligands *via* the central metal.

In the same pattern, the heteroleptic complex shows an irreversible reduction peak at -1.19 V, which takes place on the LUMO which is globally localized on the thioether ligand. A further monoelectronic reversible reduction peak was observed at $E_{1/2} = -1.74$ V with $\Delta E_p = 64$ mV, which is attributed to the reduction process occurring on the tpy ligand in complex **19**. Furthermore, an irreversible reduction peak was observed at -2.39 V, which can be attributed to a second reduction process again on the thioether ligand.

Lastly, the dramatic shifts of the reduction potentials for both tpy and **dtdsa** thioether ligands towards less negative values are explained by imine and sulfur lone pair donation to the Ru(II) metal upon complexation. Therefore, complexed ligands have less electron density and can be reduced more easily.

IV. Photophysics

The photophysical properties of the thioether ligand **17**, along with its corresponding homoleptic and heteroleptic Ru(II) complexes (**18** and **19** respectively) were studied in deaerated acetonitrile solution at room temperature, and in a butyronitrile rigid matrix at 77 K.

All the recorded photophysical data were collected and analyzed, and they are shown later in this chapter in Table 4.3.

IV.1. Ligand spectroscopic properties

The absorption spectrum of the free thioether ligand **17** which was recorded in acetonitrile (10^{-5} M) at room temperature is presented in Figure 4.9-(a), and the emission spectra recorded at both room temperature and 77 K are illustrated in Figure 4.9-(b).

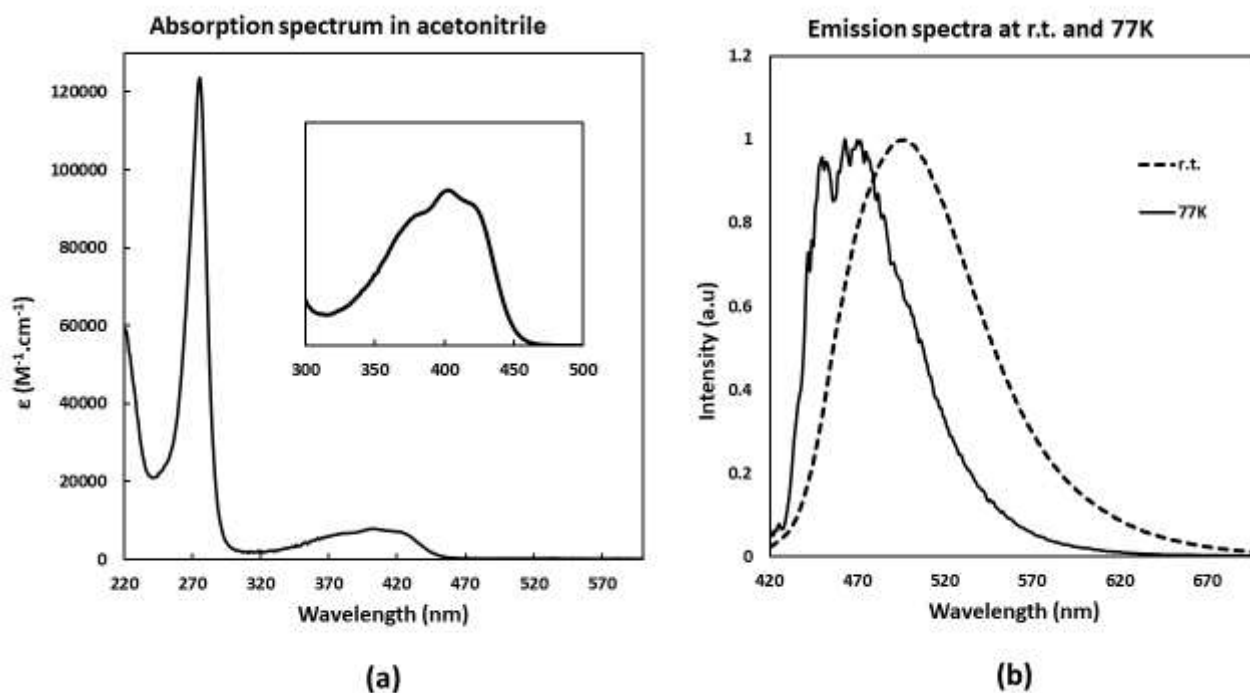


Figure 4.9. Absorption (a) and emission (b) spectra of the thioether ligand **17**.

This acridine-based thioether ligand **17** displays the expected, typical absorbance of both previously described (NNN) acridine-based trimine ligands, **11** and **14**, in the UV and in the visible region. As shown in Figure 4.9-(a), the thioether ligand exhibits a strong absorption in UV region from 250 nm to 290 nm with a maximum centered at 275 nm and a molar absorption coefficient of $1.24 \times 10^5 M^{-1} cm^{-1}$. This band results from a $\pi-\pi^*$ transition of the ligand. Another broad absorption was observed in the high frequency area of the visible region ranging from 330 nm to 460 nm, with a maximum centered at 402 nm and a molar absorption coefficient of $6.30 \times 10^3 M^{-1} cm^{-1}$. This moderately intense absorption could be attributed to the $n-\pi^*$ transition localized on the acridine platform,¹³ and not a charge transfer process between the different parts of the ligand, as it has been explained previously in details with ligand **11** and **14**.

In agreement with the observed redox potentials, the thioether ligand **17** displays lower oxidation potentials in comparison to ligands **11** and **14**, thus, this ligand **17** has a higher HOMO relative to the trimine ligands. As a result, a red shift of the absorption band of ligand **17** with respect to ligands **11** and **14** is observed.

A fluorescence emission was observed for ligand **17** at room temperature and low temperature (77 K), after excitation at 402 nm. An emission maximum centered at 496 nm was observed in deaerated acetonitrile at room temperature, with an emissive excited state lifetime of 12.7 ns and 3.9% emission quantum yield. In a frozen butyronitrile matrix at 77 K, the fluorescence emission was blue shifted to 466 nm, as shown in Figure 4.9-(b), with an excited state lifetime of 19.2 ns. Moreover, as a red shift in the absorption band of ligand **17** was observed with respect to ligands **11** and **14**, consequently, the emission at room temperature and at 77 K was also red shifted.

IV.2. Ru(II) complexes spectroscopic properties

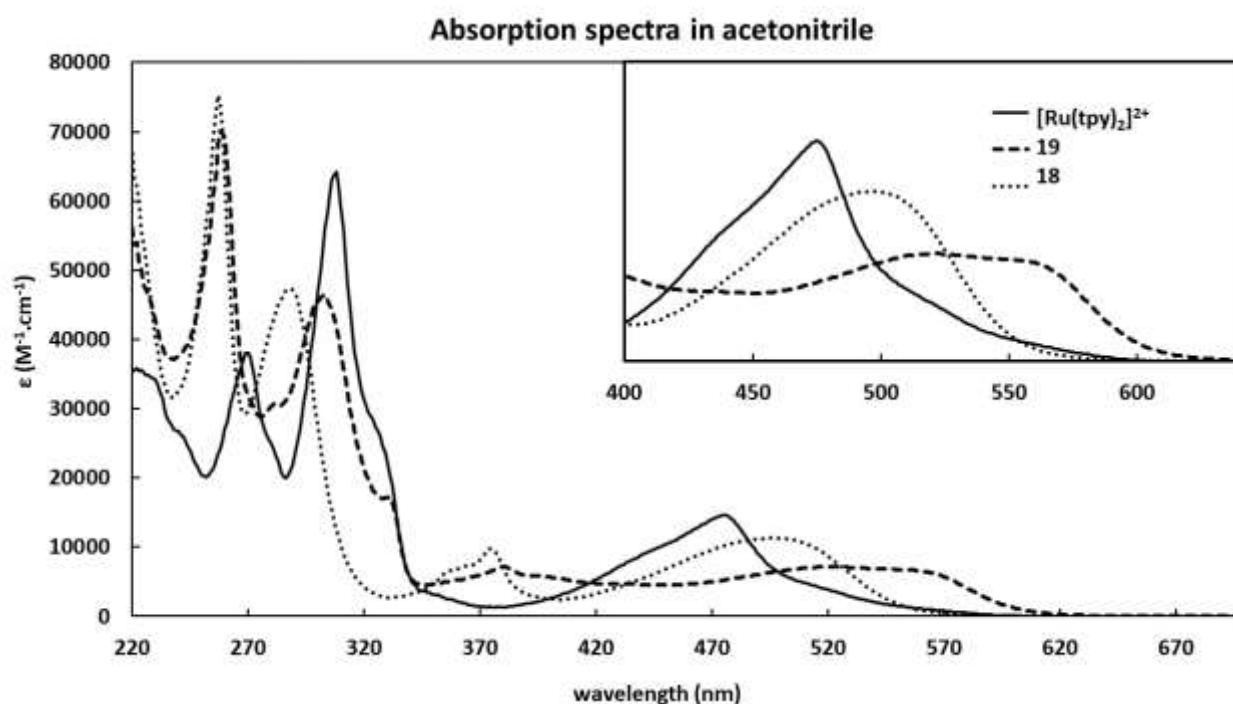


Figure 4.10. Absorption spectra of $[\text{Ru}(\text{dtDSA})_2]^{2+}$ **18** (dotted), $[\text{Ru}(\text{dtDSA})(\text{tpy})]^{2+}$ **19** (dashed), and $[\text{Ru}(\text{tpy})_2]^{2+}$ (solid line) complexes in deaerated acetonitrile solution.

The photophysical properties of the homoleptic and heteroleptic Ru(II) complexes (**18** and **19**, respectively) are presented and analyzed in this section. The UV-visible absorption spectra of both complexes were recorded in deaerated acetonitrile (10^{-5} M) and studied in comparison to the reference complex, $[\text{Ru}(\text{tpy})_2]^{2+}$, as shown above in Figure 4.10.

From Figure 4.10, both Ru(II) complexes **18** and **19** displayed a strong spin-allowed ligand centered transition (LC) with the same intensity in the UV region. The $[\text{Ru}(\text{dtdsa})_2]^{2+}$ homoleptic complex **18** (dotted line) shows two LC absorption bands with wavelengths maxima centered at 257 nm and 289 nm, having molar absorption coefficients in the range of 10^4 - 10^5 $\text{M}^{-1} \text{cm}^{-1}$. Another moderately intense absorption band was observed, centered at 375 nm with a molar absorption coefficient of 9.80×10^3 $\text{M}^{-1} \text{cm}^{-1}$. The $[\text{Ru}(\text{dtdsa})(\text{tpy})]^{2+}$ heteroleptic complex **19** (dashed line) shows two intense absorption bands in the UV region, centered at 258 nm ($\epsilon = 7.00 \times 10^4$ $\text{M}^{-1} \text{cm}^{-1}$) and 304 nm ($\epsilon = 4.59 \times 10^4$ $\text{M}^{-1} \text{cm}^{-1}$) in addition to the third moderately intensity band in the near-visible region which was centered at 380 nm ($\epsilon = 7.20 \times 10^3$ $\text{M}^{-1} \text{cm}^{-1}$). The first band in both complexes could be attributed to the π - π^* transition on the thioether ligand, whereas the second band in complex **19** could be attributed to the π - π^* transition on the terpyridine ligand.

The absorption bands in the visible region, are mainly attributed to the metal to ligand charge transfer (MLCT), $d_{(M)}-\pi^*_{(L)}$, transitions. Both Ru(II) complexes, **18** and **19**, display a broad and moderately intense MLCT absorption band expanding between 400 nm and 620, but with red shifted λ_{max} values compared to the $[\text{Ru}(\text{tpy})_2]^{2+}$ reference complex (solid line). The MLCT (metal to thioether ligand) band of complex **18** was centered at 497 nm, with a molar absorption coefficient of 1.13×10^4 $\text{M}^{-1} \text{cm}^{-1}$. On the second hand, the MLCT band of complex **19** is red shifted relative to complex **18**, showing two maxima at 522 nm ($\epsilon = 7.20 \times 10^3$ $\text{M}^{-1} \text{cm}^{-1}$), which refers to the transition from the metal to the terpyridine ligand, and at 555 nm ($\epsilon = 6.70 \times 10^3$ $\text{M}^{-1} \text{cm}^{-1}$), which refers to the transition from the metal to the thioether ligand of lower π^* -orbital.

Furthermore, both homoleptic and heteroleptic thioether complexes display blue shifted MLCT absorption bands (energetic transitions) in comparison to what was obtained before with both acridine-based triimine ligands (**11** and **14**). This result was justified, as seen in Figure 4.11, based on analysis of the electrochemical data. The geometrically distorted ligand

complexes (**11** and **14**) exhibit a small HOMO-LUMO energy gap (indicating relatively easy metal oxidation and ligand reduction processes), whereas both SNS thioether Ru(II) complexes (**18** and **19**) show the opposite redox behavior. Thus, both of these thioether Ru(II) complexes have a larger HOMO-LUMO energy gap and as a consequence, they have higher energy MLCT absorption bands in the visible region. However, the HOMO-LUMO gap of complexes **18** and **19** is still smaller relative to $[\text{Ru}(\text{tpy})_2]^{2+}$ complex, even with a lower lying HOMO, but, much lower LUMO.

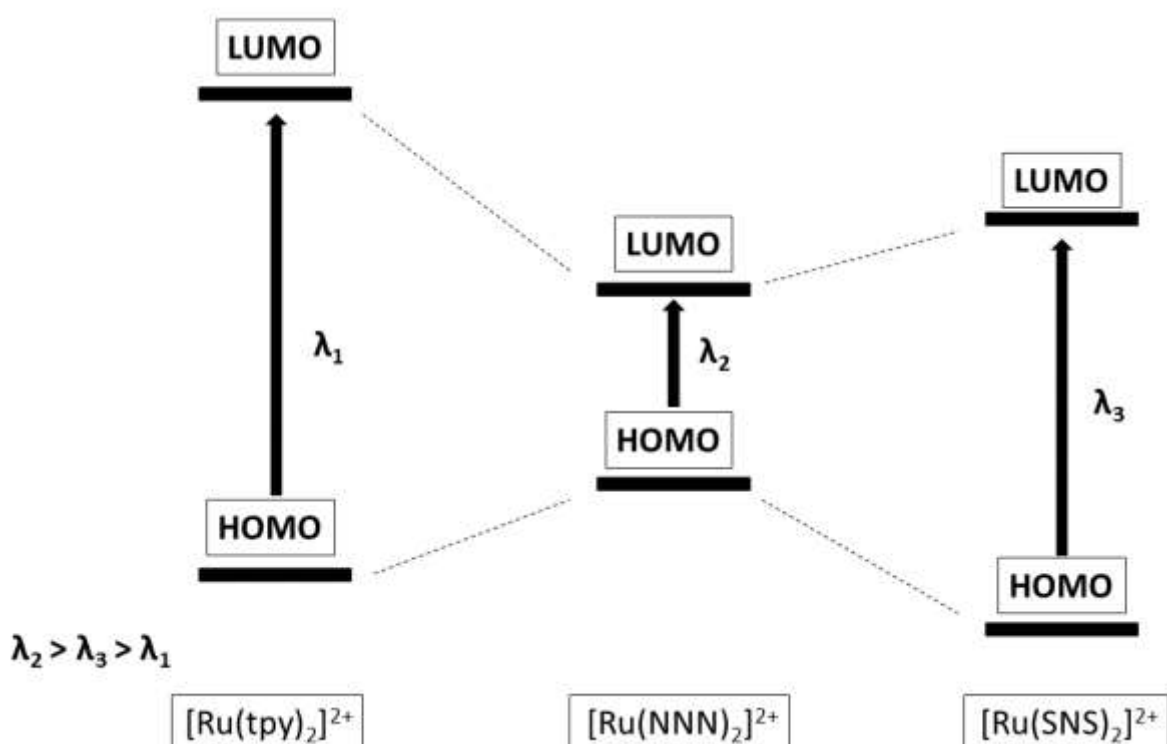


Figure 4.11. Schematic depicting the molecular orbitals of triimine (NNN) and thioether (SNS) ligand complexes in comparison to the $[\text{Ru}(\text{tpy})_2]^{2+}$ reference complex.

The luminescence properties of both complexes **18** and **19** were investigated in deaerated acetonitrile solution at room temperature and in butyronitrile rigid matrix at 77 K. Visible-light excitation of both complexes at their $^1\text{MLCT}$ wavelength maxima did not show any fluorescence or phosphorescence emission under either set of conditions. This was an unexpected result for these Ru(II) complexes with acridine-based thioether ligands, which have an energetic MLCT band in the visible region, unlike the previously reported complexes based on ligands **11** and **14**, which had very low lying MLCT bands, that deactivated in a non-

radiative pathway according to energy gap law. However, in the literature some examples of Ru(II) complexes with thioether ligands are non-emissive, especially for complexes having ligands with higher numbers of sulfur atoms.^{12,14} In these types of complexes, it is considered that the non-radiative deactivation pathway of the ³MLCT excited state is more favorable and highly induced with thioether ligand Ru(II) complexes compared with typical polypyridine complexes.

All the measured and collected spectroscopic data are illustrated in Table 4.3 below.

Table 4.6. The spectroscopic data of the thioether ligand **17**, in addition to its corresponding homoleptic and heteroleptic Ru(II) complexes (**18** and **19**) in deaerated acetonitrile solution.

Compounds	λ_{abs} , nm (ϵ , M ⁻¹ cm ⁻¹)	Room temperature			77 K	
		λ_{em} , nm	ϕ	τ , ns	λ_{em} , nm	τ , ns
[Ru(dtDSA) ₂] ²⁺ (18)	257 (75,300), 289 (47,200), 375 (9,800), 497 (11,300)					
[Ru(tpy)(dtDSA)] ²⁺ (19)	258 (70,000), 304 (45,900), 380 (7,200), 522 (7,200), 555 (6,700)					
dtDSA (17)	275 (124,000), 380 (5,300), 402 (6,300), 420 (5,700)	496	0.039	12.7	466	19.2

V. Photochemistry

Although both the homoleptic (**18**) and heteroleptic (**19**) Ru(II) thioether complexes did not show any luminescence properties from their highly energetic $^3\text{MLCT}$ excited state (in the same range of $[\text{Ru}(\text{tpy})_2]^{2+}$), these photoactive complexes may show some photochemical reactions through their non-emissive low lying ^3MC excited state.

Therefore, photochemical substitution reaction attempts were conducted for both complexes, **18** and **19**, to expel one thioether ligand (**17**) from each complex by trying to replace these coordination sites with three acetonitrile solvent molecules upon irradiation.

However, contrary to our proposition, no detectable ligand dissociation was observed with either the homoleptic or heteroleptic complexes after 2 hours of irradiation with a strong white light source in a deuterated acetonitrile solution. Hence, such acridine-based thioether ligand Ru(II) complexes, with relatively long Ru-S bonds (around 2.33 Å), were photochemically very stable.

A logical justification of such stability could be rationalized due to the high rigidity of ligand **17** (acridine-based ligand). In this case, even if the long Ru-S bond was cleaved, indeed, the rigidity of the acridine backbone would deprive the ligand of the freedom to turn around. As a result, Ru-S bond re-coordination would be faster than a solvent molecule in reaching the central Ru(II) metal.

VI. Conclusion

Grafting simple coordinating sulfur atoms at the 4 and 5 positions of the ligand acridine backbone was a successful method to open the coordination cavity of the acridine-based thioether ligand (relative to the previously described acridine-based ligands, **11** and **14**). Using this new ligand, *meridional* homoleptic and heteroleptic Ru(II) complexes (**18** and **19**) were obtained.

Moreover, the acridine platform twisting within the *mer* octahedral geometries were also resolved. Therefore, more energetic ¹MLCT absorption bands were obtained for both complexes, as a result of their larger HOMO-LUMO energy gaps.

However, even with the long C₄-S and C₅-S bonds, the trans chelation angle S-Ru-S was still not linear and gave some distortion, although these changes still represent an important geometrical improvement on the parent terpyridine ligand and other NNN ligands described in this thesis so far.

As an unexpected result, complexes **18** and **19** were not luminescent either at room temperature nor at 77 K, and this result could be due to the sulfur coordinating atoms with the central Ru(II) metal, which may quench the emission properties of the complex (as is known to be a result of some thioether Ru(II) complexes found in the literature).

Moreover, these complexes were photochemically very stable, and all attempts towards a photosubstitution reaction with solvent molecules did not succeed. This result was justified based on the high rigidity of the acridine-based ligand, **17**.

Therefore, preparing another thioether ligand having a good flexibility would be important to allow its Ru(II) complexes to be photochemically active upon light irradiation.

VII. References

- (1) Pal, A. K.; Hanan, G. S. Design, Synthesis and Excited-State Properties of Mononuclear Ru(II) Complexes of Tridentate Heterocyclic Ligands. *Chem. Soc. Rev.* **2014**, *43* (17), 6184–6197.
- (2) Canovese, L.; Visentin, F.; Chessa, G.; Uguagliati, P.; Levi, C.; Dolmella, A. Attack of Substituted Alkynes on Olefin Palladium(0) Derivatives of Pyridylthioethers. The First Kinetic Study on the Mechanism of Formation of Palladacyclopentadiene Complexes. *Organometallics* **2005**, *24* (23), 5537–5548.
- (3) Canovese, L.; Visentin, F.; Biz, C.; Scattolin, T.; Santo, C.; Bertolasi, V. Oxidative Addition of Allyl and Propargyl Halides on Palladium(0) Complexes Bearing Bidentate Ligands with Quinolinic Structure. *Journal of Organometallic Chem.* **2015**, *786*, 21–30.
- (4) Yamamoto, K.; Higashibayashi, S. Synthesis of Three-Dimensional Butterfly Slit-Cyclobisazaanthracenes and Hydrazinobisanthenes through One-Step Cyclodimerization and Their Properties. *Chem. Eur. J.* **2016**, *22*, 663–671.
- (5) Desbois, N.; Szollosi, A.; Maisonia, A.; Weber, V.; Moreau, E.; Teulade, J.-C.; Chavignon, O.; Blache, Y.; Chezal, J. M. Simple and Convenient Conversion of Acridones into 9-Unsubstituted Acridines via Acridanes Using Borane Tetrahydrofuran Complex. *Tetrahedron Lett.* **2009**, *50* (49), 6894–6896.
- (6) Page, M. J.; Wagler, J.; Messerle, B. A. Pyridine-2,6-Bis(Thioether) (SNS) Complexes of Ruthenium as Catalysts for Transfer Hydrogenation. *Organometallics* **2010**, *29* (17), 3790–3798.
- (7) Lashgari, K.; Kritikos, M.; Norrestam, R.; Norrby, T. Bis(Terpyridine) Ruthenium(II) Bis(Hexafluorophosphate) Diacetonitrile Solvate. *Acta Crystallogr. Sect. C* **1999**, *55*, 64–67.
- (8) Jacquet, M.; Lavolet, F.; Cobo, S.; Loiseau, F.; Bakkar, A.; Boggio-Pasqua, M.; Saint-Aman, E.; Royal, G. Efficient Photoswitch System Combining a Dimethyldihydropyrene Pyridinium Core and Ruthenium(II) Bis-Terpyridine Entities. *Inorg. Chem.* **2017**, *56* (8),

- 4357–4368.
- (9) Persaud, L.; Barbiero, G. Synthesis, Electrochemical and Spectroscopic Investigations of 2,2':4,4''-Terpyridine and 2,2':4,4'':6,2''-Quaterpyridine Ligands for Metal Complex Photoelectrochemistry. *Can. J. Chem.* **1991**, *69*, 315–321.
- (10) Pontinha, A. D. R.; Sparapani, S.; Neidle, S.; Oliveira-Brett, A. M. Triazole-Acridine Conjugates: Redox Mechanisms and in Situ Electrochemical Evaluation of Interaction with Double-Stranded DNA. *Bioelectrochemistry* **2013**, *89*, 50–56.
- (11) Marcoux, L.; Adams, R. N. Anodic Oxidation Of Aromatic Aza Hydrocarbons. *Electroanal. Chem. and Interfacial. Electrochem.* **1974**, *49*, 111–122.
- (12) Wallenstein, J. H.; Sundberg, J.; Mckenzie, C. J.; Abrahamsson, M. Emissive Ruthenium–Bisdiimine Complexes with Chelated Thioether Donors. *Eur. J. Inorg. Chem.* **2016**, *6*, 897–906.
- (13) Rak, J.; Blazejowski, J. Experimental and INDO CI Calculations of the Electronic Absorption Spectra of Acridine and 9-Acridinamine Free Bases and Their Protonated Forms with Regard to Tautomeric Phenomena. *J. Photochem. Photobiol. A Chem.* **1992**, *67*, 287–299.
- (14) Root, M. J.; Sullivan, B. P.; Meyer, T. J.; Deutsch, E. Thioether, Thiolato, and 1,1-Dithioato Complexes of Bis(2,2'-Bipyridine)Ruthenium(II) and Bis(2,2'-Bipyridine)Osmium(II). *Inorg. Chem.* **1985**, *24* (18), 2731–2739.

Chapter 5: SNS-thioanisole ligand and its photochemically active Ru(II) complexes

I. Introduction

It was demonstrated (in chapter 4) that having coordinating sulfur atoms on the structurally rigid acridine backbone was a successful methodology to enlarge the very tight coordination cavity of the desired ligand on the Ru(II) metal sphere.

Thus, both the homoleptic and heteroleptic Ru(II) complexes, **18** and **19**, respectively, based on the thioether ligand **17**, were obtained with *meridional* octahedral geometry, without any twisting distortion of the planar acridine. However, another geometrical distortion arose by having an S-Ru-S trans chelation angle smaller than expected (less than 180°), due to the formation of the 5-membered metallacycles between the coordinating ligand and Ru(II) metal cation.

Therefore, preparing another thioether ligand capable of coordinating Ru(II) with the favorable 6-membered metallacycles, as in chapters 2 and 3, could be a suitable solution to open the S-Ru-S trans chelation angle, and consequently obtain a perfect octahedron.

For this reason, a new (SNS) thioether ligand **20**, suiting all our demands by having a good flexibility in addition to the ability to form 6-membered metallacycles, was prepared based on inspiration from the known (NNN) tridentate ligand, 2,6-di(quinolin-8-yl)pyridine, which was already prepared and described,¹ as shown in Figure 5.1 below.

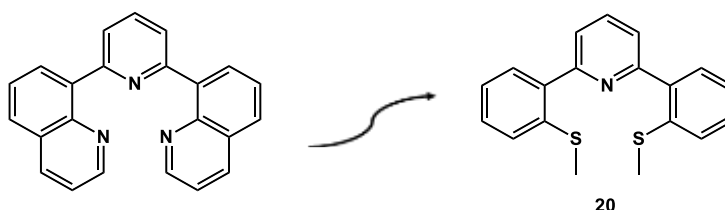
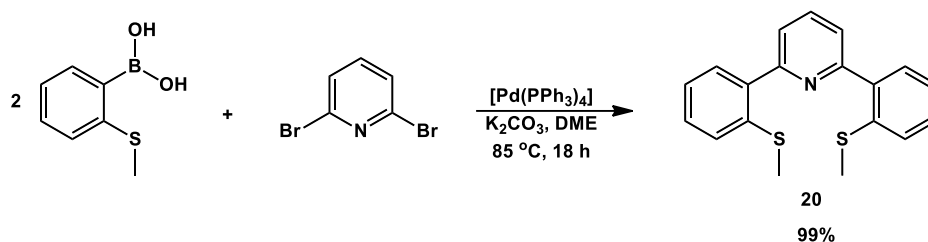


Figure 5.9. The new flexible (SNS) thioether ligand **20**, derived from another (NNN) ligand design.

II. Synthesis

II.1. Ligand synthesis

The newly proposed thioether ligand **20**, named 2,6-bis(2-(methylthio)phenyl)pyridine, presented in Figure 5.1 was prepared previously by the J. E. Bercaw lab and published in 2012.² The desired ligand **20**, referred to as the 'thioanisole ligand' herein to differentiate it from the previously prepared thioether ligand **17**, was prepared following the same synthetic procedure described by Bercaw with some modifications. Ligand **20** was quantitatively prepared (99% yield) in one synthetic step *via* Suzuki coupling between two molar equivalents of (2-(methylthio)phenyl)boronic acid and one molar equivalent of 2,6-dibromopyridine in the presence of palladium(0) and a weak base (already dissolved in water), all in 1,2-dimethoxyethane solvent at 85 °C overnight, as shown in Scheme 5.1 below.



Scheme 5.2. The thioanisole target ligand (**20**) synthesis.

All ligand **20** protons in its ¹H-NMR spectrum, recorded in deuterated acetone on a 500 MHz NMR spectrometer, were assigned as shown in Figure 5.2.

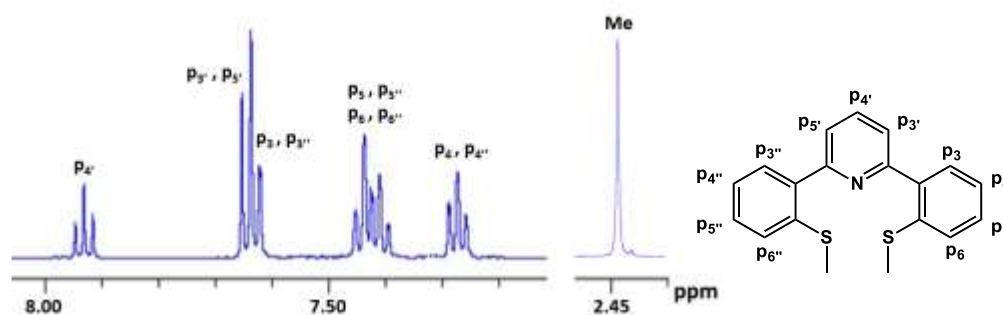


Figure 5.10. ¹H-NMR spectral assignment of ligand **20**, recorded in D₆-acetone on a 500 MHz NMR spectrometer.

II.2. Ru(II) complexes synthesis

The corresponding homoleptic Ru(II) complex (**21**) composed of two thioanisole ligands, as well as the heteroleptic complex (**22**) composed of one thioanisole ligand and one terpyridine ligand, were isolated as hexafluorophosphate salts (Figure 5.3) and then fully characterized by NMR spectroscopy and mass spectrometry.

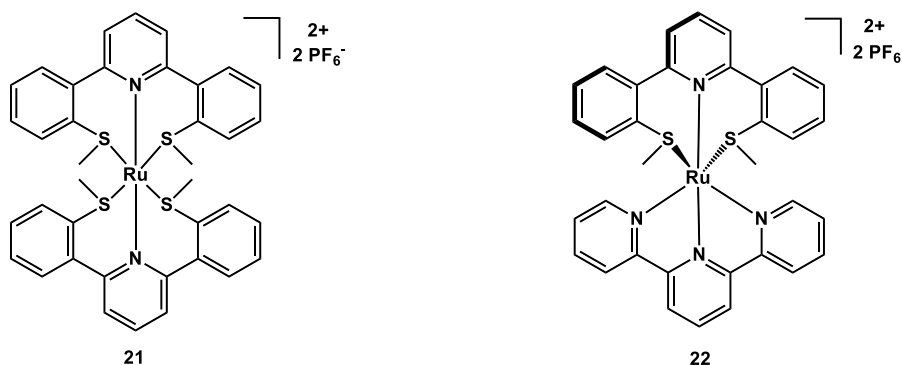
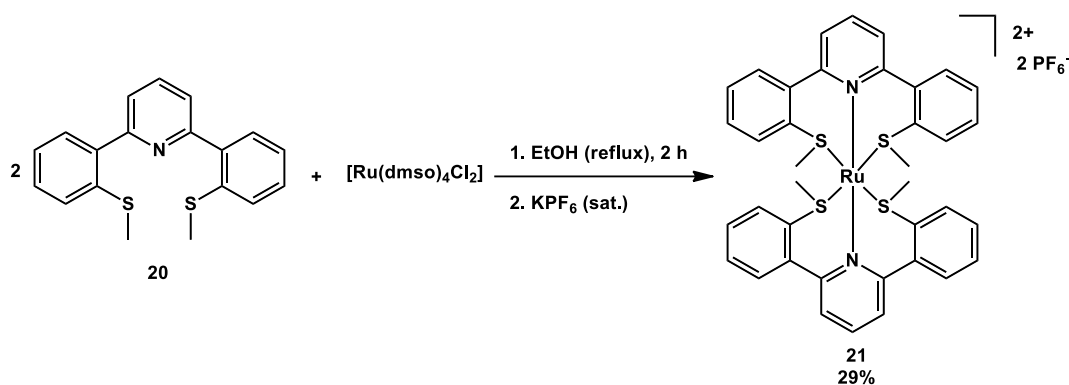


Figure 5.11. The thioanisole Ru(II) complexes **21** (homoleptic) and **22** (heteroleptic).

II.2.1. Homoleptic Ru(II) complex

A light yellowish powder of the homoleptic Ru(II) complex **21** was obtained after refluxing a 1:2 mixture of the Ru(II) precursor with compound **20** in dry ethanol solution for two hours. Complex **21** was purified on silica gel and then isolated in 29% yield as a hexafluorophosphate salt after anion exchange with a saturated aqueous solution of KPF_6 , to have the following molecular formula $[\text{Ru}(\mathbf{20})_2](\text{PF}_6)_2$, as shown in Scheme 5.2.



Scheme 5.3. The homoleptic Ru(II) complex **21** synthesis.

ESI mass spectrometry was performed for the complex **21** and verifies its proposed molecular formula $[\text{Ru}(\mathbf{20})_2](\text{PF}_6)_2$. In the spectrum, a mass peak at $m/z = 374.0$ with 2+ charge was detected, which matches with $[\text{Ru}(\mathbf{20})_2]^{2+}$ (m/z calculated to be 374.1), in addition to the observation of a peak at $m/z = 892.9$ with 1+ charge, which matches with $[\text{Ru}(\mathbf{20})_2](\text{PF}_6)^+$ (m/z calculated to be 893.0).

Compound **20** coordinates with the Ru(II) cation through a remarkable distortion of its octahedral geometry, by giving the unexpected, non-symmetrical *facial* geometry. This result is common with the previously prepared homoleptic complexes that formed the 6-membered metallacycles with the Ru(II) metal (complexes **12** and **15**).

Following the same reasoning as for the previous homoleptic complexes which adopt the *fac* geometry, the C_2 -*fac* geometry of complex **21** was deduced directly from its $^1\text{H-NMR}$ spectrum, as shown in Figure 5.4. All proton signals of the thioanisole ligand (bottom) were split into two sets of peaks (top) as the complexation reaction proceeded.

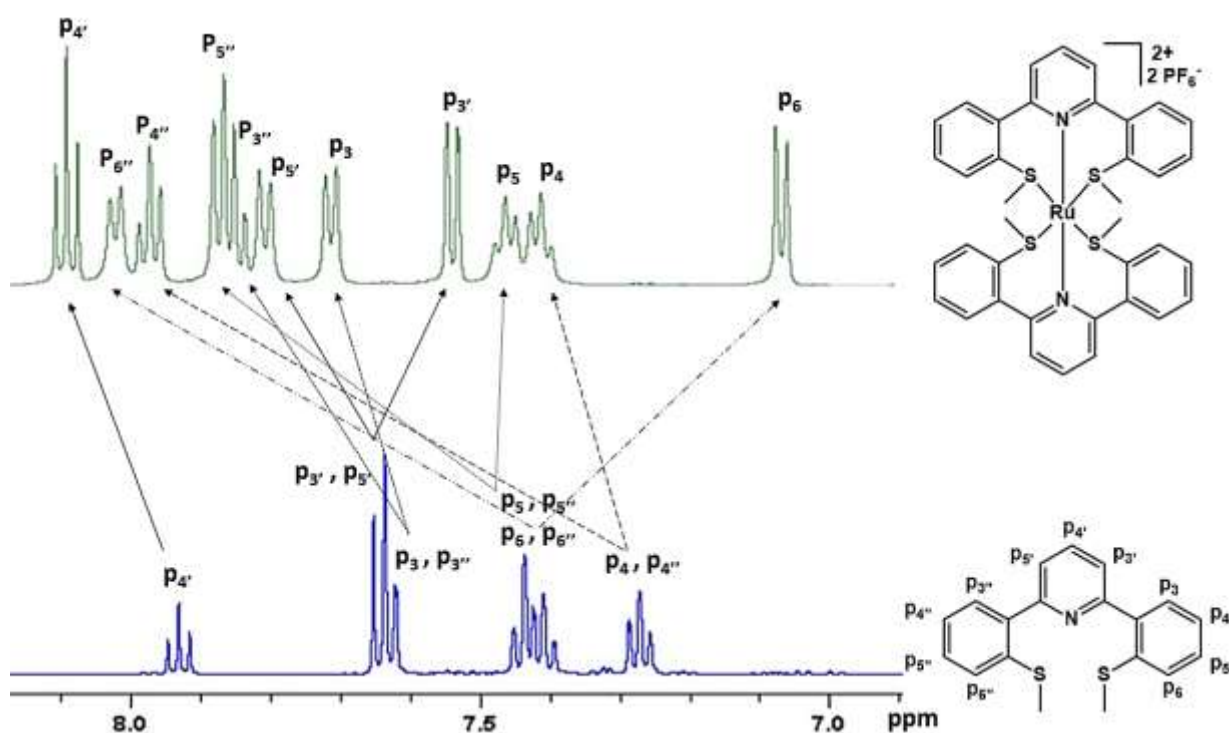


Figure 5.12. $^1\text{H-NMR}$ spectra of ligand **20** (bottom) and its homoleptic Ru(II) complex **21** (top), recorded in D_6 -acetone on a 500 MHz NMR spectrometer.

Single crystals of complex **21** suitable for X-ray diffraction were obtained following slow diethylether vapor diffusion into an acetone solution of complex **21**. The X-ray crystal structure verified the *facial* geometry of complex **21**.

Different perspectives of the homoleptic complex **21** crystals, with atom labeling, are illustrated in Figure 5.5, and selected bond lengths and bond angles are collected in Table 5.1.

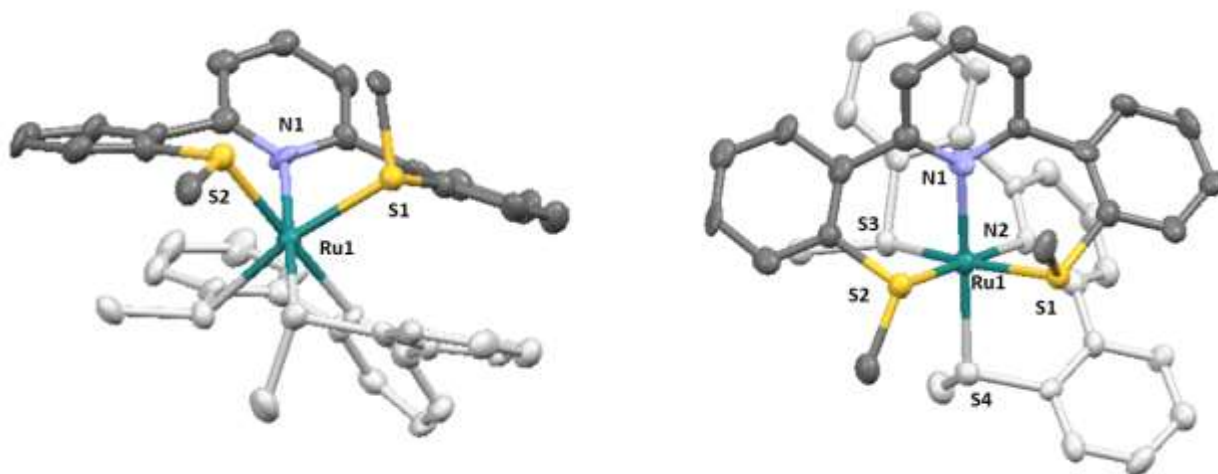


Figure 13.5. Different views of the crystal structure of complex **21** (40% ellipsoids). Solvent molecules, H-atoms and counter anions are omitted for clarity.

Table 5.7. Selected bond angles and bond lengths of the homoleptic complex **21**.

Bond angle (°)		Bond length (Å)	
N1 Ru1 S1	77.1(3)	Ru1 N1	2.181(12)
N1 Ru1 S2	87.7(4)	Ru1 S1	2.377(4)
S1 Ru1 S2	88.65(16)	Ru1 S2	2.338(4)
N2 Ru1 S3	85.3(4)	Ru1 N2	2.178(13)
N2 Ru1 S4	82.4(4)	Ru1 S3	2.374(4)
S3 Ru1 S4	87.82(15)	Ru1 S4	2.335(5)
N1 Ru1 N2	97.9(5)		

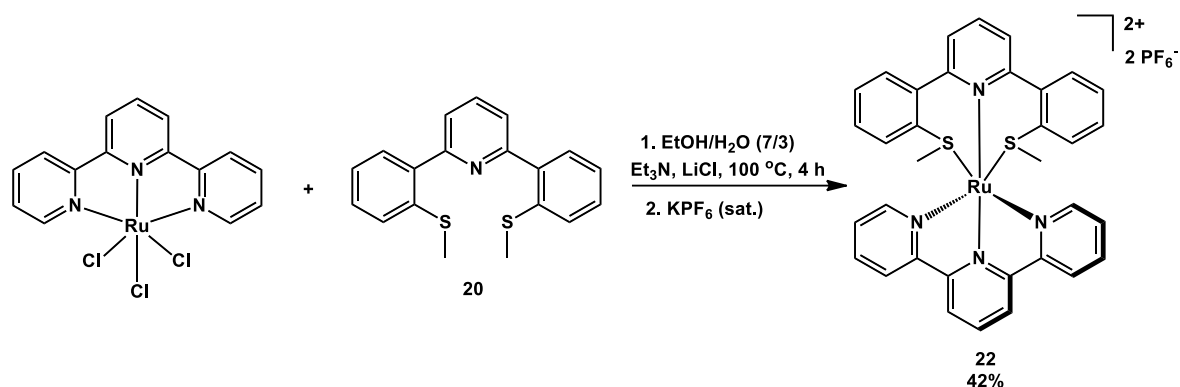
It is clear from the X-ray crystal structure shown in Figure 5.5 and the data collected in Table 5.1, that both sulfur atoms of each thioanisole ligand are in *cis* position, with approximate S-Ru-S bond angles around 88°. Moreover, we can see that the pyridine rings of both thioanisole ligands are positioned in *cis* manner relative to each other with an N1-Ru-N2 angle of 97.9°. This observation verifies, in addition to the ¹H-NMR spectral analysis, the non-symmetrical *fac* geometry of complex **21**.

Furthermore, all the selected Ru-S bond lengths are in agreement with the bond lengths reported in the literature for similar chelates.³ However, this thioanisole ligand **20** coordinates with ruthenium metal with slightly longer Ru-S bond lengths in comparison to the previously studied acridine-based thioether ligand **17**, by 0.006 to 0.026 Å. These longer bond lengths can be justified by the 6-membered metallacycles that ligand **20** can form with Ru(II). In contrast, ligand **17**, which makes 5-membered metallacycles, coordinates closer to the central metal, thus, it contains shorter Ru-S bond lengths.

II.2.1. Heteroleptic Ru(II) complex

In order to force the thioanisole ligand **20** to coordinate in a planar fashion and thus obtain a *meridional* octahedral geometry around the central ruthenium cation, a heteroleptic complex (**22**) was prepared using one thioanisole ligand **20** and one terpyridine ligand.

The heteroleptic Ru(II) complex **22** was prepared using the same protocol as for the previously prepared heteroleptic Ru(II) complexes (**13**, **16** and **19**), by refluxing a one-to-one molar equivalents of ligand **20** and [Ru(tpy)Cl₃] precursor for 4 hours in the presence of excess lithium chloride in an ethanol-water solution led to complexation. The orange-red colored heteroleptic complex **22** was obtained in 42% yield and isolated as a hexafluorophosphate salt after silica gel column chromatography followed by anion exchange with a saturated aqueous solution of KPF₆, as shown in Scheme 5.3.



Scheme 5.4. The heteroleptic Ru(II) complex **22** synthesis.

The isolated complex **22**, with molecular formula $[\text{Ru}(\mathbf{20})(\text{tpy})](\text{PF}_6)_2$, was characterized by ESI-mass spectrometry. In the spectrum, a mass peak at $m/z = 329.04$ with 2+ charge was detected, which matches with $[\text{Ru}(\mathbf{20})(\text{tpy})]^{2+}$ (m/z calculated to be 329.04), in addition to the observation of peak at $m/z = 803.04$ with 1+ charge, which matches with $[\text{Ru}(\mathbf{20})(\text{tpy})](\text{PF}_6)^+$ (m/z calculated to be 803.04).

The symmetrical nature and *mer* coordination of the thioanisole ligand in complex **22** was deduced directly from the $^1\text{H-NMR}$ spectrum, as shown in Figure 5.6.

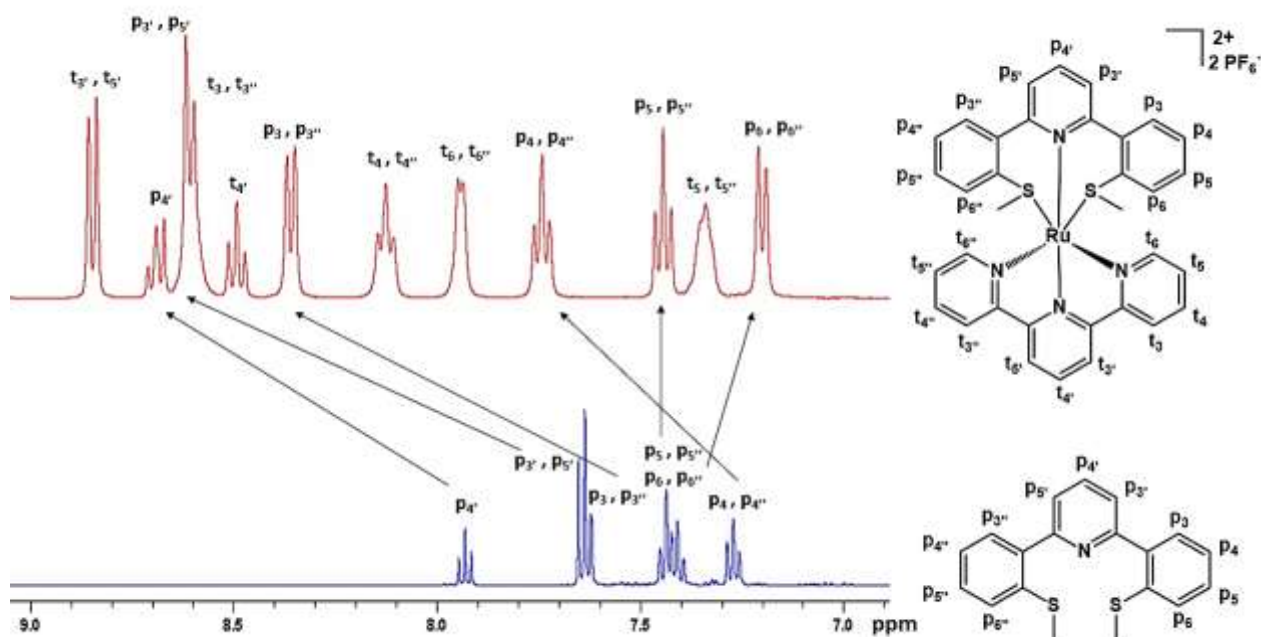


Figure 5.14. $^1\text{H-NMR}$ spectra of ligand **20** (bottom) and its heteroleptic Ru(II) complex **22** (top), recorded in D_6 -acetone on a 500 MHz NMR spectrometry.

Both ligand **20** and the terpyridine ligand display signals corresponding to half of the molecule (in contrast to the homoleptic complex **21** which has a *fac* geometry). Moreover, all proton signals of both ligands on the complex **22**, recorded in deuterated acetone on a 500 MHz NMR spectrometer, were assigned and attributed on its $^1\text{H-NMR}$ spectrum as shown above in Figure 5.6.

Slow diethylether vapor diffusion into an acetone solution of the heteroleptic complex **22** allowed for the growth of an orange-red needle shaped single crystals.

Subsequently, an X-ray diffraction experiment was performed, and the *mer* geometry of complex **22** was verified, supporting the $^1\text{H-NMR}$ spectral analysis (Figure 5.7).

Different structural perspectives of complex **22**, with atom labeling, are shown in Figure 5.7.

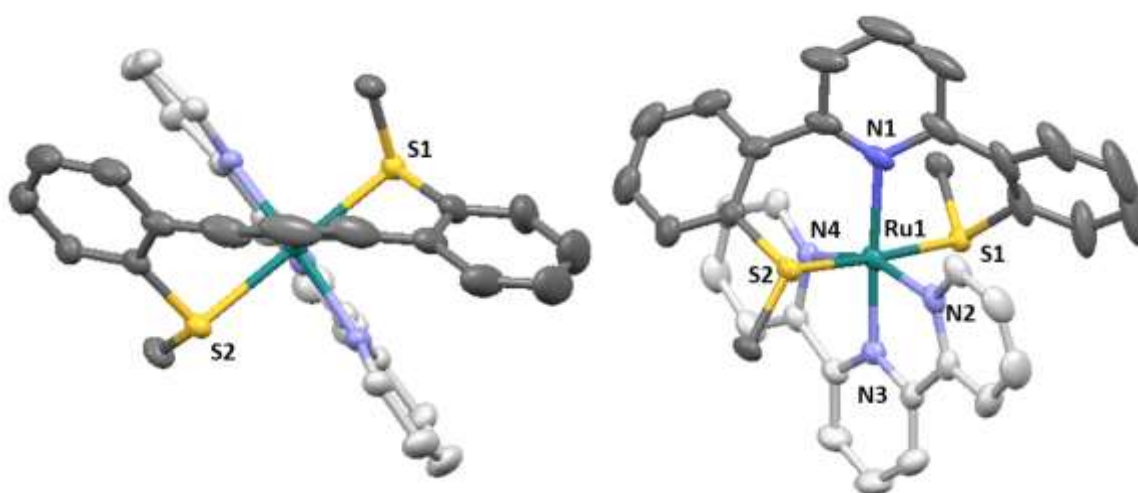


Figure 5.15. Different views of the heteroleptic complex **22** (40% ellipsoids). Solvent molecules, H-bonds, and PF_6^- counter anions are omitted for clarity.

All the selected bond lengths and selected bond angles measurements are collected in Table 5.2, and analyzed with respect to the reference complex $[\text{Ru}(\text{tpy})_2](\text{PF}_6)_2$.⁴

Table 5.8. Selected bond angles and bond lengths of the complexes **22** of molecular formula [Ru(**20**)(tpy)](PF₆)₂, and [Ru(tpy)₂](PF₆)₂.

Complex	[Ru(20)(tpy)](PF ₆) ₂	[Ru(tpy) ₂](PF ₆) ₂
Angle (°)		
N1 Ru1 S1	90.80(13)	
N1 Ru1 S2	85.11(10)	
S1 Ru1 S2	175.83(9)	
N3 Ru1 N2	79.32(14)	79.5(3)
N3 Ru1 N4	78.79(13)	79.0(3)
N2 Ru1 N4	157.94(14)	158.4(3)
N1 Ru1 N3	176.23(14)	
Bond length (Å)		
Ru1 N1	2.134(3)	
Ru1 S1	2.3317(17)	
Ru1 S2	2.3375(11)	
Ru1 N3	1.964(3)	1.981(7)
Ru1 N2	2.106(3)	2.079(6)
Ru1 N4	2.082(3)	2.067(7)

From the crystal structure (Figure 5.7) and the measured bond lengths and bond angles (Table 5.2), the heteroleptic complex clearly has a *mer* geometry, and both sulfur atoms of the SNS ligand, in addition to the two central pyridine rings of each ligand are in *trans* positions with approximate trans chelation angles S1-Ru-S2 around 175.83° and N1-Ru-N3 around 176.23°, respectively. These trans chelation angles of both sulfur atoms show again how 6-membered metallacycles open the coordination cavity to obtain a geometry close to a perfect octahedron. The S-Ru-S bond angle was expanded by around 9° in comparison to that obtained for complex **19** with one thioether ligand **17** which coordinates to Ru(II) with 5-membered metallacycles. The tpy ligand in this complex (which forms 5-membered

metallacycles) has the same distorted trans chelation angle as its parent complex, $[\text{Ru}(\text{tpy})_2](\text{PF}_6)_2$, even though in the heteroleptic complex, the tpy ligand coordinates closer to Ru(II) metal with 0.017 Å Ru-N3 bond length reduction.

Additionally, all the selected Ru-S bonds are longer by approximately 0.23-0.25 Å relative to the Ru-N bonds, which is in agreement with the length of most Ru-S bonds reported in the literature.³

Furthermore, from the crystal structure we can clearly see the high degree of flexibility of this new ligand, by its dramatic torsion angle of around 68° between the planes formed by both phenyl rings. This flexibility would be the main factor to have a photochemically active bis-tridentate Ru(II) complex, to the best of our knowledge. Bis-tridentate Ru(II) complexes are usually more stable and non-photochemically active as it is known and described before with the tris-bidentate Ru(II) complexes.

III. Electrochemistry

The electrochemical behavior of ligand **20**, as well as its corresponding Ru(II) metal complexes (**21** and **22**) were investigated by cyclic voltammetry, in a supporting electrolyte solution composed of 0.1 M tetrabutylammonium hexafluorophosphate in deaerated acetonitrile solution.

All the peak potentials obtained from the cyclic voltammograms, shown in Figure 5.8 and Figure 5.9 for ligand **20** and for both Ru(II) complexes respectively, were collected and displayed in Table 5.3, below.

The measured potentials of both ligand **20** and its corresponding Ru(II) metal complexes (in black) were analyzed, respectively, in comparison to the potentials obtained for the thioether ligand **17** and its Ru(II) metal complexes (gray), and to the potentials reported for the terpyridine ligand and its homoleptic complex $[\text{Ru}(\text{tpy})_2]^{2+}$.^{5,6}

Table 5.9. The obtained redox potentials of ligand **20** and its corresponding Ru(II) complexes (**21** and **22**), in black, in comparison to that obtained of the thioether ligand **17** and its Ru(II) complexes (**18** and **19**), in gray. $E_{1/2}$ (V) = $(E_{pa} + E_{pc})/2$, $(\Delta E_p$ (mV) = $E_{pc} - E_{pa}$) vs $Ag^+(0.01\text{ M})/Ag$. *Irreversible redox process.

Compounds	$E_{1/2}$ Reduction (ΔE_p , mV)		$E_{1/2}$ Oxidation (ΔE_p , mV)		
$[Ru(tpy)_2]^{2+}$	-1.83 (70)	-1.57 (60)	0.97 (80)		
19	-2.39*	-1.74 (64)	-1.19*	1.01 (61)	
22	-2.24*	-2.16*	-1.82 (60)	-1.56*	1.14 (60)
18	-1.35*		-1.16*	1.22 (170)	
21	-2.72*	-2.49*	-1.65*	1.39 (70)	
17	-2.67*		-1.99 (90)	0.86*	1.18*
20	-2.85*		-2.71*	0.83*	1.40*
tpy	-2.95 (221)	-2.36 (151)			

The HOMO-LUMO energy gap of both homoleptic and heteroleptic Ru(II) complexes with the thioanisole ligand **20** can be measured, 3.04 eV and 2.70 eV respectively, based on the electrochemical data. The energies needed to expel an electron from the HOMO, which is globally localized on Ru(II), were deduced from the first oxidation wave potentials in the anodic region, whereas the energies needed to add an electron to the LUMO, which is globally localized on the different ligands, were deduced from the first reduction wave potentials in the cathodic region both each complex.

III.1. Thioanisole ligand redox properties

The cyclic voltammogram of the flexible thioanisole ligand **20** is presented in Figure 5.8.

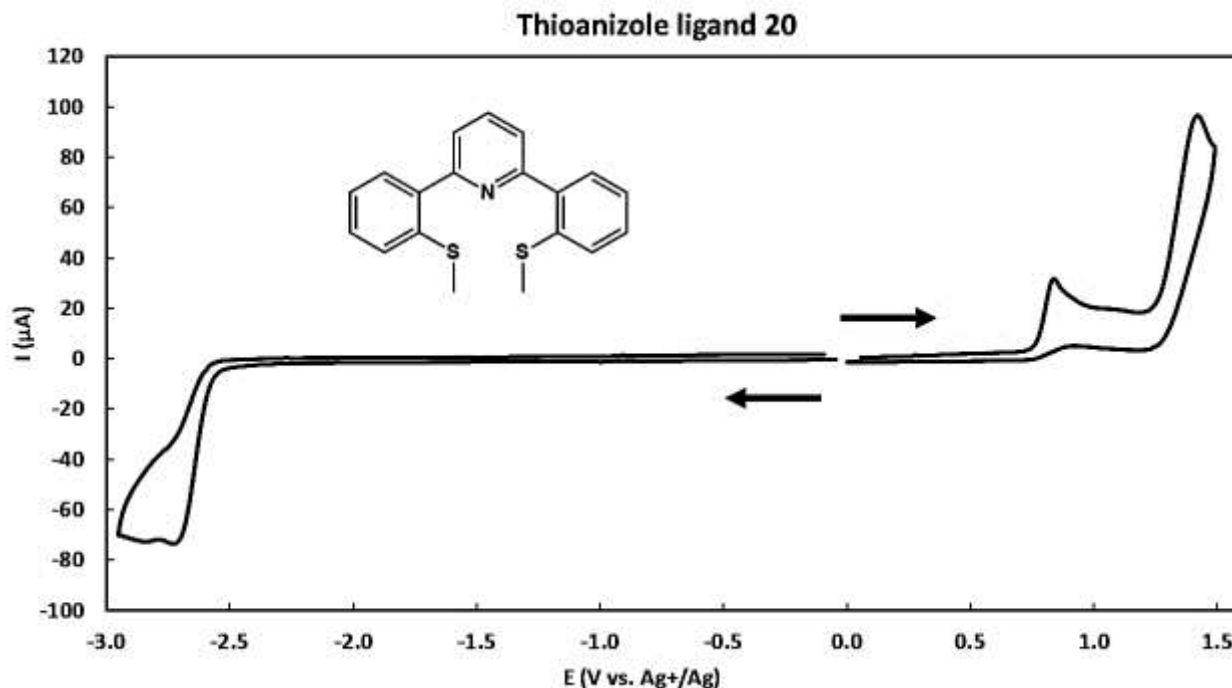


Figure 5.16. Cyclic voltammogram of the thioanisole ligand **20** (10^{-3} M) in deaerated acetonitrile solution containing 0.1 M of TBAPF₆, at a scan rate of $100 \text{ mV}\cdot\text{s}^{-1}$ using vitreous carbon working electrode (5 mm diameter), $E_p(\text{V})$ vs AgNO_3 (0.01 M)/Ag.

From the cyclic voltammogram (Figure 5.8), it is clear that the SNS free ligand **20** exhibits two successive irreversible oxidation waves at $E_{pa} = 0.83 \text{ V}$ and $E_{pa} = 1.40 \text{ V}$, in the same range as the previously described thioether ligand **17**. These two oxidation processes could occur globally on the thioanisole arms of the ligand **20**, by considering that the energy needed to oxidize a free pyridine ring ($1.6 \text{ V vs Ag}^+/\text{Ag}$ in acetonitrile solution)⁷ is 1.5 fold greater than the energy needed to oxidize the free thioanisole compound ($1.1 \text{ V vs Ag}^+/\text{Ag}$ in acetonitrile solution).⁸

Moreover, two successive irreversible reduction processes were observed in the cathodic region of the ligand **20**'s cyclic voltammogram at $E_{pc} = 2.71 \text{ V}$ and $E_{pc} = 2.85 \text{ V}$. Such low reduction potential values indicate how difficult it is to reduce the thioanisole ligand **20** in comparison to both the thioether ligand **17** and the free tpy ligand (which have less negative reduction potential values relative to ligand **20**). Therefore, the thioanisole ligand **20** has the highest π^* -energy orbital in comparison to the tpy ligand and the thioether ligand **17**.

III.2. Redox properties of the Ru(II) complexes

The cyclic voltammograms of the Ru(II) complexes **21** and **22** are presented in Figure 5.9.

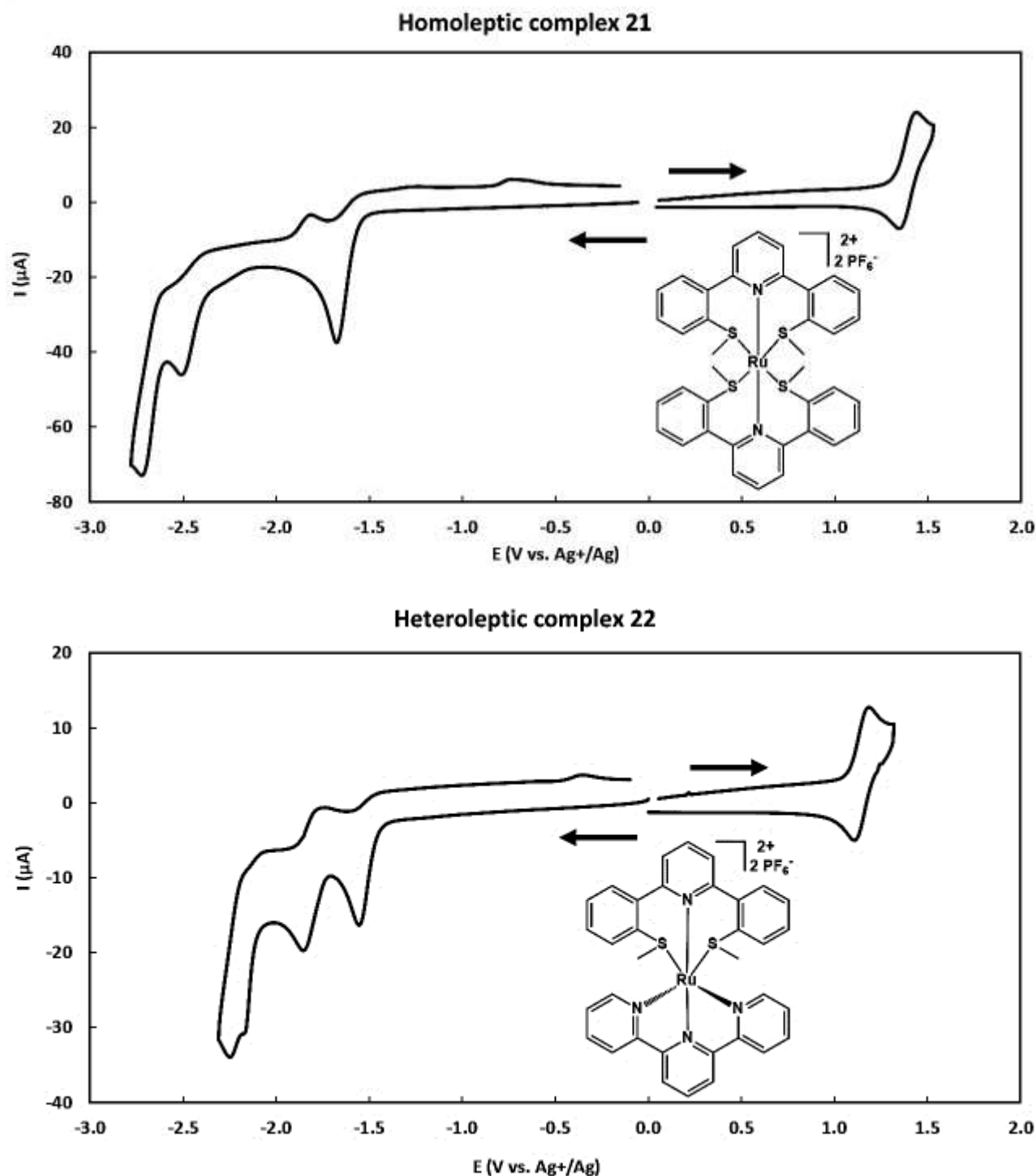


Figure 5.17. Cyclic voltammograms of the homoleptic complex **21** (top), and the heteroleptic complex **22** (bottom) at 10^{-3} M concentrations in deaerated acetonitrile solution with 0.1 M of TBAPF₆, at a scan rate of $100 \text{ mV}\cdot\text{s}^{-1}$ using vitreous carbon working electrode (5 mm diameter), $E_p(\text{V})$ vs AgNO₃ (0.01 M)/Ag.

The effect of the flexible thioanisole ligand **20** on the $\text{Ru}^{3+}/\text{Ru}^{2+}$ redox potential in complexes **21** and **22** was analyzed, based on comparison to the $\text{Ru}^{3+}/\text{Ru}^{2+}$ couple potential for the $[\text{Ru}(\text{tpy})_2]^{2+}$ parent complex and that obtained with the planar, acridine-based thioether $\text{Ru}(\text{II})$ complexes **18** and **19**.

The heteroleptic complex **22** with molecular formula $[\text{Ru}(\mathbf{20})(\text{tpy})]^{2+}$ shows a fully reversible oxidation potential at $E_{1/2} = 1.14$ V of $\Delta E_p = 60$ mV. Thus, as one thioanisole ligand **20** replaces one tpy ligand of the $[\text{Ru}(\text{tpy})_2]^{2+}$ complex, the oxidation potential of complex **22** increased by 170 mV, which is more important than the effect of the thioether ligand **17** in complex **19** (increased by 40 mV relative to the parent $[\text{Ru}(\text{tpy})_2]^{2+}$). The greater effect of ligand **20** over ligand **17** in increasing the oxidation potential of $\text{Ru}(\text{II})$ metal can be justified by the greater π -accepting ability of the linearly coordinated sulfur atoms in complex **22** (S-Ru-S is $\approx 176^\circ$) with respect to those in complex **19** which has a smaller S-Ru-S trans chelation angle ($\approx 167^\circ$), as shown in Figure 5.10. Therefore, complex **19** will have less π - d_{xy} orbital alignment, which results in less efficient π -back donation from the central metal to the coordinated ligand **17**. For that reason, the $\text{Ru}(\text{II})$ metal in complex **22** is more electron deficient than in complex **19**, and consequently, more energy is needed to oxidize the $\text{Ru}(\text{II})$ central metal in complex **22**.

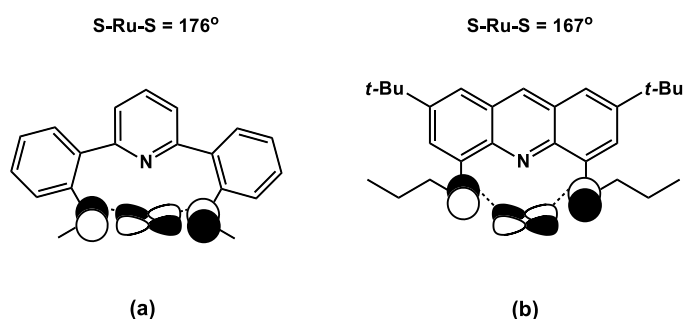


Figure 5.18. Schematic illustration of the $\pi_{(L)}-d_{xy}$ orbitals alignment between the $\text{Ru}(\text{II})$ central metal and the thioanisole ligand **20** (a), the thioether ligand **17** (b).

Furthermore, as the second terpyridine ligand is replaced by another thioanisole ligand **20**, to form the homoleptic complex **21** with molecular formula, $[\text{Ru}(\mathbf{20})]^{2+}$, the oxidation potential of the $\text{Ru}^{3+}/\text{Ru}^{2+}$ couple increased further by 250 mV to have a fully reversible oxidation process at $E_{1/2} = 1.39$ V with $\Delta E_p = 70$ mV. As a result, this thioanisole ligand **20** has a greater

electronic effect in comparison to the thioether ligand **17** by increasing the energy needed to oxidize the Ru(II) central metal.

All the reduction processes, which mainly take place on the π^* -orbitals of the different ligands in both Ru(II) complexes **21** and **22**, could be assigned in the cathodic regions of both complexes' cyclic voltammograms.

The homoleptic complex **21** shows three successive irreversible reduction waves at $E_{pc} = -1.65$ V, -2.49 V, and -2.72 V. These reduction potentials are attributed to the thioanisole reduction processes occurring on each ligand. As expected, all of these reduction potentials on complex **21** are more negatively shifted in comparison to those obtained with complex **18** due to the π^* -orbitals energy differences between both free ligands, as explained before.

The heteroleptic complex **22** shows one monoelectronic irreversible reduction potential at $E_{pc} = -1.56$ V and one monoelectronic reversible reduction potential at $E_{1/2} = -1.82$ V with $\Delta E_p = 60$ mV. The first irreversible reduction peak can be attributed to the thioanisole ligand **20** reduction process, whereas, the reversible one is attributed to the terpyridine ligand reduction process. This result is deduced based on the free ligands' redox potentials, in which the thioanisole ligand is more electron rich than tpy ligand. Thus, in the heteroleptic complex **22** the thioanisole ligand plays the role of electron donor, whereas the tpy ligand would be the electron acceptor via electronic communication between both ligands through the ruthenium central metal. Therefore, with such push-pull ligands set, the electron donor-thioanisole ligand would be easier to reduce, and the electron acceptor-tpy ligand would be more difficult to reduce. Moreover, two overlapped irreversible reduction potentials were observed at $E_{pc} = -2.16$ V and $E_{pc} = -2.24$ V, in which these two processes could be attributed to the reduction processes of both tpy and thioanisole ligands.

Lastly, both the thioanisole ligand and the tpy ligand displayed reduction potentials toward less negative values when they are coordinated to the ruthenium metal. This observation is justified by the lone pair donation from the ligands' heteroatoms to the central metal upon complexation, thus, less electron density is present on both ligands and consequently, easier reduction processes were observed.

IV. Photophysics

The photophysical properties of the free ligand **20** and its Ru(II) metal complexes were measured and investigated in deaerated acetonitrile solution at room temperature, as well as in a frozen butyronitrile matrix at 77 K.

All the recorded photophysical data for each compound are collected in Table 5.4.

IV.1. Thioanisoie ligand spectroscopic properties

The absorption spectrum of ligand **20** recorded in acetonitrile is illustrated in Figure 5.11-(a), and its emission spectra at both room temperature and 77 K are presented in Figure 5.11-(b).

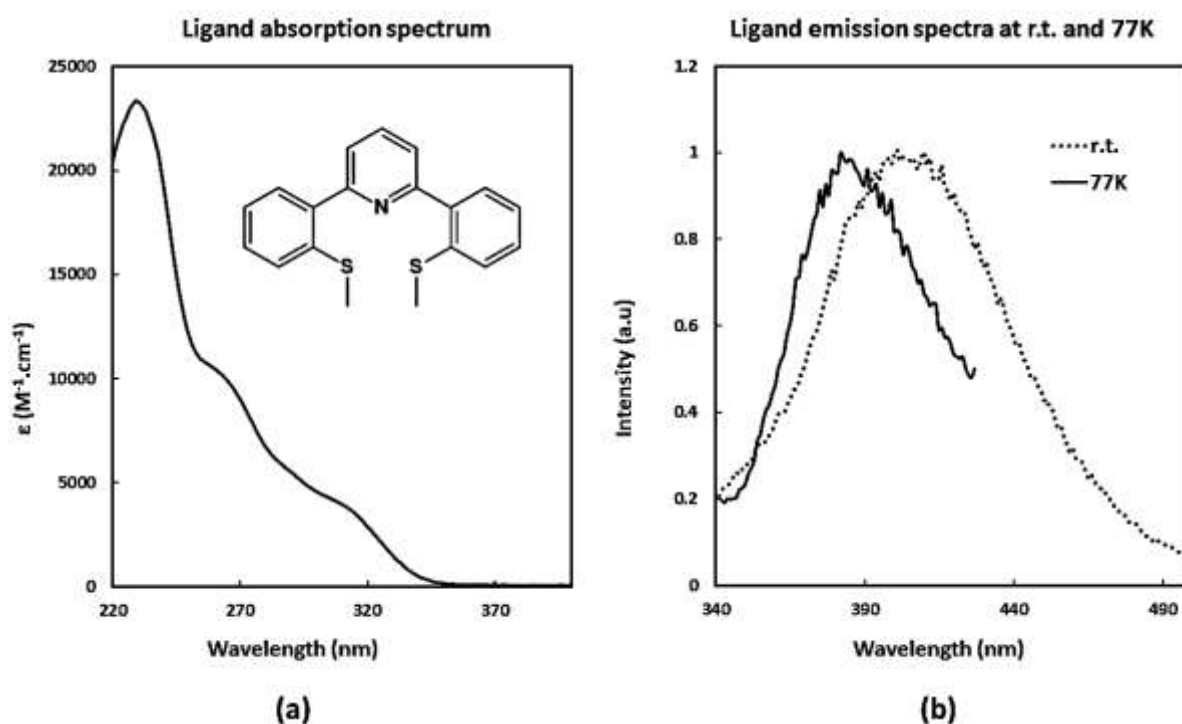


Figure 5.19. Absorption (a) and emission (b) thioanisoie ligand **20** spectra.

In the absorption spectrum (Figure 5.11-(a)), the flexible thioanisoie ligand **20** absorbs exclusively in the UV-region, unlike all the highly conjugated and rigid acridine-based ligands (**11**, **14** and **17**), which absorbed in the UV and visible regions.

Ligand **20** exhibits a strong absorption in the range between 220 nm and 350 nm, with a maximum wavelength centered at 229 nm having a molar absorption coefficient of $2.33 \times 10^4 \text{ M}^{-1} \text{ cm}^{-1}$. This $\pi\text{-}\pi^*$ transition on ligand **20** is highly blue shifted relative to what was obtained with the thioether ligand **17**, which absorbs at 275 nm. This higher energetic absorption of ligand **20** is justified by the larger $\pi\text{-}\pi^*$ energy gap for this less conjugated ligand with higher π^* orbital energy, in agreement with the obtained redox potentials.

The fluorescence properties of this ligand were investigated and measured at room temperature and 77 K after excitation 317 nm, as shown in Figure 5.11-(b). A fluorescence emission was detected at 404 nm in an acetonitrile solution at room temperature, as the ligand was excited in the UV-region, with an emissive excited state lifetime of 7.6 ns. This fluorescence emission was blue shifted to 382 nm at 77 K in a frozen butyronitrile solution, and has an emissive excited state lifetime of 3.7 ns.

IV.2. Ru(II) complexes spectroscopic properties

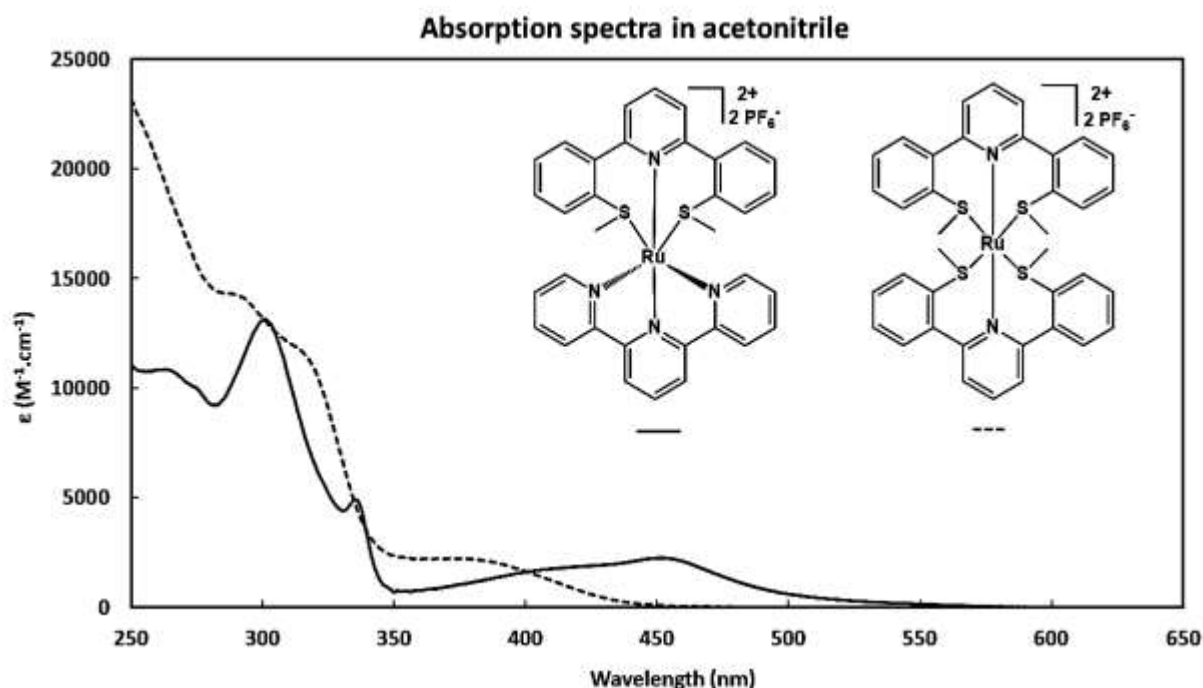


Figure 5.20. Absorption spectra of the homoleptic Ru(II) complex **21** (dotted) and the heteroleptic Ru(II) complex **22** (solid line) in deaerated acetonitrile solution.

The absorbance spectra of both the homoleptic complex **21** and the heteroleptic complex **22** were recorded in deaerated acetonitrile solution ($C = 10^{-5}$ M) and shown in Figure 5.12.

Both Ru(II) complexes show a strong spin-allowed, ligand centered (LC) transition in the UV region. The homoleptic complex **21** (dotted line) displays two absorption bands with wavelength maxima at 290 nm and 319 nm and molar absorption coefficients of 1.40×10^4 $M^{-1} \text{ cm}^{-1}$ and 1.10×10^4 $M^{-1} \text{ cm}^{-1}$, respectively. These bands are attributed to the π - π^* transition on the coordinated thioanisole ligand **20**. In contrast, the heteroleptic complex **22** (solid line) displays three absorption bands with wavelength maxima at 263 nm, 301 nm, and 335 nm with molar absorption coefficients $\epsilon = 1.08 \times 10^4$, 1.31×10^4 and 0.49×10^4 $M^{-1} \text{ cm}^{-1}$, respectively. The first two energetic bands could be attributed to the π - π^* transition on ligand **20** of higher π^* orbital energy, while the third one at 335 nm could be attributed to the transition on the tpy ligand (in the same range of ϵ as $[\text{Ru}(\text{tpy})_2]^{2+}$).

The metal to ligand charge transfer (MLCT) transition of both complexes were assigned in the visible region. The moderately intense MLCT band of the homoleptic complex **21** was centered at 390 nm (3.18 eV) with a molar absorption coefficient of 2.00×10^3 $M^{-1} \text{ cm}^{-1}$. The MLCT band of the heteroleptic complex **22** was red shifted relative to the homoleptic complex **21**, expanding from 350 nm to 550 nm, with two maxima at 411 nm ($\epsilon = 1.80 \times 10^3$ $M^{-1} \text{ cm}^{-1}$) and 451 nm ($\epsilon = 2.20 \times 10^3$ $M^{-1} \text{ cm}^{-1}$), in which the higher energy transition (at 411 nm) corresponds to the transition from the metal to the tpy ligand, and the second one at 451 nm (2.75 eV) corresponds to the transition from the metal to the thioanisole ligand (in agreement with the electrochemical data analysis above for the heteroleptic complex **22**). Both MLCT transitions from the metal to the thioanisole ligand in both complexes are in agreement with the HOMO-LUMO energy gap calculated depending on the measured electrochemical potentials (3.04 eV and 2.75 eV for complex **21** and complex **22** respectively).

The MLCT bands of these two complexes were blue shifted in comparison to all the MLCT bands observed for all the Ru(II) complexes described earlier in this thesis. This blue shifting is justified by the large HOMO-LUMO energy gap in both complexes **21** and **22** relative to all other complexes, in agreement with the electrochemical data (most negative LUMO reduction potentials and most positive HOMO oxidation potentials). Moreover, the

homoleptic complex **21** has the largest HOMO-LUMO energy gap, and accordingly, it has an even more energetic MLCT band relative to the heteroleptic complex **22**.

The luminescence properties of complexes **21** and **22** were investigated in deaerated acetonitrile solution at room temperature and in butyronitrile rigid matrix at 77 K, after excitation at their ¹MLCT obtained in the visible region. As expected, the geometrically distorted (*fac*) homoleptic complex **21** did not display any emission under either set of conditions. However, the heteroleptic *mer* complex **22** shows a very weak emission at 582 nm with an excited state lifetime of 146 ns at 77 K, with no detected emission at room temperature. The mediocre emissive properties of these complexes based on the thioanisole ligand **20**, is similar to the result obtained with the Ru(II) complexes based on the thioether ligand **17**, and most of the Ru(II) complexes with sulfur-containing chelates found in the literature, showing the quenching effect of sulfur atoms on the luminescence properties.^{9,10}

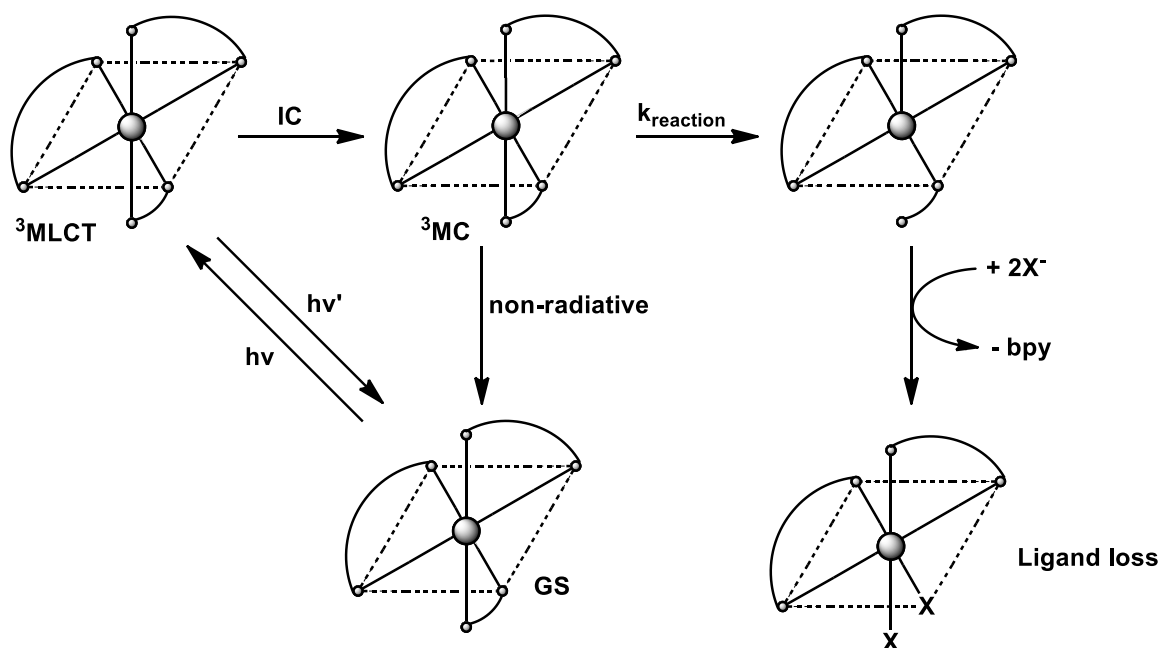
All the spectroscopic data are collected in the Table 5.4, below.

Table 5.10. Spectroscopic data of the free ligand **20** and its Ru(II) complexes **21** and **22** in a deaerated acetonitrile solution.

Compounds	λ_{abs} , nm (ϵ , M ⁻¹ cm ⁻¹)	Room temperature		77 K	
		λ_{em} , nm	τ , ns	λ_{em} , nm	τ , ns
[Ru(20) ₂] ²⁺ (21)	290 (14,000), 319 (11,000), 390 (2,000)				
[Ru(tpy)(20)] ²⁺ (22)	263 (10,800), 301 (13,100), 335 (4,900), 411 (1,800), 451 (2,200)			582	146
20	229 (23,300), 265 (9,900), 317 (3,300)	404	7.6	382	3.7

V. Photochemistry

As it has been discussed before by V. Balzani and others, most of the tris-bidentate Ru(II) complexes (i.e. $[\text{Ru}(\text{bpy})_3]^{2+}$) which have low photostability, possess longer bonds in the ground state¹¹ and ^3MC excited state,¹² and undergo a photoinduced ligand dissociation upon white light irradiation (Scheme 5.4).



Scheme 5.4. Proposed mechanistic pathway of the photoinduced bpy ligand dissociation from the tris-bidentate $[\text{Ru}(\text{bpy})_3]^{2+}$ complex. IC is internal conversion.¹¹

In the literature, several photoactive Ru(II) complexes based on bis-thioether or bis-imine chelating ligands have been studied photochemically. It has therefore been reported that their longer Ru-S and Ru-N bond lengths, respectively, induced by a decrease in their ligand field, allowing for a photosubstitution reaction of these ligands to take place efficiently upon visible light irradiation.^{13,14,15}

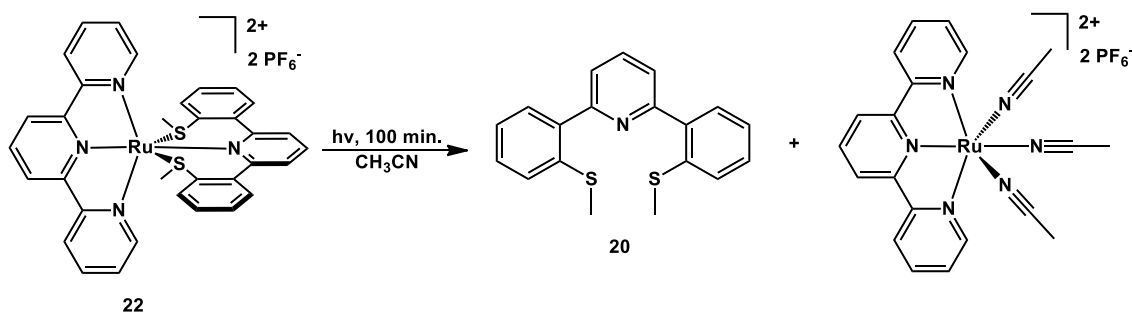
On the second hand, bis-tridentate Ru(II) complexes are usually more stable and non-photochemically active, in which no examples have been described before in the literature. Therefore, the photochemical activity of both Ru(II)-thioanisole complexes **21** and **22**, with their long Ru-S bonds, was studied. Interestingly, if they can undergo a ligand loss reaction through their non-emissive ^3MC excited states upon visible light irradiation, thus, we will

observe the first photochemically active, bis-tridentate Ru(II) complexes in the literature to the best of our knowledge.

V.1. Heteroleptic complex photoactivity

The bis-tridentate Ru(II) complex **22** with the molecular formula, $[\text{Ru}(\mathbf{20})(\text{tpy})](\text{PF}_6)_2$, displays a ligand loss reaction upon light irradiation in the visible region (400-700 nm), using a mono-fiber xenon lamp source with 1840 mW intensity.

In an acetonitrile solution of complex **22**, the ligand-solvent exchange reaction proceeded quantitatively within 100 minutes under white light exposure, in which, a thioanisole ligand was replaced by three acetonitrile solvent molecules, as shown in Scheme 5.5.



Scheme 5.5. The heteroleptic complex **22** photochemical ejection reaction.

The photoinduced thioanisole ligand ejection reaction from complex **22** was easily followed by UV-Visible spectroscopy, in which both the starting complex **22** and the newly formed $[\text{Ru}(\text{tpy})(\text{CH}_3\text{CN})_3](\text{PF}_6)_2$ complex have different absorption spectra. More interestingly, in the visible region, we can clearly see the gradual disappearance of the ¹MLCT (metal to thioanisole ligand charge transfer) band centered at 451 nm (Figure 5.13).

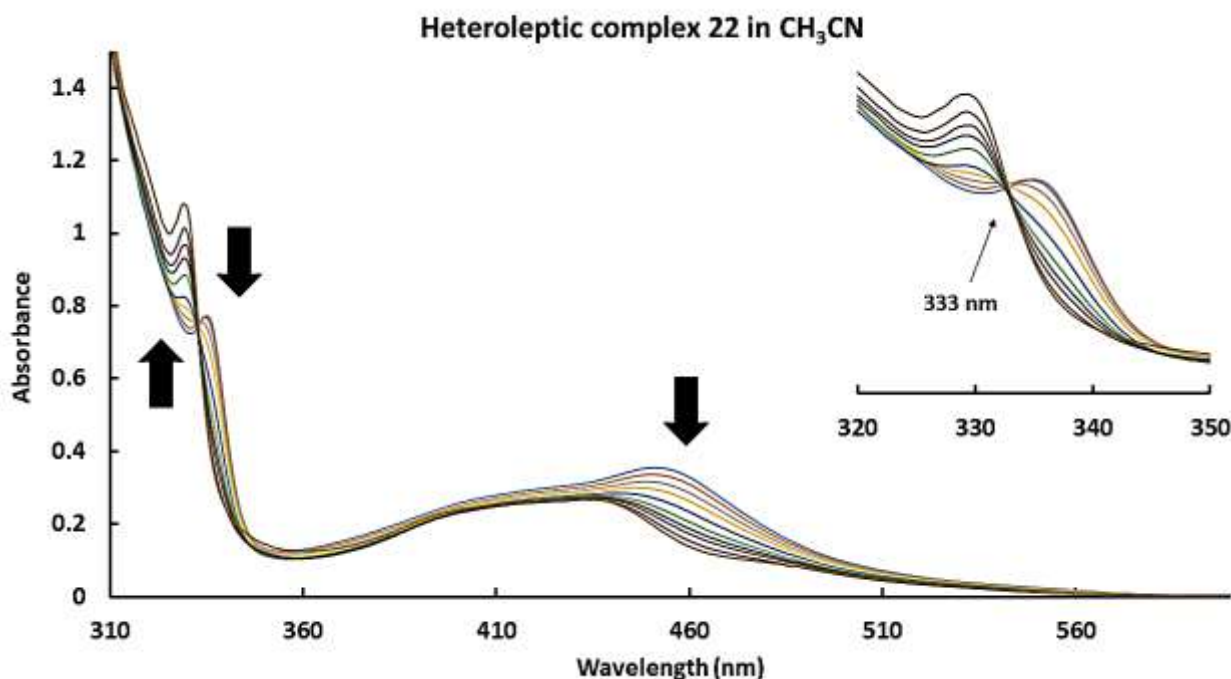


Figure 5.13. UV-Visible spectra following the ligand **20** ejection reaction from its heteroleptic complex **22**, upon white light irradiation using a xenon lamp in a solvent-ligand acetonitrile solution.

The UV-Visible spectra were displayed with a clear isobestic point at 333 nm, which indicates the single-step nature of the photo-dissociation reaction of the tridentate thioanisole ligand from complex **22**.

The short Ru-N_{pyridine} bond length compared to the Ru-S bonds length in the ground state ($\approx 2.13 \text{ \AA}$ for Ru-N_{pyridine} vs $\approx 2.33 \text{ \AA}$ for both R-S bonds) and in the ³MC excited state,¹² suggests that the Ru-S bonds are faster and more susceptible to photo-dissociate than the Ru-N bond. Therefore, the Ru-S bond dissociation would most likely be the initial step of the photochemical ejection reaction, followed by the Ru-N_{pyridine} bond dissociation (after rotation in space) to completely expel the flexible tridentate thioanisole ligand **20** from its Ru(II) complex **22**.

This photochemical reaction was also followed by ¹H-NMR spectroscopy as shown in Figure 5.14.

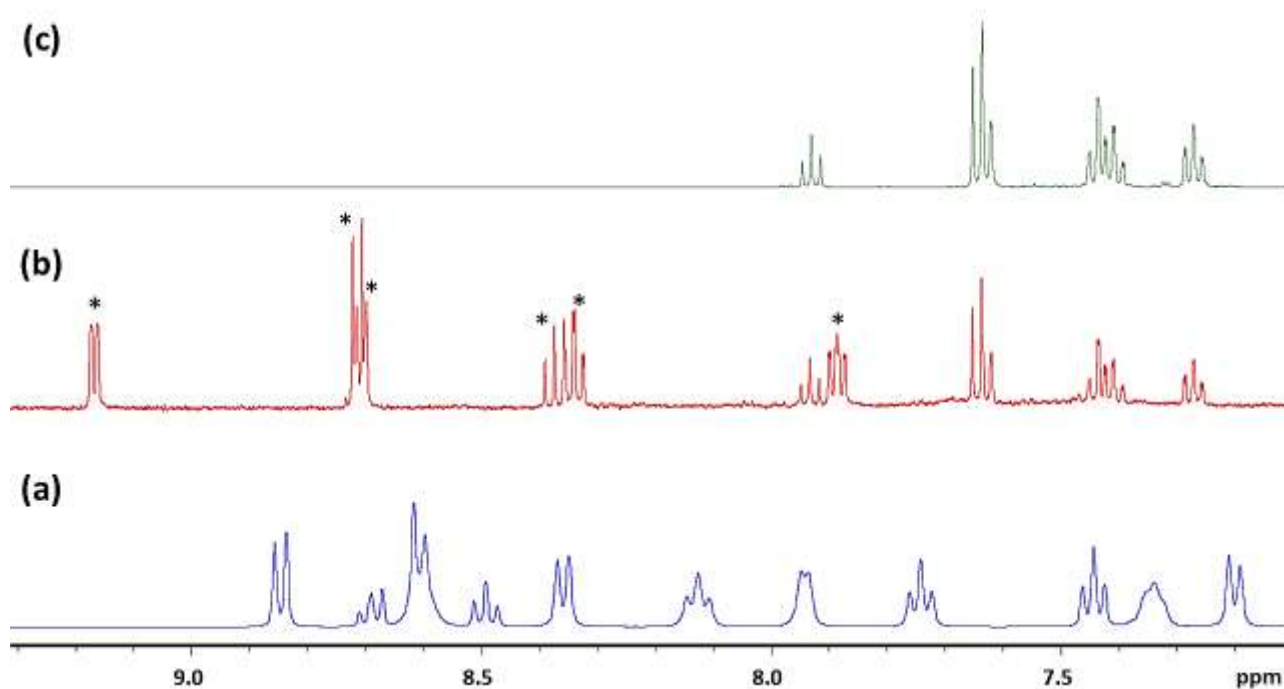


Figure 5.14. $^1\text{H-NMR}$ spectra recorded in D_6 -acetone at 500 MHz spectrometer for complex **22** at $t = 0$ min. (a), after 100 min. irradiation (b), and for comparison the free ligand **20** (c). *peaks corresponded to $[\text{Ru}(\text{tpy})(\text{CH}_3\text{CN})_3](\text{PF}_6)_2$ intermediate complex.

Monitoring and characterizing the photochemical reaction by $^1\text{H-NMR}$ spectroscopy was of great importance, especially in order to confirm the quantitative transformation of complex **22** (Figure 5.14-(a)) and to verify the end of the photo-ejection reaction by its chemical composition (i.e. no longer observing signals representing complex **22**).

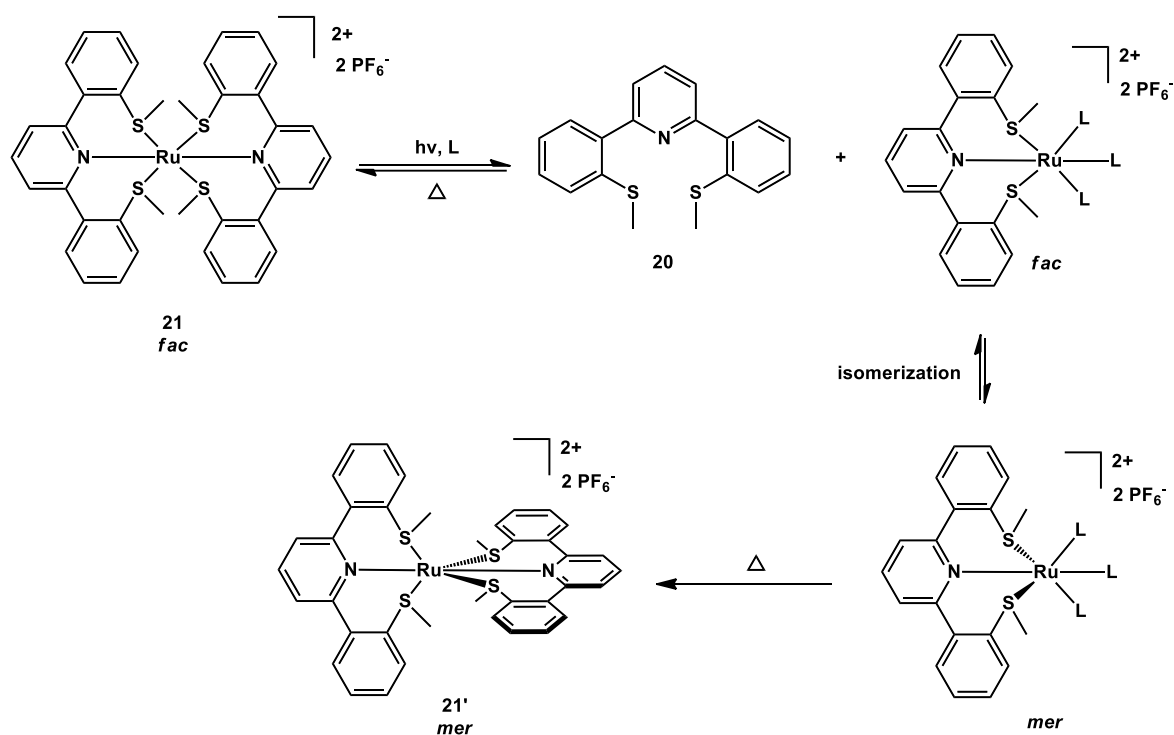
The $^1\text{H-NMR}$ spectrum of the solution after 100 minutes irradiation (Figure 5.14-(b)) corresponds to the superposition of the spectra of the free thioanisole ligand **20** (Figure 5.14-(c)) and the $[\text{Ru}(\text{tpy})(\text{CH}_3\text{CN})_3](\text{PF}_6)_2$ complex (denoted by stars), which is already reported in the literature.¹⁶ After 100 minutes' irradiation, nothing was changed either in the UV-Visible spectrum nor in the $^1\text{H-NMR}$ spectrum, indicating the end of the photochemical reaction.

Although the photo-ejection reaction was carried out in acetonitrile solution, the $^1\text{H-NMR}$ spectrum of the complex after irradiation was recorded in D_6 -acetone for clear comparison and analysis in reference to the previously recorded complex **22** and free thioanisole ligand in D_6 -acetone.

V.2. Homoleptic complex photoactivity

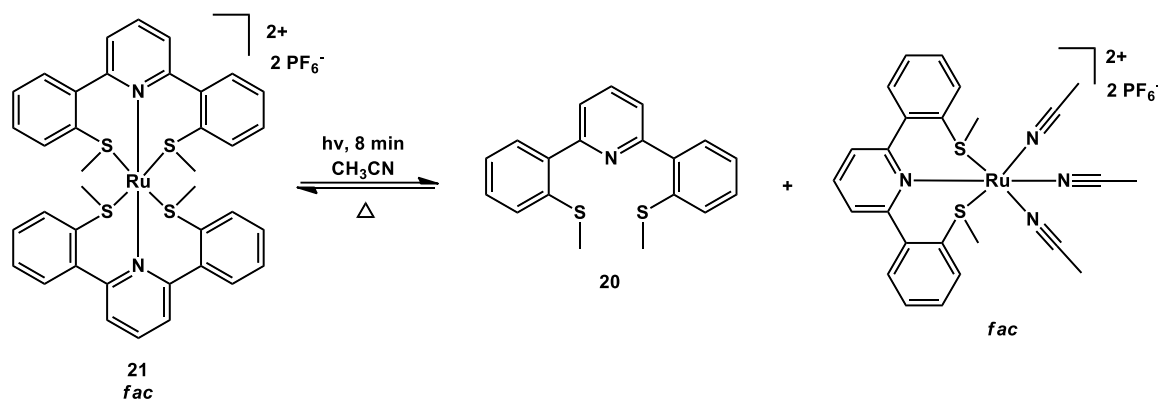
As the heteroleptic Ru(II) complex **22** undergoes a photochemical reaction, by losing one thioanisole ligand upon visible light irradiation, the same reaction, using the same conditions, was attempted with the bis-thioanisole homoleptic Ru(II) complex **21** which has the *facial* octahedral geometry.

Our initial goal was to see if this photoactive complex could change its octahedral geometry by changing from the *fac* to the *mer* homoleptic complex, as one thioanisole ligand is ejected by irradiation and then re-complexes thermally after the geometrical isomerization of the $[\text{Ru}(\mathbf{20})(\text{L})_3](\text{PF}_6)_2$ intermediate complex, as proposed in Scheme 5.6.



Scheme 5.6. Proposed pathway for complex **21** to go from its *facial* octahedral geometry to the *meridional* geometry, through photochemical-thermal successive reactions.

In an acetonitrile solution of complex **21**, the ligand-solvent exchange reaction between a thioanisole ligand and three acetonitrile solvent molecules was rapidly achieved within 8 minutes of light exposure using the same xenon lamp with 1840 mW intensity, Scheme 5.7, indicating the high degree of photoreactivity for complex **21** which adopts the *fac* geometry.



Scheme 5.7. The homoleptic complex **21** photochemical ejection and thermal complexation reactions.

The photochemical reaction, was followed by UV-Visible spectroscopy, as shown in Figure 5.15.

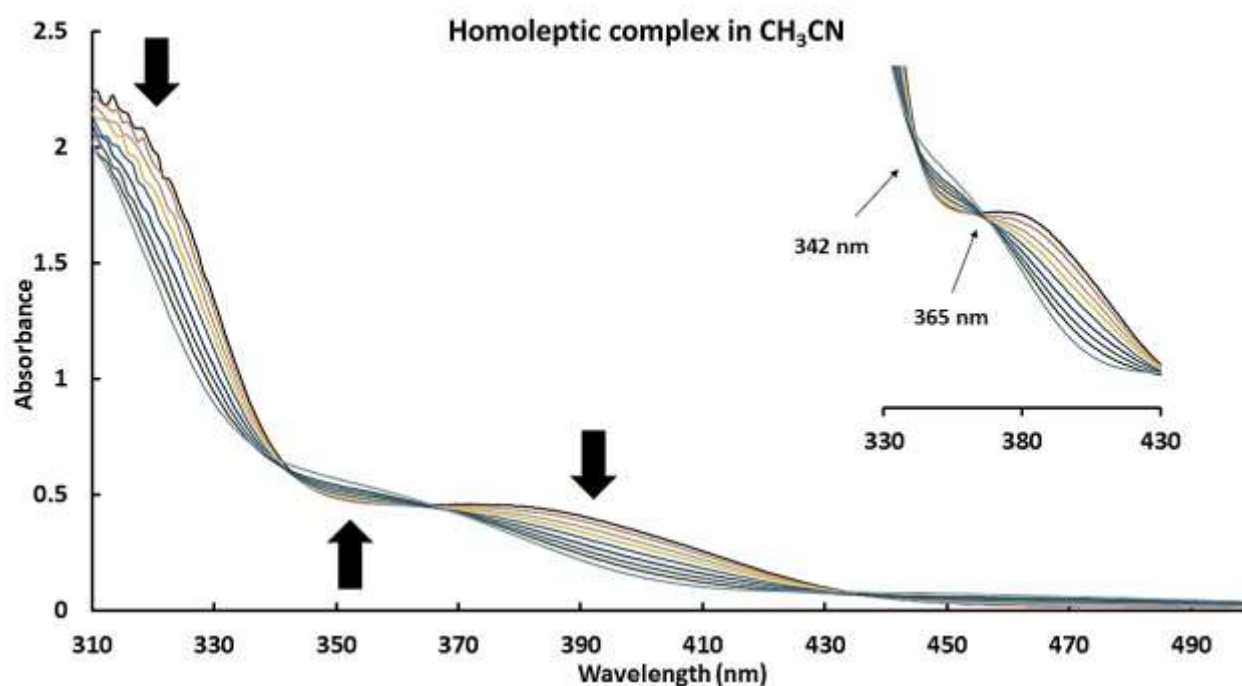


Figure 5.15. UV-Visible spectra following the ligand **20** ejection reaction from its homoleptic complex **21**, upon white light irradiation using a xenon lamp in a solvent-ligand acetonitrile solution.

In the visible region, the $^1\text{MLCT}$ (metal to thioanisole ligand charge transfer) at 390 nm gradually disappeared as the photo-ejection reaction proceeded, followed by the gradual appearance of a new $^1\text{MLCT}$ at 354 nm, which is globally corresponding to the MLCT transition of the created $[\text{Ru}(\mathbf{20})(\text{CH}_3\text{CN})_3]^{2+}$ intermediate complex.

The blue shift of the new $^1\text{MLCT}$ is attributed to the π -accepting nature of the CN groups from the Ru(II) central metal, resulting in stabilization of the HOMO, and consequently, a larger HOMO-LUMO energy gap is formed, leading to a more energetic transition.

Moreover, as it was described before, the ligand photo-ejection was performed in a multi-step photo-dissociation reaction, as evidenced by the absence of isosbestic points around 342 nm and 365 nm (Figure 5.15).

Moreover, this photochemical reaction was followed by $^1\text{H-NMR}$ spectroscopy (Figure 5.16).

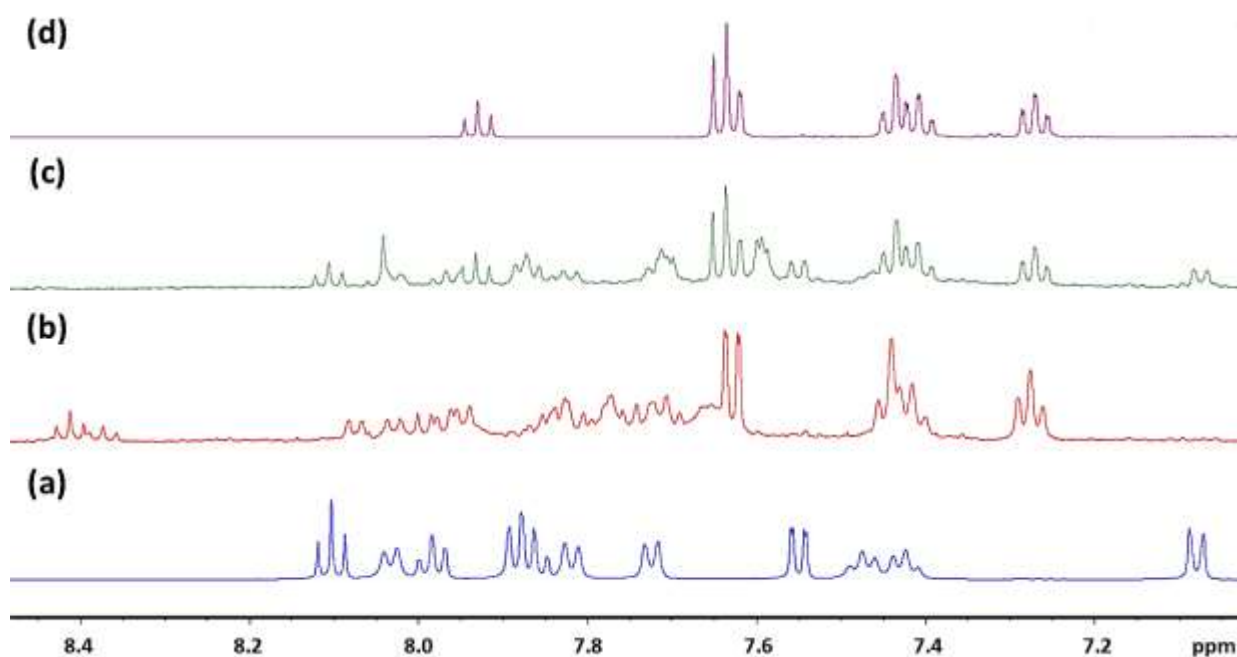


Figure 5.16. $^1\text{H-NMR}$ spectra recorded in D_6 -acetone with a 500 MHz spectrometer for complex **21** at $t = 0$ min. (a), after 8 min. irradiation (b), after thermal re-complexation reaction (c), and for comparison, the free ligand **20** (d).

The $^1\text{H-NMR}$ spectrum confirmed the total disappearance of complex **21**, in which, no more signals corresponding to complex **21** were present after 8 minutes of irradiation (Figure 5.16-(b)).

The chemical composition of the species obtained after irradiation was deduced from the ^1H -NMR spectrum (Figure 5.16-(b)), which shows the presence of the free thioanisole ligand **20** with set of peaks that probably could be attributed to the proposed $[\text{Ru}(\mathbf{20})(\text{CH}_3\text{CN})_3](\text{PF}_6)_2$ intermediate complex, and which is probably still adopting the *fac* octahedral geometry.

Therefore, a thermal re-complexation reaction was performed to verify the proposed hypothesis. Based on the recorded ^1H -NMR spectrum (Figure 5.16-(c)) after re-complexation reaction, the homoleptic complex was obtained again with the *fac* geometry and not with the *mer* one, contrary to our expectation proposed in Scheme 5.6. In consequence, verifying that the created intermediate complex preferred to stay in the *fac* geometrical design without any isomerization.

Moreover, in the re-complexation reaction, it also seems that some free ligand is still present (Figure 5.17-(c)), which suggests the fast degradation of the unstable intermediate $[\text{Ru}(\mathbf{20})(\text{CH}_3\text{CN})_3](\text{PF}_6)_2$ complex. When the reaction mixture was left for one hour under air atmosphere following irradiation, no signals were present in the ^1H -NMR spectrum except for those of the free ligand, verifying also the low stability of the created intermediate complex.

Another attempt of a monodentate ligand exchange reaction with the homoleptic complex **21** was performed, but using electron donating chloride ligands instead of solvent molecules. Going from acetonitrile electron withdrawing ligands to chloride electron donating ligands could change the reactivity of the intermediate complex, and allow the photo-isomerization reaction to proceed.

Accordingly, a 1,2-dichloroethane solution of complex **21**, with excess tetraethylammonium chloride was irradiated, using the same xenon lamp with 1840 mW intensity, for 8 minutes. As a result, a thioether ligand was ejected and an unidentified $[\text{Ru}^{\text{II}}(\mathbf{20})(\text{X})_3]$ complex was created (Scheme 5.8).

Moreover, it was difficult to follow the photochemical reaction by ^1H -NMR spectrum probably due to the formation of the paramagnetic ruthenium intermediate complex. Thus, in all spectra, only the free ligand was clearly observed.

In the thermal re-complexation reaction, the obtained $^1\text{H-NMR}$ spectrum did not show the re-formation of the homoleptic complex **21** again and just the free thioether ligand was observed.

The photochemical reaction was followed by UV-Visible spectroscopy, as shown in Figure 5.17.

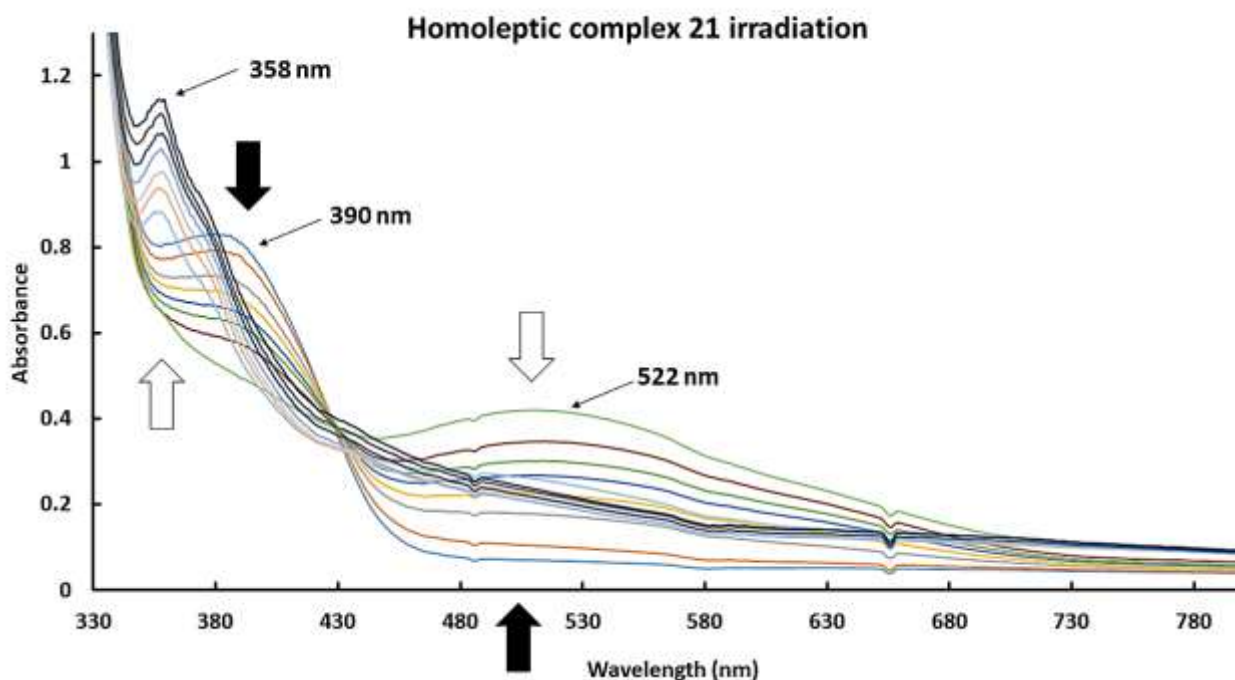


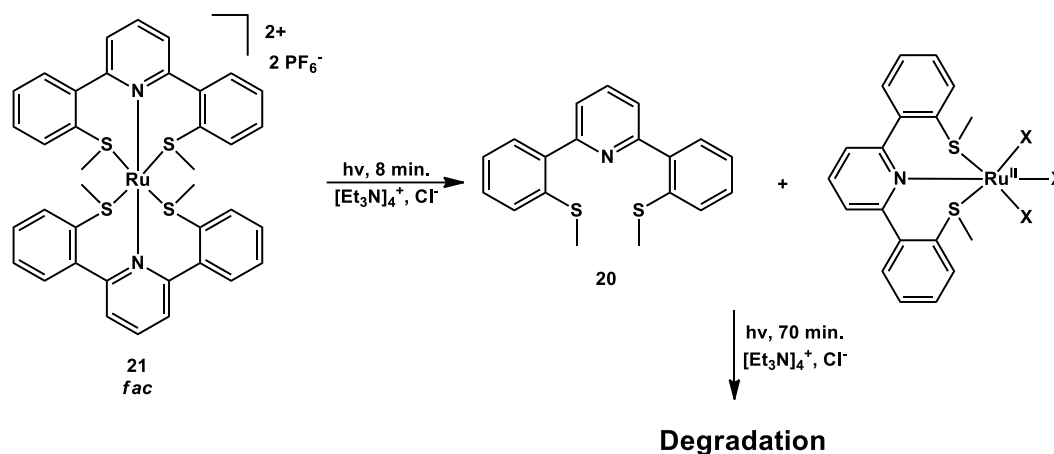
Figure 5.17. UV-Visible spectra following the ligands **20** ejection from its homoleptic complex **21**, upon white light irradiation using a xenon lamp in the presence of excess chloride.

In the visible region, during the first 8 minutes of the photo-ejection reaction, the $^1\text{MLCT}$ centered at 390 nm gradually disappears and then reappears with a red shift to 522 nm, which could be corresponding to the formation of the $[\text{Ru}^{\text{II}}(\mathbf{20})(\text{X})_3]$ intermediate complex (this behavior is denoted by the black arrows in Figure 5.17). The red shift of the $^1\text{MLCT}$ is attributed to the π electron donating effect of the Cl^- group on the central ruthenium metal, resulting in destabilization of the HOMO, and consequently, a smaller HOMO-LUMO energy gap and a less energetic transition.

As the photochemical reaction continues longer than 8 minutes, till 70 minutes of irradiation (this behavior is denoted by the white arrows in Figure 5.17), the $^1\text{MLCT}$ at 522 nm starts to

gradually disappear, which most probably could be attributed to the degradation of the intermediate $[\text{Ru}^{\text{II}}(\mathbf{20})(\text{X})_3]$ complex, followed by the gradual appearance of a new band in the UV region at 358 nm, which could not be attributed.

Therefore, this tridentate ligand Ru(II) complex was unstable and degrades upon irradiation in the presence of monodentate ligands, Scheme 5.8.



Scheme 5.8. The homoleptic complex **21** photochemical ejection reaction, in the presence of excess chloride anion.

Furthermore, as it was described before by the absence of an isosbestic point around 430 nm, the ligand photo-ejection occurs in a multi-step photo-dissociation reaction.

VI. Conclusion

Preparing a new thioether ligand capable of coordinating the central Ru(II) metal *via* the favorable 6-membered metallacycles was successful in opening the S-Ru-S trans chelation angle and obtaining a nearly perfect octahedral geometry, as shown clearly in the crystallographic structure of the obtained heteroleptic complex **22**. However, the homoleptic complex **21** still prefers the *facial*, distorted octahedral geometry.

Moreover, despite the fact that both Ru(II) complexes display an energetic metal to ligand charge transfer transition resulting from the large HOMO-LUMO energy gaps in agreement with the electrochemical data, they did not show any luminescence properties at room temperature nor at 77 K. This observation shows the effect of the coordinated sulfur atoms on quenching the emission properties of Ru(II) complexes.

More interestingly, having a high degree of structural flexibility on the ligand was of great importance, allowing its Ru(II) complexes to be photochemically active. Therefore, here we report the first bis-tridentate Ru(II) complexes, to the best of our knowledge, that have undergone photosubstitution reactions by monodentate ligands upon light irradiation.

This pioneering work could be of great importance for many potential applications. It can be a useful building block for promising light-driven molecular machines based on Ru(II) complexes,^{13,17} or could be used in photo-active chemotherapy for anticancer agents.¹⁸

VII. References

- (1) Abrahamsson, M.; Jäger, M.; Österman, T.; Eriksson, L.; Persson, P.; Becker, H. -christian.; Johansson, O.; Hammarström, L. A 3.0 Micro-Second Room Temperature Excited State Lifetime of a Bistridentate Ru(II)-Polypyridine Complex for Rod-like Molecular Arrays. *J. Am. Chem. Soc.* **2006**, *128*, 12616–12617.
- (2) Lenton, T. N.; VanderVelde, D. G.; Bercaw, J. E. Synthesis of a Bis(Thiophenolate)Pyridine Ligand and Its Titanium, Zirconium, and Tantalum Complexes. *Organometallics* **2012**, *31*, 7492–7499.
- (3) Page, M. J.; Wagler, J.; Messerle, B. A. Pyridine-2,6-Bis(Thioether) (SNS) Complexes of Ruthenium as Catalysts for Transfer Hydrogenation. *Organometallics* **2010**, *29* (17), 3790–3798.
- (4) Lashgari, K.; Kritikos, M.; Norrestam, R.; Norrby, T. Bis(Terpyridine) Ruthenium(II) Bis(Hexafluorophosphate) Diacetonitrile Solvate. *Acta Crystallogr. Sect. C* **1999**, *55*, 64–67.
- (5) Jacquet, M.; Lafolet, F.; Cobo, S.; Loiseau, F.; Bakkar, A.; Boggio-Pasqua, M.; Saint-Aman, E.; Royal, G. Efficient Photoswitch System Combining a Dimethyldihydropyrene Pyridinium Core and Ruthenium(II) Bis-Terpyridine Entities. *Inorg. Chem.* **2017**, *56* (8), 4357–4368.
- (6) Persaud, L.; Barbiero, G. Synthesis, Electrochemical and Spectroscopic Investigations of 2,2':4,4''-Terpyridine and 2,2':4,4'':6,2''-Quaterpyridine Ligands for Metal Complex Photoelectrochemistry. *Can. J. Chem.* **1991**, *69*, 315–321.
- (7) Turner, W. R.; Elving, P. J. Electrooxidation in Pyridine at Pyrolytic Graphite Electrode. *Anal. Chem.* **1965**, *37* (4), 467–469.
- (8) Gilmore, J. R.; Mellor, J. M. Oxidation of Alkyl Aryl Sulphides by One Electron Transfer. *Tetrahedron Lett.* **1971**, No. 43, 3977–3980.
- (9) Wallenstein, J. H.; Sundberg, J.; Mckenzie, C. J.; Abrahamsson, M. Emissive Ruthenium–Bisdiimine Complexes with Chelated Thioether Donors. *Eur. J. Inorg. Chem.* **2016**, *6*,

- 897–906.
- (10) Root, M. J.; Sullivan, B. P.; Meyer, T. J.; Deutsch, E. Thioether, Thiolato, and 1,1-Dithioato Complexes of Bis(2,2'-Bipyridine)Ruthenium(II) and Bis(2,2'-Bipyridine)Osmium(II). *Inorg. Chem.* **1985**, *24* (18), 2731–2739.
- (11) Campagna, S.; Puntoriero, F.; Nastasi, F.; Bergamini, G.; Balzani, V. Photochemistry and Photophysics of Coordination Compounds: Ruthenium. *Springer berlin Heidel-b. New York* **2007**, *280*, 117–214.
- (12) Jarenmark, M.; Fredin, L. A.; Hedberg, J. H. J.; Doverbratt, I.; Persson, P.; Abrahamsson, M. A Homoleptic Trisbidentate Ru(II) Complex of a Novel Bidentate Biheteroaromatic Ligand Based on Quinoline and Pyrazole Groups: Structural, Electrochemical, Photophysical, and Computational Characterization. *Inorg. Chem.* **2014**, *53*, 12778–12790.
- (13) Collin, J.-P.; Jouvenot, D.; Koizumi, M.; Sauvage, J.-P. Ru(Phen)₂(Bis-Thioether)₂₊ Complexes: Synthesis and Photosubstitution Reactions. *Inorganica. Chim. Acta.cta.* **2007**, *360*, 923–930.
- (14) Wallenstein, J. H.; Fredin, L. A.; Jarenmark, M.; Abrahamsson, M.; Persson, P. Chemical Consequences of Pyrazole Orientation in RuII Complexes of Unsymmetric Quinoline–pyrazole Ligands. *Dalton. Trans.* **2016**, *45*, 11723–11732.
- (15) Collin, J.-P.; Jouvenot, D.; Koizumi, M.; Sauvage, J.-P. Light-Driven Expulsion of the Sterically Hindering Ligand L in Tris-Diimine Ruthenium(II) Complexes of the Ru(Phen)₂(L)₂₊ Family: A Pronounced Ring Effect. *Inorg. Chem.* **2005**, *44* (13), 4693–4698.
- (16) Schulze, B.; Escudero, D.; Friebe, C.; Siebert, R.; Gorls, H.; Sinn, S.; Thomas, M.; Mai, S.; Popp, J.; Dietzek, B.; Leticia, G.; Schubert, U. S. Ruthenium(II) Photosensitizers of Tridentate Click-Derived Cyclometalating Ligands: A Joint Experimental and Computational Study. *Chem. Eur. J.* **2012**, *18*, 4010–4025.
- (17) Colasson, B.; Credi, A.; Ragazzon, G. Light-Driven Molecular Machines Based on Ruthenium(II) Polypyridine Complexes: Strategies and Recent Advances. *Coord. Chem.*

Rev. **2016**, 325, 125–134.

- (18) Howerton, B. S.; Heidary, D. K.; Glazer, E. C. Strained Ruthenium Complexes Are Potent Light-Activated Anticancer Agents. *J. Am. Chem. Soc.* **2012**, 13, 8324–8327.

General Conclusion

It is well known that the photophysical, photochemical, and electrochemical properties of most ruthenium polypyridine complexes are directly affected by their electronic structural design. This can be clearly described by comparing $[\text{Ru}(\text{py})_6]^{2+}$, $[\text{Ru}(\text{bpy})_3]^{2+}$, and $[\text{Ru}(\text{tpy})_2]^{2+}$, which are each hexa-coordinated by pyridine rings, however, they have different octahedral geometrical structures, leading to different properties and therefore different applications in various fields. Thus, the main interest of this thesis was to explore the coordination properties of new tridentate ligands on ruthenium transition metal.

The goal of separating the emitting $^3\text{MLCT}$ excited state and non-emitting ^3MC excited state in all of the complexes described in this thesis was achieved by imparting a low lying π^* orbital to stabilize the $^3\text{MLCT}$ excited state, in addition to destabilizing the ^3MC excited state by increasing the ligand field (Δ_o) through optimizing the complexes' octahedral geometries.

Generally, all homoleptic complexes decorated with 6-membered metallacycles around the central Ru(II) metal were characterized as having exclusively a *facial* geometry, whereas all heteroleptic complexes, which include a terpyridine ligand locked in a plane, were obtained with the *meridional* geometry.

Due to the constrained coordinating cavity for the acridine-based ligands (**11** and **14**), their heteroleptic complexes were synthesized with an important twisting of the acridine backbone. This twisting distortion lead to a weak electron retrodonation from the central metal to the ligands. Due to the resulting decrease in the HOMO-LUMO energy gap, very low-lying $^3\text{MLCT}$ excited states were formed, and therefore, these complexes have weak photophysical properties, according to the energy gap law.

Additionally, new Ru(II) complexes decorated with thioether ligands have been described and showed an effect of quenching of the luminescence properties, most probably due to the coordinating sulfur atoms, at different temperatures despite the high energy of the $^3\text{MLCT}$ excited state.

A pioneering work was described showing the first photochemical ejection of a tridentate ligand from its bis-tridentate Ru(II) complexes (complex **21** and complex **22**), in which these Ru(II) complexes can undergo a tridentate ligand photosubstitution reaction by monodentate ligands upon visible light irradiation.

This result is of great importance; such a complex could be a useful building block for promising light-driven molecular machines based on Ru(II) complexes. Interestingly, these photochemically active complexes could also be investigated to possibly be used as a new light-activated anticancer agent for photodynamic therapy (PDT), mimicking the activity of the cytotoxin cisplatin molecules that are responsible for DNA damage and cancer cell death.

Moreover, as other future work based on this thesis, it is interesting to prepare other metal complexes decorated with the rigid tri-imine (NNN) acridine based ligands (**11** and **14**), for instance, with Cu(I) metal which adopts the tetrahedral geometry. The luminescence properties of such complexes could be investigated, especially, by taking into consideration the high rigidity of these ligands of constrained cavities and which is useful in avoiding the complex flattening (distortion) at its excited state.

Experimental Section

➤ Experimental methods

The standard handling techniques under inert atmosphere were used for air and moisture sensitive reagents. Column chromatography was performed on silica gel 60 [Merk, 63-270 mesh]. Thin layer chromatography (TLC) was carried on glass plates coated with silica gel 60 F₂₅₄ (Merk).

In Nuclear Magnetic Resonance (NMR), the ¹H-NMR and ¹³C-NMR spectra were recorded on Bruker 500 (¹H: 500 MHz, ¹³C: 125 MHz), 400 (¹H: 400 MHz, ¹³C: 101 MHz), or 300 (¹H: 300 MHz, ¹³C: 75 MHz) spectrometers. ¹H and ¹³C chemical shifts, given in ppm, are referenced to residual solvent peaks, and the *J*-coupling constants values are given in Hz. ¹H-NMR spectra are reported as the following sequence: **chemical shift** (ppm), **multiplicity** (s: singlet; d: doublet; dd: doublet of doublet; ddd: doublet of doublet of doublet; dt: doublet of triplet; t: triplet; td: triplet of doublet; sex: sextet; m: multiplet), ***J*-coupling** constants (Hz), and **proton integration**.

The electrospray ionization mass spectrometry (ESI-MS) analysis was performed on an amazon speed (Bruker Daltonics) - Ion Trap Spectrometer.

UV-Visible absorption spectra were recorded on a Varian Cary 300 Scan UV-Visible spectrophotometer. For luminescence properties, the steady state emission spectra were recorded on a Horiba Scientific Fluoromax-4 spectrofluorimeter. Samples in acetonitrile solutions were placed in 1 cm path length quartz cuvettes for room temperature measurements, and in butyronitrile rigid matrix for 77 K measurements. The compounds' excited state lifetime measurements were performed after irradiation at $\lambda = 400$ nm obtained by the second harmonic of a titanium: Sapphire laser (picosecond Tsunami laser spectra physics 3950-M1BB + 39868-03 plus picker doubler) at an 8 MHz repetition rate. For the decay acquisition, FluoTime 200 (AMS technologies) time-resolved spectrometer was utilized, consisting of a GaAs microchannel plate photomultiplier tube (Hamamatsu model R3809U-50) followed by a time-correlated single photon counting system from Picoquant (PicoHarp300). The ultimate time resolution of the system is close to 30 ps. Luminescence decays were analyzed with FLUOFIT software available from Picoquant. Emission quantum

yields were determined in acetonitrile solution at room temperature, and calculated using the following equation:

$$\phi_S = \phi_{ref} \times \frac{A_{ref}}{A_S} \times \frac{I_S}{I_{ref}} \times \left(\frac{n_S}{n_{ref}} \right)^2$$

Where Φ_S is the quantum yield of the investigated sample, Φ_{ref} is the quantum yield of the reference compound (usually is for $[\text{Ru}(\text{bpy})_3]^{2+}$ in acetonitrile solution of a value = 0.062), A represents the absorption at the excitation wavelength and I is the emission intensity (calculated from the spectrum area), n is the refractive index of the used solvents.

The experimental uncertainties were as following: absorption maxima, ± 2 nm; molar absorption, 20%; emission maxima, 5 nm; emission lifetime, 10%; emission quantum yield, 20%.

The photochemical reactions were accomplished by continuous irradiation performed under stirring at room temperature with a xenon lamp (Hamamatsu L8253, type LC8-03), equipped with a 400-700 nm large band filter, placed 4 cm from the cuvette sample.

Electrochemical measurements were recorded using a BioLogic SAS potentiostat. Tetra-*n*-butylammonium hexafluorophosphate (TBAPF₆, Aldrich) was used as supporting electrolyte (0.1 M) in dry acetonitrile, under argon atmosphere at room temperature. A standard three-electrodes electrochemical cell was used, potentials were referenced to an AgNO₃ (0.01 M)/Ag reference electrode, the auxiliary electrode was a Pt-wire in acetonitrile + 0.1 M electrolyte solution, and lastly, the working electrode was a 5 mm diameter vitreous carbon disk electrode (E_{pa} : anodic peak potential; E_{pc} : cathodic peak potential; $E_{1/2} = (E_{pa} + E_{pc})/2$; $\Delta E_p = E_{pa} - E_{pc}$). The experimental uncertainty of the redox potentials was ± 10 mV.

➤ X-ray crystallography

A single crystal of each complex was mounted and measured on a Nonius-Bruker 4 circles kappa diffractometer with an APEXII CCD detector and a multilayer mirror monochromatized MoK α radiation ($\lambda = 0.71073$ Å) from an Incoatec high brilliance microsource at 200 K. The

data were collected with phi and omega scans. Data were integrated and corrected for Lorentz and polarization factors with Eval 14, then corrected for absorption with Sadabs and merged with Xprep. The following steps were run under Olex2: the molecular structure was solved by charge flipping methods implemented by Superflip and refined on F^2 by full matrix least-squares techniques using SHELXL-2013. All non-hydrogen atoms were refined anisotropically. Hydrogen were set geometrically and constrained to ride on their carrier atoms. We used the following twin law: -1 0 0 0 1 0 0 0 -1 with 2 domains and an implicit ratio of 50% each.

➤ DFT calculations

The calculations, performed for complexes **12** and **13** (in Chapter 2), were done by using the Gaussian 09 package, and using the B3LYP hybrid density functional using a triple-z quality basis set for geometry optimization and TD-DFT calculations. The 6-311+G(d,p) basis set was used for all atoms except ruthenium for which an uncontracted lanl08(f) basis set with an effective core potential was employed. All calculations (geometry optimization, TD-DFT) are done with solvent effects included, using the IEFPCM implicit model as implemented in Gaussian, using standard parameters for acetonitrile. TD-DFT calculations were done using the Linear-Response approach for the 60 least-energetic transitions. In all calculations on these acridine-based complexes (**12**, **13**), the **dtdpa** ligand was simplified by replacing the two *tertio*-butyl groups by hydrogen atoms.

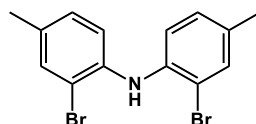
➤ Solvent and chemical compounds

All solvents (acetonitrile, acetone, dichloromethane, chloroform, diethylether, ethyl acetate, pentane, ethylene glycol, ethanol, methanol, dimethylformamide (DMF), dimethyl sulfoxide (DMSO)) were purchased and used as received unless specified (e.g. toluene). All used chemical reagents and commercially available chemical compounds (di-*p*-tolylamine (**1**) and 9(10H)acridone (**4**)) were purchased from their commercial selling companies and used directly without any further purification.

➤ **Synthesis procedures**

Bis(2-bromo-4-methylphenyl)amine (**2**),¹ 2,7-ditertbutyl-9(10H)acridone (**5**),² 4,5-dibromo-2,7-ditertbutyl-9(10H)acridone (**6**),² and 2,6-bis(2-(methylthio)phenyl)pyridine (**20**)³ were synthesized according to previously described procedures in the literature, with some modifications.

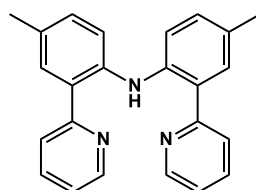
- Bis(2-bromo-4-methylphenyl)amine (**2**)



To a solution of di-*p*-tolylamine (**1**) (7.1 g, 20.0 mmol) in dry dichloromethane (75 mL), was added *N*-bromosuccinimide (7.1 g, 40.0 mmol) over 2.5 hours in 10 portions. The reaction mixture was vigorously stirred at ambient temperature for 48 hours, under argon atmosphere. All solvents were removed under vacuum and the resulting black solid was then dissolved in pentane (60 mL), and vigorously stirred over silica gel for 30 minutes, and then filtered through a celite pad and washed with cold pentane. All solvents were removed under vacuum, to afford a pure white powder of the desired compound, (9.08 g, 71% yield).

¹H-NMR (400 MHz; CDCl₃): δ 7.38 (s, 2H), 7.09 (d, *J* = 8.0 Hz, 2H), 6.98 (d, *J* = 8.0 Hz, 2H), 6.16 (s, 1H), 2.26 (s, 6H).

- bis(4-methyl-2-(pyridin-2-yl)phenyl)amine (**3**)



To a solution of bis(2-bromo-4-methylphenyl)amine (**2**) (177 mg, 0.500 mmol) and [Pd(PPh₃)₄] (30 mg, 0.026 mmol) in dry toluene (2 mL), was added 2-(tributylstannyl)pyridine (85%) (0.60 mL, 1.585 mmol). The reaction mixture was allowed to reflux for 18 hours, under argon atmosphere. After cooling to room temperature, the reaction mixture was quenched by the addition of 1 mL of distilled water. All solvents were removed under vacuum and the crude

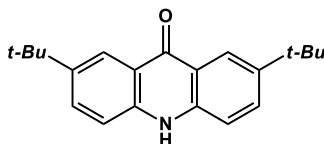
mixture was purified by column chromatography (SiO₂; diethylether/pentane 30%, R_f = 0.23) to afford the pure white powder of the desired product, (90 mg, 51% yield).

¹H-NMR (300 MHz; CDCl₃): δ 10.60 (s, 1H), 8.59 (dd, *J* = 4.4, 2.0 Hz, 2H), 7.69 (m, 4H), 7.34 (m, 4H), 7.17 (ddd, *J* = 7.6, 6.1, 1.3 Hz, 2H), 7.05 (dd, *J* = 8.5, 1.7 Hz, 2H), 2.32 (s, 6H).

¹³C-NMR (75 MHz, CDCl₃): δ 149.2, 148.2, 136.9, 136.5, 130.7, 129.9, 129.2, 123.7, 123.2, 121.1, 118.5, 20.6.

ESI-MS: *m/z* = 352.20 ([M+H]⁺); calculated for C₂₄H₂₁N₃H⁺ = 352.18, *m/z* = 374.20 ([M+Na]⁺); calculated for C₂₄H₂₁N₃Na⁺ = 374.16.

- 2,7-ditertbutyl-9(10H)acridone (**5**)

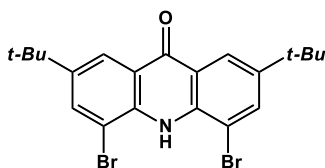


To a suspension of 9(10H)acridone (**4**) (5.00 g, 25.6 mmol) and AlCl₃ (6.83 g, 51.2 mmol) in dry dichloromethane (125 mL) at 0 °C, under argon atmosphere, was added 2-chloro-2-methylpropane (22.8 mL, 205.0 mmol). The suspension was stirred at 0 °C for 24 hours. The reaction was quenched by 150 mL distilled water and the mixture was extracted by CH₂Cl₂ (3 x 100 mL). The combined organic layer was dried over Na₂SO₄ and filtered through Na₂CO₃ and then silica gel pad. All solvents were removed under vacuum. The solid was suspended in hot methanol (100 mL) and then cooled to 0 °C. The precipitate was filtered to afford the yellowish solid product (≈ 1.6 g). The filtrate was suspended in hot methanol (120 mL) and distilled water (20 mL) was added. After cooling to 0 °C again, the precipitate was filtered to afford brown-orange solid, that was recrystallized by acetone (50 mL) and pentane (200 mL) to give the yellowish pure product (≈ 6.2 g). The combined yield was quantitative.

¹H-NMR (400 MHz; CDCl₃): δ 9.33 (s, 1H), 8.49 (d, *J* = 2.4 Hz, 2H), 7.68 (dd, *J* = 8.6, 2.4 Hz, 2H), 7.44 (d, *J* = 8.6 Hz, 2H), 1.34 (s, 18H).

¹³C-NMR (101 MHz; CDCl₃): δ 178.8, 144.6, 138.7, 131.6, 122.4, 120.8, 116.6, 34.6, 31.3.

- 4,5-dibromo-2,7-ditertbutyl-9(10H)acridone (**6**)

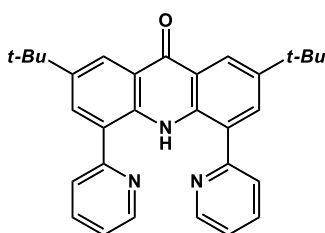


To a solution of 2,7-ditertbutyl-9(10H)acridone (**5**) (2.00 g, 6.52 mmol) in dry chloroform (66 mL), was added bromine (2.68 mL, 52.00 mmol) dropwise at room temperature. The solution was stirred for 2 hours at room temperature. Cs₂CO₃ (16.96 g, 52.00 mmol) was added and the reaction mixture was stirred for 18 hours at room temperature. The excess bromine was quenched by sodium bisulfite (10 g in 100 mL water) after cooling the reaction to 0 °C in ice bath. The mixture was extracted by CHCl₃ (3 x 60 mL). The combined organic layer was dried over Na₂CO₃, and filtered on celite. All solvents were evaporated under vacuum and the crude mixture was purified by column chromatography (SiO₂; diethylether/pentane 5%, R_f = 0.24) to afford the desired pure product, (2.64 g, 87% yield).

¹H-NMR (400 MHz; CDCl₃): δ 8.98 (s, 1H), 8.39 (d, *J* = 2.0 Hz, 2H), 7.96 (d, *J* = 2.0 Hz, 2H), 1.38 (s, 18H).

¹³C-NMR (101 MHz; CDCl₃): δ 177.7, 146.0, 135.4, 134.6, 122.8, 121.7, 110.9, 34.9, 31.3.

- 2,7-ditertbutyl-4,5-di(pyridin-2-yl)-9(10H)acridone (**7**)



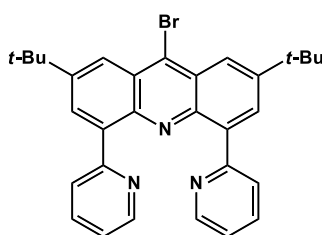
To a solution of 4,5-dibromo-2,7-ditertbutyl-9(10H)acridone (**6**) (233 mg, 0.500 mmol) and [Pd(PPh₃)₄] (30 mg, 0.026 mmol) in dry toluene (2 mL), was added 2-(tributylstannyl)pyridine (85%) (0.60 mL, 1.585 mmol). The reaction mixture was allowed to reflux for 18 hours, under argon atmosphere. After cooling to room temperature, the reaction mixture was quenched by the addition of 1 mL of distilled water. All solvents were removed under vacuum and the crude mixture was purified by column chromatography (SiO₂; diethylether/pentane 1/1 v/v, R_f = 0.24) to afford the yellowish pure powder of the desired product, (208 mg, 90% yield).

$^1\text{H-NMR}$ (400 MHz; CDCl_3): δ 13.97 (s, 1H), 8.64 (d, $J = 2.3$ Hz, 2H), 8.53 (dd, $J = 4.6, 0.8$ Hz, 2H), 8.01 (d, $J = 2.3$ Hz, 2H), 7.88 (td, $J = 8.0, 1.9$ Hz, 2H), 7.81 (d, $J = 8.0$ Hz, 2H), 7.34 (ddd, $J = 7.5, 5.27, 0.8$ Hz, 2H), 1.46 (s, 18H).

$^{13}\text{C-NMR}$ (101 MHz, CDCl_3): δ 178.6, 158.1, 148.4, 143.4, 137.4, 131.8, 125.7, 124.4, 123.3, 121.9, 121.8, 34.7, 31.4.

ESI-MS: $m/z = 462.20$ ($[\text{M}+\text{H}]^+$); calculated for $\text{C}_{31}\text{H}_{31}\text{N}_3\text{OH}^+ = 462.25$, $m/z = 484.20$ ($[\text{M}+\text{Na}]^+$); calculated for $\text{C}_{31}\text{H}_{31}\text{N}_3\text{ONa}^+ = 484.24$.

- 9-bromo-2,7-ditertbutyl-4,5-di(pyridin-2-yl)acridine (**8**)

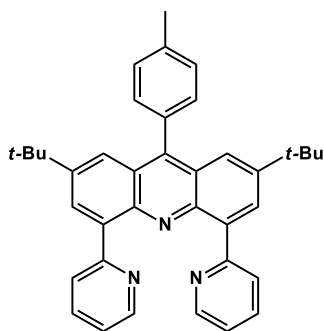


2,7-ditertbutyl-4,5-di(pyridin-2-yl)-9(10H)acridone (**7**) (600 mg, 1.30 mmol) and phosphorus(V) oxybromide (4.1 g, 14.73 mmol) were mixed and heated at 75 °C over 48 hours and then added to an ice bath. The mixture was neutralized by aqueous K_2CO_3 (60 mL, 2 M) and then solid K_2CO_3 was added, to give the orange-yellow precipitate. The aqueous phase was then extracted by dichloromethane (3x30 mL) and the combined organic extracts were dried over sodium sulfate. All the volatiles were removed under vacuum. Column chromatography (SiO_2 ; diethylether/pentane 1/1 v/v, $R_f = 0.18$) afforded the desired pure compound as a bright yellowish solid (475 mg, 70% yield).

$^1\text{H-NMR}$ (400 MHz; CD_3CN): δ 8.69 (d, $J = 5.06$ Hz, 2H), 8.48 (d, $J = 2.01$, 2H), 8.35 (d, $J = 2.01$ Hz, 2H), 8.02 (dt, $J = 7.88, 1.01$ Hz, 2H), 7.71 (td, $J = 7.88, 2.01$ Hz, 2H), 7.35 (ddd, $J = 7.88, 5.06, 1.01$ Hz, 2H), 1.56 (s, 18H).

ESI-MS: $m/z = 524.20$ ($[\text{M}+\text{H}]^+$); calculated for $\text{C}_{31}\text{H}_{30}\text{BrN}_3\text{H}^+ = 524.17$.

- 2,7-ditertbutyl-4,5-di(pyridin-2-yl)-9-(*p*-tolyl)acridine (**9**)



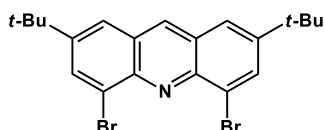
To a solution of 9-bromo-2,7-ditertbutyl-4,5-di(pyridin-2-yl)acridine (**8**) (180 mg, 0.344 mmol) and $[\text{Pd}(\text{PPh}_3)_4]$ (36 mg, 0.031 mmol) in toluene (20 mL), under argon atmosphere, was added dropwise a solution of *p*-tolylboronic acid (327 mg, 2.408 mmol) in ethanol (12 mL), followed by the addition of aqueous K_2CO_3 solution (3.5 mL, 1M). The suspension was allowed to reflux at 90 °C for 22 hours. After cooling to room temperature, the reaction mixture was filtered off, and the filtrate was washed with 1 M NaOH (2x12 mL) and then with distilled water (2x12 mL). The combined organic layers were then dried on sodium sulfate and all volatiles were evaporated under reduced pressure. Column chromatography (SiO_2 ; MeOH/ CHCl_3 1%, R_f = 0.52) afforded the pure yellowish compound of the desired product (118 mg, 65% yield).

$^1\text{H-NMR}$ (500 MHz; CDCl_3): δ 8.78 (d, J = 4.69 Hz, 2H), 8.34 (d, J = 1.51 Hz, 2H), 8.11 (d, J = 8.06, 2H), 7.70 (d, J = 1.51 Hz, 2H), 7.43 (m, 6H), 7.25 (ddd, J = 8.06, 6.31, 0.51 Hz, 2H), 2.57 (s, 3H), 1.37 (s, 18H).

$^{13}\text{C-NMR}$ (125 MHz; CDCl_3): δ 157.7, 149.0, 147.6, 146.7, 144.9, 138.1, 137.8, 134.8, 133.6, 130.5, 129.0, 128.0, 125.1, 122.2, 121.6, 35.3, 31.0, 21.5.

ESI-MS: m/z = 536.30 ($[\text{M}+\text{H}]^+$); calculated for $\text{C}_{38}\text{H}_{37}\text{N}_3\text{H}^+$ = 536.31.

- 4,5-dibromo-2,7-ditertbutylacridine (**10**)



To a refluxing solution of 4,5-dibromo-2,7-ditertbutyl-9(10H)acridone (**6**) (10 g, 21.5 mmol) in dry THF (100 mL), under argon, was added dropwise a 1 M borane tetrahydrofuran complex solution (107 mL, 107 mmol). The reaction mixture was allowed to reflux for 1 hour. After

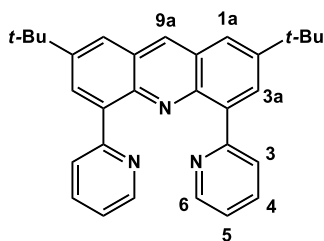
cooling to room temperature, aqueous hydrochloric acid solution (3 N, 250 mL) was slowly added. The pH was then raised by addition of Na₂CO_{3(sat)} (1 L) and this aqueous phase was extracted with dichloromethane. The organic phases were combined and dried on sodium sulfate and the solvent was evaporated under vacuum. This crude solid was stirred in a mixture of ethanol (180 mL) and water (35 mL), in the presence of iron(III) chloride hexahydrate (8 g) for 2 hours at 50 °C. After cooling to room temperature, Na₂CO_{3(sat)} (400 mL) was added, and the mixture was extracted with dichloromethane. The organic phases were combined, dried over sodium sulfate and the solvent was evaporated under vacuum. Column chromatography (SiO₂; EtOAc/Pentane 5%) afforded the title compound as a yellowish solid (9.2 g, 95% yield).

¹H-NMR (400 MHz; CDCl₃): δ 8.66 (s, 1H), 8.25 (d, *J* = 2.0 Hz, 2H), 7.83 (d, *J* = 2.0 Hz, 2H), 1.43 (s, 18H).

¹³C-NMR (101 MHz; CDCl₃): δ 149.6, 144.7, 136.8, 133.5, 127.7, 125.5, 122.1, 35.2, 31.0.

ESI-MS: *m/z* = 448.0 ([M+H]⁺); calculated for C₂₁H₂₄Br₂NH⁺ = 448.03.

- 2,7-ditertbutyl-4,5-di(pyridin-2-yl)acridine (**11**, **dtdpa**)



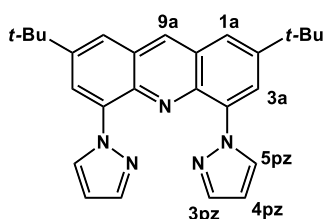
To a solution of 4,5-dibromo-2,7-ditertbutylacridine (**10**) (225 mg, 0.500 mmol) and [Pd(PPh₃)₄] (30 mg, 0.026 mmol) in dry toluene (2 mL), was added 2-(tributylstannyl)pyridine (85%) (0.60 mL, 1.585 mmol). The reaction mixture was allowed to reflux for 18 hours, under argon atmosphere. After cooling to room temperature, the reaction mixture was quenched by the addition of 1 mL of distilled water. All solvents were removed under vacuum and the crude mixture was purified by column chromatography (SiO₂; diethylether/pentane 1/1 v/v, R_f = 0.28) to afford the pure beige powder of the desired product, (201 mg, 90% yield).

$^1\text{H-NMR}$ (400 MHz; CD_3CN): δ 8.99 (s, 1H; H_{9a}), 8.70 (d, $J = 4.4$ Hz, 2H; H_6), 8.35 (d, $J = 2.4$ Hz, 2H; H_{3a}), 8.17 (dd, $J = 8.0, 1.0$ Hz, 2H; H_3), 8.11 (d, $J = 2.4$ Hz, 2H; H_{1a}), 7.72 (td, $J = 7.6, 2.7$ Hz, 2H; H_4), 7.33 (ddd, $J = 7.5, 4.9, 1.1$ Hz, 2H; H_5), 1.49 (s, 18H; $\text{H}_{t\text{-Bu}}$).

$^{13}\text{C-NMR}$ (75 MHz; CDCl_3): δ 157.4, 149.2, 148.3, 145.3, 138.0, 136.0, 134.9, 131.1, 127.9, 126.9, 123.5, 121.8, 35.3, 31.2.

ESI-MS: $m/z = 446.20$ ($[\text{M}+\text{H}]^+$); calculated for $\text{C}_{31}\text{H}_{31}\text{N}_3\text{H}^+ = 446.26$.

- 2,7-ditertbutyl-4,5-di(pyrazol-1-yl)acridine (**14**, **dtdpza**)



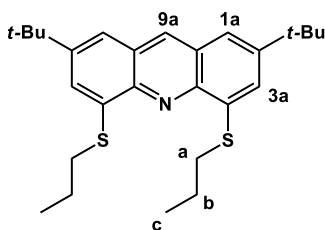
To a solution of 4,5-dibromo-2,7-ditertbutylacridine (**10**) (900 mg, 2 mmol) and 1H-pyrazole (288 mg, 4.2 mmol) in dry dimethylformamide (DMF) (8 mL) were added L-proline (464 mg, 4.04 mmol), anhydrous K_2CO_3 (1.145 g, 8.3 mmol), and copper(I) iodide (380 mg, 2 mmol). The solution mixture was heated at 120 °C for 22 hours, under inert atmosphere. After cooling to room temperature, 40 mL of distilled water was added. The organic phase was extracted by ethyl acetate (3 x 60 mL). Then the organic phases were combined and dried on sodium sulfate and all the volatiles were evaporated under vacuum. The obtained dark brown crude mixture was purified by flash column chromatography (SiO_2 ; EtOAc/Pentane 10%, $R_f = 0.31$), and the desired bright yellowish pure compound was isolated (335 mg, 40% yield).

$^1\text{H-NMR}$ (400 MHz; $(\text{CD}_3)_2\text{CO}$): δ 9.21 (s, 1H; H_{9a}), 8.81 (d, $J = 2.0$ Hz, 2H; H_{3pz}), 8.46 (d, $J = 1.5$ Hz, 2H; H_{3a}), 8.11 (d, $J = 1.5$ Hz, 2H; H_{1a}), 7.80 (d, $J = 2.0$ Hz, 2H; H_{5pz}), 6.53 (t, $J = 1.8$ Hz, 2H; H_{4pz}), 1.53 (s, 18H; $\text{H}_{t\text{-Bu}}$).

$^{13}\text{C-NMR}$ (101 MHz, CDCl_3): δ 149.0, 140.5, 139.9, 136.8, 136.3, 134.0, 127.6, 124.0, 121.4, 106.4, 35.4, 30.9.

ESI-MS: $m/z = 424.20$ ($[\text{M}+\text{H}]^+$); calculated for $\text{C}_{27}\text{H}_{29}\text{N}_5\text{H}^+ = 424.25$, $m/z = 446.20$ ($[\text{M}+\text{Na}]^+$); calculated for $\text{C}_{27}\text{H}_{29}\text{N}_5\text{Na}^+ = 446.23$.

- 2,7-ditertbutyl-4,5-bis(propylthio)acridine (**17**, **dtdsa**)



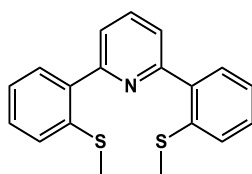
Calcined fine potassium hydroxide powder (1.8 g, 32 mmol) was added to a solution of 4,5-dibromo-2,7-ditertbutylacridine (**10**) (900 mg, 2 mmol) and 1-propanethiol (2.17 mL, 24 mmol) in 5 mL dry dimethylsulfoxide (DMSO). The reaction mixture was covered with aluminum foil to avoid light-induced degradation, and was heated at 80 °C for 18 hours, under inert atmosphere. After cooling to room temperature, distilled water (20 mL) and brine (10 mL) were added. The crude mixture was extracted with dichloromethane (3 x 20 mL), then dried on sodium sulfate and all volatiles were removed under reduced pressure. Column chromatography (SiO₂; EtOAc/Pentane 2%, R_f = 0.25) afforded the desired pure compound as a yellowish solid (207 mg, 24% yield).

¹H-NMR (500 MHz; CDCl₃): δ 8.56 (s, 1H; H_{9a}), 7.61 (d, *J* = 1.8 Hz, 2H; H_{3a}), 7.58 (d, *J* = 1.8 Hz, 2H; H_{1a}), 3.19 (t, *J* = 7.4 Hz, 4H; H_a), 1.88 (sex, *J* = 7.4 Hz, 4H; H_b), 1.45 (s, 18H; H_{t-Bu}), 1.15 (t, *J* = 7.4 Hz, 6H; H_c).

¹³C-NMR (125 MHz, CDCl₃): δ 148.0, 144.3, 138.1, 135.7, 126.7, 124.4, 118.5, 35.1, 33.3, 30.9, 22.1, 13.9.

ESI-MS: *m/z* = 440.20 ([M+H]⁺); calculated for C₂₇H₃₇NS₂H⁺ = 440.24.

- 2,6-bis(2-(methylthio)phenyl)pyridine (**20**)



To a solution of 2-(methylthio)phenylboronic acid (882 mg, 5.30 mmol), 2,6-dibromopyridine (414 mg, 1.8 mmol) and [Pd(PPh₃)₂(Cl)₂] (122 mg, 0.18 mmol) in dry 1,2-dimethoxyethane (20 mL), was added a solution of potassium carbonate (741 mg, 70 mmol) in 50 mL distilled water. The reaction mixture was heated at 85 °C for 12 hours, under argon atmosphere. After cooling

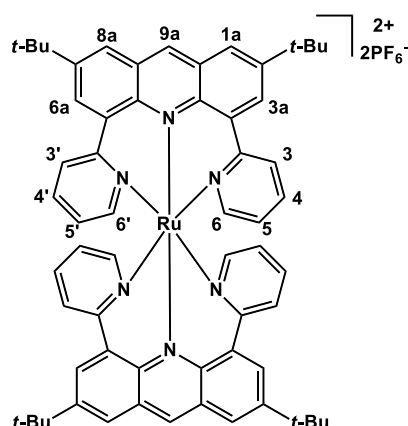
to the room temperature, all solvents were removed under vacuum and the crude mixture was purified by column chromatography (SiO₂; ethyl acetate/pentane 2%) to afford the white powder of the pure desired product, (600 mg, 96% yield).

¹H-NMR (500 MHz; (CD₃)₂CO): δ 7.93 (t, *J* = 7.9 Hz, 1H), 7.64 (m, 4H), 7.42 (m, 4H), 7.27 (td, *J* = 7.9, 1.4 Hz, 2H), 2.41 (s, 6H).

- **General procedure for the Ru(II) homoleptic complex preparation:**

[RuCl₂(dmsO)₄] (30 mg, 0.062 mmol) and the desired free ligand (0.137 mmol, 2.2 molar equivalents) were dissolved in dry ethanol (2 mL). The reaction mixture was refluxed overnight. After cooling to room temperature, a precipitate of ruthenium(II) complex (in the form of hexafluorophosphate salt) was obtained by addition of excess of saturated aqueous solution of KPF₆. The resulting solid was purified by column chromatography (SiO₂) to give the desired pure homoleptic Ru(II) complex.

- [Ru(dtdpa)₂](PF₆)₂ (**12**)



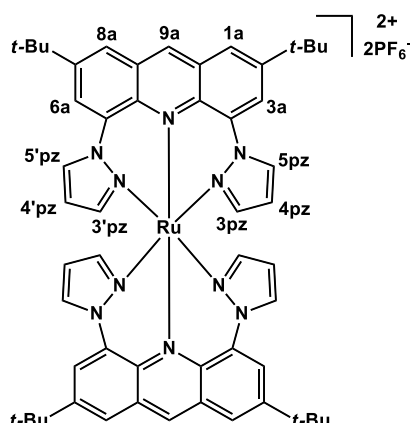
Prepared according to the general procedure for the Ru(II) homoleptic complex preparation, from 2,7-ditertbutyl-4,5-di(pyridin-2-yl)acridine (**11**, **dtdpa**) (61 mg, 0.137 mmol). The column chromatography purification (SiO₂; acetone/H₂O/KNO_{3(sat)} 100/5/0.5 v/v/v, R_f = 0.2) afforded the greenish Ru(II) complex **12** (32 mg, 41% yield).

$^1\text{H-NMR}$ (500 MHz; $(\text{CD}_3)_2\text{CO}$): δ 9.85 (d, $J = 6.0$ Hz, 2H; $\text{H}_{6'}$), 9.20 (d, $J = 6.0$ Hz, 2H; H_6), 8.90 (s, 2H; H_{9a}), 8.30 (t, $J = 7.8$ Hz, 2H; $\text{H}_{4'}$), 8.25 (d, $J = 1.9$ Hz, 2H; H_{6a}), 8.18 (d, $J = 7.0$ Hz, 2H; $\text{H}_{3'}$), 8.17 (d, $J = 1.9$ Hz, 2H; H_{8a}), 7.97 (d, $J = 1.6$ Hz, 2H; H_{1a}), 7.93 (ddd, $J = 7.3, 6.1, 1.4$ Hz, 2H; $\text{H}_{5'}$), 7.88 (td, $J = 7.7, 1.3$ Hz, 2H; H_4), 7.70 (d, $J = 7.3$ Hz, 2H; H_3), 7.66 (d, $J = 1.9$ Hz, 2H; H_{3a}), 7.54 (td, $J = 6.7, 1.3$ Hz, 2H; H_5), 1.66 (s, 18H), 1.44 (s, 18H).

$^{13}\text{C-NMR}$ (101 MHz; $(\text{CD}_3)_2\text{CO}$): δ 158.1, 157.7, 156.0, 155.5, 153.8, 151.4, 151.0, 149.4, 140.1, 139.5, 136.6, 135.2, 134.2, 132.6, 130.6, 129.7, 128.8, 128.1, 126.5, 126.05, 125.97, 125.85, 125.1, 35.91, 35.85, 31.5, 31.0.

ESI-MS: $m/z = 496.20$ ($[\text{Ru}(\text{dtdpa})_2]^{2+}$); calculated for $\text{C}_{62}\text{H}_{62}\text{N}_6\text{Ru}^{2+} = 496.21$, $m/z = 1137.30$ ($[\text{Ru}(\text{dtdpa})_2](\text{PF}_6)^+$); calculated for $\text{C}_{62}\text{H}_{62}\text{F}_6\text{N}_6\text{PRu}^+ = 1137.37$.

- $[\text{Ru}(\text{dtdpza})_2](\text{PF}_6)_2$ (**15**)



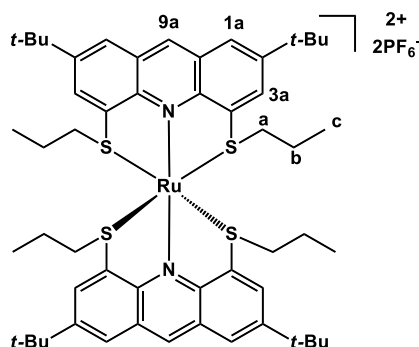
Prepared according to the general procedure for the Ru(II) homoleptic complex preparation, from 2,7-ditertbutyl-4,5-di(pyrazol-1-yl)acridine (**14**, **dtdpza**) (58 mg, 0.137 mmol). The column chromatography purification (SiO_2 ; acetone/ $\text{H}_2\text{O}/\text{KNO}_3(\text{sat})$ 100/5/0.5 v/v/v, $R_f = 0.3$) afforded the light blue Ru(II) complex **15** (60 mg, 35% yield).

$^1\text{H-NMR}$ (500 MHz; $(\text{CD}_3)_2\text{CO}$): δ 9.08 (s, 2H; H_{9a}), 9.00 (d, $J = 2.1$ Hz, 2H; $\text{H}_{3\text{pz}}$), 8.99 (d, $J = 2.9$ Hz, 2H; $\text{H}_{5\text{pz}}$), 8.49 (d, $J = 1.7$ Hz, 2H; H_{3a}), 8.41 (d, $J = 2.9$ Hz, 2H; $\text{H}_{5'\text{pz}}$), 8.27 (d, $J = 2.1$ Hz, 2H; $\text{H}_{3'\text{pz}}$), 8.21 (d, $J = 1.5$ Hz, 2H; H_{8a}), 7.89 (d, $J = 1.5$ Hz, 2H; H_{1a}), 7.62 (d, $J = 1.7$ Hz, 2H; H_{6a}), 7.19 (t, $J = 2.65$ Hz, 2H; $\text{H}_{4\text{pz}}$), 6.77 (t, $J = 2.65$ Hz, 2H; $\text{H}_{4'\text{pz}}$), 1.60 (s, 18H), 1.53 (s, 18H).

$^{13}\text{C-NMR}$ (101 MHz, CD_3CN): δ 152.1, 150.3, 148.3, 147.5, 147.4, 146.4, 136.5, 136.4, 134.8, 133.1, 130.2, 126.9, 126.8, 125.4, 123.5, 122.7, 122.2, 111.9, 111.2, 36.3, 36.1, 31.1, 30.8.

ESI-MS: $m/z = 474.20$ ($[\text{Ru}(\text{dtdpza})_2]^{2+}$); calculated for $\text{C}_{54}\text{H}_{58}\text{N}_{10}\text{Ru}^{2+} = 474.19$, $m/z = 1093.30$ ($[\text{Ru}(\text{dtdpza})_2](\text{PF}_6)^+$); calculated for $\text{C}_{54}\text{H}_{58}\text{F}_6\text{N}_{10}\text{PRu}^+ = 1093.35$.

- $[\text{Ru}(\text{dtdsa})_2](\text{PF}_6)_2$ (**18**)



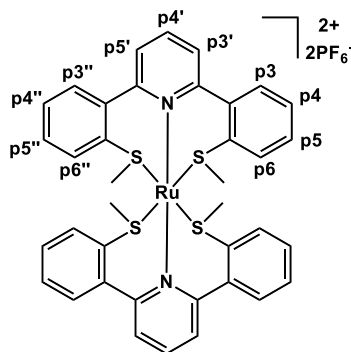
Prepared according to the general procedure for the Ru(II) homoleptic complex preparation, from 2,7-ditertbutyl-4,5-bis(propylthio)acridine (**17**, **dtdsa**) (60 mg, 0.137 mmol). The column chromatography purification (SiO_2 ; acetone/ $\text{H}_2\text{O}/\text{KNO}_3(\text{sat})$ 100/8/0.8 v/v/v, $R_f = 0.27$) afforded the red-orange Ru(II) complex **18** (32 mg, 24% yield).

$^1\text{H-NMR}$ (500 MHz; $(\text{CD}_3)_2\text{CO}$): δ 9.60 (s, 1H; H_{9a}), 8.94 (d, $J = 1.65$ Hz, 2H; H_{3a}), 8.49 (d, $J = 1.65$ Hz, 2H; H_{1a}), 3.58 (t, $J = 7.85$ Hz, 4H; H_a), 1.54 (s, 18H; $\text{H}_{t\text{-Bu}}$), 0.52 (t, $J = 7.27$ Hz, 6H; H_c).

$^{13}\text{C-NMR}$ (125 MHz, CD_3CN): δ 152.3, 149.8, 139.7, 135.2, 129.6, 127.2, 118.3, 40.9, 36.3, 30.9, 22.1, 12.9.

ESI-MS: $m/z = 490.20$ ($[\text{Ru}(\text{dtdsa})_2]^{2+}$); calculated for $\text{C}_{54}\text{H}_{74}\text{N}_2\text{RuS}_4^{2+} = 490.19$, $m/z = 1125.30$ ($[\text{Ru}(\text{dtdsa})_2](\text{PF}_6)^+$); calculated for $\text{C}_{54}\text{H}_{74}\text{F}_6\text{N}_2\text{PRuS}_4^+ = 1125.34$.

- $[\text{Ru}(\text{20})_2](\text{PF}_6)_2$ (**21**)



Prepared according to the general procedure for the Ru(II) homoleptic complex preparation, from 2,6-bis(2-(methylthio)phenyl)pyridine (**20**) (44 mg, 0.137 mmol). The column

chromatography purification (SiO₂; acetonitrile/H₂O/KNO_{3(sat)} 100/50/5 v/v/v, R_f = 0.34) afforded the pure Ru(II) complex **21** (34 mg, 24% yield).

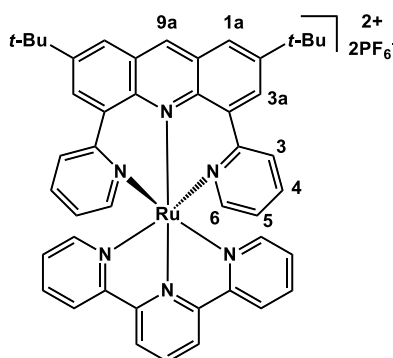
¹H-NMR (500 MHz; (CD₃)₂CO): δ 8.08 (t, *J* = 7.91 Hz, 2H; H_{p4'}), 8.02 (d, *J* = 7.60 Hz, 2H; H_{p6''}), 7.96 (td, *J* = 7.60, 0.88 Hz, 2H; H_{p4''}), 7.86 (m, 4H; H_{p5'', p3''}), 7.80 (d, *J* = 7.91 Hz, 2H; H_{p5'}), 7.71 (d, *J* = 7.91, Hz, 2H; H_{p3}), 7.54 (dd, *J* = 7.91, 1.38 Hz, 2H; H_{p3'}), 7.45 (t, *J* = 7.24 Hz, 2H; H_{p5}), 7.40 (t, *J* = 7.24 Hz, 2H; H_{p4}), 6.77 (dd, *J* = 7.91, 0.88 Hz, 2H; H_{p6}), 2.82 (s, 6H), 1.73 (s, 6H).

ESI-MS: *m/z* = 374.00 ([Ru(**20**)₂]²⁺); calculated for C₃₈H₃₄N₂RuS₄²⁺ = 374.03, *m/z* = 892.90 ([Ru(**20**)₂](PF₆)⁺); calculated for C₃₈H₃₄F₆N₂PRuS₄⁺ = 893.03.

- **General procedure for the Ru(II) heteroleptic complex preparation:**

[RuCl₃(tpy)] (66 mg, 0.15 mmol), the desired free ligand (0.15 mmol, 1 molar equivalents), and LiCl (32 mg, 0.75 mmol) were all dissolved in 10 mL of an ethanol/water mixture (7/3 v/v). Triethylamine (0.2 mL, 1.44 mmol) was then added to the solution and the mixture was allowed to reflux for 4 hours. After cooling to room temperature, a dark precipitate of ruthenium(II) complex (in the form of hexafluorophosphate salt) was obtained by addition of an excess of saturated aqueous solution of KPF₆. The resulting solid was purified by column chromatography (SiO₂) affording the desired pure heteroleptic Ru(II) complex.

- [Ru(tpy)(**dtdpa**)](PF₆)₂ (**13**)



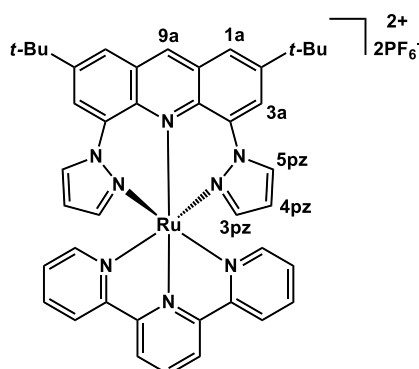
Prepared according to the general procedure for the Ru(II) heteroleptic complex preparation, from 2,7-ditertbutyl-4,5-di(pyridin-2-yl)acridine (**11**, **dtdpa**) (67 mg, 0.15 mmol). The column

chromatography purification (SiO₂; acetone/H₂O/KNO_{3(sat)} 100/10/1 v/v/v, R_f = 0.23) afforded the dark blue Ru(II) complex **13** (67 mg, 42% yield).

¹H-NMR (500 MHz; (CD₃)₂CO): δ 9.58 (s, 1H; H_{9a}), 8.98 (d, *J* = 8.1 Hz, 2H), 8.82 (d, *J* = 8.1 Hz, 2H), 8.78 (d, *J* = 2.0 Hz, 2H; H_{3a}), 8.54 (d, *J* = 2.0 Hz, 2H; H_{1a}), 8.44 (t, *J* = 8.1 Hz, 1H), 8.13 (td, *J* = 7.8, 1.5 Hz, 2H), 7.99 (dd, *J* = 5.6, 0.8 Hz, 2H), 7.81 (dd, *J* = 8.2, 1.0 Hz, 2H; H₃), 7.76 (ddd, *J* = 8.3, 7.2, 1.4 Hz, 2H; H₄), 7.43 (dd, *J* = 5.9, 1.0 Hz, 2H; H₆), 7.35 (ddd, *J* = 7.4, 5.8, 1.5 Hz, 2H), 6.98 (ddd, *J* = 7.3, 5.9, 1.5 Hz, 2H; H₅), 2.82 (s, 18H; H_{t-Bu}). ¹³C-NMR (125 MHz; (CD₃)₂CO): δ 159.6, 159.5, 156.7, 155.5, 151.3, 151.2, 145.2, 139.8, 138.7, 138.5, 137.6, 135.0, 132.4, 129.5, 129.0, 128.4, 127.6, 125.9, 125.6, 124.8, 35.8, 30.9.

ESI-MS: *m/z* = 390.10 ([Ru(tpy)(dtdpa)]²⁺); calculated for C₄₆H₄₂N₆Ru²⁺ = 390.13, *m/z* = 925.20 ([Ru(tpy)(dtdpa)](PF₆)⁺); calculated for C₄₆H₄₂F₆N₆PRu⁺ = 952.22.

- [Ru(tpy)(dtdpza)](PF₆)₂ (**16**)

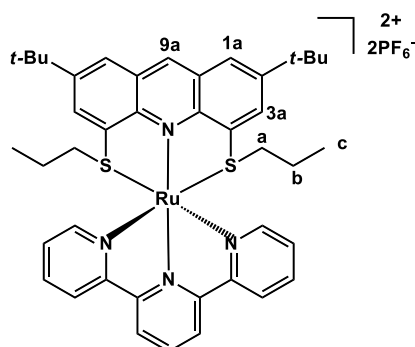


Prepared according to the general procedure for the Ru(II) heteroleptic complex preparation, from 2,7-ditertbutyl-4,5-di(pyrazol-1-yl)acridine (**14**, **dtdpza**) (64 mg, 0.15 mmol). The column chromatography purification (SiO₂; acetone/H₂O/KNO_{3(sat)} 100/8/0.8 v/v/v, R_f = 0.25) afforded the dark blue Ru(II) complex **16** (46 mg, 29% yield).

¹H-NMR (500 MHz; (CD₃)₂CO): δ 9.68 (s, 1H; H_{9a}), 8.93 (d, *J* = 8.1 Hz, 2H), 8.75 (dt, *J* = 8.1, 0.8 Hz, 2H), 8.58 (d, *J* = 2.1 Hz, 2H; H_{3a}), 8.52 (t, *J* = 8.1 Hz, 1H), 8.45 (dd, *J* = 3.0, 0.8 Hz, 2H; H_{1a}), 8.44 (d, *J* = 2.0 Hz, 2H; H_{5pz}), 8.14 (td, *J* = 7.9, 1.5 Hz, 2H), 8.06 (ddd, *J* = 5.6, 1.5, 0.6 Hz, 2H), 7.37 (ddd, *J* = 7.9, 5.6, 1.3 Hz, 2H), 6.95 (dd, *J* = 2.4, 0.6 Hz, 2H; H_{3pz}), 6.48 (td, *J* = 2.7, 0.5 Hz, 2H; H_{4pz}), 1.57 (s, 18H; H_{t-Bu}). ¹³C-NMR (125 MHz; (CD₃)₂CO): δ 159.3, 159.1, 153.8, 151.0, 143.1, 141.2, 140.3, 139.4, 138.0, 136.6, 131.5, 130.0, 129.9, 128.0, 125.6, 124.9, 124.0, 110.9, 42.7, 35.7.

ESI-MS: $m/z = 379.07$ ($[\text{Ru}(\text{tpy})(\text{dtdpza})]^{2+}$); calculated for $\text{C}_{42}\text{H}_{40}\text{N}_8\text{Ru}^{2+} = 379.12$.

- $[\text{Ru}(\text{tpy})(\text{dtdsa})](\text{PF}_6)_2$ (**19**)

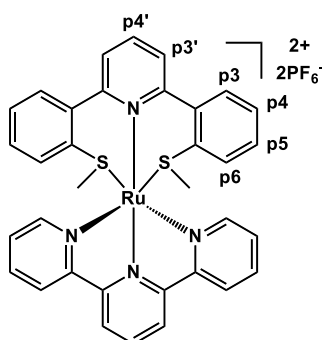


Prepared according to the general procedure for the Ru(II) heteroleptic complex preparation, from 2,7-ditertbutyl-4,5-bis(propylthio)acridine (**17**, **dtdsa**) (66 mg, 0.15 mmol). The column chromatography purification (SiO_2 ; acetonitrile/ $\text{H}_2\text{O}/\text{KNO}_3(\text{sat})$ 100/8/0.8 v/v/v, $R_f = 0.25$) afforded the violet Ru(II) complex **19** (57 mg, 36% yield).

$^1\text{H-NMR}$ (500 MHz; $(\text{CD}_3)_2\text{CO}$): δ 9.63 (s, 1H; H_{9a}), 8.92 (d, $J = 8.1$ Hz, 2H), 8.88 (d, $J = 8.1$ Hz, 2H), 8.63 (d, $J = 1.0$ Hz, 2H; H_{3a}), 8.56 (d, $J = 1.0$ Hz, 2H; H_{1a}), 8.50 (t, $J = 8.1$ Hz, 1H), 8.28 (t, $J = 8.8$ Hz, 2H), 7.79 (d, $J = 4.9$ Hz, 2H), 7.48 (t, $J = 6.5$ Hz, 2H), 2.52 (broad, 4H; H_a), 1.52 (s, 18H; $\text{H}_{t\text{-Bu}}$), 1.12 (broad, 4H; H_b), 0.54 (t, $J = 7.3$ Hz, 6H; H_c). $^{13}\text{C-NMR}$ (125 MHz; $(\text{CD}_3)_2\text{CO}$): δ 159.1, 157.3, 154.0, 151.5, 149.7, 140.0, 139.5, 138.5, 138.0, 134.0, 130.2, 129.4, 127.2, 125.7, 124.4, 43.6, 35.9, 30.7, 21.5, 12.6.

ESI-MS: $m/z = 387.14$ ($[\text{Ru}(\text{tpy})(\text{dtdsa})]^{2+}$); calculated for $\text{C}_{42}\text{H}_{48}\text{N}_4\text{RuS}_2^{2+} = 387.12$.

- $[\text{Ru}(\text{tpy})(\text{20})](\text{PF}_6)_2$ (**22**)



Prepared according to the general procedure for the Ru(II) heteroleptic complex preparation, from 2,6-bis(2-(methylthio)phenyl)pyridine (**20**) (48 mg, 0.15 mmol). The column chromatography purification (SiO₂; acetonitrile/H₂O/KNO_{3(sat)} 100/5/0.5 v/v/v, R_f = 0.15) afforded the bright red Ru(II) complex **22** (60 mg, 42% yield).

¹H-NMR (400 MHz; (CD₃)₂CO): δ 8.78 (d, *J* = 8.1 Hz, 2H), 8.61 (t, *J* = 8.0 Hz, 1H; H_{p4'}), 8.53 (m, 4H), 8.41 (t, *J* = 8.1 Hz, 1H), 8.26 (d, *J* = 8.0 Hz, 2H; H_{p3}), 8.04 (t, *J* = 7.6 Hz, 2H), 7.87 (d, *J* = 5.3 Hz, 2H), 7.64 (t, *J* = 7.6 Hz, 2H; H_{p4}), 7.35 (t, *J* = 7.6 Hz, 2H; H_{p5}), 7.24 (t, *J* = 6.1 Hz, 2H), 7.11 (d, *J* = 7.8 Hz, 2H; H_{p6}), 1.96 (broad s, 6H, H_{Me}).

ESI-MS: *m/z* = 329.04 ([Ru(tpy)(**20**)]²⁺); calculated for C₃₄H₂₈N₄RuS₂²⁺ = 329.04, *m/z* = 803.04 ([Ru(tpy)(**20**)](PF₆)⁺); calculated for C₃₄H₂₈F₆N₄PRuS₂⁺ = 803.04.

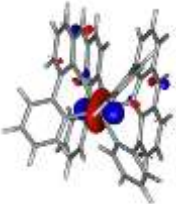
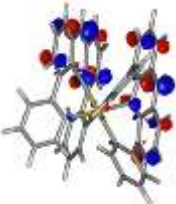
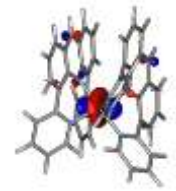
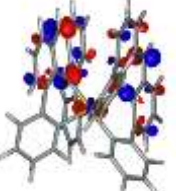
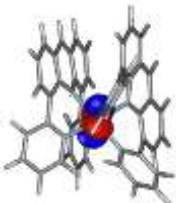
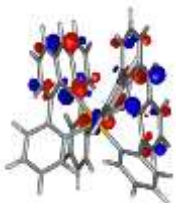

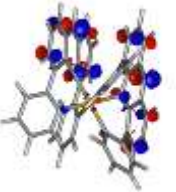
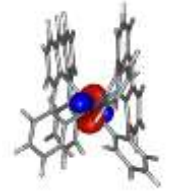
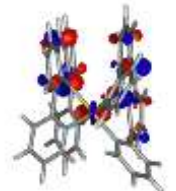
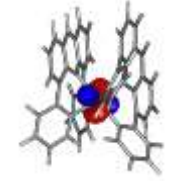
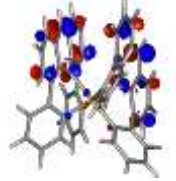
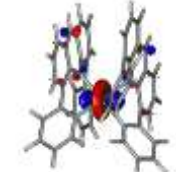
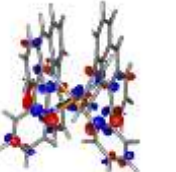
➤ References

- (1) Davidson, J. J.; Demott, J. C.; Douvris, C.; Fafard, C. M.; Bhuvanesh, N.; Chen, C. H.; Herbert, D. E.; Lee, C. I.; McCulloch, B. J.; Foxman, B. M.; Ozerov, O. V. Comparison of the Electronic Properties of Diarylamido-Based PNZ Pincer Ligands: Redox Activity at the Ligand and Donor Ability toward the Metal. *Inorg. Chem.* **2015**, *54*, 2916–2935.
- (2) Yamamoto, K.; Higashibayashi, S. Synthesis of Three-Dimensional Butterfly Slit-Cyclobisazaanthracenes and Hydrazinobisanthenes through One-Step Cyclodimerization and Their Properties. *Chem. Eur. J.* **2016**, *22*, 663–671.
- (3) Lenton, T. N.; VanderVelde, D. G.; Bercaw, J. E. Synthesis of a Bis(Thiophenolate)Pyridine Ligand and Its Titanium, Zirconium, and Tantalum Complexes. *Organometallics* **2012**, *31*, 7492–7499.

Appendix

➤ DFT calculations

Table App.1. Homoleptic complex **12** transitions in the visible region. Optimized by DFT calculations.

$S_0 \rightarrow S_i$	$\Delta E, \lambda$	NTO: detach.	NTO: attach	Interpretation
1	1.8482eV 670.83 nm			HOMO/LUMO
2	1.9513 eV 635.40 nm			MLCT
3	2.1299 eV 582.11 nm			MLCT
4	2.1899 eV 566.16 nm			MLCT
5	2.2471 eV 551.76 nm			MLCT
6	2.2791 eV 543.99 nm			MLCT
7	2.7231 eV 455.31 nm			MLCT

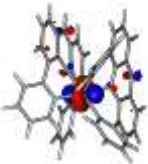
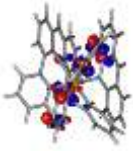

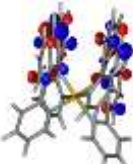
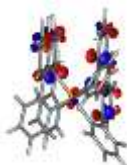
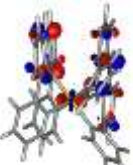
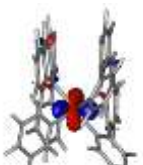
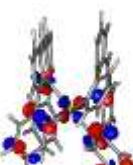
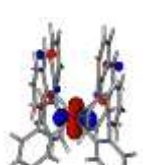

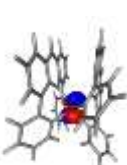
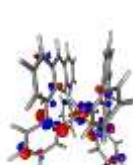

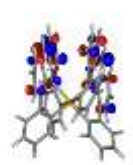
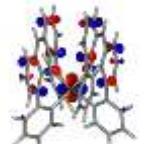

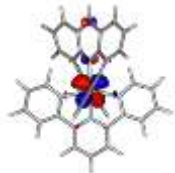
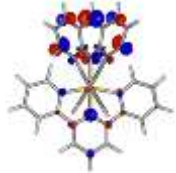

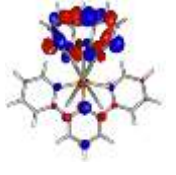
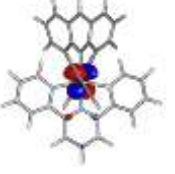
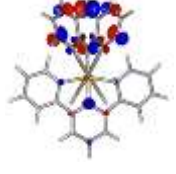
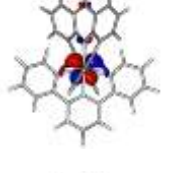
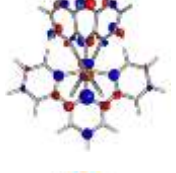
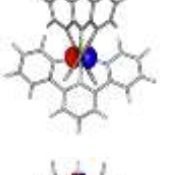
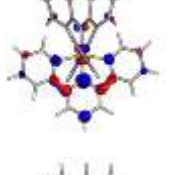
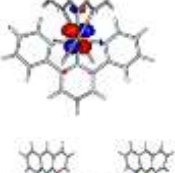
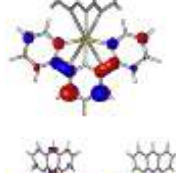
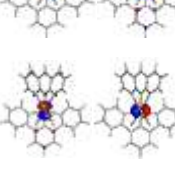
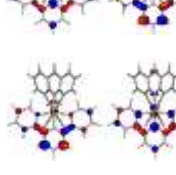
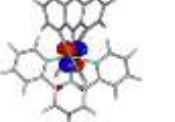
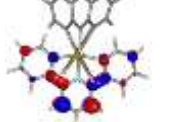
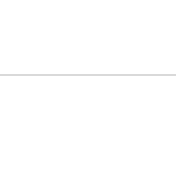
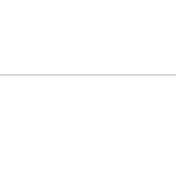

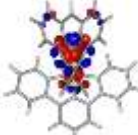
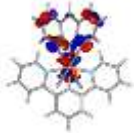
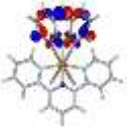
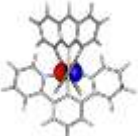
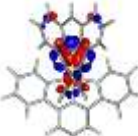
8	2.8117 eV 440.96 nm			MLCT
9	2.8314 eV 437.88 nm			Mixed
10	2.8591 eV 433.66 nm			Mixed
11	2.9774 eV 416.42 nm			MLCT
12	3.0507 eV 406.42 nm			MLCT
13	3.0953 eV 400.56 nm			MLCT
14	3.1404 eV 394.81 nm			MLCT
15	3.1779 eV 390.14 nm			Mixed

Table App.2. Heteroleptic complex **13** transitions in the visible region. Optimized by DFT calculations.

$S_0 \rightarrow S_i$	$\Delta E, \lambda$	NTO: detach.	NTO: attach	Interpretation
1	2.0776 eV 596.76 nm			$d_{xz} \rightarrow \pi(\text{dtdpa})$ HOMO \rightarrow LUMO
2	2.1327 eV 581.35 nm			$d_{xy} \rightarrow \pi(\text{dtdpa})$ HOMO-1 \rightarrow LUMO
3	2.3102 eV 536.68 nm			$d_{yz} \rightarrow \pi(\text{dtdpa})$ HOMO-2 \rightarrow LUMO
4	2.3917 eV 518.40 nm			$d_{xz} \rightarrow \pi(\text{ligands})$ HOMO \rightarrow LUMO+1
5	2.3925 eV 518.21 nm			$d_{xy} \rightarrow \pi(\text{tpy})$
6	2.5476 eV 486.68 nm			$d_{yz} \rightarrow \pi(\text{tpy})$
7	2.6350 eV 470.52 nm			$d \rightarrow \pi(\text{tpy})$
8	2.7936 eV 443.81 nm			MLCT
9	2.8381 eV 436.85 nm			MLCT

10	2.9080 eV 426.35 nm			MLCT
11	2.9542 eV 419.69 nm			LLCT
12	3.1856 eV 389.20 nm			MLCT

➤ General crystallography data

Table App.3. Heteroleptic complex **13**.

Compound reference	Heteroleptic complex 13
Chemical formula	C ₄₆ H ₄₂ F ₁₂ N ₆ P ₂ Ru
Formula mass	1069.86
Crystal system	Monoclinic
Space group	P21/c
a/ Å	14.488(3)
b/ Å	16.907(3)
c/ Å	19.286(4)
α (°)	90.00
β (°)	109.27(3)
γ (°)	90.00
Unit cell volume/ Å ³	4459.2(17)
T / K	200.0
No. of formula units per cell, Z	4
No. of reflections measured	39932
No. of independent reflections	10014
No. params refined	697
Final R ₁ values (all data)	0.0942
Final wR(F ²) values (all data)	0.2320
Goodness-of-fit on F ²	1.053

Table App.4. Homoleptic complex **15**.

Compound reference	Homoleptic complex 15
Chemical formula	C ₅₄ H ₅₈ F ₁₂ N ₁₀ P ₂ Ru
Formula mass	1238.32
Crystal system	Orthorhombic
Space group	P _{bca}
a/ Å	16.851(3)
b/ Å	16.362(3)
c/ Å	43.245(9)
α (°)	90.00
β (°)	90.00
γ (°)	90.00
Unit cell volume/ Å ³	11923(4)
T / K	200.0
No. of formula units per cell, Z	8
No. of reflections measured	97207
No. of independent reflections	10418
No. params refined	803
Final R ₁ values (all data)	0.0791
Final wR(F ²) values (all data)	0.1960
Goodness-of-fit on F ²	1.285

Table App.5. Heteroleptic complex **16**.

Compound reference	Heteroleptic complex 16
Chemical formula	C ₄₂ H ₄₀ F ₁₂ N ₈ P ₂ Ru
Formula mass	1047.82
Crystal system	monoclinic
Space group	C2/c
a/ Å	26.357(5)
b/ Å	9.303(19)
c/ Å	40.918(18)
α (°)	90.00
β (°)	108.24(3)
γ (°)	90.00
Unit cell volume/ Å ³	9528(4)
T / K	200.0
No. of formula units per cell, Z	8
No. of reflections measured	51467
No. of independent reflections	8243
No. params refined	800
Final R ₁ values (all data)	0.0720
Final wR(F ²) values (all data)	0.1668
Goodness-of-fit on F ²	1.159

Table App.6. Heteroleptic complex **19**.

Compound reference	Heteroleptic complex 19
Chemical formula	C ₄₂ H ₄₈ F ₁₂ N ₄ P ₂ S ₂ Ru
Formula mass	1064.21
Crystal system	monoclinic
Space group	C2/c
a/ Å	42.799(9)
b/ Å	14.584(3)
c/ Å	14.462(3)
α (°)	90.00
β (°)	100.01(3)
γ (°)	90.00
Unit cell volume/ Å ³	8889(3)
T / K	200.0
No. of formula units per cell, Z	8
No. of reflections measured	35940
No. of independent reflections	7746
No. params refined	576
Final R ₁ values (all data)	0.2126
Final wR(F ²) values (all data)	0.4354
Goodness-of-fit on F ²	1.135

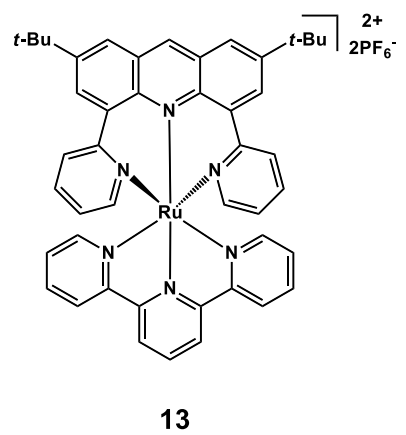
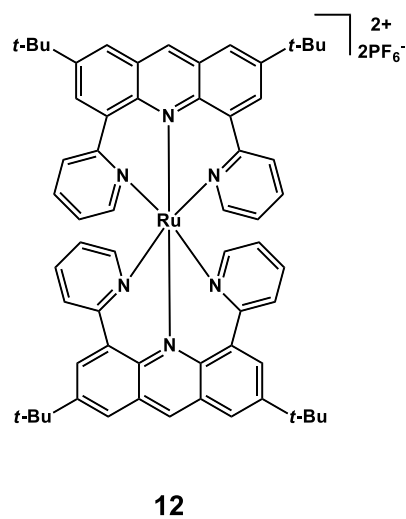
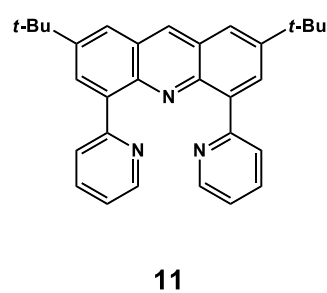
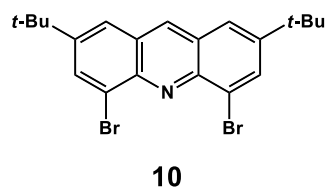
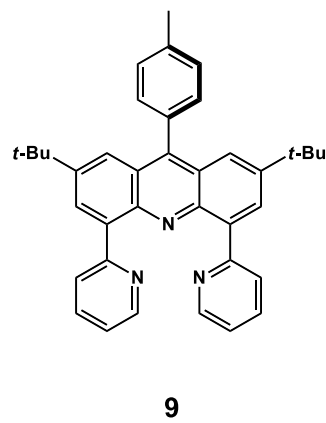
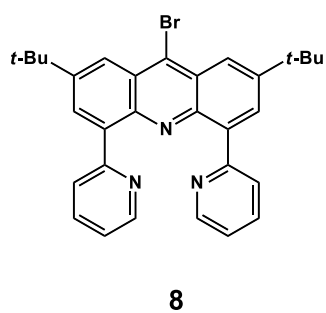
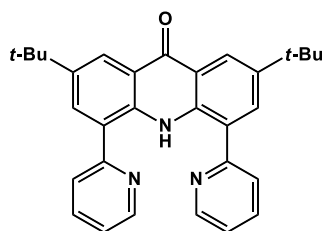
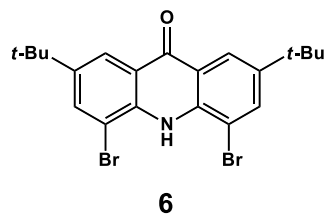
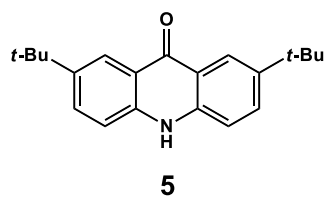
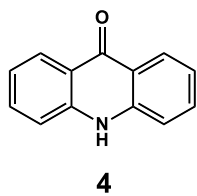
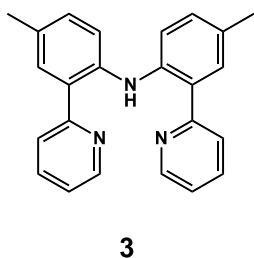
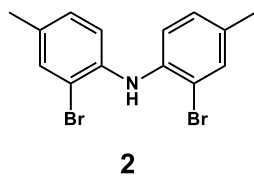
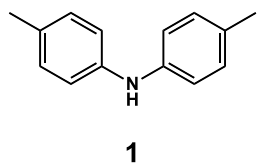
Table App.7. Homoleptic complex **21**.

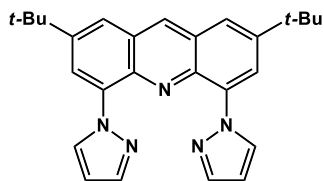
Compound reference	Homoleptic complex 21
Chemical formula	C ₃₈ H ₃₄ F ₁₂ N ₂ P ₂ S ₄ Ru
Formula mass	1037.99
Crystal system	triclinic
Space group	P ₋₁
a/ Å	13.671(3)
b/ Å	17.335(4)
c/ Å	21.741(4)
α (°)	89.92(3)
β (°)	74.07(3)
γ (°)	73.91(3)
Unit cell volume/ Å ³	4744.8(19)
T / K	200.0
No. of formula units per cell, Z	4
No. of reflections measured	73177
No. of independent reflections	16540
No. params refined	1349
Final R ₁ values (all data)	0.1591
Final wR(F ²) values (all data)	0.3191
Goodness-of-fit on F ²	1.043

Table App.8. Heteroleptic complex **22**.

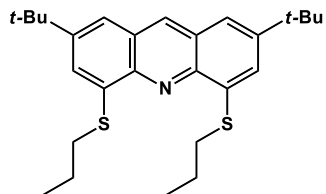
Compound reference	Heteroleptic complex 22
Chemical formula	C ₃₄ H ₂₈ F ₁₂ N ₄ P ₂ S ₂ Ru
Formula mass	948.01
Crystal system	orthorhombic
Space group	<i>P</i> _{bca}
a/ Å	15.338(3)
b/ Å	20.692(4)
c/ Å	26.013(5)
α (°)	90.00
β (°)	90.00
γ (°)	90.00
Unit cell volume/ Å ³	8256(3)
T / K	200.0
No. of formula units per cell, Z	8
No. of reflections measured	54828
No. of independent reflections	12001
No. params refined	627
Final R ₁ values (all data)	0.0588
Final wR(F ²) values (all data)	0.1155
Goodness-of-fit on F ²	1.099

List of molecules

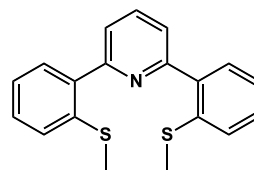




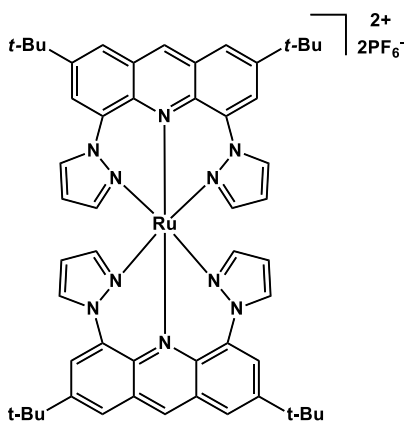
14



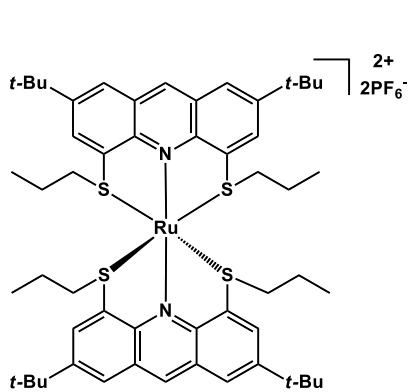
17



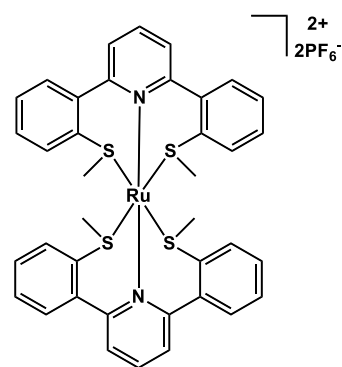
20



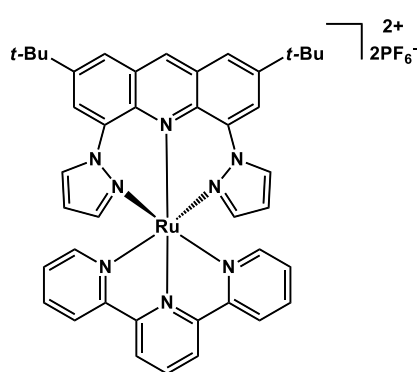
15



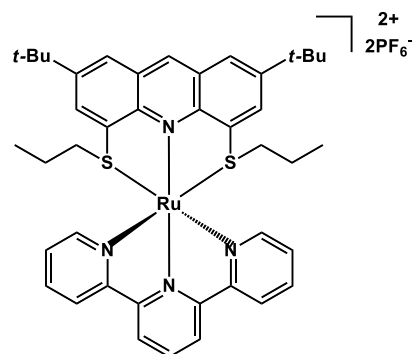
18



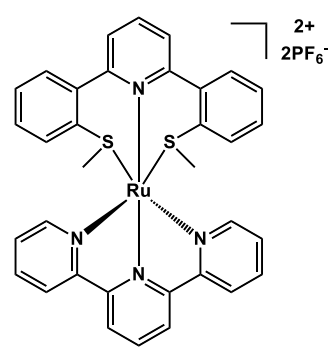
21



16



19



22

Abstract

Light-induced electron and energy transfer in molecular arrays is being extensively studied in view of artificial photosynthesis. In this context, $[\text{Ru}(\text{bpy})_3]^{2+}$ derivatives have been widely used, due to their favorable photophysical properties, i.e. lifetimes in the μs range at room temperature, high emission quantum yields, and strong oxidizing and reducing capability. The electronic structural design of most ruthenium(II) complexes is of great importance by specifying the complexes' photophysical, photochemical, and electrochemical properties. As a consequence, the main theme of this thesis is to explore the coordination properties of new tridentate ligands on the ruthenium cation. This work describes the synthesis of these new tridentate ligands based on the acridine heterocycle with different moieties at positions 4 and 5. Octahedral ruthenium(II) complexes were then constructed around these acridine-based ligands, with tuned energy levels of the functionally active ^3MC and $^3\text{MLCT}$ excited states. Very few acridine derivatives are substituted at positions 4 and 5. The synthetic strategy for the target ligands starts from acridone. The 4,5-dibromoacridine was obtained in four synthetic steps and this common precursor was subsequently used for the construction of tridentate (NNN) ligands with pyridine and pyrazole. In addition, a thioether acridine-based tridentate ligand (SNS) analogue was synthesized, and another tridentate thioether (SNS) ligand, without an acridine heterocycle, was prepared to gain some flexibility within the ligand scaffold. The corresponding homoleptic complexes with 6-membered metallacycles only adopted a *facial* octahedral geometry. Thus, the heteroleptic complexes were prepared in combination with a planar terpyridine ligand in order to force the constrained and rigid ligands to coordinate in a *meridional* fashion on the metal. The electrochemical, photophysical, and photochemical properties of all complexes were studied and the structure for most of these Ru(II) complexes was deduced by X-ray diffraction crystallography experiments. The bis-tridentate Ru(II) complexes based on the flexible (SNS) thioether ligand were photoactive: they were able to undergo a photosubstitution reaction, by replacing the tridentate thioether ligand with monodentate ligands, upon white light exposure.

Résumé

Le transfert d'électron et d'énergie induit par la lumière dans des dispositifs moléculaires est largement étudié dans le domaine de la photosynthèse artificielle. Dans ce contexte, les dérivés du $[\text{Ru}(\text{bpy})_3]^{2+}$ ont été très utilisés, en raison de leurs propriétés photophysiques favorables, à savoir des durées de vie de l'ordre des μs à température ambiante, des rendements quantiques d'émission élevés et un fort pouvoir d'oxydation et de réduction. La conception de la structure électronique des complexes de ruthénium(II) revêt une très grande importance, car celle-ci dictera les propriétés photophysiques, photochimiques et électrochimiques de ces complexes. En conséquence, le sujet principal de cette thèse est d'explorer les propriétés de coordination de nouveaux ligands tridentes sur le cation ruthénium. Ce travail décrit la synthèse de ces nouveaux ligands basés sur l'hétérocycle acridine avec différents fragments en positions 4 et 5. Les complexes de ruthénium(II) octaédriques correspondants ont ensuite été construits autour de ces ligands à base d'acridine, avec des niveaux d'énergie ajustés des états excités ^3MC et $^3\text{MLCT}$ fonctionnellement actifs. Très peu de dérivés d'acridine sont substitués aux positions 4 et 5. La stratégie de synthèse pour les ligands cibles commence sur l'acridone. La 4,5-dibromoacridine a été obtenue en quatre étapes synthétiques et ce précurseur commun a ensuite été utilisé pour la construction de ligands tridentés (NNN) avec de la pyridine et du pyrazole. De plus, un analogue de ligand tridentate (SNS) à base de thioéther acridine a été synthétisé, et un autre ligand tridentate de thioéther (SNS), sans hétérocycle acridine, a été préparé dans le but d'acquérir une certaine flexibilité dans la structure. Les complexes homoleptiques correspondants avec des métallacycles à 6 chaînons ont tous adopté une géométrie octaédrique *faciale*. Ainsi, les complexes hétéroleptiques ont été préparés en combinaison avec un ligand terpyridine plan afin de forcer les ligands contraints et rigides à se coordiner de manière *méridienne* sur le métal. Les propriétés électrochimiques, photophysiques et photochimiques de tous les complexes ont été étudiées et la structure de la plupart de ces complexes de Ru(II) a été déduite par des expériences de cristallographie par diffraction des rayons X. Les complexes bis-tridentés de Ru(II) basés sur le ligand thioéther flexible (SNS), se sont montrés photoactifs: lors d'une exposition à la lumière blanche ils subissent une réaction de photosubstitution, remplaçant le ligand thioéther tridentate par des ligands monodentates.

